ON THE ASSEMBLY OF NANODEVICES

A Thesis by

by

ALFREDO DOUGLAS BOBADILLA LLERENA

Submitted to the Office of Graduate and Professional Studies of
Texas A&M University
in partial fulfillment of the requirements for the degree of

DOCTOR OF PHILOSOPHY

Chair of Committee,	Jorge M. Seminario
Committee Members,	Chin Su
	Laszlo Kish
	Mustafa Akbulut
Head of Department,	Chanan Singh

December 2014

Major Subject: Electrical Engineering

ABSTRACT

Carbon nanostructures are 1D and 2D materials with potential to enable new markets in the electronic industry due to their novel properties which have been recognized recently with the awarding of two Nobel Prizes in physics. But their very small size constitutes a new challenge in the manufacturing industry.

We adapt molecular simulation tools and microfabrication techniques to enable the analysis of different scenarios on the assembly and characterization of carbon-based nanodevices.

In an in silico experiment, by using molecular dynamics we analyze the outcome of bombarding carbon nanotube with argon ions, we find that for very high energies the type of defect created is almost exclusively single vacancy which is important in the development of spin-based electronics.

An electric field can selectively guide nanoparticles in liquid media. We are able to guide the positioning of carbon nanotubes suspended in a four-electrode configuration; and after inducing an electrical breakdown event in a parallel array of nanotube devices we find a strong nonlinear electrical characteristic.

Combining carbon nanostructures with DNA molecules offers the possibility of exploiting the chemical sensitivity of DNA and transducing it in an electrical signal. By using molecular dynamics, we predict a stable structure for a non-covalent DNA junction; we explore two different cases, with carbon nanotube or graphene as interface electrodes. Electronic structure calculations predict the DNA electronic structure is coupled to the carbon electron nano devices and would allow sensing of a chemical environment.

In the field of drug-delivery, biological barriers and the immune system constitute challenges for the effective delivery of a drug to targeted areas of the human organism. By using molecular dynamics, we predict the structure and stability of maximum PEGylated carbon nanotube and predict it is in the nano-sized regime (~40 nm) which is an important requirement in the effective delivery of drugs.

New fabrication techniques are required in the manufacturing of carbon nano devices. We fabricate fluidic devices and analyze in a novel configuration the electrochemical response of graphene ribbons. We find this device promising for detecting very low level of europium in liquid solution.

DEDICATION

To my grandparents.

TABLE OF CONTENTS

Page

LIST OF FIGURES

FIGURE Page

FIGURE Page

FIGURE Page

FIGURE Page

FIGURE Page

FIGURE Page

FIGURE Page

FIGURE Page

FIGURE Page

FIGURE Page

LIST OF TABLES

TABLE Page

1. INTRODUCTION AND LITERATURE REVIEW

Carbon nanostructures can exhibit unique properties that include extremely high mechanical strength, high thermal conductivity, and excellent chemical and thermal stability. Furthermore, carbon nanostructures can be complexed with other molecules showing different functional capabilities. Because the nanoscale devices are comparable in size to molecules and are much smaller than biological cells, potential applications of these devices are on single-molecule analytical sensors, biosensors, single cell diagnostics, implantable devices and drug-delivery.

1.1 Engineering carbon nanostructures

Irradiation of carbon nanostructured materials with electron or ion beams constitutes a novel technique to engineer the structure and properties of these nanomaterials with high precision. [1-4] Guo *et al*. (2006) [5] got cutting a carbon nanotube (CNT) by opening a window in a PMMA thin film covering CNT, and then exposing this zone to reactive oxygen plasma. Under optimized conditions, ~ 25% of the tubes are completely cut among ~2500 devices tested. Other technique used to engineer nanostructured materials is electrical breakdown, which occur in SWCNT depending on the contact resistances, nanotube length, applied gate voltage, heat transfer to the contacts and its structural perfection. [6-8] Hadeed and Durkan (2007) [9] controlled the size and position of a gap in gold-palladium nanowires by changing the electromigration and joule heating regimes which determine the electrical breakdown of the nanowire.

1.2 A peptide covalent bond between carbon nanotube and DNA

Guo *et al*. (2008) [10] developed a method to connect a gapped carbon nanotube (CNT) with single DNA molecules. In their method, a gap is created in the carbon nanotube by oxidative cutting with reactive ion etching; all the CNT is covered with a PMMA film but a small CNT zone is exposed to oxygen plasma by selectively opening a small window on the film with e-beam lithography. During the etching process, carbon nanotube is functionalized with carboxyl groups. Amine functionalization of DNA molecules allowed a covalent amide linkage to CNT functionalized with carboxyl groups. Using this method they obtained 10 working devices out of 370 that were tested. This low yield on successful interconnection of carbon nanotube with DNA is due to an inherent difficulty on creating a covalent bond. Interestingly they found a dsDNA molecule does not conduct electricity when a base mismatch is present.

1.3 A carbon nanotube-DNA origami junction

A nucleic acid-labelled single-walled carbon nanotube (NL-SWCNT) can be aligned along patterns of the corresponding complementary single-stranded DNAs (ssDNA) ‘hooks’ on DNA origami. Nucleic acid labels are partially protected by complementary strands before they bind to the hooks on DNA origami. Each linker also has a 40-base poly-thymine nucleobase domain that adsorbs onto the SWCNT sidewall via vdW forces. The protection strand prevents adsorption of the labelling domain onto SWCNT. By using this technique, two carbon nanotubes can be aligned on a DNA origami structure, with a carbon nanotube on each side of the DNA origami template, and an orthogonal orientation between carbon nanotubes [11].

1.4 Observation of electrical gating by ssDNA upon binding to carbon nanotube

It has been reported that a DNA wrapped carbon nanotube device can change from metallic behavior in dry conditions to semiconductor behavior in wet conditions [12]. Ouellette (2008) [13] analyzed the time evolution of electrical current in a suspended carbon nanotube positioned in a microfluidic channel through which DNA molecules were allowed to flow. Electrical spikes were observed when DNA molecules were present in the microfluidic channel; DNA molecules constantly flowed through the microfluidic channel and electrostatic screening of van der Waals interaction due to ions was minimized. Spikes current levels are below or above the original CNT current level depending on the type of DNA molecule tested.

Those spikes are produced every time a DNA molecule reaches the carbon nanotube surface, and a different change in current level, positive or negative spikes, is observed for different DNA molecules. A DNA sequence dependence is further suggested by the known correlation between nucleobases polarizability and CNT-DNA interaction strength reported by Gowtham *et al*. [14, 15].

1.5 A need for a simple and low-cost detection method of actinides in the environment

Actinide elements are radioactive and find applications in nuclear weapons and as fuel in nuclear reactors. A serious concern is the radiotoxicity as well as chemical toxicity of actinides and their migration in the environment [16-18]. The techniques typically available for trace analysis are efficient but complex and costly [19-21].

Anions of phosphate, carbonate, oxalate, and acetate have been reported to increase the adsorption of Eu (III) to carbon materials, whereas nitrate, chloride and cations have a negative effect on the adsorption capacity [22-24]. Electrical gate electrodes can induce a negative charge in solid state graphene-based field-effect transistors (FET) devices [25, 26] and could play a role on the performance of ion-sensitive FETs.

2. IRRADIATION-INDUCED DEFECTS IN CARBON NANOTUBE[*]

Ion beams can be used to tailor the structure and properties of carbon nanostructures. We explore, by using molecular dynamics simulations, the effects of irradiating silica-supported single walled carbon nanotube with an ion beam. We analyze defects produced at several energy levels when one argon atom collides with a single-walled carbon nanotube. At beam energies higher than 32 keV, generated defects were mainly single-vacancy defects. We find, in addition to vacancy defects, chemisorption on CNT sidewall, doping of the silica substrate, and covalent cross linking between CNT and the substrate; these types of complex defects have a maximum probability of occurrence around 100 eV and close to null probability around 100 keV.

2.1 Introduction

Carbon nanostructures are of high technological importance due to their unique mechanical [27-29] and electrical properties [30-33], and rich physics phenomena [34-39] encountered in many studies. Electron-beam [40-42] and ion-beam irradiation [43-46] are standard techniques to fabricate carbon-based nanodevices. Scanning probe microscopy (SPM) techniques can be used to modify carbon nanostructure properties but they are not adequate for mass production [2, 47]. Focused ion beam and e-beam lithography systems, on the other hand, can be scanned on carbon structure, orders of magnitudes faster than mechanical tips, producing an ion-beam spot of a few nanometers

---

[*] Reproduced in part with permission from A.D. Bobadilla and J.M. Seminario, J. Phys. Chem. C, Article In Press DOI: 10.1021/jp5098074. Copyright 2014 American Chemical Society.

in diameter [48, 49]. Alternatively, a high-speed stream of glow discharge plasma allows selective etching of carbon nanostructures [10, 50, 51].

Imaging, at the atomistic detail, of defects produced in carbon nanostructures by particle beam irradiation is very difficult to obtain from experiments [4, 52-56]. Irradiation-induced vacancy defects appear as bright spots in atomically resolved STM images [57-60]. Molecular dynamics simulations allow predicting structural configurations adopted by carbon nanostructures after exposure to a particle beam [61-65].

The effect of argon ion irradiation on carbon nanotube structure has been studied mainly in the energy range from 100 eV to 3 keV [57, 58, 60, 66]. The effects of ion irradiation on suspended graphene have been reported for the energy range 10 eV-10 MeV by molecular dynamics with a mixed Ziegler-Biersack-Littmark/Brenner potential and an adaptive timestep with minimum timescale of attoseconds [67, 68].

The most common defects produced upon exposure to ion irradiation are vacancy defects. Magnetism has been associated with single and triple vacancy defects in single walled carbon nanotubes, this due mainly to the presence of dangling bonds in the most stable structure for these type of defects [69, 70], enabling possible scenarios for spin-based electronics [71, 72].

In the present work, we perform molecular dynamics simulations to analyze defects induced by an argon atom accelerated against a single-walled carbon nanotube supported on a silicon dioxide substrate. The argon beam energy range studied is from 32 eV to 320 keV.

2.2 Methodology

C-C, Si-C and Si-Si interactions are modeled with the three-body Tersoff potential [73, 74], which smoothly connects to a Ziegler-Biersack-Littmark (ZBL) repulsive potential [75]. The standard universal ZBL potential fit to reasonably accurate quantum calculations of interatomic potentials in the repulsive region and can be easily evaluated for any atom pair [76]. Ion beam bombardment with argon involves no chemical reaction since it is a noble gas; therefore, argon-carbon interactions are modeled with the ZBL potential. Electrostatic interactions between atoms due to nuclear charges are taken into account in the ZBL potential. In previous works on ion bombardment of carbon nanotubes, it was necessary applying a constraint to carbon nanotube edges to avoid reflection of pressure waves; in our case, the silicon dioxide substrate plays an important role on the dissipation of heat generated during ion collision. Our choice of interatomic potentials for CNT-SiO_2 does not take into account long-range Coulombic interactions since interfacial thermal transport depends only on the vdW interaction between the CNT and substrate atoms.

2.2.1 The Tersoff/ZBL potential

The total potential energy, V, is represented by an empirical interatomic potential V_{ij},

$$V = \frac{1}{2}\sum_i \sum_{j \neq i} V_{ij} \tag{2.1}$$

where V_{ij} includes contributions from ZBL and Tersoff potentials,

$$V_{ij} = \left(1 - f_F(r_{ij})\right) V_{ij}^{ZBL} + f_F(r_{ij}) V_{ij}{}^{Tersoff} \tag{2.2}$$

The f_F term is a Fermi-like function

$$f_F(r_{ij}) = \frac{1}{1+e^{-A_F(r_{ij}-r_C)}} \tag{2.3}$$

which allows a smooth transition between ZBL and Tersoff potentials. Two parameters from Equation 3 allow fitting the transition between potentials; A_F controls how sharp is the transition between ZBL and Tersoff potential, and r_c represents a cutoff distance for the ZBL potential. We use the Tersoff/ZBL force field as implemented in the program LAMMPS [77] (vide infra).

$$V_{ij}^{ZBL} = \frac{1}{4\pi\varepsilon_0} \frac{Z_i Z_j q^2}{r_{ij}} \emptyset\left(\frac{r_{ij}}{a}\right) \tag{2.4}$$

The first factor in the ZBL potential is the Coulomb repulsive term; Z_i and Z_j are the number of protons in each nucleus, q is the electron charge, and ε_0 as the permittivity of vacuum. The second factor is the ZBL universal screening function $\emptyset(x)$,

$$\emptyset(x) = 0.1818e^{-3.2x} + 0.5099e^{-0.9423x} + 0.2802e^{-0.4029x} + 0.02817e^{-0.2016x} \tag{2.5}$$

with

$$a = \frac{0.8854 a_0}{Z_i^{0.23} + Z_j^{0.23}} \tag{2.6}$$

and a_o is the Bohr radius. The Tersoff potential considers two-body (f_R) and three-body (f_A), repulsive and attractive, respectively, interactions,

$$V_{ij}^{Tersoff} = f_C(r_{ij})\left[f_R(r_{ij}) + b_{ij} f_A(r_{ij})\right] \tag{2.7}$$

The summations in Equation 1 are over all neighbors of atom *i* within a cutoff distance $R + D$,

$$f_C(r) = \begin{cases} 1 & ; \quad r < R - D \\ \frac{1}{2} - \frac{1}{2}\sin\left(\frac{\pi}{2}\frac{r-R}{D}\right) & ; \quad R - D < r < R + D \\ 0 & ; \quad r > R + D \end{cases} \tag{2.8}$$

The f_C term corresponds to smooth cutoff functions, which decrease from 1 to 0 in the range $R - D < r < R + D$

$$f_R(r) = Ae^{-\lambda_1 r} \tag{2.9}$$

and

$$f_A(r) = Be^{-\lambda_2 r} \tag{2.10}$$

The Tersoff potential is based on the concept of bond order; the strength of a bond between two atoms is not constant, but depends on the local environment. The bond order for the bond joining atoms *i* and *j* is represented by the parameter b_{ij},

$$b_{ij} = \left(1 + \beta^n \zeta_{ij}^n\right)^{-\frac{1}{2n}} \tag{2.11}$$

and it is a decreasing function of a coordination parameter ζ_{ij} assigned to the bond. The bond *ij* is weakened by the presence of other bonds *ik* involving atom *i*, and the amount of weakening is determined depending on where the other bonds are placed. The term b_{ij}, thus, accentuates or diminishes the attractive force relative to the repulsive force, according to the environment. The effective coordination number of atom *i* is defined by ζ_{ij}; it represents the number of nearest neighbors, taking into account the relative distance of two neighbors (r_{ij} and r_{ik}) and the bond-angle θ.

$$\zeta_{ij} = \sum_{k \neq ij} f_C(r_{ik}) g(\theta_{ijk}) e^{-\left[\lambda_3^3 (r_{ij} - r_{ik})^m\right]} \tag{2.12}$$

Different chemical effects affecting the strength of the covalent bonding interaction, such as coordination numbers, bond angles, and conjugation effects, are all accounted for in the b_{ij} term (Equation 11).

The function $g(\theta)$ has a minimum for $cos(\theta) = cos(\theta_0)$, and the parameter d determines how sharp the dependence on angle is, and c expresses the strength of the angular effect.

$$g(\theta) = \gamma_{ijk}\left(1 + \frac{c^2}{d^2} - \frac{c^2}{|d^2 + (cos\theta - cos\theta_0)^2|}\right) \tag{2.13}$$

Table 2.1. Tersoff/ZBL parameters for carbon, oxygen and silicon. For the Fermi-like function, A_F and r_C values are 14 Å^{-1} and 0.95 Å respectively. Argon atom interaction with silica and carbon atoms is modeled with a ZBL potential.

Tersoff parameter	C	O	Si
A (eV)	1.3936×10^3	1.88255×10^3	1.8308×10^3
B (eV)	3.467×10^2	2.18787×10^2	4.7118×10^2
λ (Å^{-1})	3.4879	4.17108	2.4799
μ (Å^{-1})	2.2119	2.35692	1.7322
β	1.5724×10^{-7}	1.1632×10^{-7}	1.1×10^{-6}
n	7.2751×10^{-1}	1.04968	7.8734×10^{-1}
c	3.8049×10^4	6.46921×10^4	1.0039×10^5
d	4.384	4.11127	1.6217×10^1
h	-5.7058×10^{-1}	-8.45922×10^{-1}	-5.9825×10^{-1}
R (Å)	1.8	1.7	2.7
S (Å)	2.1	2.0	3.0
Z_i	6	8	14

The argon atom is positioned such that it will collide with carbon atoms around the 10nm length gray zone (Figure 2.1) of CNT; therefore, interaction between this gray carbon atoms and SiO_2 is modeled with a Tersoff/ZBL potential since the argon atom causes the breaking and formation of chemical bonds when travelling through this zone.

2.2.2 The Lennard-Jones potential

Interactions between SiO_2 and green carbon atoms (Figure 2.1.) are modeled with van der Waals forces using the 12-6 Lennard-Jones potential.

$$V(r) = 4\varepsilon\left[\left(\frac{\sigma}{r}\right)^{12} - \left(\frac{\sigma}{r}\right)^{6}\right] \tag{2.14}$$

where ε is the energy depth of the potential well, σ is the finite distance at which the inter-particle potential is zero, and r is the interatomic distance.

The r^{-12} term describes Pauli repulsion at short ranges due to overlapping electron orbitals and the r^{-6} term describes attraction at long ranges due to dispersion forces. Our Lennard Jones parameters are based on those reported by Rappe *et al.* [78], $\varepsilon_{Si\text{-}C}$=8.909 meV, $\varepsilon_{O\text{-}C}$=3.442 meV, $\sigma_{Si\text{-}C}$=3.326 Å, and $\sigma_{O\text{-}C}$=3.001 Å. The parameters are calculated using the Lorentz-Berthelot mixing rules.

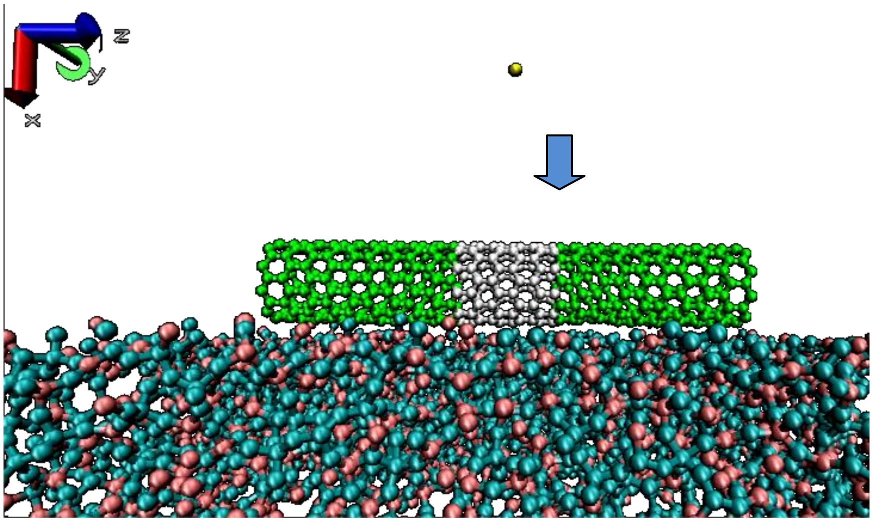

Figure 2.1. Argon ion (yellow) travels in the x-direction (red arrow) towards the central region of the CNT (gray), which is supported on a silicon dioxide surface (SiO_2). Left and right carbon atoms (green) interact via vdW forces with the SiO_2, and central (gray) ones via a hybrid Tersoff/ZBL potential. Silicon and oxygen atoms are also modeled with a hybrid Tersoff/ZBL potential. Argon atom interactions with other atoms are modeled with a ZBL universal repulsive potential.

2.2.3 Creation of initial CNT/SiO_2 structure

The Large-scale Atomic/Molecular Massively Parallel Simulator (LAMMPS) [77] is used to perform molecular dynamics simulations of CNT interaction with argon ions. To generate the native amorphous silicon dioxide layer that typically covers a silicon wafer, a β-cristobalite crystal structure (59.6 Å × 29.8 Å × 69.3 Å) is annealed at 6,000K for 20 ps, at a fixed pressure of 1 bar using a time step of 0.1 fs and with periodic boundary conditions in all three directions; temperature is decreased towards 300K at a rate of 1 K/ps.

To create the silicon dioxide substrate, silica atoms with negative y-coordinates are deleted to obtain an amorphous SiO_2 slab with 4,301 atoms. This structure is rotated 90° degrees around its z-axis, and an additional equilibration is performed at 300K under a canonical ensemble with the Nose-Hoover thermostat during 0.5 ns in a rectangular simulation domain of 132×61×70 Å^3. A (10,0) CNT of 480-atoms, 49.7 Å long, is constructed and inserted into the top half of the simulation domain just above the amorphous SiO_2 slab; the argon atom is positioned 20 Å apart from the CNT (Figure 2.1). The atoms at the bottom of the silicon dioxide are kept fixed to anchor the substrate. Using the conjugate gradient algorithm, an energy minimization of the CNT-SiO_2-Ar system is performed to reach a local potential energy minimum. Then the temperature of the system is raised from 1K to 300K progressively in a 0.75 ns run, followed by an equilibration at 300K during 0.25 ns (Figure 2.2). During this initial process, a Berendsen thermostat is applied to all atoms in the silicon dioxide and carbon nanotube to control temperature and the argon atom is kept fixed. Then an additional equilibration is performed at 300K during 1 ns under a canonical ensemble with the Nose-Hoover thermostat.

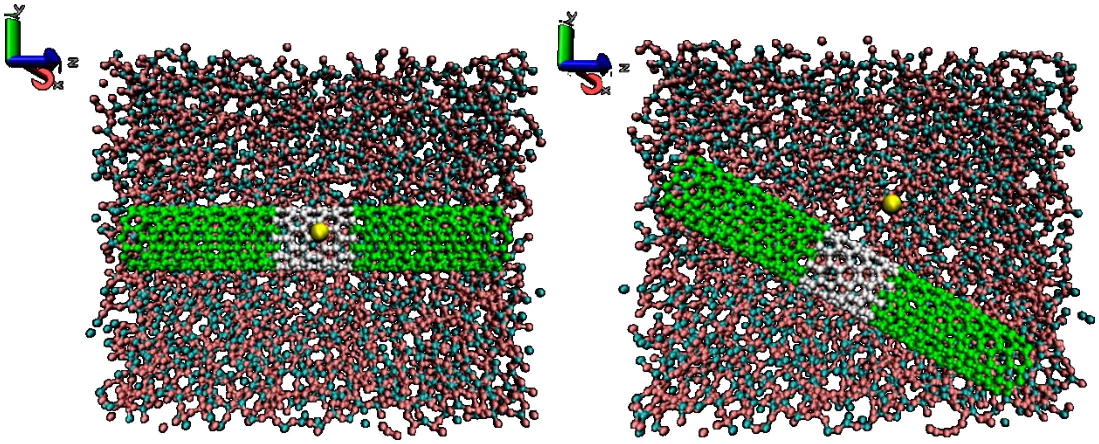

(A) (B)

Figure 2.2. (A) Initial structure for carbon nanotube (CNT) supported on amorphous silicon dioxide substrate with an argon ion (yellow) 20 Å apart from the CNT sidewall. (B) CNT rotates to different orientation on silica substrate during initial temperature increase from 1 to 300 K.

2.2.4 Particle beam energy and MD time step

The argon atom velocity is set to test ion-CNT collision at different energy levels from 32 eV to 320 keV and the argon atom position is set to test collision at 43 different points (Figure 2.3). A microcanonical ensemble is use for the silicon dioxide atoms and carbon atoms during and after ion collision.

For the energy range from 32 eV to 1 keV, a time-step of $5 \times 10^{-18} s$ (5 as) is chosen to simulate the ion-CNT collision. During collision time, creation and breaking of bonds occur. After the collision time, the nanotube experience mainly bending-mode vibrations, and to speed up the simulation the time-step is changed to $5 \times 10^{-17} s$ (50 as), performing a 20 ps simulation time with this time-step. For the energy range from 3.2 keV to 320 keV, a time-step of $1 \times 10^{-18} s$ (1 as) is chosen to simulate the ion-CNT collision. After collision, the time-step is changed to $1 \times 10^{-17} s$ (10 as).

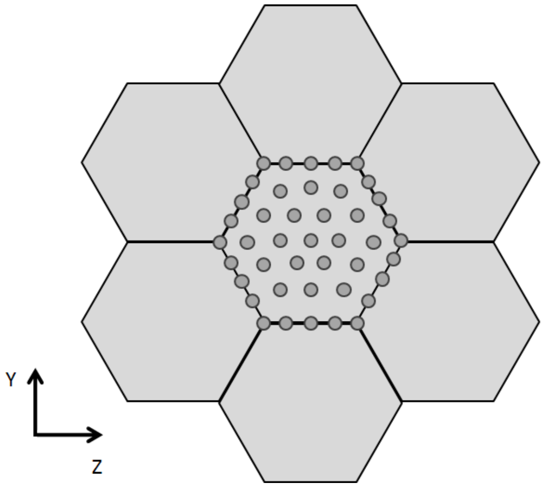

Figure 2.3. Sidewall of single walled carbon nanotube. Gray circles represent chosen points where an argon atom collides with CNT wall. An argon atom travels along X direction. Initial position of Argon atom is 20 Å from CNT sidewall. For every chosen collision point, ten energy levels are tested, 32 eV, 100 eV, 214 eV, 457 eV, 1 keV, 3.2 keV, 10 keV, 32 keV, 100 keV and 320 keV.

Due to the very small scale (1-5 atto seconds) of the initial time step chosen for our MD simulations we compare the de Broglie wavelength (λ) and the distance traveled by the particle beam in a time step, pointing out the Heisenberg uncertainty relation. We find the L distance traveled in a time step is comparable ($L/\lambda<1$) to the de Broglie wavelength for particle beam energy of 32 eV-3.2 keV. However the time uncertainty (t) is larger than the timestep only at particle beam energy of 32 eV.

2.2.5 Defects probability

We perform 430 simulations for each value of incident energy. We obtain the rates of interactions by using probability theory as follows. The variable $X_i^{(\alpha)}$ becomes 1 if the result of the i-th simulation is a defect of type $'\alpha'$ and 0 if the outcome of the i-th simulation is different:

$$X_i^{(\alpha)} = \begin{cases} 1, & \text{if defect is of type } \alpha \\ 0, & \text{if not type } \alpha \end{cases} \tag{2.15}$$

The mean of the results from the first simulation to the n^th^ simulation is defined by

$$\bar{X}_n^{(\alpha)} \equiv \frac{1}{n}\sum_{i=1}^{n} X_i^{(\alpha)} \tag{2.16}$$

By the central limit theorem, when $n \to \infty$, $\bar{X}_{\infty}^{(\alpha)}$ coincides with the defect probability. Number of our simulations is finite, but our n value is big enough so as to make the variance small enough.

And, we define the average number of defects under occurrence as

$$\bar{Y}_n^{(\alpha)} \equiv \frac{\sum_{i=1}^{n} m_i X_i^{(\alpha)}}{\sum_{i=1}^{n} X_i^{(\alpha)}} \qquad (2.17)$$

Where m_i is the number of defects in the i-th simulation.

2.3 Results and discussion

A summary of types of defects and probability of defects produced after argon atom collision on CNT wall is shown in Figure 2.4 and 2.5 respectively, with energy values in logarithmic scale. The probability of defect production on CNT wall (Figure 2.5) increases quickly as energy approach 100 eV, and is maximum and near to constant (about 0.8) in the range from 214 eV to 3.2 keV, then it decreases almost linearly to 0.42 in the range from 3.2 keV to 100 keV. The probability of defect production on CNT wall is low at very high energies, with 0.23 probability at 320 keV (Figure 2.5).

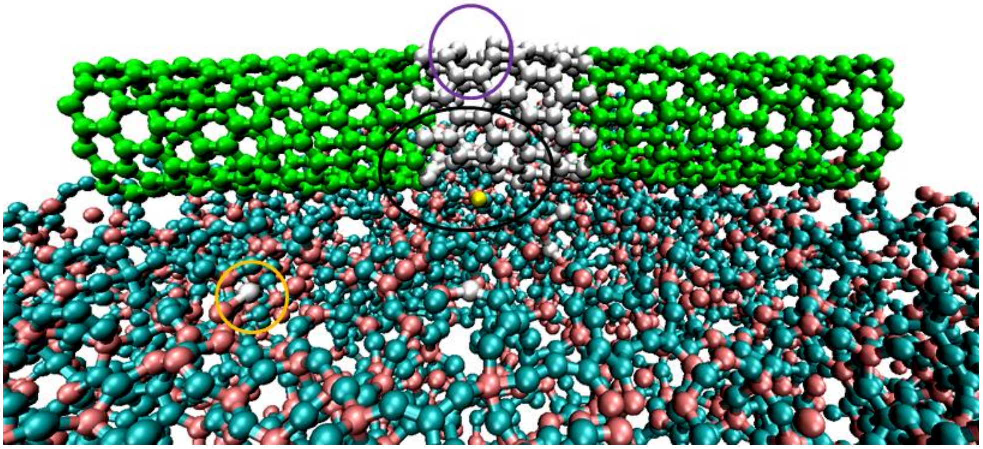

Figure 2.4. Several types of defects generated on carbon nanotube wall and silicon dioxide substrate after argon atom collision. Single vacancy (purple circle), kink (complex) defect (black circle), carbon chemisorption and doping on SiO2 substrate (orange circle).

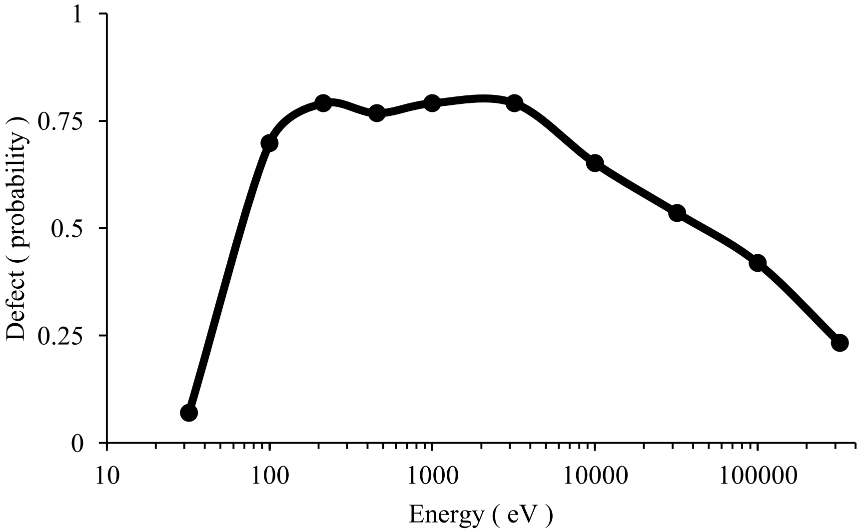

Figure 2.5. Probability of defect occurrence on CNT wall after argon atom collision at different argon beam energy levels. Energy range is in logarithmic scale.

2.3.1 Silica substrate doping

The probability of sputtered carbons shows a similar characteristic to the SiO_2 doping (Figure 2.6a) curve. The probabilities of sputtered C and SiO_2 doping are both maximum in the range between 214 eV and 3.2 keV. The higher number of sputtered carbons is around 3.2 keV and the higher number of substrate doping is around 214 eV (Figure 2.6b).

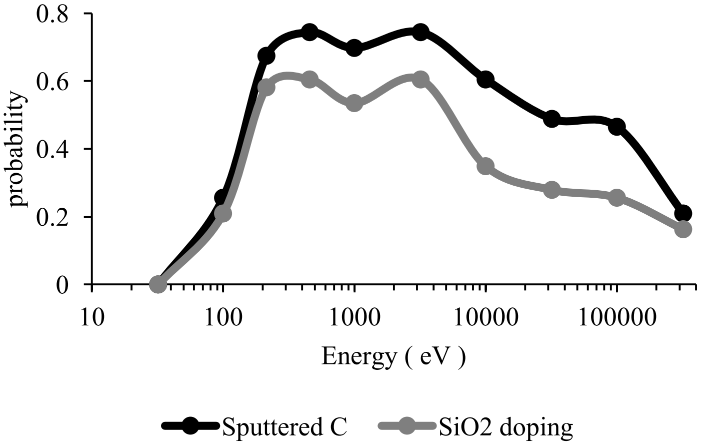

(A)

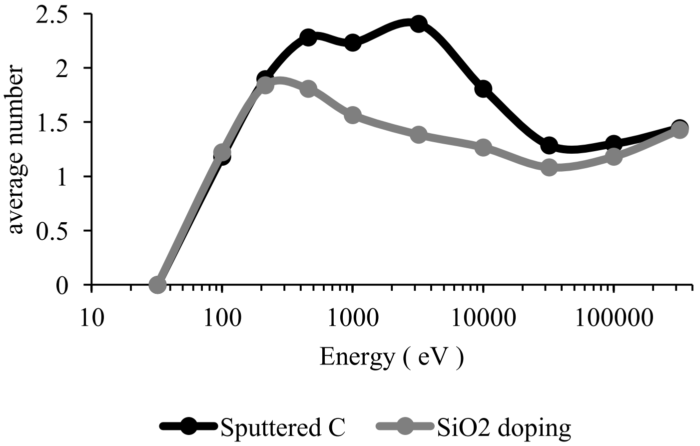

(B)

Figure 2.6. CNT damage by sputtering and silica substrate damage by doping at different argon beam energy levels. (A) Probability of carbon atom sputtered from CNT and probability of SiO_2 doping with carbon atom, (B) average number of carbon atoms sputtered from CNT and average number of carbon atoms doping SiO_2.

Probability of vacancy defect is maximum (0.74) at 457 eV and decreases at a slow rate until it reaches 0.67 value at 10 keV. Then, in the range from 10 keV to 320 keV it decreases linearly but at a higher rate reaching 0.19 at 320 keV. The probability of complex defect has a maximum value of 0.28 at 214 eV and is lower than 0.1 for beam energy higher than 10 keV. Most complex defects are due to interstitial defects or Stone-Wales defects. Kink defects (Figure 2.4) are produced only in the range from 214 eV to 1 keV with probability lower than 0.1. The probability of vacancy defect is higher than 0.65 in the range from 100 eV to 10 keV and the probability of chemisorption has a maximum of 0.58 at 100 eV.

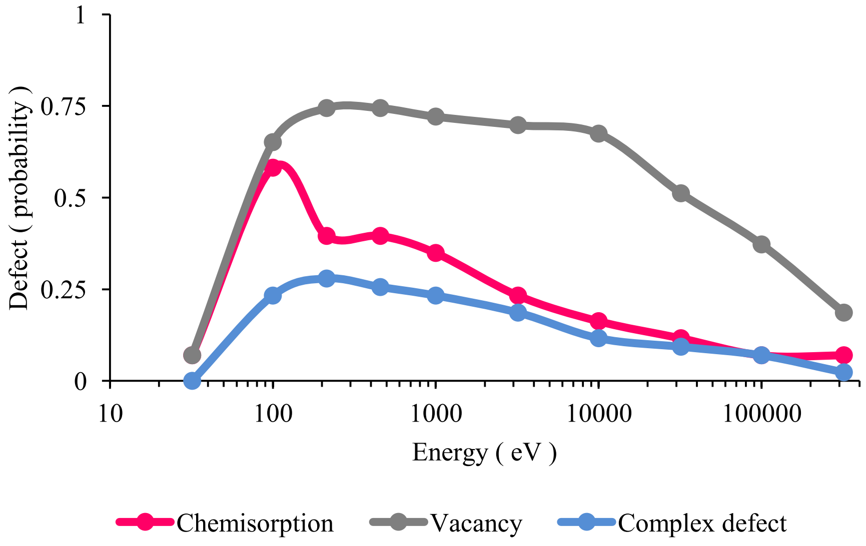

Figure 2.7. Types of defects generated on CNT sidewall after argon atom collision at different argon beam energy levels. Probability of silicon, carbon or oxygen chemisorption on CNT wall (red). Probability of CNT vacancy defect (gray), vacancy defect can be single, double or multiple. And probability of complex defect on CNT wall (blue).

2.3.2 CNT vacancy defects

Probability for Vacancy defect is always higher than those for chemisorption and complex defects (Figure 2.7); this is consistent with the fact that most sputtered carbon atoms end up doping the silica substrate, according to the trend in Figure 2.6a. And for very high energies, the probability for chemisorption and complex defect is low (less than 0.1 at 320 keV).

The probability of single vacancy defect is almost constant in the range from 100 eV to 3.2 keV, with a value of about 0.6, and then it decreases to 0.16 at 320 keV (Figure 2.8a). The average number of single vacancies has a peak value of 1.7 at 1 keV (Figure 2.8b). The probability of double vacancy is always low with a maximum value of 0.33 at 457 eV (Figure 2.8a) and there is no double vacancy defect at very low energy (32 eV) and very high energy (320 keV). The average number of double vacancies is about 1 in the range from 100 eV to 32 keV, and show a peak value of 1.5 at 100 keV while the average number of single vacancies show a peak value of 1.7 at 1 keV (Figure 2.8b).

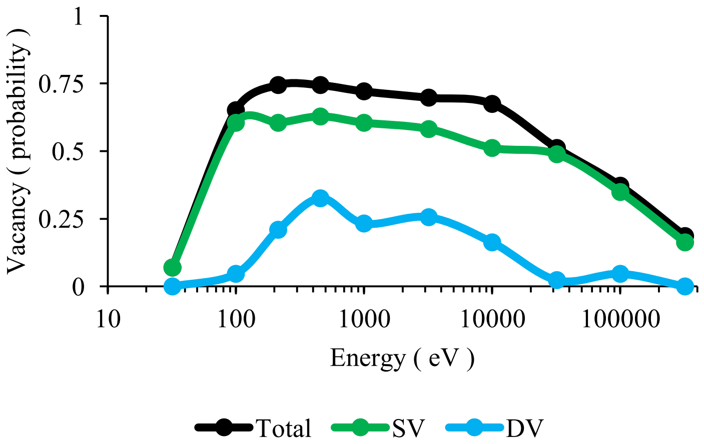

(A)

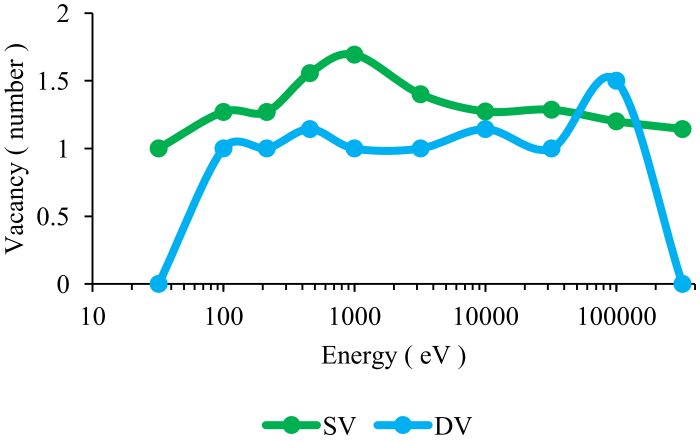

(B)

Figure 2.8. (A) Probability of single and double vacancy at different argon beam energy levels. (B) Average number of single and double vacancies.

2.3.3 CNT chemisorption defects

The probability of chemisorption defects on the CNT wall (Figure 2.9) reaches a maximum at about 100 eV and decreases almost linearly in the energy range from 457 eV to 32 keV. Chemisorption can occur on the internal or external sides of the CNT wall. The former is always due to a carbon atom while the latter can be due to oxygen, silicon or carbon atoms. Probability of chemisorption on internal side of CNT wall is always very low, maximum value being 0.14 at 1 keV (Figure 2.9a).

The probability for C chemisorption is always near to the one for O chemisorption in the range from 32 eV to 320 keV (Figure 2.9b). The probability for C chemisorption shows two peak values, 0.39 at 100 eV and 0.33 at 457 eV, while the probability for O chemisorption has a peak value of 0.28 at 214 eV. For beam energy higher than 1 keV both probabilities decrease, approaching to ~ 0.1 at 3.2 keV and near to zero at 320 keV. The average number of carbon atoms chemisorbed on CNT wall has a minimum value of 0.6 at 10 keV. And the average number of oxygen atoms chemisorbed on CNT wall has a local minimum around 10 keV as well (Figure 2.9c).

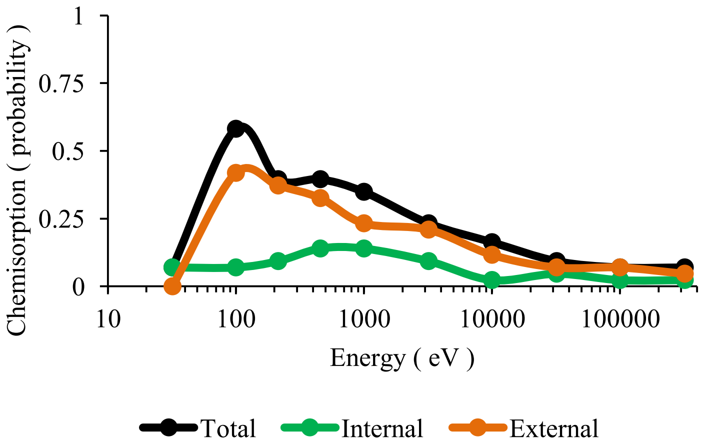

(A)

Figure 2.9. (A) Probability of chemisorption on CNT wall, and probability of chemisorption on internal side of CNT wall or external side of CNT wall. (B) Probability of carbon and oxygen chemisorption. (C) Average number of carbon and oxygen atoms chemisorbed on CNT wall at different argon beam energy levels.

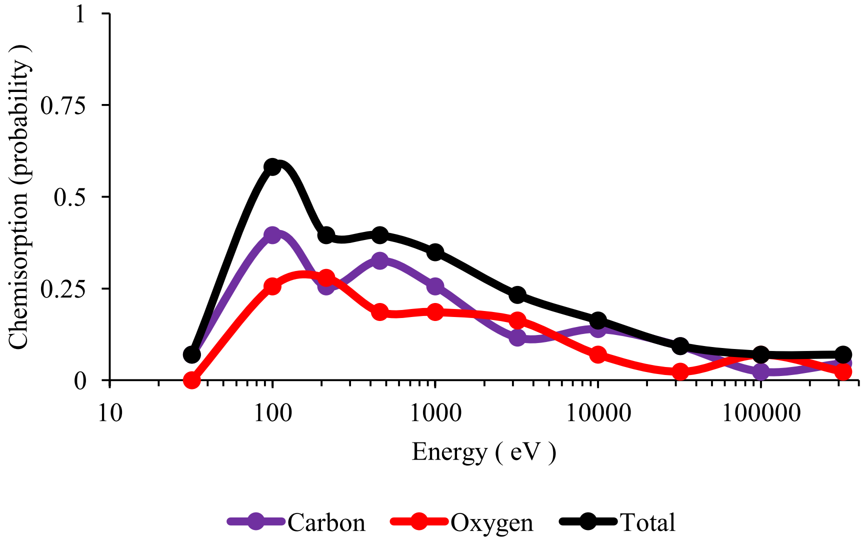

(B)

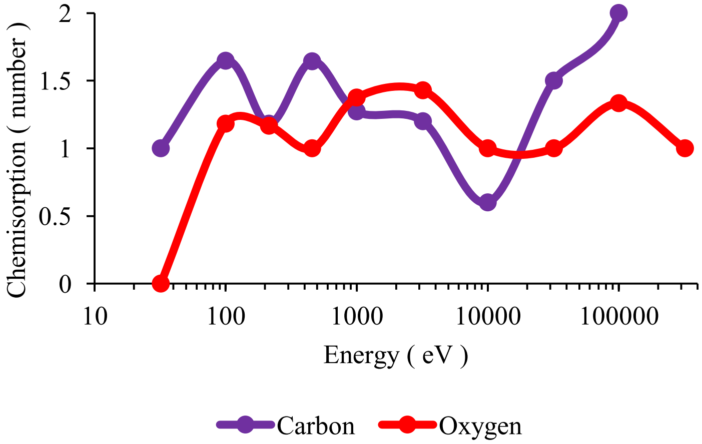

(C)

Figure 2.9. Continued.

2.3.4 CNT-substrate crosslinking

The probability for CNT-substrate crosslinking (Figure 2.10) shows a peak value of 0.53 at beam energy of 100 eV and decreases steadily for higher energy levels (Figure

2.11a). The average number of crosslinkings is maximum at 100 eV and 320 keV with values of 1.43 and 1.5 respectively (Figure 2.11b).

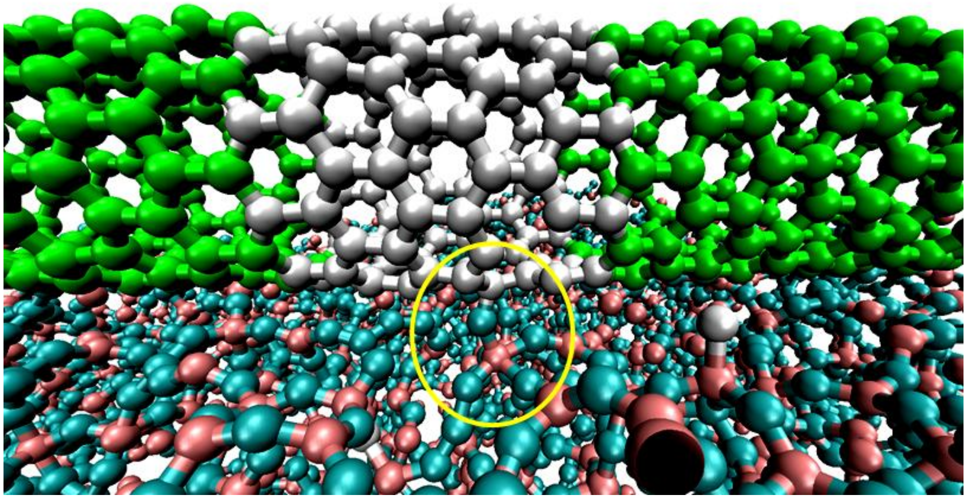

Figure 2.10. Crosslink between CNT and SiO_2 substrate by an oxygen atom (cyan highlighted in yellow).

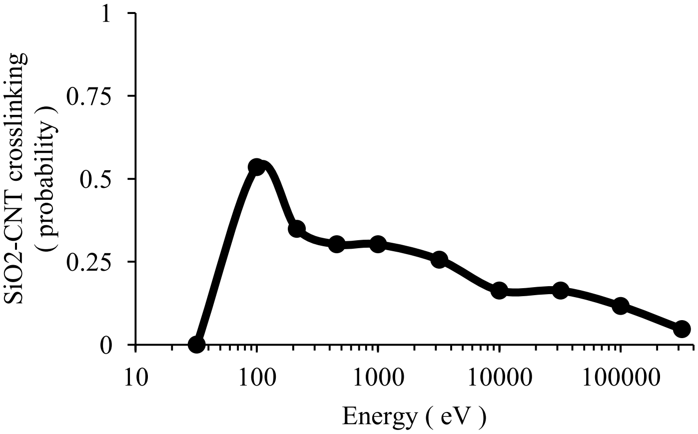

(A)

Figure 2.11. (A) CNT-SiO_2 crosslinking probability and (B) average number of links at different argon beam energy levels.

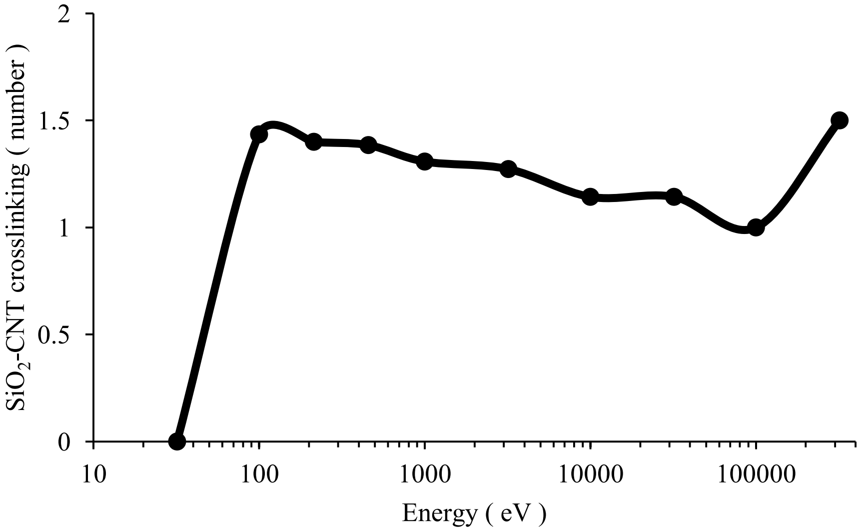

(B)

Figure 2.11. Continued.

2.3.5 Energy transferred to CNT after argon collision

We observe a tendency for low average number of defects and low probability of defects at high beam energies, either on the carbon nanotube or in the silica substrate. We correlate it with a general tendency for decrease on kinetic energy transferred to carbon nanotube when beam energy is higher than 3.2 keV (Figure 2.12). At high beam energy, larger than 3.2 keV, damage occurs mainly when the ion beam atom collides directly with a carbon nanotube atom which is a low probability event.

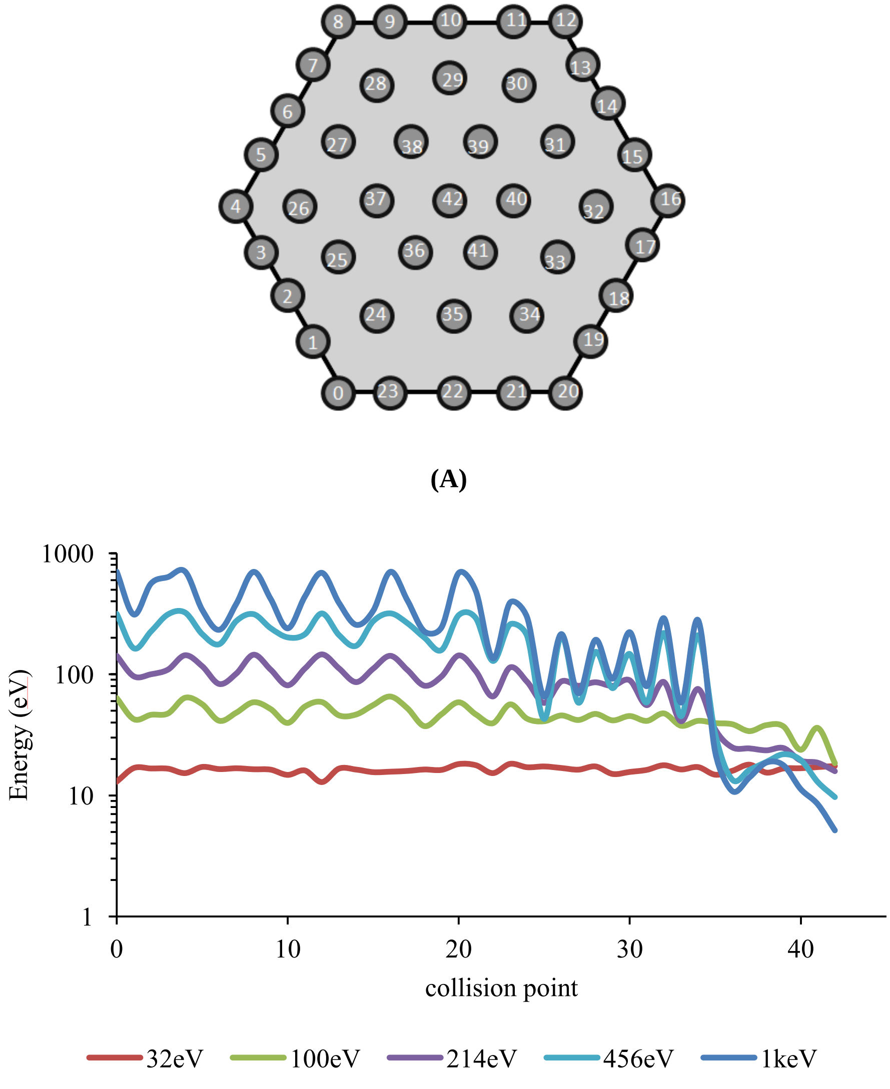

(A)

(B)

Figure 2.12. (A) Ion beam (X,Y) collision points in a benzene ring on CNT sidewall, numbered from 0 to 42; and (B,C) kinetic energy transferred to CNT after ion beam collision. Argon atom travels initially along Z direction and energy transferred to CNT depends on the (X,Y) point of collision on CNT sidewall. Horizontal axis in (b,c) represents the point of collision as labeled in (a). Energy level of Argon atom is color coded (b) from 32 eV to 1 keV and (c) from 3.2 keV to 320 keV.

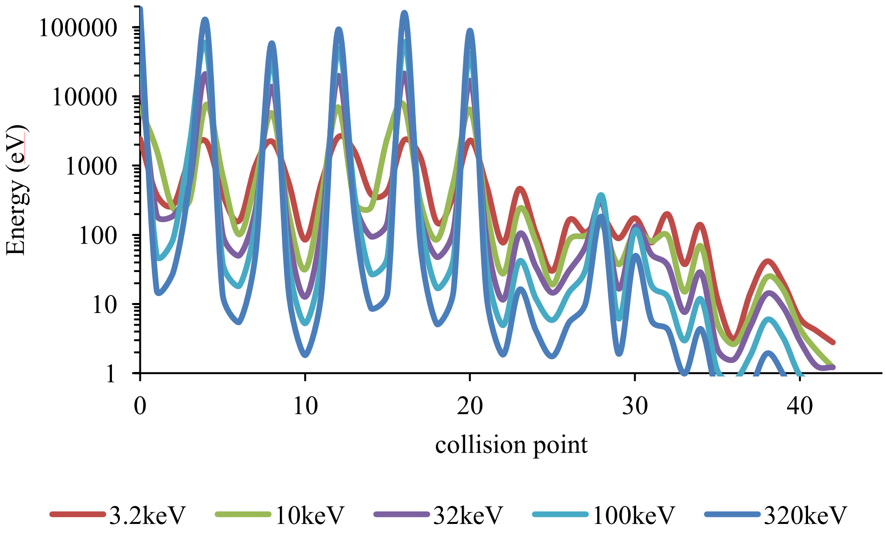

(C)

Figure 2.12. Continued.

2.4 Conclusions

Molecular dynamics simulations were performed on bombardment of single-walled carbon nanotube by argon atoms in the range of 32 eV-320 keV. The probability and average number of irradiation induced defects was quantified at different beam energy levels. We found crosslinking of silica substrate with the carbon nanotube and doping of the silicon dioxide substrate with higher probabilities around 100 eV and 214 eV, respectively. Oxygen and carbon chemisorption on the nanotube sidewall are events with similar probabilities of occurrence in the whole range of energy analyzed and with probability lower than 0.2 for beam energy higher than 3.2 keV. The possibility of defects on the substrate, CNT sidewall and at the interface has to be considered in the performance analysis of carbon nanotubes engineered by ion beam irradiation. We suggest 10 keV as adequate level of ion beam energy to etch carbon nanotube structure with low level of defects by chemisorption, complex defects, CNT-substrate crosslinking or substrate doping. Besides, above 32 keV, the main type of defect is almost exclusively single vacancy defects, therefore argon beam irradiation can allow selective introduction of magnetic impurities, which can be exploited for the development of spintronics devices.

3. NON LINEAR ELECTRON TRANSPORT IN DEFECTIVE CARBON NANOTUBE

Carbon nanotubes are mechanically strong, chemically non-reactive, and excellent devices to obtain a variety of electron transport characteristics needed for an extensive set of applications that goes from medicine to electronics. Therefore they show promise as fundamentals elements in nanotechnology. We report strong nonlinear electron transport behavior in single-walled carbon nanotubes suspended in a four-gold electrode configuration at room temperature after performing electrical breakdown on a parallel array of carbon nanotube devices. Aided by electron transport calculations we suggest multiple double-vacancy defects as the type of nanostructure giving origin to this behavior.

3.1 Introduction

The advent of nanotechnology has allowed developing several possibilities to build nanostructured devices for a variety of applications in practically all science and engineering fields [79, 80]. New raw materials such as carbon nanostructures have become central players. In addition to nanofabrication capabilities, still in exponential development, it allows us to build devices for sensing [81-84] of chemical and biological agents [85, 86] and the fabrication of molecular and nano devices suitable for a post silicon era [87, 88]. Field effect transistor (FET) [89, 90] and nanoelectromechanical devices [91, 92] can be built using carbon nanotubes (CNT) assembled in two-electrode configuration; and this configuration was also used for mass fabrication of CNT-integrated microchips [93, 94]. However, these studies exploit the properties of pristine CNT. A novel electronic structure can be engineered by means of altering the surface of a one-atom thick nanotube [95-98].

Nonlinear electron transport in molecular structures such as the decrease of the rate of electron transport when the bias voltage is progressively increased allows the development of sensors, transistors, photovoltaics, and other devices at higher speeds of operation and at lower power dissipation due to tunneling transfer processes than traditional devices [84, 99-109]. Therefore, molecules showing highly nonlinear electron transport behavior are essential components for a variety of applications.

It has been observed such a nonlinear electron transport behavior in devices where the response current under an increasing potential decreases in a determined range of potentials. A typical implementation of this negative differential impedance also known as negative differential resistance (NDR) has been observed in suspended carbon nanotubes (CNT) due to self-heating effects and increased electron-phonon scattering at relatively large bias voltages [110]. Rinkio *et al.* [111] showed that NDR behavior in suspended CNT can be engineered by integrating a substrate with a high-κ oxide.

In the present work we explore the effects of oxidation on the electrical property of a parallel array of single-walled CNTs. We report a very pronounced NDR behavior of such device and complement our finding by quantum chemical calculations of electron transport.

3.2 Methodology

3.2.1 Device fabrication

An array of electrodes in four-electrode configuration is fabricated by electron–beam lithography (Figure 3.1). The two central electrodes serve as support to obtain a suspended CNT. The gap distance between central electrodes is 150 nm and the distance between end electrodes is 600 nm. The metal electrodes are composed of 90 nm thick gold on 10 nm thick chromium. For dielectrophoresis of CNTs we follow the design rules by Chung *et al.* (2004) [93]. Single-wall CNTs (SWCNT) of ~1.5 nm diameter and ~1-5 μm long and a carbon nanotube dispersant (NanoSperse AC) purchased from Nanolab, Inc, USA are used to prepare a 0.15 μg/mL ethanol solution. An aliquot of this solution (0.1 uL) was placed on the gap while a composite electric field (0.6 Vac at 5 MHz and 0.3 Vdc) is applied between the metal electrodes as shown in Figure 3.1a. The composite DC-AC electric field is applied until the ethanol solution is completely evaporated. A metallic or semiconducting current-voltage characteristic is obtained when correctly positioning the CNTs.

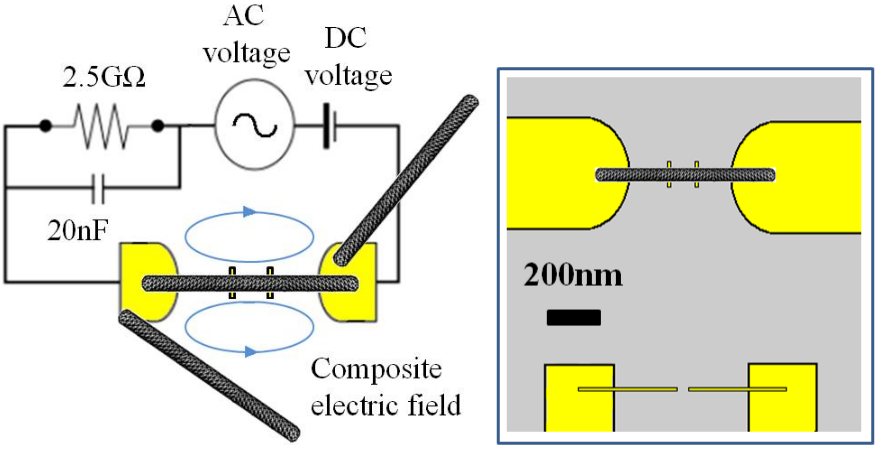

(A) **(B)**

Figure 3.1. Schematic for dielectrophoretic positioning of CNT. (A) A composite DC-AC electric field applied between metal electrodes guides an individual carbon nanotube. Central electrodes are small enough to not interfere with the electric field. (B) Carbon nanotube after succesful positioning. Materials are color coded: gold electrodes (yellow), carbon nanotube (dark gray), SiO_2 substrate (light gray).

Since a carbon nanotube is typically non-reactive, we assume oxygen will react with carbon nanotube sidewall mainly at defect sites. Before measurements at high bias voltage, we induce damage on carbon nanotube sidewall by exposure to oxygen plasma (Figure 3.2a) at 10 W, 45 sccm, 240 mTorr for 20 s and perform SEM imaging of CNTs.

An electrical breakdown is then performed by applying a bias voltage larger than 15 Vdc (Figure 3.2b), which induces a strong electron scattering and increases CNT temperature catalyzing the oxidative damage of CNT by the interaction with the oxygen from air [7, 112].

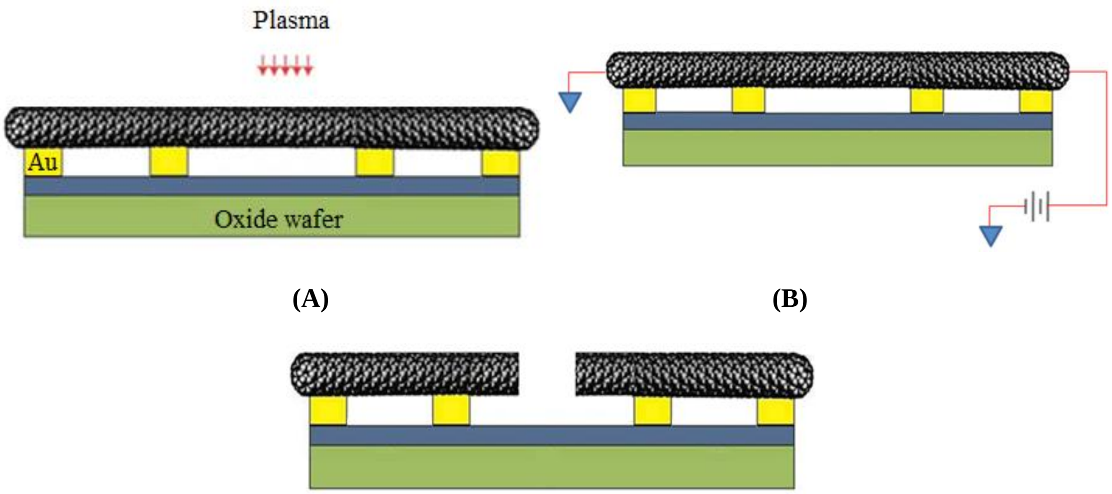

(A) (B)

(C)

Figure 3.2. Flow chart of the carbon nanotube breakdown process. CNT dimensions are not scaled. (A) A damage is induced in carbon nanotube by exposure to ion beams through a small window created by e-beam lithography. (B) An electrical breakdown is induced in carbon nanotube by applying a high bias voltage. (C) Carbon nanotube after electrical breakdown.

3.2.2 Electron transport calculations

Electronic structure calculations of small diameter CNTs are performed in the Gaussian 09 program [113-115], and a semiconducting CNT is identified. The density functional theory (DFT) optimized structure serves as input to the GENIP-07 program [116-118] for a non-equilibrium Green's function calculation of the electron transport characteristic. The outputs of the program are the electron transmission probabilities, the current-voltage characteristic of the molecular junction and the DOS at the junction where the effect of the gold electrodes are fully considered.

The transmission probabilities and the density of states (DOS) follow the next relations:

$$T(E,V) = Tr\left(\Gamma_{\mathrm{L}}(\mathrm{E,V})\mathrm{G}_{\mathrm{M}}(\mathrm{E,V})\, \Gamma_{\mathrm{R}}(\mathrm{E,V})\mathrm{G}_{\mathrm{M}}^{+}(\mathrm{E,V})\right) \tag{3.1}$$

$$D(E,V) = Tr\left(i[G_M(E,V) - G_M^{+}(E,V)]S(V)\right) \tag{3.2}$$

Where $\Gamma_{\mathrm{k}} = \mathrm{i}(\sum_{\mathrm{k}}(\mathrm{E,V}) - \sum_{\mathrm{k}}^{+}(\mathrm{E,V}))$ (for k=L,R) is the imaginary part of the self-energy Σ_{k}. Γ_{k} represents the coupling between the contacts and the molecule, and $\mathrm{G}^{\mathrm{R}+}$is the adjoint of G^{R}. i is the imaginary unit, and $S(V)$ is the overlap matrix at each applied field. The extended Landauer equation as a function of V is given by

$$I(V) = \frac{2e}{h}\int_{-\infty}^{\infty} T(E,V)\left[f_L\left(E - \frac{eV}{2}\right) - f_R\left(E + \frac{eV}{2}\right)\right] dE \tag{3.3}$$

Where E is the energy of the crossing electron, e is the charge of the electron, h is the Planck's constant, and $f_j(E,V_j)$ is the Fermi-Dirac distribution of the gold tip at an electric potential V_j. Thus the current through the junction depends on the Fermi level, the transmission function, the bias voltage applied to the system and the coupling of the pairs to the tips.

3.3 Results and discussion

3.3.1 CNT assembly and electrical measurements

We investigated the deposition of individual SWCNTs with a diameter of 1.5nm and a length of 1-1.5 µm. To guide the positioning of CNTs between electrodes we applied an electric field composed of an AC with a DC offset as shown in Figure 3.1a. The central electrodes are small to minimize interference to the electric field applied during the dielectrophoresis procedure (Figure 3.3).

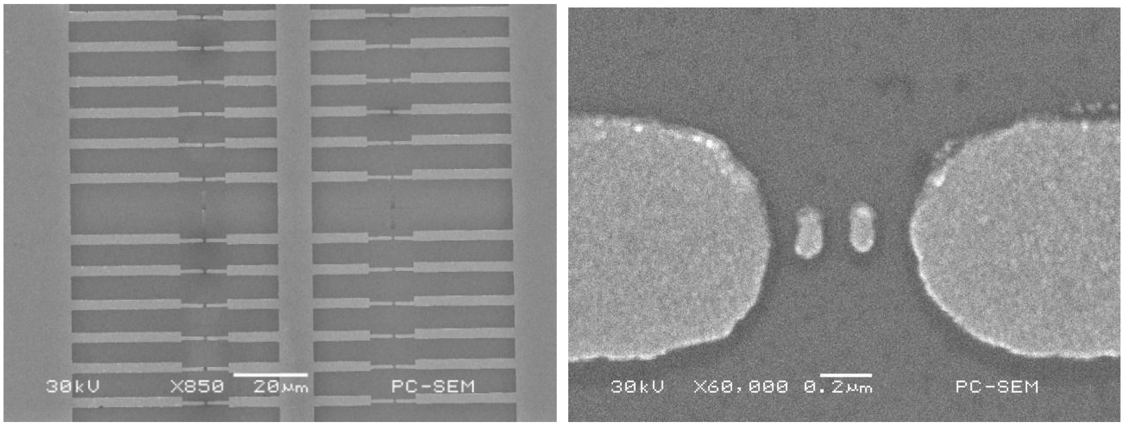

(A) **(B)**

Figure 3.3. SEM images of (A) array of gold electrodes and (B) a magnified image of the corresponding four- electrode configuration fabricated by e-beam lithography.

After successful deposition of carbon nanotubes, we obtain a current-voltage characteristic corresponding to a semiconducting behavior (Figure 3.4a). To improve the contact resistance we bake the sample at 180 °C for 1 minute.

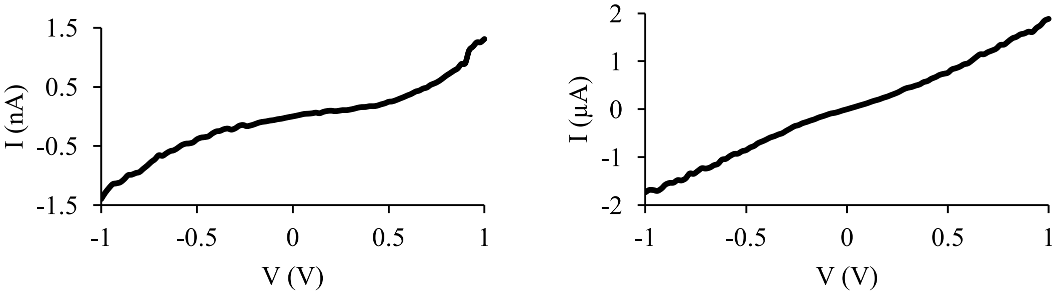

(A) **(B)**

Figure 3.4. Current-voltage characteristic of CNTs (A) after succesful deposition CNTs positioning on electrodes and (B) after baking at 180 °C and plasma exposure.

We then expose the sample to oxygen plasma (10W, 240 mTorr, 20s) to induce a slight damage to the CNT sidewall and perform current-voltage measurements (Figure 3.4b) and SEM imaging (Figure 3.5). We confirm the presence of CNTs bridging the electrodes, and we observe CNTs not necessarily bridge both central electrodes.

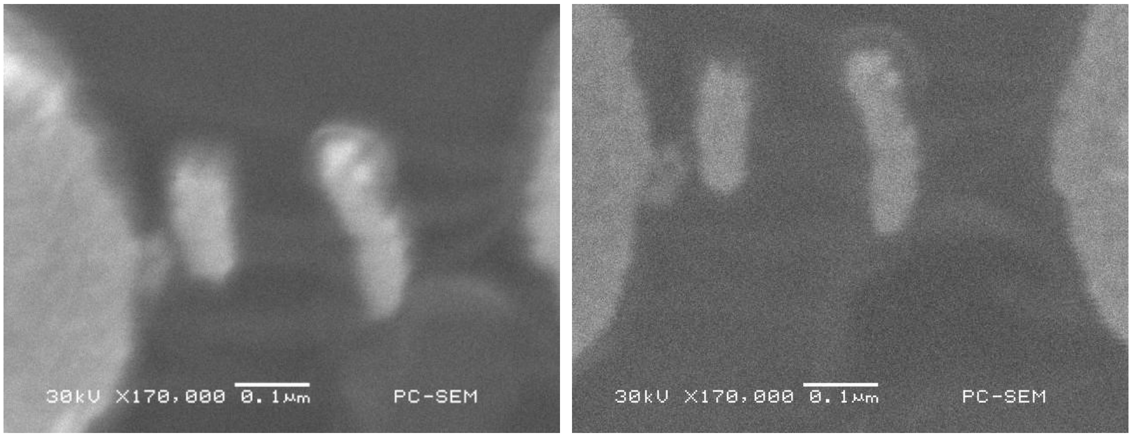

(A) **(B)**

Figure 3.5. SEM imaging of different pair of electrodes (a,c) before and (b,d) after exposure to oxygen plasma at 10W and 240 mTorr for 20 seconds. (a,b) corresponds to two CNT molecules bridging the electrodes; while (c,d) corresponds to a single-molecule CNT bridging the electrodes, in this case the CNT was clearly visible (d) only after plasma exposure.

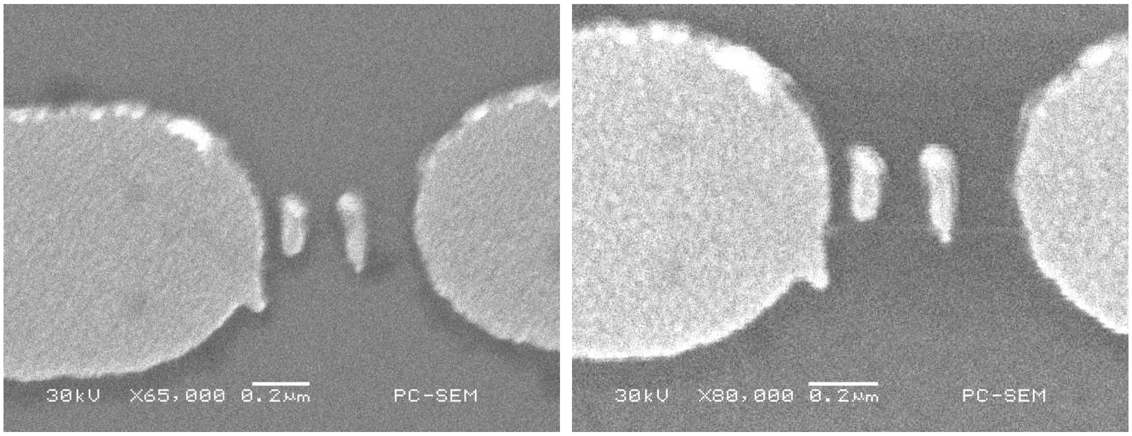

(C) **(D)**

Figure 3.5. Continued.

A high bias voltage (15 Vdc) is applied to the defective CNT to induce an electrical breakdown. A high current flowing through the nanotube increases its temperature by joule heating, and therefore catalyzes the oxidative damage due to CNT interaction with the oxygen present in the air environment. Analyzing the current-voltage characteristic (Figure 3.6b), we notice electrical spikes in the current-voltage characteristic which are a sign of nanotube near to fail by electrical breakdown. In electrical breakdown experiments with single-molecule carbon nanotube of ~ 1 nm diameter bridging a pair of electrodes, strong oscillations in the electrical current at saturation have been reported by Seidel *et al.* (2011) and attributed to semiconducting nanotubes [6]. The oscillations in the electrical current with increasing bias voltage must be due to an increase of electron-phonon scattering and the corresponding self-heating. After producing the oxidative cutting on CNT associated with the electrical spikes in the current-voltage characteristic, we repeat the current-voltage measurement, and since we have a parallel array of carbon nanotubes we still detect a non-zero current but this time we observe a negative differential resistance behavior (Figure 3.6c) in the electrical characteristic at positive bias voltage around 3.5 Vdc. We then produce a second electrical breakdown (Figure 3.6g), not observing NDR behavior after that (Figure 3.6i). However we observe again NDR behavior (Figure 3.6k) after producing a third electrical breakdown (Figure 3.6j). We atribute this NDR effect to a change in the carbon nanotube electronic band structure due to oxidative damage of carbon nanotube originated during the electrical breakdown.

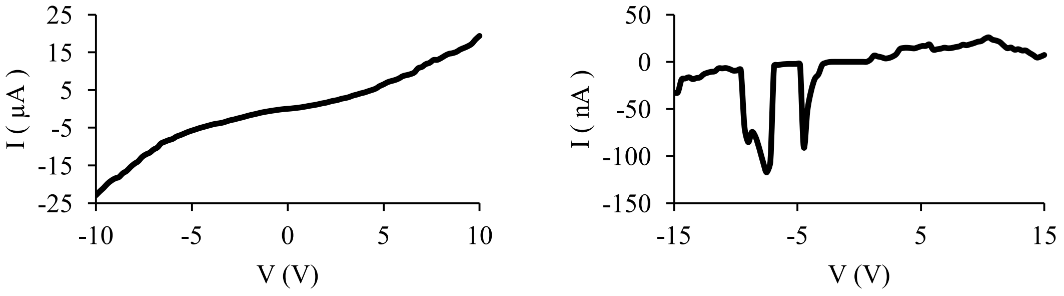

(A) **(B)**

Figure 3.6. Evolution of current-voltage characteristic of CNT array after consecutive electrical breakdown events. (A) Initial current-voltage characteristic of single walled carbon nanotubes (SWCNT) arranged in a parallel configuration. (B) Electrical characteristic during electrical breakdown of one carbon nanotube. (C), (D), (E), (F) Negative differential resistance behavior after the electrical breakdown. Curves are at different bias voltages and at different times. (G) Electrical characteristic during second electrical breakdown. (H), (I) Electrical characteristic of carbon nanotubes after the second electrical breakdown. (J) Electrical characteristic during third electrical breakdown. (K) Negative differential resistance behavior after the third electrical breakdown.

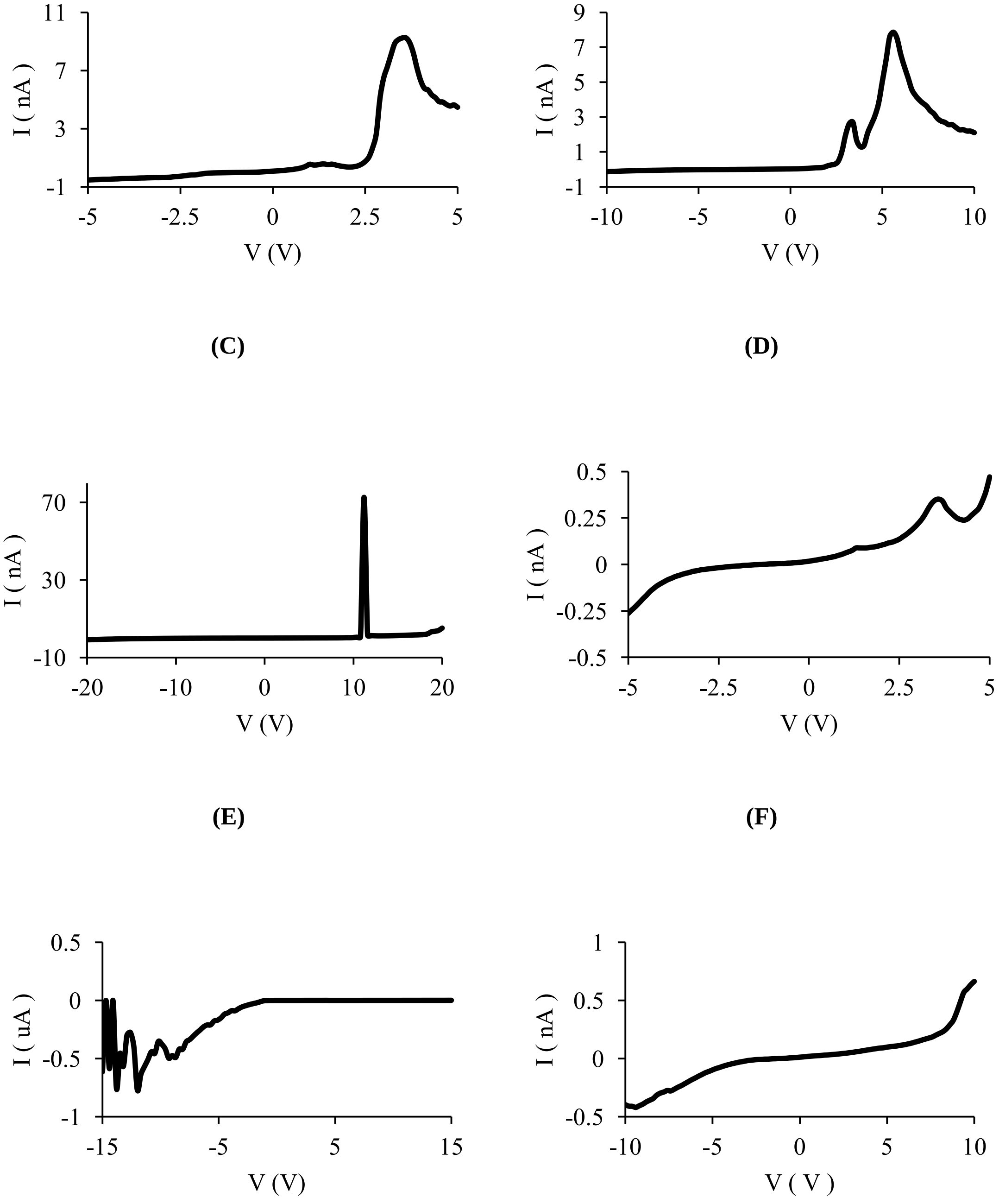

(C)

(D)

(E)

(F)

(G)

(H)

Figure 3.6. Continued.

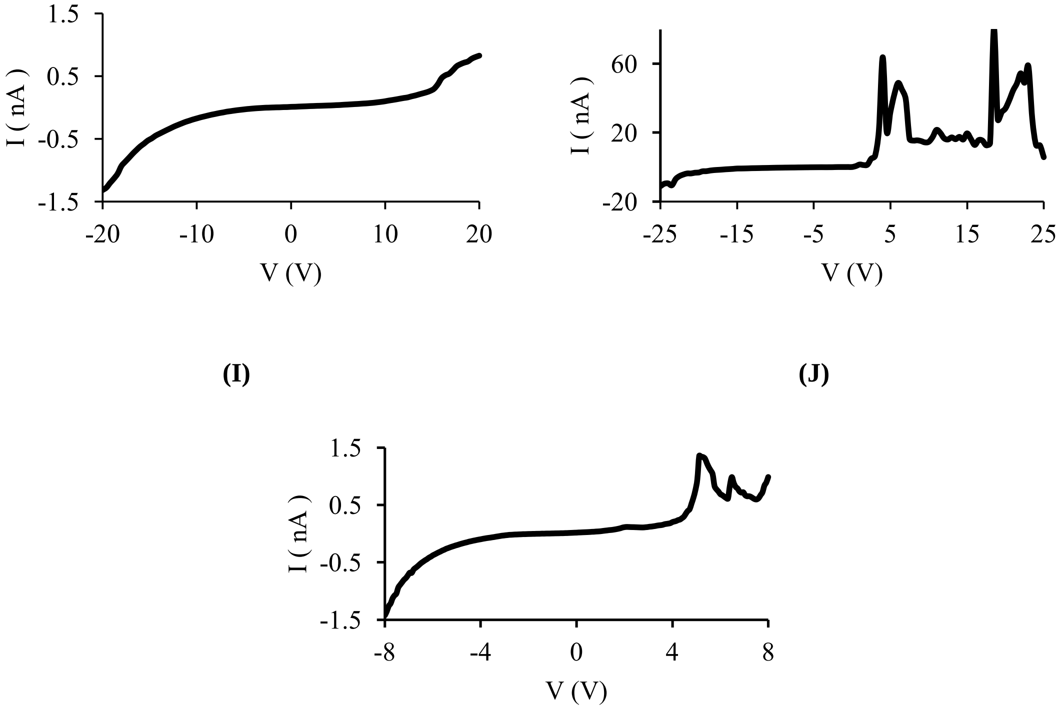

(I) **(J)**

(K)

Figure 3.6. Continued.

3.3.2 Electronic structure calculations

To test our hypothesis, we calculate the electron transport characteristic of a defective single walled carbon nanotube. For that purpose and to make it amenable the heavy computational cost of electronic structure calculations, we first identify the smallest diameter single walled carbon nanotube with semiconducting character. We explore different types of chirality (Table 3.1) and find chirality (4,3) (Figure 3.7a) as showing a large energy band gap (2.45 eV) and a corresponding semiconducting behavior (Figure 3.7b).

Table 3.1. Energy band gap for small diameter single walled carbon nanotube of different chirality types.

chirality	diameter (Å)	band gap (eV)
(4,0)	3.13	1.06
(3,3)	4.27	1.15
(4,2)	4.07	0.37
(4,3)	5.05	2.45
(5,0)	4.07	1.06
(5,1)	4.46	0.38
(6,0)	4.82	0.50

To estimate the structure of CNT after a breakdown event, we assume an oxygen molecule reacts with CNT sidewall by displacing two carbon atoms and then evaporating as two CO molecules. We suggest the high temperature induced during the electrical breakdown will anneal the double vacancies on CNT sidewall. To analyze the effect of this damage on the electrical property of CNT, we consider the double vacancies have affected practically all the atoms around the center of CNT (Figure 3.7c). After DFT-optimization we observe the transformation of double vacancies into octagon rings on CNT sidewall (Figure 3.7d), which gives origin to an NDR behavior in the electron transport characteristic (Figure 3.7e).

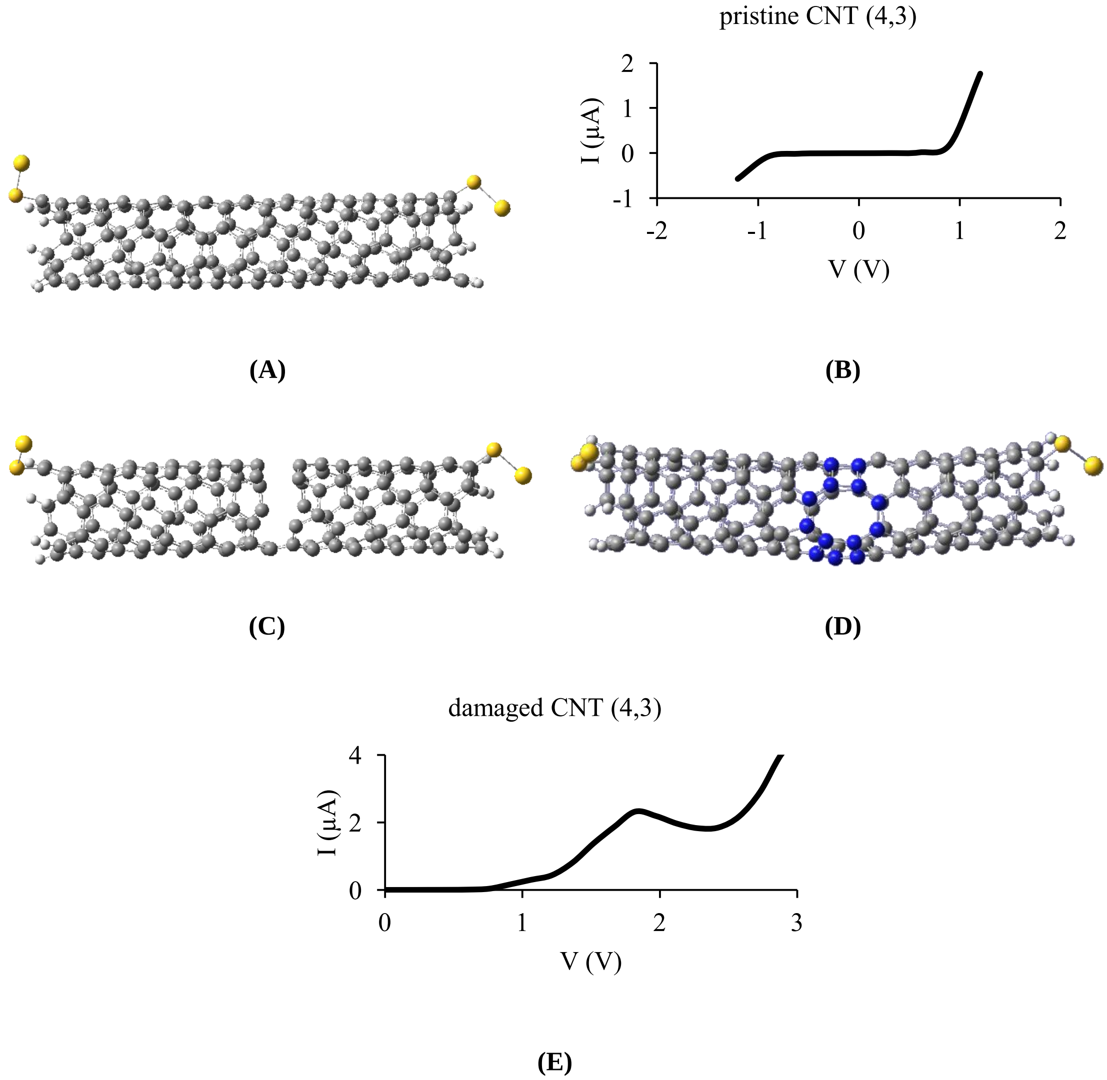

(A) **(B)**

(C) **(D)**

(E)

Figure 3.7. (A) Structure and (B) electron transport characteristic of pristine SWCNT (4,3). (C) Initial guess for damaged CNT (4,3), multiple double-vacancies correspond to a gap around the center of CNT. (D) DFT-optimized structure and (E) corresponding electron transport characteristic. In (D), a group of carbon atoms has been highlighted with blue color.

3.4 Conclusions

We have reported the assembly of a large array of suspended carbon nanotubes on a four-electrode configuration, engineering defective CNTs with a NDR behavior and a corresponding high peak to valley current ratio in the electron transport characteristic.

We consider a hypothetical CNT with semiconducting behavior and a defective structure due to multiple double vacancies; by DFT-based methods we predict the stable structure and corresponding electronic property, and are able to reproduce the observed nonlinear electron-transport behavior. This type of configuration allows increased complexity and functionality of CNT devices.

4. GATING MECHANISM OF DNA WRAPPING ON CARBON NANOTUBE[*]

DNA molecules are able to wrap carbon nanotubes (CNTs) in water solution, thus merging advantages of DNA chemistry with CNT physics as a natural way to design sensor devices. Using electrical means, a reversible semiconductor-metallic behavior has been found in CNT-DNA hybrid structures. Classical molecular dynamics simulations of the CNT-DNA wrapping process are performed. Then, structural conformations are analyzed by first-principles electronic structure methods; we correlate our results with previous experimental reports on carbon-DNA complexes, providing complementary information to understand better their electrical behavior.

4.1 Introduction

Diverse efforts have been performed on carbon nanotube (CNT) [119-122] and DNA-based nanoelectronics devices [10, 123-126] because both show potential as fundamental elements for molecular electronics [127-133]. The combination of the chemical sensing capabilities of DNA and the electrical properties of CNT in a hybrid nanodevice has been proposed for very sensitive detection of chemical events at the single-molecule level [134, 135] and a molecular understanding of CNT-DNA interaction can yield new insights to develop devices for rapid DNA sequencing [136, 137] as well as to improve the development of nanosensors, especially for chemical and biological agents [102, 123, 125, 138-144].

---

[*] Reproduced in part with permission from A.D. Bobadilla and J.M. Seminario, *J. Phys. Chem. C*, **2011**, *115* (8), pp 3466-3474. Copyright 2011 American Chemical Society.

Gowtham *et al.* [15] studied the physisorption of individual nucleobases on graphene using DFT methods, finding significant differences between interaction strengths when a nucleobase is physisorbed on graphene; based on an analysis of binding energies, they suggested that the base molecule polarizabilities are the main factors determining the nucleobase-graphene interaction strength. In another study by the same authors, the strength of the interaction was analyzed between DNA bases and a small diameter carbon nanotube of chirality (5,0) [14]. It is known that π-π interaction is the main factor driving single-stranded DNA (ssDNA) wrapping around large diameter carbon nanotube [145]. Nevertheless, the high curvature surface in a small diameter nanotube implies a nonplanar hexagonal geometry which would decrease π-π stacking interaction. Analyzing this kind of interaction, Gowtham *et al.* [14] found a correlation between nucleobases polarizability and CNT-nucleobase binding energies which resulted to follow the hierarchy G > A > T > C > U, concluding that molecular polarizability of nucleobases plays the dominant role in the interaction strength of nucleobases with CNT [14].

It has been reported that a DNA wrapped carbon nanotube device can change from metallic behavior in dry conditions to semiconductor behavior in wet conditions [48]. Ouellette *et al.* [13] analyzed the time evolution of electrical current in a suspended carbon nanotube positioned in a microfluidic channel through which DNA molecules were allowed to flow. They observed the appearance of spikes when DNA molecules were present in the microfluidic channel; DNA molecules constantly flowed through the microfluidic channel and electrostatic screening of van der Waals interaction due to ions was minimized.

In the present work, structural conformations and electronic structure of CNT-DNA hybrids are analyzed with molecular dynamics and first-principles quantum chemistry techniques searching for further insights on the mechanisms responsible for semiconductor-metallic behavior in DNA wrapped carbon nanotube.

4.2 Methodology

The Large-scale Atomic/Molecular Massively Parallel Simulator (LAMMPS) [146] program is used to perform molecular dynamics simulations of solvated CNT–DNA. The chosen single stranded DNA sequence is TAGGAT and the single walled carbon nanotube is a zigzag (4,0). Ions are added to the water solution to neutralize the negative charge in DNA backbone due to negatively charged phosphate groups thus yielding a neutral whole system. The solution contains 11 Na^+, 6 Cl^- and 1,869 TIP3P [147, 148] water molecules in a simulation box of 40 Å × 40 Å × 40 Å. The initial atomic coordinate file is generated with the Packing Optimization for Molecular Dynamics Simulations (Packmol) [149]. Periodic boundary conditions are applied to the box and run under the micro-canonical NVE ensemble. Electrostatic interactions are calculated by the particle-particle and particle-mesh (PPPM) [150] method using a grid order of 4.

To control the temperature, within the NVE ensemble, atom velocities are rescaled at every time-step with the Berendsen thermostat [151], which is applied to only the translational degrees of freedom. The positions of all CNT atoms are constrained by not updating the velocity for atoms in the CNT as expected applications consider the CNT fixed to metal electrodes.

In the initial conformation for the molecular system, the closest distance between ssDNA and CNT is 11.5 Å (Figure 4.1). An energy minimization of the system is performed to reach a local potential energy minimum. Then, the temperature of the system is raised from 5 K to 300 K in a 0.525 ns run. This is followed by a 1.05 ns run at 300 K to ensure equilibration. To accelerate the wrapping process the temperature is raised to 340 K in a 1.05 ns MD run, then the system is allowed to equilibrate at 340 K for 7.5 ns. Visualization of trajectories is performed using the graphics software package VMD [152].

Table 4.1. Lennard-Jones and Coulombic interactions are computed with an additional switching function S(r) detailed in equation 4.3.

cutoff	Lennard Jones	Coulombic
$r < r_{in}$	$V_{LJ}(r)$	$C(r)$
$r_{in} < r < r_{out}$	$S(r) \times V_{LJ}(r)$	$S(r) \times C(r)$
$r > r_{out}$	0	0

To model the system, the CHARMM force field [153] is used, in which the van der Waals energy is calculated with a standard 12-6 Lennard-Jones potential,

$$V_{LJ}(r) = 4\epsilon\left[\left(\frac{\sigma}{r}\right)^{12} - \left(\frac{\sigma}{r}\right)^{6}\right], \tag{4.1}$$

modeling nonbonded interactions between pairs of atoms at distance r, separated by at least three consecutive bonds. It is composed of two terms: the first describes the Pauli repulsive interaction at short ranges due to overlapping electron orbitals and the second describes the van der Waals attractive interactions, which at long ranges are due to dipole-dipole interactions and to the fluctuating molecular dipole moments. ϵ is the Lennard-Jones well depth and σ is the distance at the Lennard-Jones minimum.

The electrostatic energy with a Coulombic potential,

$$C(r) = \frac{1}{4\pi\varepsilon}\frac{q_i q_i}{r_{ij}}, \tag{4.2}$$

represents interactions between static atomic charges q_i and q_j at distance r_{ij}, and ε is the dielectric constant.

The coefficients σ and ϵ are defined for each pair of atoms according to the CHARMM force field . The Lennard-Jones parameters between pairs of different atoms are obtained from the Lorentz–Berthelodt combination rules, in which ϵ_{ij} values are based on the geometric mean of ϵ_i and ϵ_j and σ_{ij} values are based on the arithmetic mean between σ_i and σ_j. Both Lennard-Jones and Coulombic interactions are computed with an additional switching function S(r) [148],

$$S(r) = \frac{\left[r_{out}^2 - r^2\right]^2}{\left[r_{out}^2 - r_{in}^2\right]^3}\left[r_{out}^2 + 2r^2 - 3_{r_{in}}^2\right], \tag{4.3}$$

which decreases the interaction energies smoothly to zero from an inner (r_{in}) cutoff to an external cutoff (r_{out}), in order to decrease the number of hot spots in the simulation. We use, r_{in} = 8 Å and r_{out} =10 Å, for both, Lenard-Jones and Coulombic non-bonded interactions (Table 4.1). CNTs are modeled as uncharged Lennard-Jones particles using sp^2 carbon parameters from the CHARMM force field.

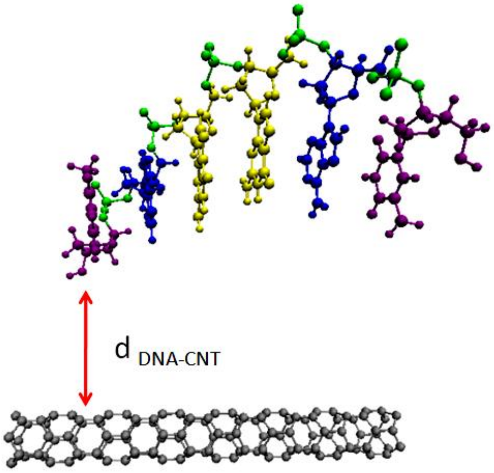

Figure 4.1. Initial conformation for molecular dynamics simulation of solvated CNT-DNA, CNT chirality is (4,0). Water molecules (density = 1 g/cm^3) and counterions have been removed for the sake of visualization. DNA molecule is color coded: thymine (violet), adenine (blue), guanine (yellow), phosphate groups (green). $d_{DNA-CNT}$ = 11.5 Å is the distance between the thymine base and the carbon nanotube.

4.3 Results and discussion

At the initial stage of the process at 340 K the DNA molecule approaches the carbon nanotube as shown in Figure 4.2. During the first 2.5 ns of the equilibration process at 340K the DNA molecule stay non-covalently linked to the carbon nanotube and only two or three bases participate in the CNT-DNA interaction. From 2.5 ns to 5 ns the DNA molecule wraps the carbon nanotube forming a circle around the nanotube (Figure 4.3a,b). At the end of the process at 340 K, from 5 ns to 7.5 ns, the DNA molecule changes its structural conformation forming a helical wrapping around the nanotube (Figure 4.3c,d), and 5 bases, out of six, are oriented parallel to the CNT. Nevertheless in the following process from 340 K to 300 K all bases prefer an orientation parallel to the carbon nanotube, keeping that tendency during the final equilibration at 300 K (Figure 4.4). The system is considered to be in equilibrium when the root mean square deviation (RMSD), calculated for DNA structure with respect to its initial conformation, keeps a constant value.

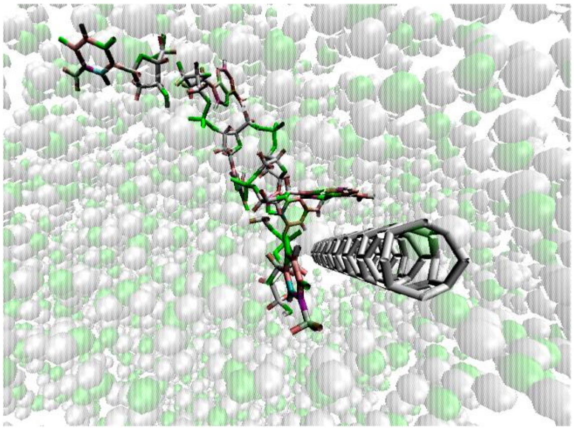

Figure 4.2. Snapshot at t = 2.6 ns: DNA molecule approaching CNT at the initial stage of the process at 340 K. The high temperature accelerates the van der Waals attraction between DNA bases and the carbon nanotube surface.

We calculate the van der Waals (vdW) energy (Figure 4.5b) between DNA molecule and single-walled carbon nanotube; the time evolution of this energy shows significant energy jumps (Figure 4.5b) occurring due to absorption of DNA bases on the carbon nanotube surface. The electrostatic energy of interaction between adjacent phosphate atoms is shown in Figure 4.5c. During the first 2 ns of equilibration process at 340K, the ssDNA adopts a conformational structure in which the phosphate atoms are closer between them; this causes an increase of their electrostatic energy. Then, as ssDNA conformational changes around CNT progress, a decrease in electrostatic energy corresponding to an increase in distance between phosphate atoms when ssDNA adopts a helical conformation around CNT.

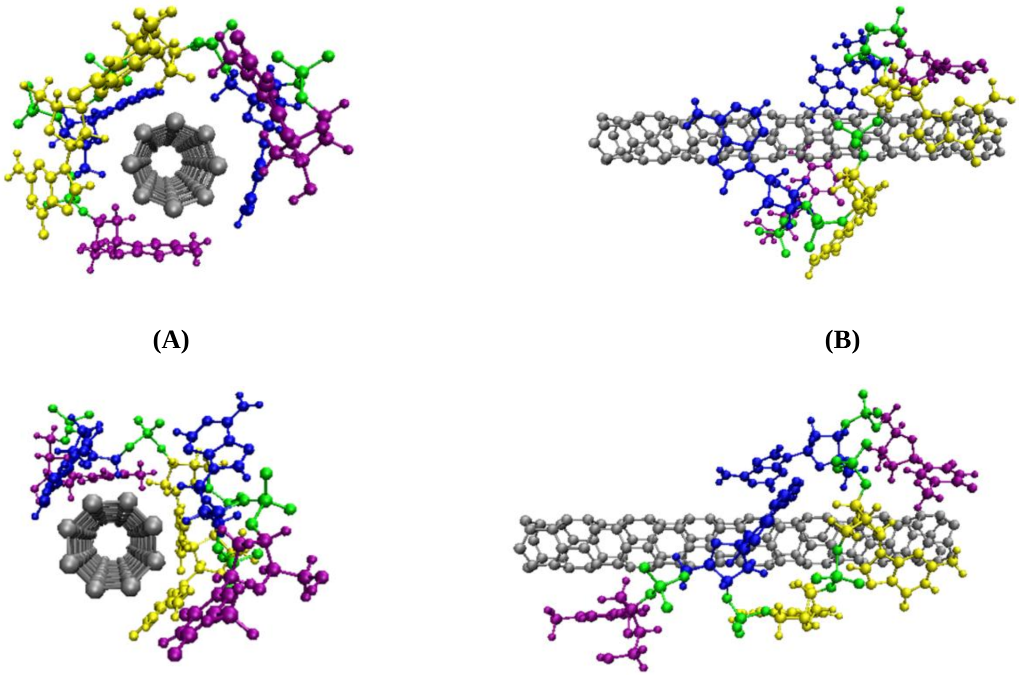

(A) **(B)**

(C) **(D)**

Figure 4.3. (A) Front and (B) side view of DNA-CNT circular wrapping after 6.4 ns, at the middle stage of the process at 340 K. (C) Front and (D) side views of the DNA-CNT helical wrapping after 10.1 ns, at the final stage of the process at 340 K (color code as in Figure 4.1).

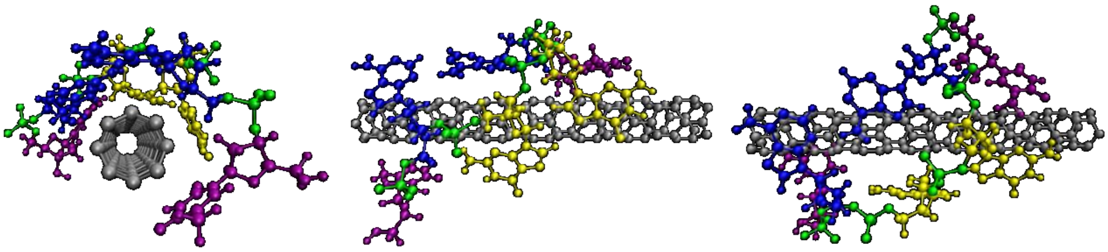

(A) (B) (C)

Figure 4.4. (A) Front view of DNA-CNT helical wrapping after 12.2 ns, at the final stage of equilibration at 300 K. (B) and (C) show two side views (color code as in Figure 4.1)

The final structural conformation shows that each base type prefers a particular orientation with respect to the DNA backbone; the two thymine bases and the two guanine bases prefer an orientation opposite to that preferred by the two adenine bases. The ssDNA form a right-handed helical wrapping around the carbon nanotube.

After the ssDNA is physisorbed on the carbon nanotube (CNT) surface, the DNA experiences free translational and angular movements along the CNT surface, persisting through the equilibration process at room temperature.

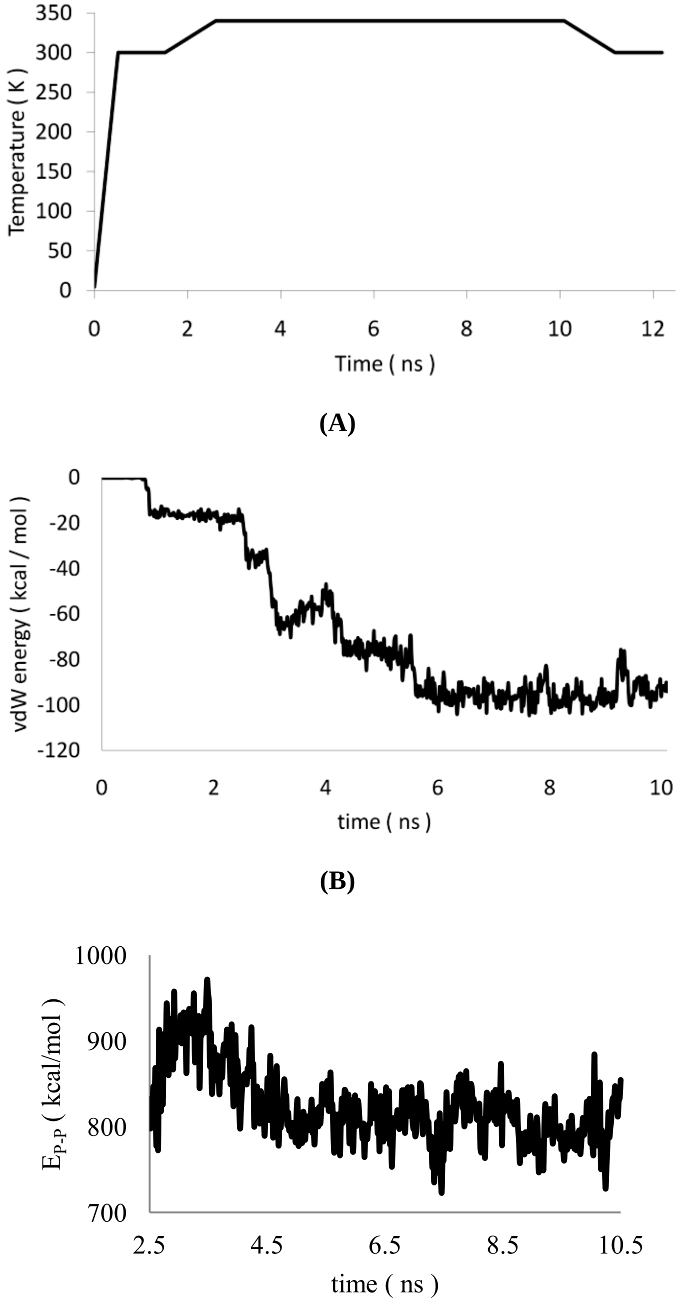

(A)

(B)

(C)

Figure 4.5. (A) Input temperature temperatures: the equilibration process at 340K begins at t = 2.6 ns and finishes at t = 10.1 ns. (B) Energy jumps are observed in van der Waals (vdW) energy as each nucleotide base binds to the carbon nanotube surface. (C) Electrostatic energy of phosphate atoms in the ssDNA backbone during equilibration process at 340K.

The self-assembly of carbon nanotube and DNA is usually driven mainly by π-π stacking interactions, enabled by the planar hexagonal conjugated π-systems in single-walled CNT. However, in a CNT (4,0), the carbon skeleton forms boat-like nonplanar hexagonal conjugates (Figure 4.6) due to the high curvature surface in small diameter nanotubes; we expected this to be an obstacle for π-π stacking interactions. Despite of the large strain energy imposed on the CNT (4,0), ab initio molecular orbital calculations at the B3PW91/6-31G(*d*) level still show a large delocalization of a benzene strained to the same curvature that it would have in the small CNT(4,0). Figure 4.7 shows a comparison of the relevant molecular orbitals of the two benzene conformations. The injection of a small sp^3 contribution with a dangling bond might increase the interaction with any part of the DNA and not only with its π regions. There is still certain similarity between the molecular orbitals of the two conformations but energies of the frontier molecular orbitals are strongly affected decreasing the effect away from the frontier orbitals.

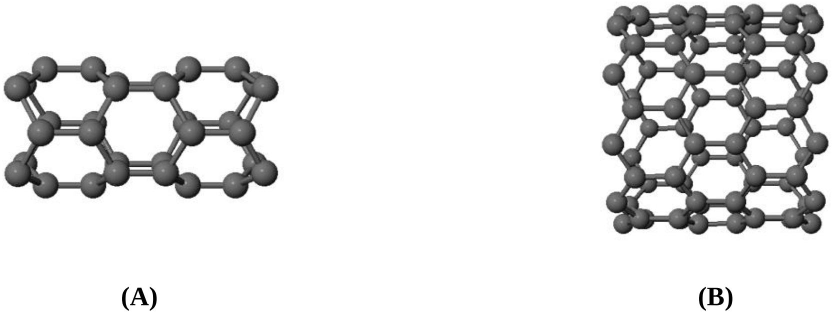

Figure 4.6. (A) Boat-like nonplanar hexagonal conjugates in CNT(4,0) and (B) planar hexagonal conjugated π-systems in CNT(10,0).

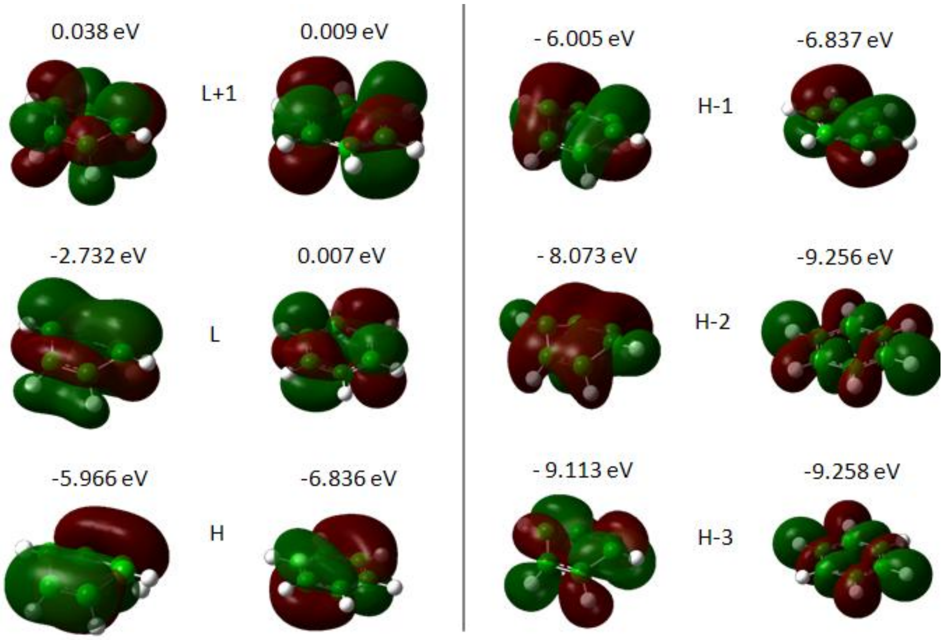

Figure 4.7. Comparison of molecular orbitals (H = HOMO, L = LUMO) and energies for benzene (2nd and 4th columns) and strained benzene with the curvature of a CNT(4,0) (1st and 3rd columns).

To analyze the electronic band structure, ab initio electronic structure calculations are performed in vacuum and aqueous conditions at the B3LYP/6-31G(d) level for the carbon nanotube, DNA molecule and DNA-wrapped carbon nanotube system.

Table 4.2. Number of atoms involved in the molecular DFT B3LYP/6-31G(d) calculations. Length of the CNT(4,0) is 3 nm and the ssDNA sequence is TAGGAT. Carbon nanotube and DNA molecule are passivated with hydrogen atoms.

System	Number of atoms in vacuum conditions	Number of water molecules in aqueous conditions	Number of atoms in aqueous conditions
CNT	136	172	652
ssDNA	198	334	1200
ssDNA-CNT	334	179	871

To simulate aqueous conditions with low computational cost, the Tomasi's polarizable continuum model (PCM) [154] is used; in this method, the solvent is modeled as a continuum of uniform dielectric constant. The molecular system is placed into a cavity within the solvent and the calculation of the molecular electrostatic potential or the electric field at a discrete number of preselected points is utilized to evaluate the environmental effects of a solvent on the properties of the molecular system.

For more accurate results, we consider the water molecules surrounding the hybrid structure (Figure 4.8c). We also perform molecular dynamics simulations for individual carbon nanotube (Figure 4.8b) and individual DNA (Figure 4.8a) in water solvent in order to get the corresponding structural conformation and to analyze differences in electronic structure with respect to the hybrid structure.

As shown in Table 4.2, our results using the PCM method differ much from those with water molecules surrounding carbon nanotube and DNA. The lack of accuracy of the PCM method arises from considering only electrostatic effects in the interaction between the solvent and the molecular system.

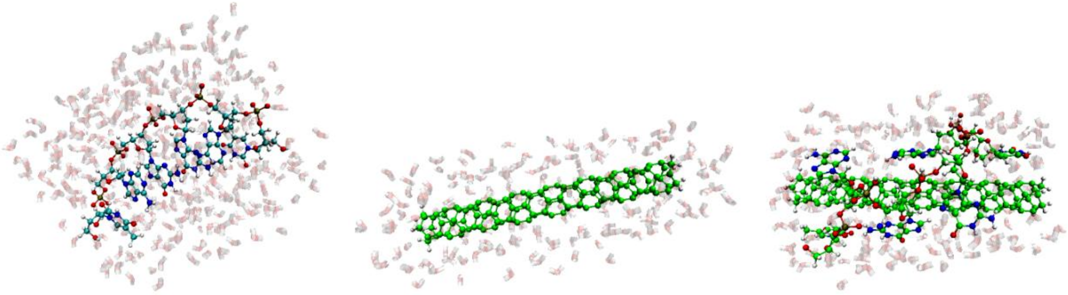

(A) (B) (C)

Figure 4.8. Structural conformations from molecular dynamics simulations for the ab initio calculations performed in water solvent: (A) DNA, (B) carbon nanotube and (C) CNT-DNA nanostructure.

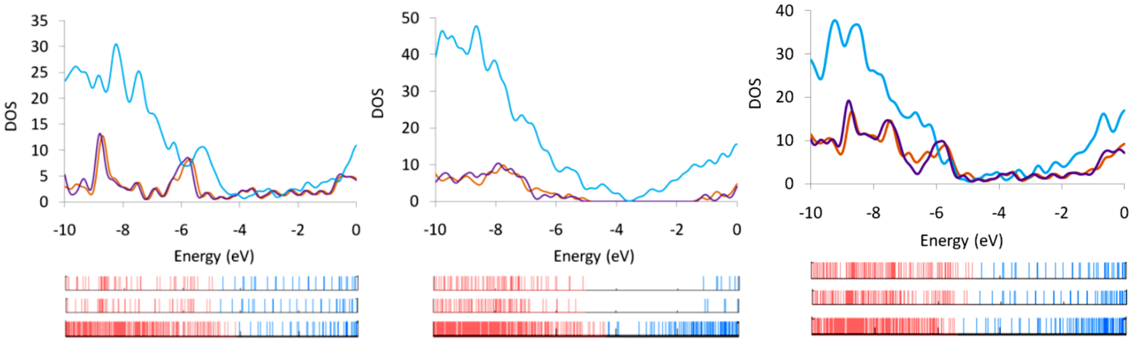

(A) (B) (C)

Figure 4.9. Density of states (DOS) spectrum for (A) carbon nanotube, (B) DNA, and (C) hybrid CNT-DNA structures using the DFT B3LYP/6-31G(d) level of theory. Top: curves for vacuum conditions (red), solvent conditions using PCM method (purple) and including water solvent molecules (cyan). Vertical lines at the bottom represent molecular orbital energies: red (occupied orbitals) and blue (unoccupied orbitals). The three sets of vertical lines correspond respectively, from top to down, to vacuum conditions, solvent conditions by using PCM method and solvent conditions by including water molecules.

We find slight differences in the density of states for CNT in vacuum and under the PCM solvent (Figure 4.9); there is a strong difference when the actual water molecules are considered in the calculation as they are able to fill states around the frontier orbitals of the CNT and DNA. To be able to analyze contributions from the carbon nanotube (CNT) and DNA to the DOS of the hybrid structure, we identify the highest occupied molecular orbitals (HOMO) and the lowest unoccupied molecular orbitals (LUMO) for CNT and DNA when they are part of the hybrid structure; this is done by visualizing the molecular orbitals (MO) for each energy state and identifying the molecules on which each MO is localized. These results are summarized in Table 4.2 and Figure 4.10.

Comparing individual molecules with the hybrid structure at vacuum conditions (Table 4.3), we observe that the HOMO and LUMO orbitals corresponding to the carbon nanotube are almost unaffected by the wrapping of DNA molecule; however, we observe that the DNA HOMO orbital shifts to an energy level higher than the energy of the CNT HOMO, producing a hybrid structure energy gap of 0.31 eV smaller than the one of the carbon nanotube. We also observe that the DNA energy gap decreases, enabling an additional path for electron flow. These two factors contribute therefore to a metallic behavior. Electrons may flow not only from metal electrodes to carbon nanotube but also from metal electrodes to DNA and from DNA to carbon nanotube in a scenario similar to the experiment reported by Cha *et al.* [48] who reported a metallic behavior for the hybrid structure in vacuum conditions; in their experimental setup, it was possible a direct contact between ssDNA and metal electrodes.

Table 4.3. HOMO, LUMO and gap energies (eV) of DNA and CNT as isolated molecules and when they are part of the complex DNA-CNT. Calculations are done in vacuum, under PCM solvent, and under actual water molecules in the Hamiltonian. All systems are run as uncharged and singlets.

system		vacuum			PCM Solvent			water molecules		
		HOMO	LUMO	gap	HOMO	LUMO	Gap	HOMO	LUMO	gap
isolated	DNA	-5.14	-1.17	3.97	-5.37	-1.09	4.27	-5.93	-4.22	1.71
	CNT	-5.00	-4.59	0.41	-5.09	-4.66	0.43	-4.48	-4.04	0.44
complex	DNA	-4.89	-1.48	3.41	-5.50	-1.55	3.95	-5.98	-3.38	2.60
	CNT	-5.00	-4.58	0.43	-5.09	-4.66	0.43	-5.54	-5.15	0.39

The individual carbon nanotube in water conditions shows a less stable behavior than in vacuum conditions, with a significant energy shift of HOMO and LUMO orbital towards higher energy levels (Table 4.3) due to the known hydrophobic character of a carbon nanotube molecule produced by its highly symmetric and non-polar electronic structure. However the electronic structure seems slightly harder with water as its hardness increases by 0.03 eV; on the other hand, DNA suffers a strong change to lower hardness when the water molecules are included in the complex or isolated.

There is a ~0.5 eV energy shift in carbon nanotube HOMO and LUMO to lower energy levels from vacuum to water solvent conditions for the hybrid structure. This increase in global stability of DNA wrapped in a carbon nanotube in water is due to the highly hydrophilic character of phosphate groups located on the DNA backbone; and also because a DNA molecule wrapped around the CNT breaks the symmetric electronic structure in the CNT-DNA hybrid system. The latter is because of the CNT highly polarizable electrons [155] since a polar electronic structure for the CNT-DNA hybrid make it more stable in water solvent conditions. Hardness of the complex decreases with water, making possible to absorb electromagnetic radiation at higher wavelengths.

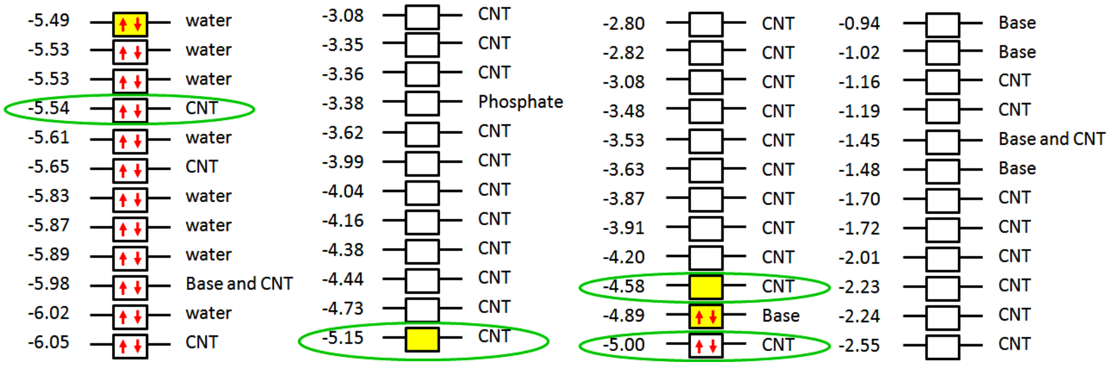

(A) **(B)**

Figure 4.10. Molecular orbital energies (eV) for the CNT-DNA nanostructure in (A) water and (B) vacuum. Highlighted squares indicate HOMO and LUMO of the complex system. Green ellipses indicate carbon nanotube HOMO and LUMO. Orbitals are localized in the carbon nanotube (CNT), water molecules (water), bases (Base), and Phosphate groups (Phosphate).

Molecular orbital shapes corresponding to representative energy levels of CNT-DNA system are shown for water conditions and vacuum conditions in Figure 4.11a-d. The molecular orbitals corresponding to lower energy levels above the LUMO orbital are mainly localized in CNT (Figure 4.10). In vacuum conditions, for energy levels above the LUMO, molecular orbitals are also localized in DNA bases. In water conditions, for energy levels above the LUMO, molecular orbitals are also localized on phosphate groups and DNA bases, with molecular orbitals corresponding to phosphate groups being mostly at lower energy levels than those corresponding to DNA bases. Molecular orbitals corresponding to phosphate groups are also localized in neighbor water molecules (Figure 4.11b).

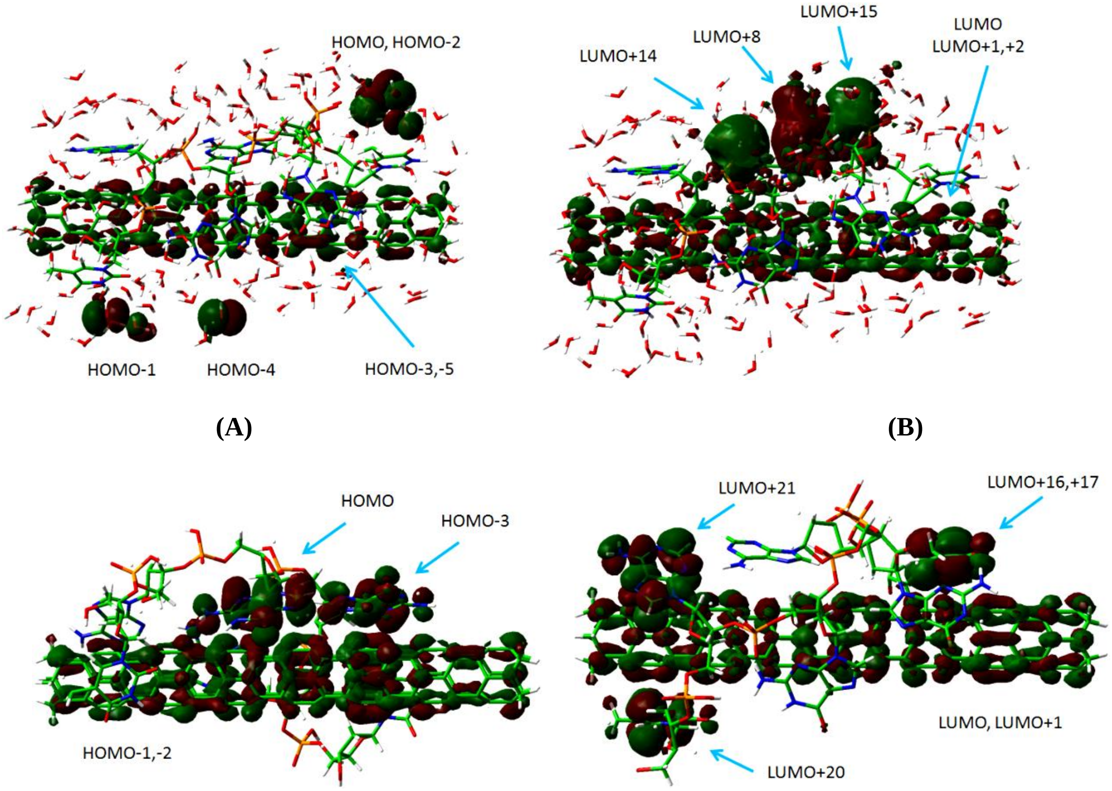

(A) (B)

(C) (D)

Figure 4.11. DNA sequence is (T1)(A1)(G1)(G2)(A2)(T2). Molecular orbital shapes for CNT-DNA system in water (A) HOMO (-5.49 eV) and HOMO-2 (-5.53 eV) are localized on the same region of water molecules. HOMO-3 (-5.54 eV) and HOMO-5 (-5.65 eV) are localized on CNT surface. (B) LUMO (-5.15 eV), LUMO+1 (-4.73 eV) and LUMO+2 (4.44 eV) are localized on CNT surface. LUMO+8 (-3.38 eV), LUMO+14 (-2.74 eV) and LUMO+15 (-2.72 eV) are localized in phosphate groups and its neighboring water molecules. LUMO+14 is localized between A1 and G1, LUMO+8 is localized between G1 and G2, LUMO+15 is localized between G2 and A2. Molecular orbital shapes for CNT-DNA system in vacuum (C) HOMO-1 (-5.0 eV) and HOMO-2 (-5.1 eV) are localized on CNT surface. HOMO (-4.89 eV) and HOMO-3 (-5.36 eV) are localized on G1 and G2 respectively. (D) LUMO and LUMO+1 are localized on CNT surface. LUMO+16 (-1.48 eV) and LUMO+17 (-1.45 eV) are both localized on T2 and CNT surface. LUMO+20 (-1.02 eV) and LUMO+21 (-0.94 eV) are localized on T1 and A1 respectively. Representative hybrid orbitals for CNT-DNA system in water (E) HOMO-9 (-5.98 eV) is localized on G1 and its neighboring CNT surface. (F), (G) LUMO+18 (-2.26 eV) and LUMO+19 (-2.25 eV) are both localized on water molecules and CNT surface. Water molecules are neighbors to G2. (H) LUMO+37 (-1.21 eV) is localized on G2 and CNT surface. Representative hybrid orbitals for CNT-DNA system in vacuum (I) HOMO-3 (-5.36 eV) is localized on G2 and its neighboring CNT surface. (J) LUMO+17 (-1.45 eV) is localized on T2 and CNT surface.

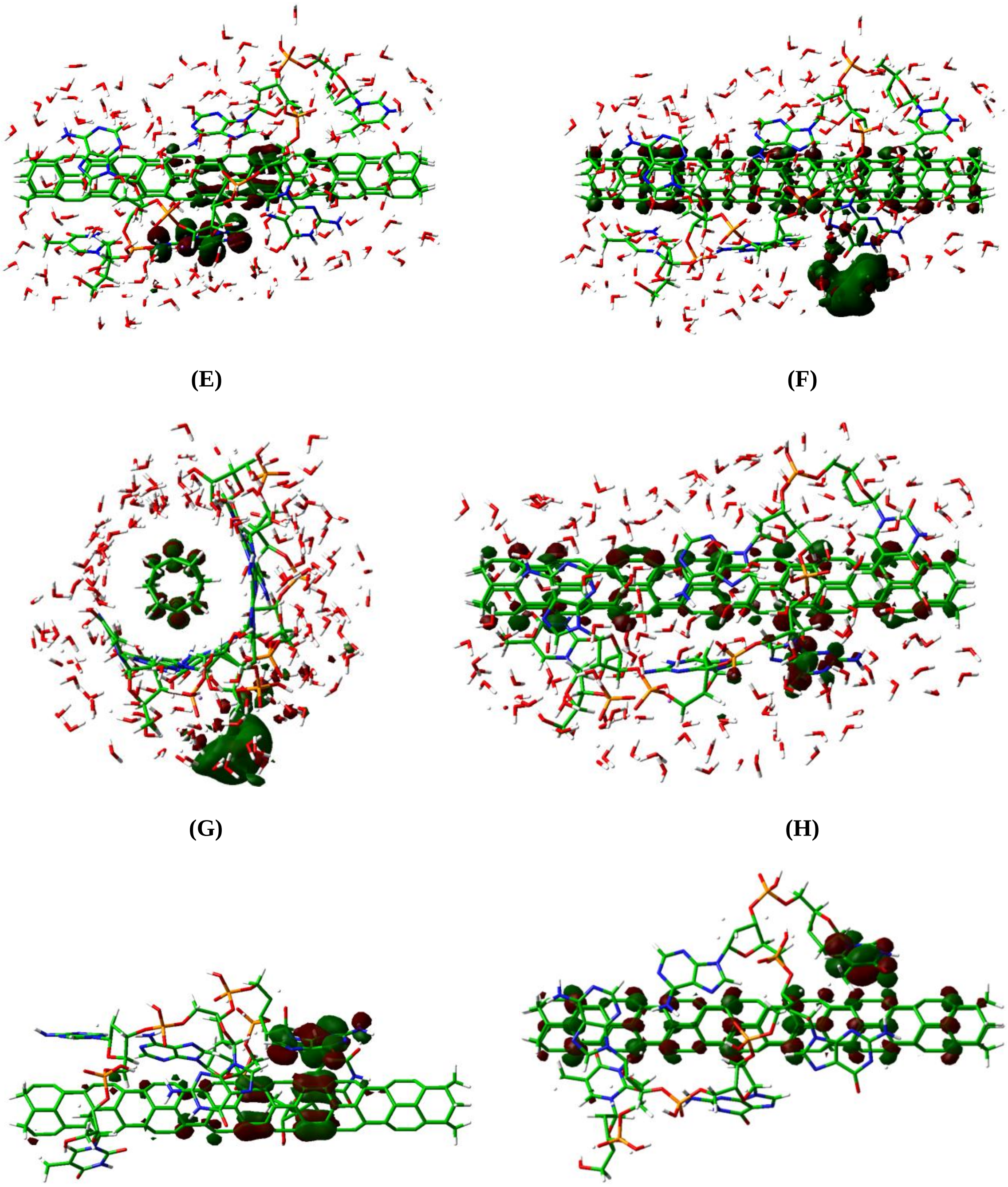

(E) **(F)**

(G) **(H)**

(I) **(J)**

Figure 4.11. Continued.

We observe the presence of hybrid molecular orbitals, which allows a flow of electrons between carbon nanotube, DNA and water molecules. Molecular orbital shapes are shown in Figure 4.11e-j. Relative positions of energy levels for some hybrid orbitals are depicted in Figure 4.12. A DNA base is able to polarize the carbon nanotube electronic density in the region lying near to the DNA base as shown in Figure 4.11e,i, breaking the nanotube electronic symmetry. The asymmetry, with respect to nanotube axial axis, of electronic density induced in carbon nanotube surface by the DNA base is higher in water conditions than in vacuum conditions. Molecular orbitals localized in DNA bases at relatively high energy levels, such as LUMO+17 and LUMO+37, are not able to produce an asymmetry in nanotube electronic density, as shown in Figure 4.11g,j. Water molecules are able to produce a different kind of polarization as shown in Figure 4.11f,g.

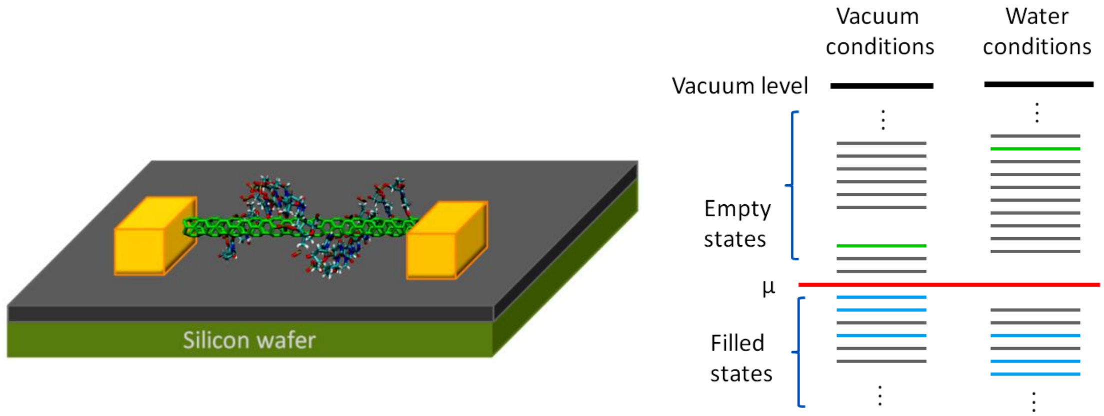

(A) **(B)**

Figure 4.12. (A) Carbon nanotube-DNA based transistor and (B) its corresponding energy level diagram for vacuum conditions and water solvent conditions. Gray lines correspond to CNT energy states, green lines correspond to DNA molecule energy states, and cyan lines correspond to molecular orbitals shared by CNT and DNA. μ represents the gold electrode work function. Energy levels corresponding to water molecules are omitted for clarity.

By constructing an energy level diagram (Figure 4.12b), and considering an approximate value of -5.3 eV for the gold electrode Fermi level, the DNA molecule yields a transistor-like gating mechanism as shown in Figure 4.12. Similar gating mechanism has been reported for a hybrid graphene-ssDNA system [124].

Ouellette *et al.* [13] reported spikes in the time evolution of CNT electrical current as DNA molecules were allowed to flow through a microfluidic channel. Spikes current levels are below or above the original CNT current level depending on the type of DNA molecule tested. We suggest those spikes are produced every time a DNA molecule reaches the carbon nanotube surface, and a different change in current level, positive or negative spikes, is indicative of a DNA sequence dependent transistor-like gating mechanism. This DNA sequence dependence is further suggested by the known correlation between nucleobases polarizability and CNT-DNA interaction strength [14], as well as the shift of HOMO and LUMO toward lower energy levels induced by DNA wrapping and reported in the present work. Changes in the electronic structure of CNT occur due to the breaking of electronic symmetry of CNT after DNA wrapping and to CNT having highly polarizable electrons, therefore, we expect a stronger DNA gating mechanism effect for single walled carbon nanotubes with higher polarizability.

4.4 Conclusions

Ab initio electronic structure calculations have been performed for single walled carbon nanotube, single stranded DNA molecule, and DNA wrapped carbon nanotube considering in all cases vacuum conditions and water solvent conditions. Stable structural conformations in water solvent conditions are obtained from molecular dynamics simulations. In vacuum conditions, two factors contribute to a metallic behavior for CNT-DNA hybrid structure, mainly a decrease in DNA energy gap and the production of a hybrid structure energy gap smaller than in carbon nanotube. In water solvent conditions, an energy shift is produced in the HOMO and LUMO energy levels for the hybrid structure; we suggest this is due to the breaking of electronic symmetry in carbon nanotube produced by the wrapping of DNA molecule. Our results complement previous experimental and theoretical results on CNT-DNA interaction [13, 14, 48, 155], providing further support for a DNA sequence dependent gating mechanism in suspended carbon nanotube (CNT) transistors, due to the key role played by CNT molecular polarizability on the breaking of electronic symmetry in the hybrid structure and to a correlation between nucleobases polarizability and CNT-DNA interaction strength. We hope to trigger further experiments needed to elucidate the specific DNA sequence dependence of this transistor-like gating mechanism in the carbon nanotube electrical characteristics.

5. SELF-ASSEMBLY OF DNA ON A GAPPED CARBON NANOTUBE*

We perform molecular dynamics simulations to analyze the wrapping process of a single-stranded (ss) DNA around a gapped CNT immersed in a bath of water. We observe the formation of a stable molecular junction with the ssDNA adopting a helical or circular conformation around one CNT electrode and a linear conformation around the opposite electrode. We find that DNA undergoes several conformational changes during equilibration of the self-assembled molecular junction. This process would allow a higher yield of successful CNT-DNA interconnections, which constitutes a novel structure of interest in chemical and biological sensing at the single-molecule level.

5.1 Introduction

Biological molecules integrated in nanosensors offer novel possibilities to reach a higher degree of chemical sensitivity and specificity due to the variety on structure-function and molecular recognition mechanisms of molecules in the living cell. Specifically, DNA has been investigated recently in several nanotechnology applications [123, 125, 126, 144, 156-171]. On the other hand, carbon nanotubes (CNT) are suitable as molecular interfaces due to their unique electrical conductivity and mechanical stiffness [129, 156, 172-180] as well as due to the possibility to manipulate their structure and function through oxidative processes using ion or electron beams [1].

---

* Part of this chapter is reprinted with permission from A.D. Bobadilla and J.M. Seminario, J Mol Model (2012) 18:3291–3300. Copyright 2012 Springer-Verlag.

DNA base-pair recognition properties allow us making arbitrary DNA-based nanostructures [140, 181, 182] and some efforts on the electrical characterization of these nanostructures have been already performed [183, 184]. DNA-CNT interactions in water solution show self-assembly properties [185], which can be exploited for making hybrid nanodevices [11, 186-188] and be combined with other molecular electronics approaches [131-133, 189-191].

Molecular imaging instruments such as scanning electron microscope (SEM) and atomic force microscope (AFM) do not allow getting details at the atomistic level and they have limitations on imaging suspended nanostructures. On the other hand, molecular dynamics simulations allow the analysis and prediction of structural conformations of CNT wrapped by DNA. [145, 192]. For instance Zheng *et al*. [193] proposed, based on AFM measurements, that poly GT (sequences of repeating guanine and thymine nucleotides) wraps helically around CNT as a hydrogen-bonded dimer with a 18 nm pitch helix. However using molecular dynamics simulations, Johnson *et al*. [145] found that an 18 nm pitch helical wrapping is structurally unstable, but a helical conformation with denser pitch was strongly favored and hybridization between multiple adsorbed poly GT oligonucleotides was unfavorable due to geometric factors.

Guo *et al*. [10] developed a method to connect a carbon nanotube gap with single DNA molecule. In their method, amine functionalization of DNA molecules allowed the covalent amide linkage to CNT functionalized with carboxyl groups; they obtained 10 working devices out of 370 that were tested. This low yield on successful interconnection of carbon nanotube with DNA is due to an inherent difficulty on creating a covalent bond. In the present work, a self-assembly process is analyzed in which a single stranded DNA molecule bridges a gapped CNT through noncovalent bonding.

5.2 Methodology

The molecular system under study consists of a single stranded (ss) DNA molecule with an initial helical conformation positioned parallel to a single-walled CNT. The initial separation between DNA and CNT is 15 Å, and the nanotube gap is 22 Å Figure 5.3a). Two types of carbon nanotube are considered in the analysis of CNT-DNA assembly, the (4,0) and (5,0) CNTs. By making terminal carbon atoms to share a covalent bond, we get a CNT structure periodic along the z-direction. The simulation box size is 40Å×50Å×80Å and includes 4500 TIP3P water molecules as well as 14 Na^+ counterions to exactly neutralize the negatively charged ssDNA backbone. The software PACKMOL [149] is used to construct the initial configuration of the system.

The dynamics of the system is modeled with the CHARMM force field [148] included in the Large-scale Atomic/Molecular Massively Parallel Simulator (LAMMPS) program [146]. Periodic boundary conditions are applied to a canonical NVE ensemble. Electrostatic interactions are calculated by the particle-particle and particle-mesh (PPPM) [150] method using a precision of 10^{-4}. CNTs are modeled as uncharged Lennard-Jones particles using sp^2 carbon parameters from the CHARMM force field. To control the temperature, atom velocities are rescaled at every time-step by using the Berendsen thermostat [151], which is applied to only the translational degrees of freedom. The positions of all CNT atoms are constrained by not updating the velocity for atoms in the CNT, as expected applications consider the CNT attached to fixed metal electrodes. Visualization of trajectories is performed using the Visual Molecular Dynamics (VMD) software [152]. van der Waals energy corresponding to CNT interactions with the ssDNA, and coulombic energy corresponding to interactions between adjacent phosphate atoms in the ssDNA backbone are computed as defined in the CHARMM force field (Table 5.1).

Previous to every molecular dynamics simulation, an energy minimization of the system is performed to reach a local potential energy minimum to avoid hot spots. Then the temperature of the system is raised from 5 K to 300 K in a 0.5 ns run using a 2 fs time step; this time step is used in all cases. Then a 1 ns run at 300 K is performed to ensure equilibration. To accelerate the wrapping process, the temperature is raised to 330 K in a 1 ns run, and the system is allowed to equilibrate at 330 K for 42 ns, until the average root mean square deviation (avRMSD) was observed to stabilize with a deviation of less than 0.05 Å within a nanosecond of simulation time. The RMSD is calculated for the DNA structure with respect to its initial conformation according to equations (7) and (8).

Table 5.1. Lennard-Jones and Coulombic interactions are computed with an additional switching function S(r) detailed in Equation 5.3.

cutoff	Lennard Jones	Coulombic
$r < r_{in}$	$V_{LJ}(r)$	$C(r)$
$r_{in} < r < r_{out}$	$S(r) \times V_{LJ}(r)$	$S(r) \times C(r)$
$r > r_{out}$	0	0

The Lennard-Jones potential,

$$V_{LJ}(r) = 4\epsilon\left[\left(\frac{\sigma}{r}\right)^{12} - \left(\frac{\sigma}{r}\right)^{6}\right] \tag{5.1}$$

represents nonbonded interactions between pairs of atoms separated by at least three bonds. It is composed of two terms: the first describes the Pauli repulsive interaction at short ranges due to overlapping electron orbitals, and the second describes the van der Waals attractive interaction at long ranges due to dipole-dipole interactions and to fluctuating molecular dipole moments.

The Coulombic potential,

$$C(r) = \frac{Cq_iq_i}{\varepsilon r} \tag{5.2}$$

represents interactions between static atomic charges. Lennard-Jones and Coulombic interactions are computed with an additional switching function S(r),

$$S(r) = \frac{\left[r_{out}^2 - r^2\right]^2}{\left[r_{out}^2 - r_{in}^2\right]^3}\left[r_{out}^2 + 2r^2 - 3r_{in}^2\right], \tag{5.3}$$

which allows decreasing interaction energies smoothly when the interatomic distance is larger than an inner cutoff, and forcing the energies to zero if the interatomic distance exceeds an outer cutoff distance.

We use inner and outer cutoff values of r_{in} = 8 Å and r_{out} =10 Å, respectively, for Lenard-Jones and Coulombic nonbonded interactions.

Table 5.2. Pair coefficients epsilon (ε) and sigma (σ) for interactions between atoms of the same type.

Atom type	ε	σ	Atom label	Atom type	ε	σ	Atom label
1	0.110	3.563595	C	21	0.028	2.387609	HN8
2	0.100	3.385415	CN1	22	0.024	2.387609	HN9
3	0.100	3.385415	CN1T	23	0.200	3.296325	NN1
4	0.100	3.385415	CN2	24	0.200	3.296325	NN2
5	0.090	3.385415	CN3	25	0.200	3.296325	NN2B
6	0.090	3.385415	CN3T	26	0.200	3.296325	NN2U
7	0.075	3.385415	CN4	27	0.200	3.296325	NN2G
8	0.075	3.385415	CN5	28	0.200	3.296325	NN3
9	0.075	3.385415	CN5G	29	0.200	3.296325	NN3A
10	0.020	4.053589	CN7	30	0.200	3.296325	NN3G
11	0.020	4.053589	CN7B	31	0.200	3.296325	NN4
12	0.056	3.581413	CN8	32	0.1521	3.150574	OT
13	0.056	3.581413	CN8B	33	0.1200	3.029056	ON1
14	0.078	3.634867	CN9	34	0.1200	3.029056	ON1C
15	0.046	0.400014	HT	35	0.1521	3.153781	ON2
16	0.046	0.400014	HN1	36	0.1200	3.029056	ON3
17	0.046	0.400014	HN2	37	0.1521	3.153781	ON5
18	0.046	1.959977	HN3	38	0.1521	3.153781	ON6
19	0.046	0.400014	HN5	39	0.5850	3.830864	P
20	0.022	2.351973	HN7	40	0.0469	2.429926	SOD

For interactions between atoms of different type, pair coefficients, ε and σ, are determined according to the following mixing rules,

$$\epsilon_{ij} = \sqrt{\epsilon_i \times \epsilon_j} \tag{5.4}$$

and

$$\sigma_{ij} = \frac{\sigma_i + \sigma_j}{2} \tag{5.5}$$

where, *i* and *j* correspond to the atom types.

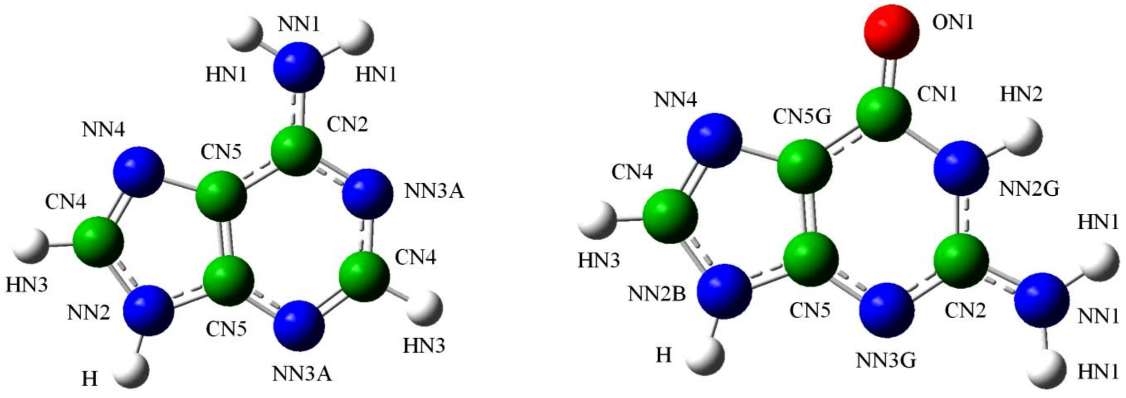

(A) **(B)**

Figure 5.1. Structures and atom labels for (A) adenine, (B) guanine, (C) cytosine, (D) thymine, (E) sugar and phosphate groups.

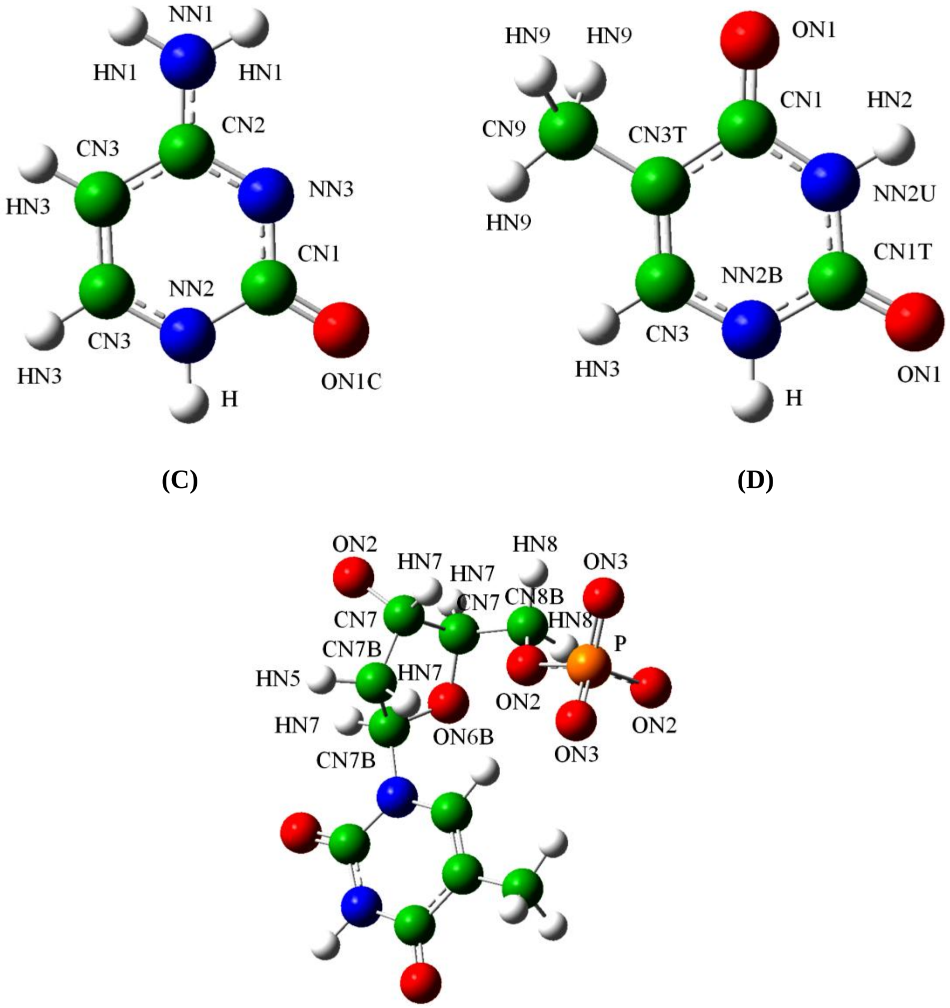

(C)

(D)

(E)

Figure 5.1. Continued.

To quantify torsional interactions, ssDNA backbone dihedral angles are also computed according to Equation (6) and Figure 5.2.

$$\tau = 2\pi + atan2(|v2|v1.[v2 \times v3], [v1 \times v2].[v2 \times v3]) \qquad (5.6)$$

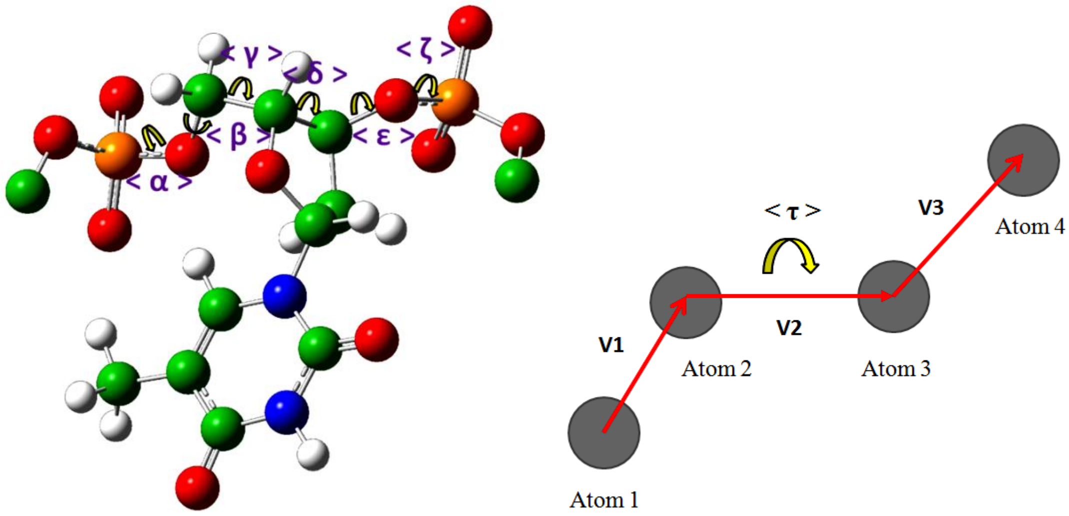

(A) **(B)**

Figure 5.2. (A) Dihedral angles in DNA backbone. (B) Definition of the dihedral angle τ.

To analyze changes in the DNA structure as a whole, we compute the root mean square deviation (RMSD) of atomic coordinates averaged over the entire simulation, which indicates the average scalar distance between atoms of the same type for ssDNA with respect to its initial structure, allowing one to assess how well the DNA structure is maintained during the simulation:

$$RMSD(i) = \sqrt{\frac{\sum_k^M |r_{ik} - r_{0k}|^2}{M}} \tag{5.7}$$

where the summation runs over all the M atom positions in the DNA molecule at the i-th snapshot. Finally the average RMSD through the snapshots is calculated from

$$avRMSD(N) = \frac{\sum_i^N RMSD(i)}{N} \tag{5.8}$$

where the summation runs over N snapshots of the simulation.

5.3 Results and discussion

Simulations are performed to analyze the interaction of a gapped single-walled carbon nanotube (CNT), interacting with a 15-base ssDNA molecule. The gap in the CNT divides the CNT in left and right electrodes. The self-assembly of the molecular junction is driven by a strong van der Waals attraction between the faces of the nucleobases and the CNT sidewall.

A 15-base ($A_1T_1C_1A_2A_3T_2A_4T_3C_2C_3A_5C_4C_5T_4G$) ssDNA, chosen at random, is initially at 1.5 nm from the gapped CNT (Figure 5.3a). During the initial process, when increasing temperature from 5K to 330K (Figures 5.3a-d), the DNA molecule approaches the CNTs (4,0) filling the gap; in this process, the DNA molecule elongates losing its helical-stacked conformation. After 8 ns of equilibration, at 330 K (Figure 5.3e), the ssDNA molecule adopts a linear conformation along the left CNT (4,0) electrode and the ($C_4C_5T_4G$) segment adopts a loop conformation on the right electrode due to stacking of cytosine (C_4) and guanine (G). Additional 8 ns of equilibration at 330K is required to observe a clear helical wrapping process (Figure 5.3f), adopting ssDNA a helical conformation around one CNT (4,0) electrode and a linear conformation on the opposite CNT (4,0) electrode, with four DNA bases filling the gap and only three bases on the right CNT (4,0) electrode.

Further equilibration at 330K is performed, after which we observe the ssDNA structural conformation changes from helical to circular (Figure 5.3g), with only three DNA bases filling the gap and five bases on the right CNT (4,0) electrode. The adoption of circular conformation in the DNA segment ($A_1T_1CA_2A_3T_2$) is aided by the formation of a hydrogen bond between adenine (A_1) and thymine (T_2) bases; this bond formation is promoted by the high temperature (330K) imposed to the system. The ssDNA circular conformation is stable for 18 ns at 330K (Figures 5.3g, 5.3h, 5.3i), after which we observe the final stable conformation adopted by ssDNA. This is a circular conformation on one CNT (4,0) electrode and a loop ($C_4C_5T_4G$) on the opposite electrode (Figure 5.3i); the loop structure is due to formation of hydrogen bond between cytosine (C_4) and guanine (G). We do observe a similar process for ssDNA wrapping around a gapped CNT(5,0) (Figure 5.4).

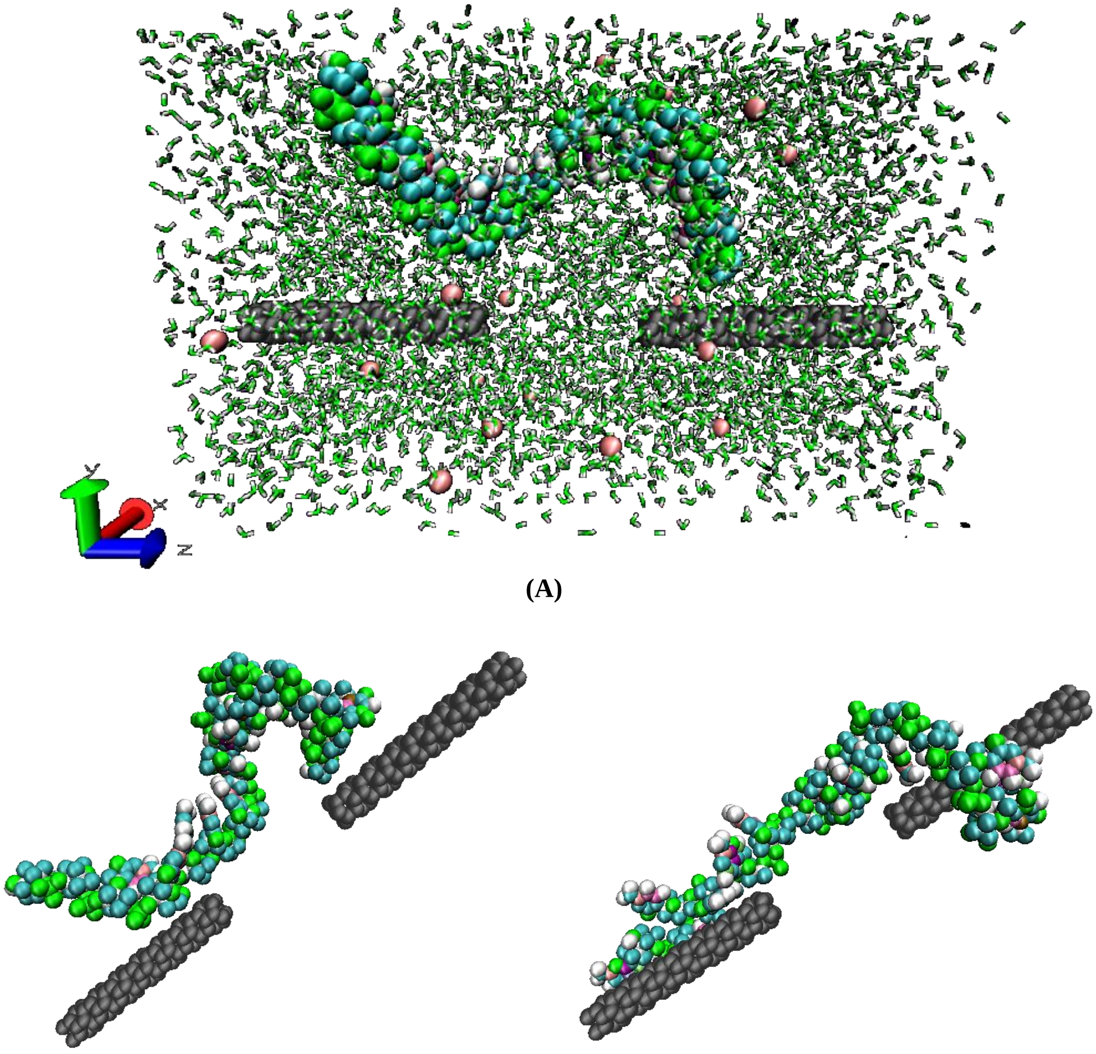

(A)

(B)

(C)

Figure 5.3. Time evolution of ssDNA structural conformation around CNT (4,0). (A) t = 0 ns, T = 0 K, initial configuration for the system. (B) t = 0.5 ns, T = 300K, ssDNA begin to approach CNT. (C) t = 1.5 ns, T = 300K, tendency for a wrapping process. (D) t = 2.5 ns, T = 330K, ssDNA gets elongated along CNT. (E) t = 10.5 ns, T =330K, beginning of wrapping process. (F) t = 18.5 ns, T = 330K, ssDNA adopts helical conformation on one of the CNT branches and loop conformation on the opposite one. (G) t = 26.5 ns, T = 330K, formation of hydrogen bond causes ssDNA changing conformation from helical to circular. (H) t = 34.5 ns, T = 330K, ssDNA keeps the same structural conformation. (I) t = 44.5 ns, T = 300K, ssDNA changes from linear conformation to loop conformation on the right CNT electrode, aided by the formation of a hydrogen bond.

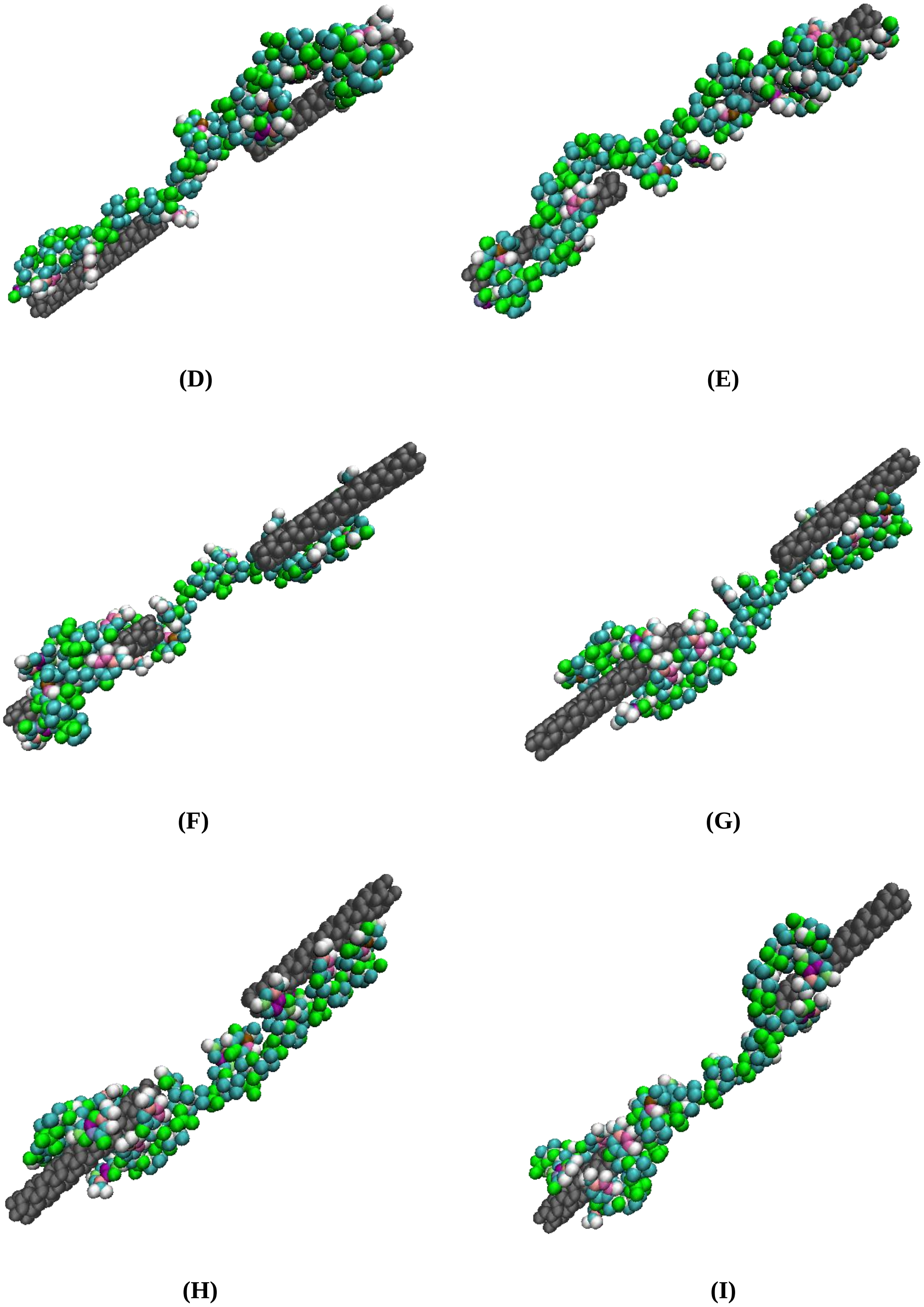

(D) (E)

(F) (G)

(H) (I)

Figure 5.3. Continued.

There is a difference in the DNA wrapping process for the CNT(4,0) and CNT(5,0) cases analyzed in this study. For interaction of ssDNA with CNT(4,0), we observe that the DNA molecule stabilizes slowly on the CNT surface, adopting at room temperature a linear conformation on the left electrode and a helical but stacked conformation on the right electrode (Figure 5.3c), with stacking of two DNA bases. While for the interaction of ssDNA with CNT(5,0), we observe the DNA molecule approaches faster the CNT surface, adopting the ssDNA a helical conformation on the left electrode at room temperature (Figure 5.4c), with DNA bases stacked to the CNT surface.

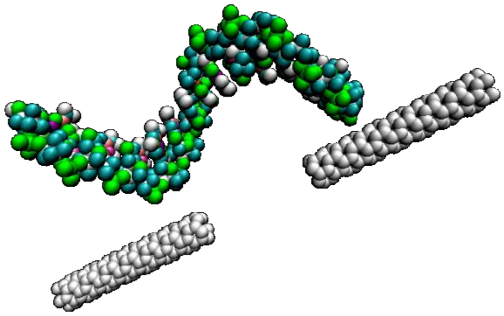

(A)

Figure 5.4. Time evolution of the ssDNA ($A_1T_1C_1A_2A_3T_2A_4T_3C_2C_3A_5C_4C_5T_4G_1$) structural conformation around CNT (5,0). (A) t = 0 ns, T = 0 K, initial configuration for the system. (B) t = 1 ns, T = 300K, ssDNA begins to approach CNT. (C) t = 1.5 ns, T = 300K, , ssDNA adopts helical conformation on one CNT branch and a linear conformation on the opposite. (D) t = 2.5 ns, T = 330K; ssDNA keeps same structural conformation. (E) t = 10.5 ns, T =330K, ssDNA adopts a helical conformation on both CNT branches, (F) t = 18.5 ns, T = 330K; ssDNA adopts circular conformation on one CNT, aided by the formation of a hydrogen bond between cytosine (C_2) and guanine (G_1), and a linear conformation on the opposite branch. (G) t = 26.5 ns, T = 330K, a new hydrogen bond is formed between thymine (T_3) and adenine (A_5), contributing to the stability of the ssDNA circular conformation. Only two bases are on the left CNT electrode and four bases filling the CNT gap. (H) t = 34.5 ns, T = 330K; ssDNA keeps same structural conformation. (I) t = 44.5 ns, T = 300K, ssDNA keeps same structural conformation.

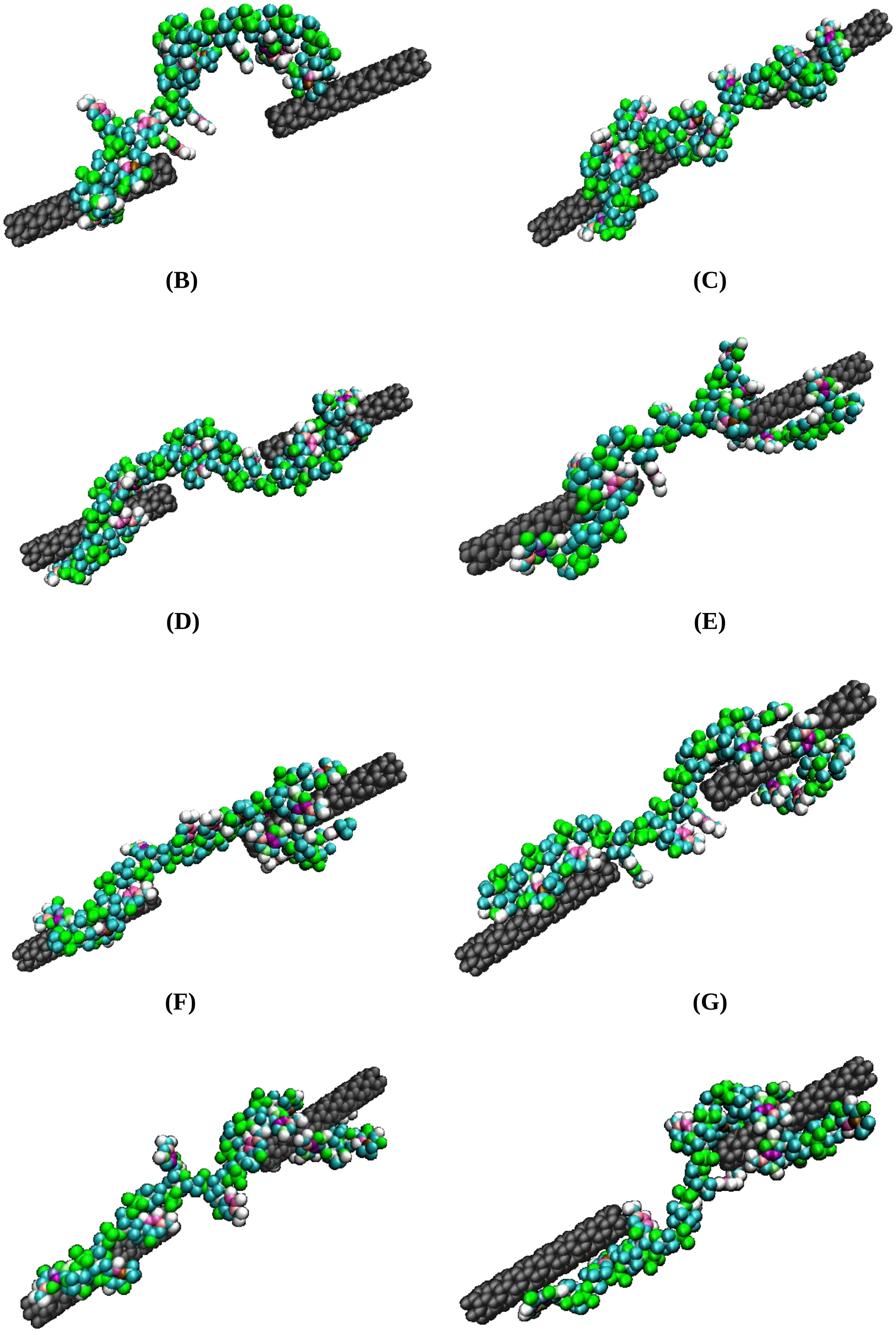

(B) (C)

(D) (E)

(F) (G)

(H) (I)

Figure 5.4. Continued.

The van der Waals (vdW) energy decreases notoriously at the beginning of the equilibration proceses at 300K (time = 0.5 ns) and at 330K (time = 2.5 ns) due to the wrapping of ssDNA around CNT surface for both chirality cases (4,0) and (5,0) (Figures 5.5 and 5.6). And the magnitude of vdW interaction energy between CNT and DNA is stronger for the CNT(5,0) case (Figure 5.6b) compared to the CNT(4,0) case (Figure 5.5b) with an oscillation of van der Waals energy smaller for the CNT(5,0) case; this due to a higher surface area on the CNT(5,0).

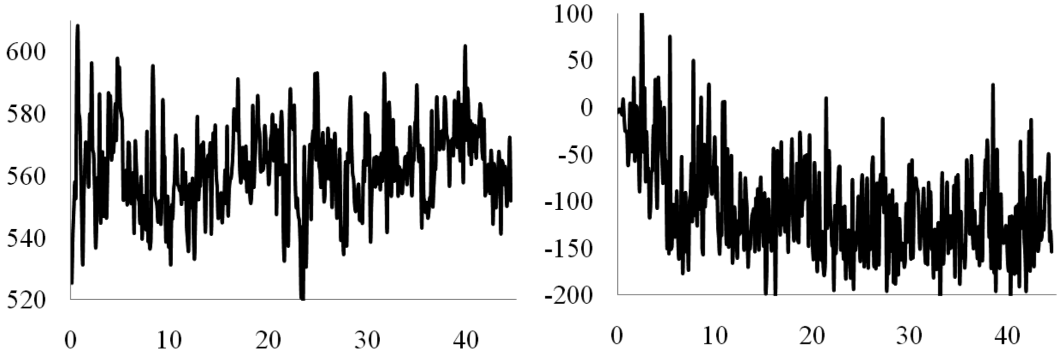

(A) **(B)**

Figure 5.5. Time evolution of (A) electrostatic energy of interaction between adjacent phosphate atoms and (B) van der Waals energy of interaction between the CNT(4,0) and the ssDNA molecule. Energy units are in kcal/mol and time in nanoseconds.

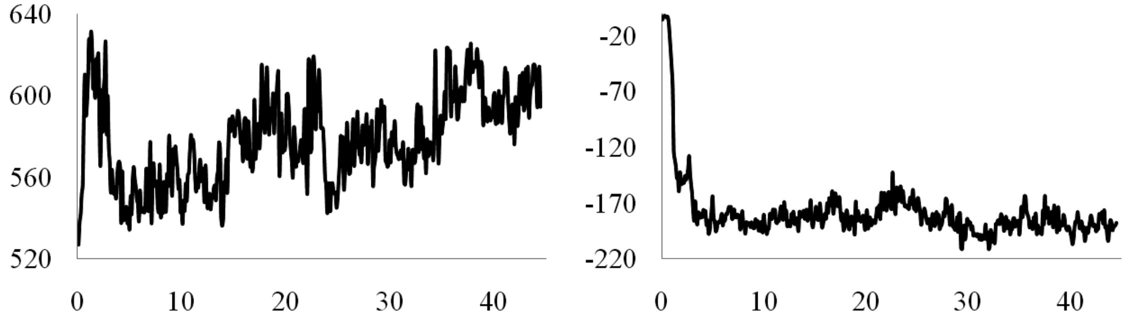

(A) **(B)**

Figure 5.6. Time evolution of (A) electrostatic energy of interaction between adjacent phosphate atoms and (B) van der Waals energy of interaction between single-walled carbon nanotube (5,0) and the ssDNA molecule. Energy units are in kcal/mol and time in nanoseconds.

A general mechanism of the wrapping process of ssDNA around carbon nanotube occurs from the 3' end to the 5' end [145]. In the present work the (4,0) and (5,0) CNTs are considered for the analysis of the interaction with the ssDNA and we observe in both cases a wrapping process from the 3' end to the 5' end. For the CNT (4,0), the ssDNA wraps the carbon nanotube adopting a circular conformation on the left electrode (Table 5.3, Figure 5.3i); however, for the CNT(5,0) case, ssDNA adopts a circular conformation on the right CNT electrode (Table 5.4, Figure 5.4i).

Table 5.3. Time evolution of ssDNA structural conformations around CNT (4,0).

time	Temperature	ssDNA conformation		Energy (kcal/mol)	
(ns)	(K)	Left CNT	Right CNT	Coulombic	vdW
1.5	300	Linear	Helical	570.9	-47.2
2.5	330	Linear	Helical	536.9	110.7
10.5	330	Linear	Loop	559.7	-155.7
18.5	330	Helical	Linear	556.9	-141.5
26.5	330	Circular	Linear	557.1	-172.1
34.5	330	Circular	Linear	553.5	-83.8
44.5	330	Circular	Loop	551.8	-154.1

Table 5.4. Time evolution of ssDNA structural conformations around CNT (5,0).

Time	Temperature	ssDNA conformation		Energy (kcal/mol)	
(ns)	(K)	Left CNT	Right CNT	Coulombic	vdW
1.5	300	Helical	Linear	603.5	-147.9
2.5	330	Helical	Linear	601.6	-146.1
10.5	330	Helical	Helical	548.2	-193.3
18.5	330	Linear	Circular	587.9	-184.7
26.5	330	Linear	Circular	588.3	-180.1
34.5	330	Linear	Circular	587.6	-183.9
44.5	330	Linear	Circular	594.6	-188.0

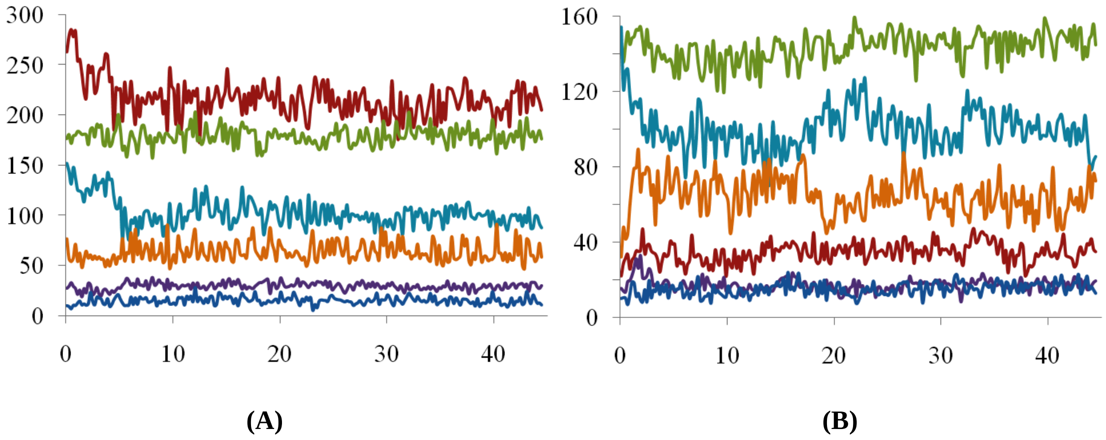

Figure 5.7. Time evolution of average ssDNA dihedral angles <τ> (°) for (A) ssDNA-CNT(4,0) and (B) ssDNA-CNT(5,0) molecular junctions. Time is in nanoseconds and curves are color coded: alpha (red), beta (green), epsilon (turquoise), gamma (orange), delta (purple), zeta (blue).

The mechanism responsible for the ssDNA overall structural conformation is credited to electrostatic and torsional interactions within the sugar-phosphate backbone because the backbone contains an intrinsic curvature and prefers a helical wrapping rather than a linear one. A decrease in electrostatic energy during the first 10 nanoseconds of simulation time (Figures 5a, 6a) is associated with an increase in phosphate-phosphate distance in the DNA backbone and a corresponding decrease in electrostatic repulsion, favoring a helical conformation for ssDNA. Structural and energetic changes in ssDNA proceed via a rearrangement of the average torsional angles <τ> (°) in the ssDNA backbone (Figure 5.7).

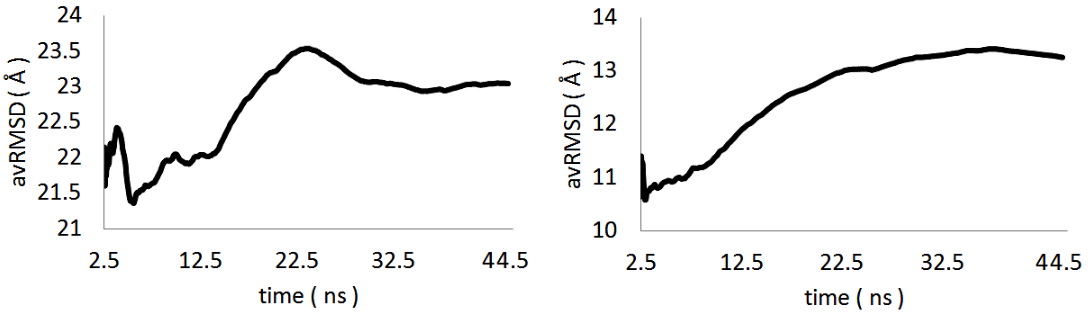

(A) **(B)**

Figure 5.8. Time evolution of root mean square deviation (RMSD) calculated for the ssDNA molecule with respect to its initial conformation. Plots correspond to (A) ssDNA-CNT(4,0) and (B) ssDNA-CNT(5,0).

Table 5.5. Summary of avRMSD values for ssDNA during the last 5 ns of simulation.

Time (ns)	avRMSD (Å)	
	ssDNA-CNT(4,0)	ssDNA-CNT(5,0)
40.5	23.03	13.35
41.5	23.03	13.33
42.5	23.04	13.31
43.5	23.05	13.29
44.5	23.05	13.26

We denote by avRMSD (Figure 5.8) the RMSD value averaged over the simulation time, stopping the simulation when the avRMSD is observed to stabilize with a deviation not bigger than 0.05 Å within a nanosecond of simulation time (Table 5.5).

We also observe a tendency for a helical conformation in ssDNA structure during the equilibration process at 330K, nevertheless, helical turns continue being generated, forcing the ssDNA conformation to change from the helical to a circular one, aided by the formation of hydrogen bonds. The final stable conformation of ssDNA is a circular one on one electrode and a linear or loop conformation on the opposite CNT electrode. Hydrogen bonds aid on the formation of circular and loop conformations (Figures 4g, 4i, 5f, 5g). When the circle forms on one end of the ssDNA, the other end is not able any more to adopt a helix shape because the remaining ssDNA is not long enough. In other trials with several initial configurations, DNA forms loops and disordered kinked structures because of steric interactions between adjacent bases and the ssDNA flexibility, being a polymer with several degrees of freedom, yielding a very irregular energy landscape with several local minima [192].

5.4 Conclusions

Atomistic molecular dynamics simulations have been performed exploring the self-assemby dynamics and structure of a molecular junction enabled by the CNT-DNA wrapping process. ssDNA is able to bridge a carbon nanotube gap adopting different structural configurations around each carbon nanotube, a helical configuration and then a circular conformation around one CNT branch during the equilibration process at 330K; this conformation is kept at room temperature; while on the other CNT, ssDNA adopts a linear elongated or otherwise loop configuration during the process at 330K and keeps that conformation at room temperature. We attribute the different conformations DNA adopts in our molecular junction, to the influence of mainly two factors, length of ssDNA on each CNT electrode and the arrangement of hydrogen bonds on the CNT surface.

6. ELECTRON TRANSPORT CHARACTERISTIC OF A DNA-GRAPHENE JUNCTION*

Single-stranded (ss) DNA readily absorbs on graphene nanoribons (GNR) due to van der Waals interactions. Such absorption can be used for a single ssDNA characterization, enabling potential applications in biotechnology as well as in chemical and biological sensing. We analyze, using molecular dynamics simulations, the attachment process of the DNA codon GAG drifted by an external electric field on a gapped graphene nanoribbon. We calculate the quantum electron transport through a noncovalent junction GNR-DNA surrounded by a water monolayer with sodium counterions. We find that the GNR-DNA junction is stable in aqueous conditions at room temperature and at 330K. The DNA molecule causes a smooth transition to the conductive state of the gapped graphene; we estimate a detectable electronic signal of ~2 nA, which allows us to identify the DNA molecule bridging the gapped graphene.

6.1 Introduction

Nanostructured materials are novel tools for the characterization of DNA molecules.[194-206] A carbon nanotube-DNA molecular junction allowed analyzing the influence of DNA bases mismatch on electron transport.[5, 207] In a different approach, a self-assembled monolayer and scanning probe measurements allowed detecting DNA electron transport on distances over 34 nm.[208, 209] In addition, one of

---

* Part of this chapter is reprinted with permission from A.D. Bobadilla, J.M. Seminario, *J. Phys. Chem. C*, **2013**, *117* (50), pp 26441–26453. Copyright 2013 American Chemical Society.

the most novel approaches for low cost DNA sequencing technology is based on monitoring the ionic current when DNA passes through a silicon nanopore.[210-212]

Different methods have been reported to obtain graphene nanoribbons, such as helium ion lithography,[213] gas-phase chemistry to etch graphene from the edges without damaging its basal plane [214], and unzipping of carbon nanotubes.[215-217] To obtain a graphene nanogap, a combined lithography and etching procedure can be used,[5, 218] but to achieve a gap of less than 2 nm in size, an electrical breakdown technique allows a precise control on the gap dimension.[112, 219]

DNA and water molecules affect the electrical characteristic of a hydrophobic carbon nanostructure;[13, 220-223] DNA absorption due to van der Waals forces produces a disturbance of the electron density in carbon nanostructures and therefore a modulation of carbon nanotube and graphene nanoribbon electrical properties.[12, 155, 224-227]

We obtain the structure of a noncovalent graphene-DNA junction in water solvent using molecular dynamics simulations and the electron transport characteristics through the junction using a Green function technique combined with a density functional theory (DFT) electronic structure calculations under an external electric field.

6.2 Methodology

The initial structure is built with the program PACKMOL.[228] Previous to every molecular dynamics simulation, an energy minimization is performed to decrease the net forces on the atoms. The Polak-Ribiere version of the conjugate gradient (CG) algorithm is followed; [229] at each iteration the gradient (force) is combined with the previous iteration information to compute a new search direction perpendicular to the previous search direction. The final state of the system after energy minimization corresponds to the configuration of atoms when the temperature of the system is approximately zero.

We perform all-atom classical molecular dynamics (MD) simulations with the LAMMPS program.[146] We use the interatomic potential energy functions from the empirical force field CHARMM,[230] which includes contributions from covalent bonded and noncovalent interactions for several types of organic molecules.

A modification of the MD scheme based on classical Newtonian equations of motion is required to generate a thermodynamical ensemble at constant temperature and to enable comparisons with experiments.[231, 232] Because the instantaneous temperature is directly related to the atomic internal velocities, maintaining the temperature constant (on average) in MD simulations requires imposing some control on the rate of change of these velocities (thermostating).[233, 234]

The equations of motion are coupled to a Nose-Hoover thermostat[234] and time integration is performed on this non Hamiltonian scheme as implemented by Shinoda *et al.*,[235] generating positions and velocities consistent with a canonical ensemble (NVT) [231, 232]. The time integration schemes closely follow the time-reversible measure-preserving Verlet integrators derived by Tuckerman *et al.*[236]

Long-range Coulombic interactions are calculated using a particle–particle particle–mesh (pppm) method,[237, 238] in which the force is calculated in two parts, a mesh part and a short-range part, determined by the ratio of the cutoff radius and the cell width of the mesh used in the particle-mesh calculation. The mesh part of the force is long range and smoothly varying while the short range part is rapidly varying, having nonzero contributions only from those particles within the cutoff radius; this cut-off scheme decreases the number of particle-particle interactions and therefore shortens the computer simulation.[237, 238] We use the visual molecular dynamics (VMD) program[239] to visualize the MD trajectories.

A Kohn-Sham (KS)[240] molecular structure theory combined with a Green's function transport procedure[140, 241, 242] is used to analyze the electron transport properties of the GNR-ssDNA-GNR junction addressed by gold nanotips. The Hamiltonian matrix is obtained from DFT calculations where few gold interfacial atoms are added to each end of the molecule of interest. The gold contacts are also calculated using a similar DFT procedure but with periodic boundary conditions using the program CRYSTAL.[243] The density of states (DOS) of gold is needed as input for the electron transfer calculations together with the extended molecule calculations; the Hamiltonian, overlap matrices of the extended molecules and the DOS of the bulk gold are the inputs for the electron transport program GENIP,[140, 241, 242] which outputs the electron transmission probabilities, the current-voltage characteristic of the molecular junction and the DOS at the junction where the effect of the gold electrodes and the effect of the bias voltage on the electronic structure of the molecule are explicitly considered.

Density functional theory (DFT) electronic structure calculations are performed using Gaussian-09 program [113]; the B3PW91[244, 245] and the M06[246] hybrid functionals are used for the graphene-gold interface studies; the latter is used especially when graphene-DNA noncovalent (pi-pi for example) interactions need to be precisely considered[247] and the former is one of the most accurate for bonded systems.[248-251] The LANL2DZ basis set[252] is used for the gold atoms and the full-electron 6-31G(d) basis set[253, 254] for all the other; the effective core potential for Au is the LANL2.[252, 255, 256] These combined levels of theory offer the best compromise of speed and accuracy for our molecular junction.[247, 250, 257-260]

6.3 Results and discussion

6.3.1 MD simulations

A ssDNA (GAG) molecule is positioned above a graphene nanogap and solvated by 1,564 water molecules in a simulation box of 40×40×40 $Å^3$ (Figure 6.1a). Two sodium counterions are also included to neutralize charges in DNA backbone due to phosphate groups. The gap distance between graphene electrodes is 6 Å. Molecular dynamics are performed with periodic boundary conditions and graphene atoms are constrained to fixed positions.

We increase the temperature from 1 K to room temperature in a 0.5 ns linear ramp, followed by energy equilibration at constant temperature during 1 ns (Figure 6.1b). During this equilibration process, ssDNA absorbs to the right graphene electrode surface (Figure 6.1c). In order to analyze the possibility of ssDNA bridging naturally the graphene gap and to speed up the exploration of DNA conformational possibilities, the temperature is increased to 330K in a 0.5 ns linear ramp followed by an energy equilibration at constant temperature. The ssDNA never bridges the gap and all nucleobases physisorp on the graphene surface (Figure 6.1d). The system is then brought back to room temperature.

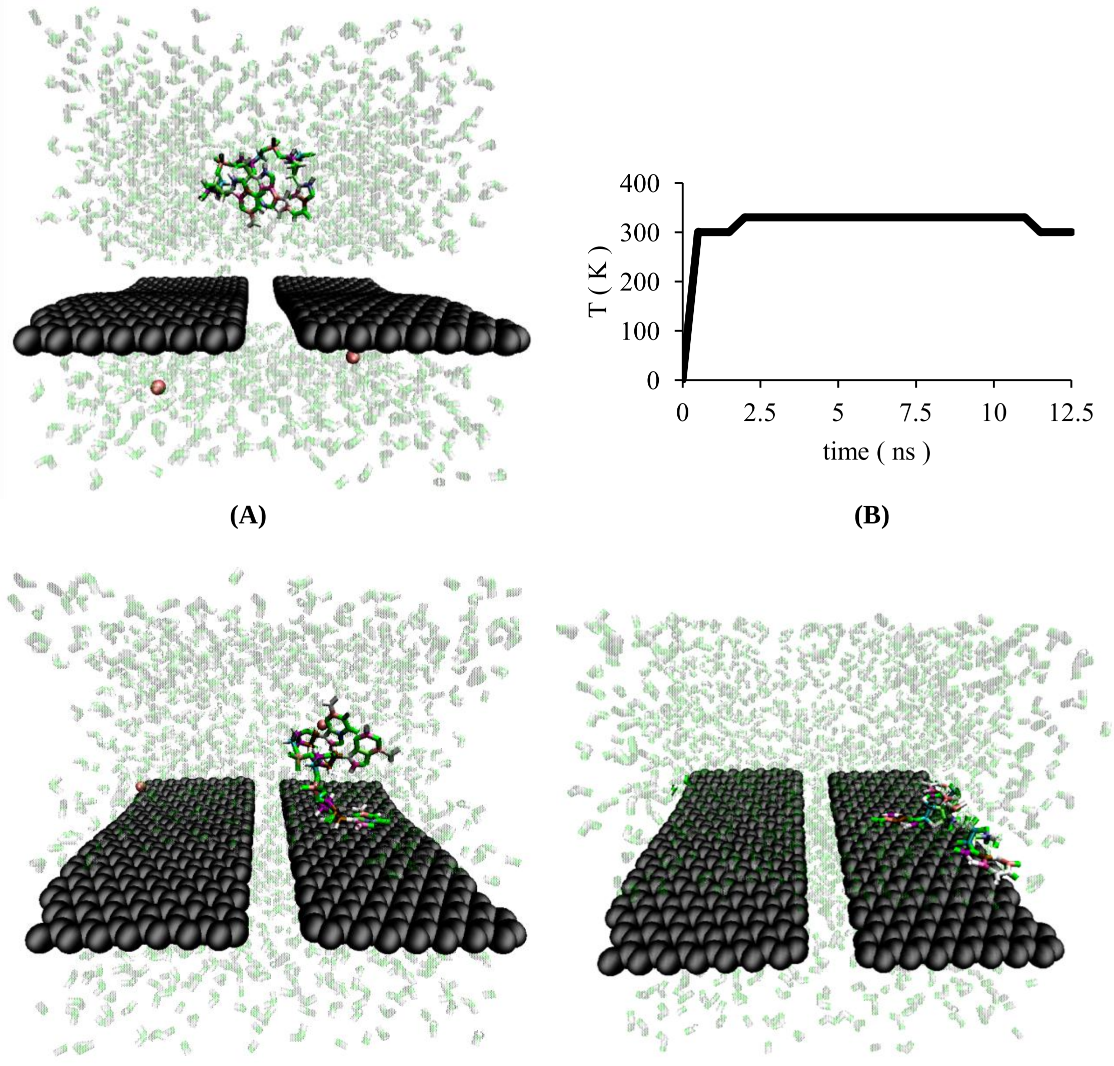

(A) **(B)**

(C) **(D)**

Figure 6.1. ssDNA (GAG) absorption to graphene nanoribbon. (A) Initial structure, (B) Time evolution of temperature, (C) ssDNA absorption on graphene at room temperature, (D) Final ssDNA conformation during equilibration at 330K with three nucleobases absorbed on graphene. Molecular dynamics (MD) simulation performed with periodic boundary conditions.

We apply an electric field (0.08 V/Å) to DNA phosphate atoms (Figures 6.2a-c) during 0.3 ns at room temperature to try to induce the formation of a graphene-DNA junction. The electric field is applied at t = 12.5 ns and stopped at t = 12.8 ns. If the electric field is applied for an additional time larger than a tenth of a nanosecond the ssDNA abandon the gap continuing its trajectory along the graphene surface and electric field direction. We calculate the van der Walls energy of interaction between graphene electrodes and ssDNA (Figure 6.2d). The energy corresponding to a conformational state when ssDNA bridges the gap is -80 kcal/mol while the energy when all nucleobases absorb to a graphene electrode is -90 kcal/mol. But during the transition between those two stable states, the vdW energy is -60 kcal/mol and it takes 0.15 ns to reach a junction conformation (Figure 6.2d) under the applied electric field (0.08 V/Å) and at room temperature.

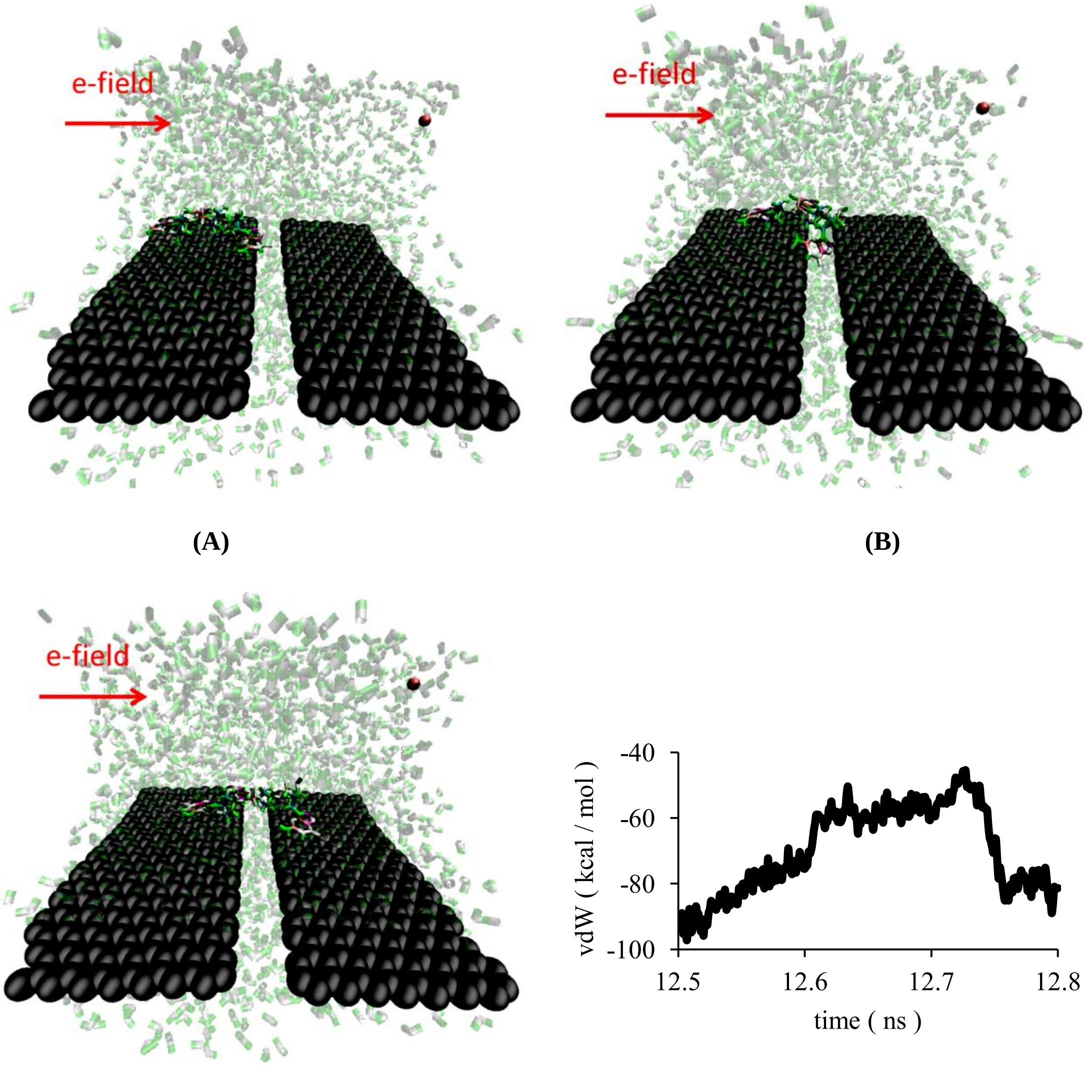

(A) (B)

(C) (D)

Figure 6.2. Electric field assisted positioning of ssDNA on graphene gap at room temperature. ssDNA conformation at (A) 12.6 ns, (B) 12.7 ns and (C) 12.8 ns under the application of an electric field with magnitude 0.08V/Å to phosphate atoms in the DNA backbone. (D) van der Waals (vdW) energy of interaction between graphene nanoribbons and ssDNA molecule. Electric field is applied at t = 12.5 ns and stopped at t = 12.8 ns. Simulation performed with periodic boundary conditions.

To test the stability of the molecular junction, an MD run is performed at 330K during 9 ns (Figure 6.3a). During this period, the ssDNA keeps bridging the graphene nanogap (Figures 6.3b-d); therefore, a temperature level as high as 330K is not high enough to switch ssDNA conformation between the two stable states.

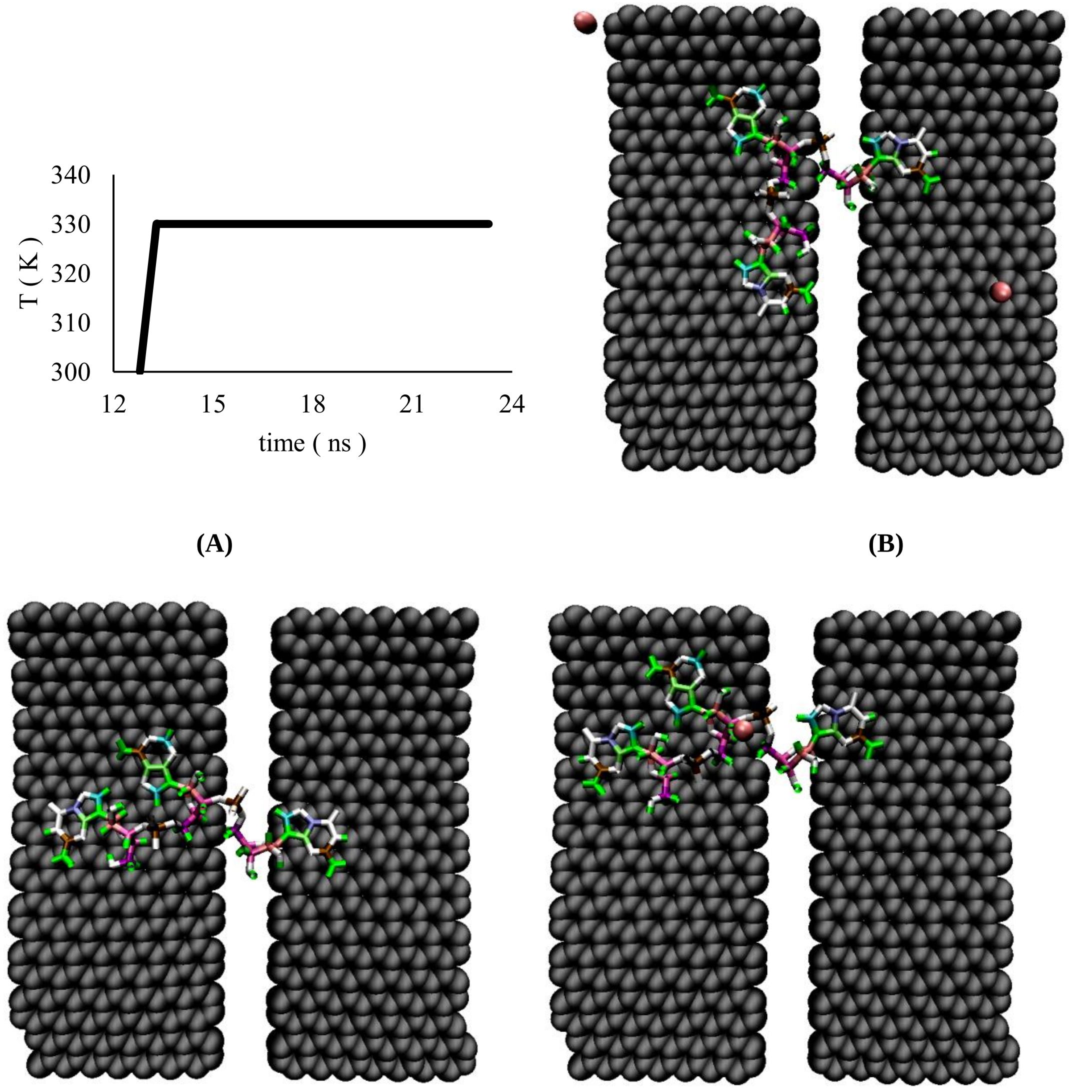

(A) **(B)**

(C) **(D)**

Figure 6.3. Stability of the molecular junction at 330K. Time evolution of temperature beginning at 12.8 ns (A) and snapshots (B-D) of the ssDNA-graphene junction during last nanosecond of equilibration. (B) t = 22.3 ns, (C) t = 22.8 ns and (D) t = 23.3 ns. Water molecules omitted for visualization purposes. Simulation performed with periodic boundary conditions.

To enable the computationally expensive electronic structure calculations, we induce evaporation of water molecules at 330K and then at 300K (Figure 6.4a) by eliminating gradually and randomly the water molecules. The evaporate command in LAMMPS software is used to simulate evaporation of water molecules, deleting a fixed number of water molecules in a specific region and at a fixed rate; water molecules to be deleted are chosen randomly. Water molecules are evaporated at 330K at a rate of 100 water molecules every 1 ns during 10 ns and then at a rate of 50 water molecules every 0.5 ns during 2.5 ns (Figure 6.4b). Further evaporation at 330 K causes breaking of the junction. After 12.5 ns of MD run at 330K, the system is brought to room temperature and evaporation is performed at a rate of 50 water molecules every 0.5 ns during 2 ns in the zone below the graphene electrodes. After this process, the remaining water molecules located below the graphene electrodes are evaporated and an energy equilibration is performed at room temperature during 1 ns (Figure 6.4c). The final conformation at 1 K for MD simulations with periodic boundary conditions is shown in Figure 6.4d.

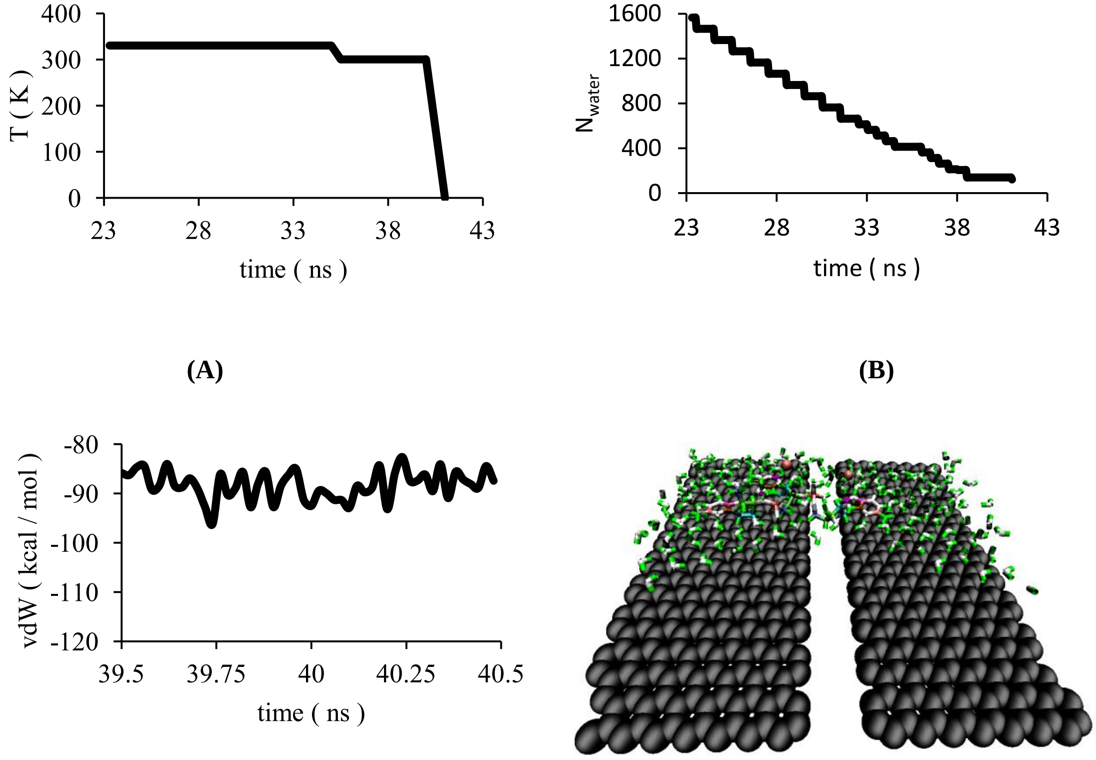

(A) **(B)**

(C) **(D)**

Figure 6.4. Water evaporation induced by eliminating gradually and randomly water molecules. The size of the system is gradually reduced to enable quantum chemistry calculations. (A) Time evolution of temperature, (B) Time evolution of number of water molecules; they are removed from the simulation box at a rate of 100 molecules/ns and chosen randomly, (C) vdW energy of the graphene-ssDNA interaction during the last nanosecond of equilibration at 300K, (D) Final ssDNA-graphene junction at 1K. Simulations were performed with periodic boundary conditions and in the absence of an external electric field.

Aiming to reduce further the size of the system, we also analyze the graphene-DNA junction with reduced width for graphene nanoribbons (Figure 6.5a) and with nonperiodic boundary conditions. During the equilibration at room temperature (Figure 6.5c) some water molecules naturally evaporate, escaping from the simulation box, and are deleted from the simulation (Figure 6.5d). We notice an average value of -89.9 kcal/mol (Figure 6.5e) for the vdW energy during the last nanosecond of equilibration at room temperature; this energy is near to the average value of -88.3 kcal/mol obtained with larger graphene nanoribbons and periodic boundary conditions (Figure 6.4c).

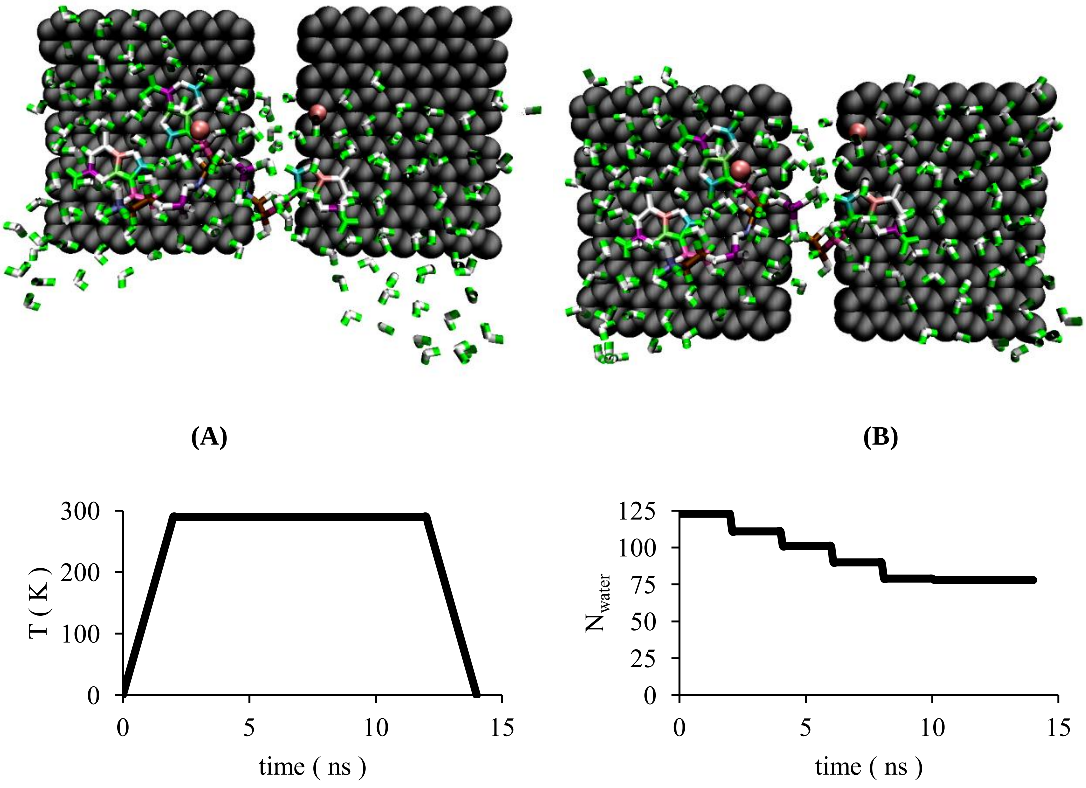

(A) **(B)**

(C) **(D)**

Figure 6.5. MD simulations with reduced width for graphene and nonperiodic boundary conditions. (A) Initial structure, (B) structure after energy minimization, (C) time evolution of temperature, (D) time evolution of number of water molecules; water molecules escaping from the simulation box are deleted from the simulation, (E) vdW interaction energy between graphene and DNA during last nanosecond of equilibration at room temperature, (F) final structure at 1 K.

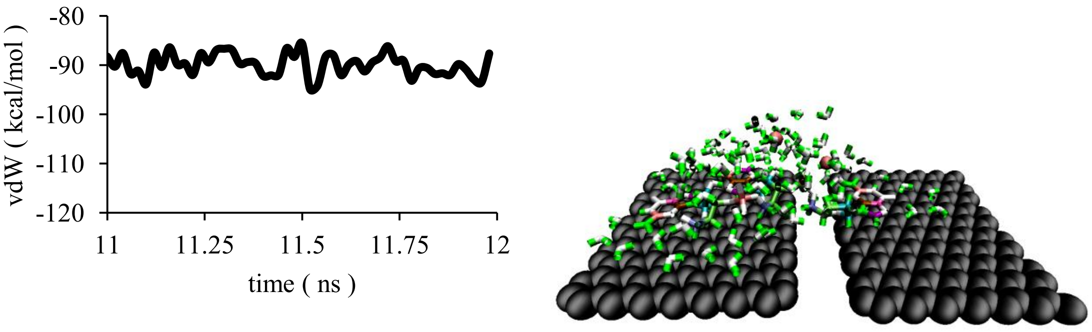

(E) **(F)**

Figure 6.5. Continued.

We then reduce further graphene nanoribbons size by decreasing graphene length (Figure 6.6a). During the first nanosecond of equilibration at room temperature, a large evaporation (22 out of 75 water molecules, Figure 6.6d) occurs, producing a conformational change in ssDNA structure: the central nucleobase (adenine) positions in the nanogap zone (Figure 6.6e,f), during the second nanosecond of equilibration with only a small change in the vdW energy (Figure 6.6g), from an average value of -77.4 kcal/mol during the first nanosecond at room temperature to -79.3 kcal/mol during the second nanosecond. This decrease in graphene size causes a significant increase of about 10 kcal/mol in the vdW energy when compared to the larger graphene cases (Figures 6.4c, 6.5e) and reaches an average value of -75.6 kcal/mol (Figure 6.6h) when the evaporation of water molecules almost stops, during the last nanosecond of equilibration at room temperature.

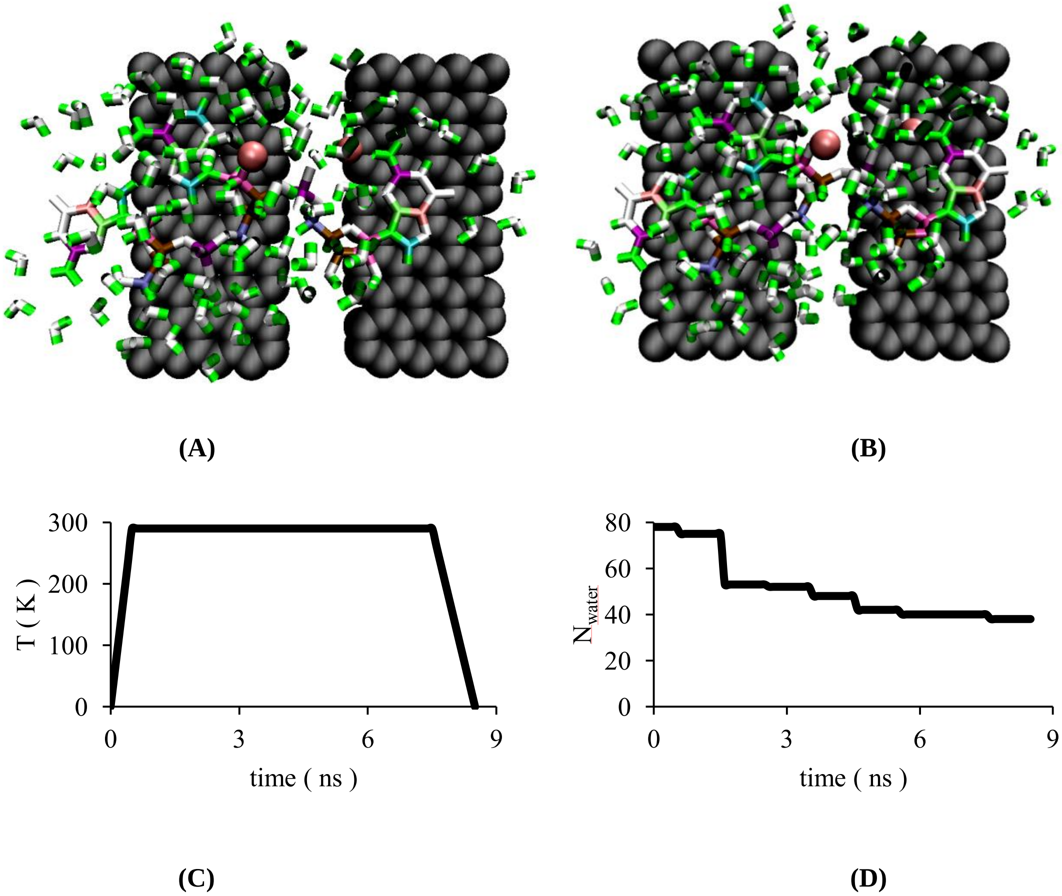

(A) (B)

(C) (D)

Figure 6.6. Reduced graphene length and nonperiodic boundary conditions. (A) Initial structure, (B) Structure after energy minimization, (C) Time evolution of temperature, (D) Time evolution of number of water molecules. Water molecules escaping from the simulation box are deleted from the simulation, (E) Structure at t = 1.5 ns with two nucleobases absorbed on left graphene electrode, (F) Structure at t = 2.5 ns with one nucleobase positioned in the nanogap zone, (G) vdW energy for graphene-ssDNA interaction during the initial 2 ns of equilibration at room temperature, (H) vdW energy for graphene-ssDNA interaction during the last nanosecond of equilibration at room temperature, and (I) Final conformation at 1 K. Water molecules are omitted in (E) and (F) for visualization purposes.

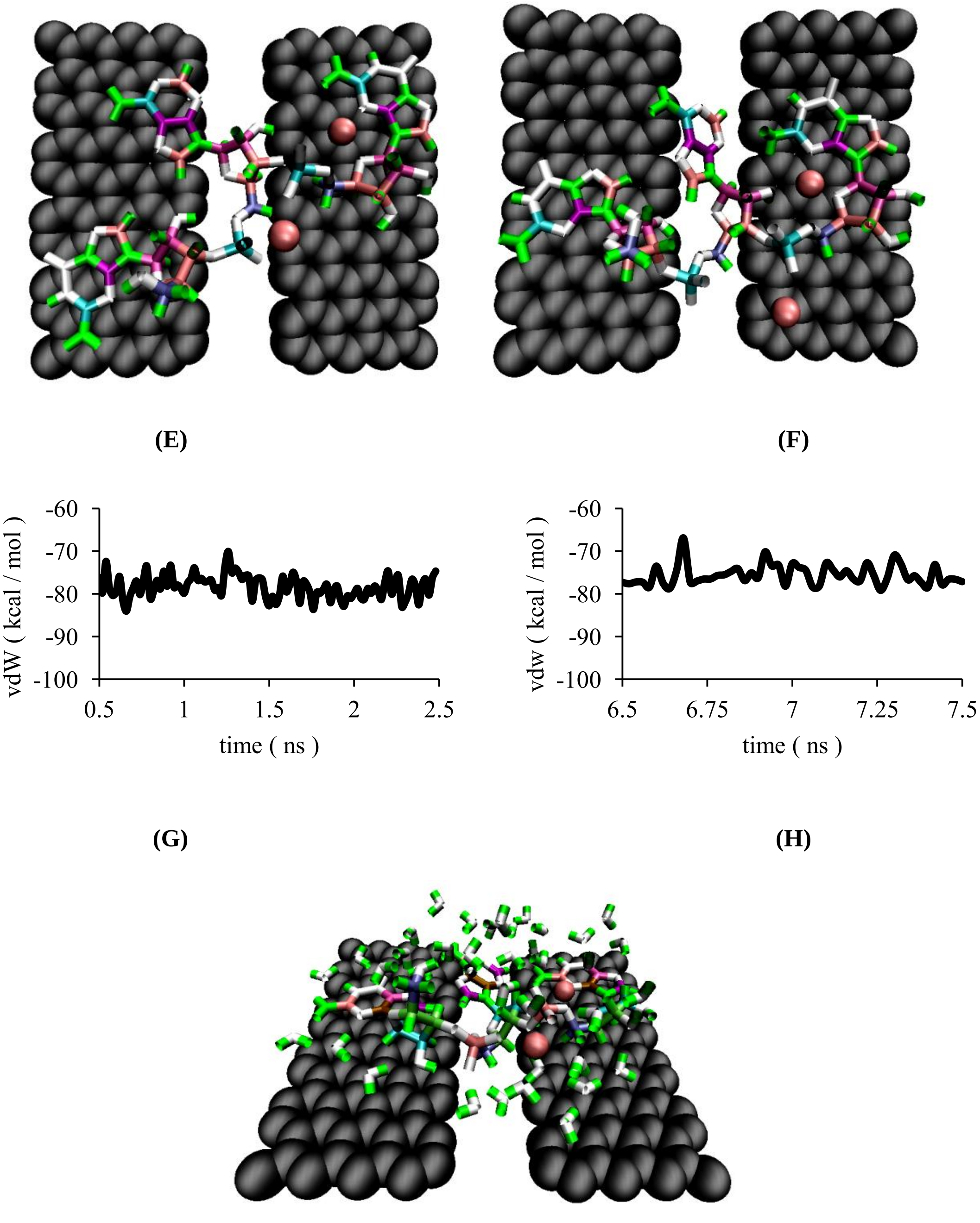

(E) **(F)**

(G) **(H)**

(I)

Figure 6.6. Continued.

In the final structure (Figure 6.6i), the ssDNA (GAG) molecule is positioned with the left nucleobase (G) and right nucleobase (G) oriented parallel to graphene nanoribbon (GNR), and the central nucleobase (A) filling the gap.

6.3.2 DFT analysis

The resultant structure, which includes graphene H-terminated, DNA, water and sodium ions, from MD simulations is then DFT optimized with total spin and charge zero using the M06 functional [246] because of the adequate estimation provided for pi-pi interactions between graphene and DNA [247]. In all DFT structure optimizations the 6-31G(d) basis set [244, 245] is used.

To add gold electrodes, a gold-graphene interface is first DFT optimized with both spin and charge zero. The LANL2DZ basis set [252] and core potentials are used for gold atoms. Gold electrodes are then added to the previously GNR-DNA-Na^+-water optimized structure. The Au-GNR-DNA-Na^+-water (Figure 6.7) is DFT optimized using the M06/6-31g*/LANL2DZ level of theory. The average gold-carbon bond distance is 2.14 Å, the average gold-gold bond distance is 2.64 Å and the average guanine nucleobase-graphene nonbonded distance is 3.2 Å.

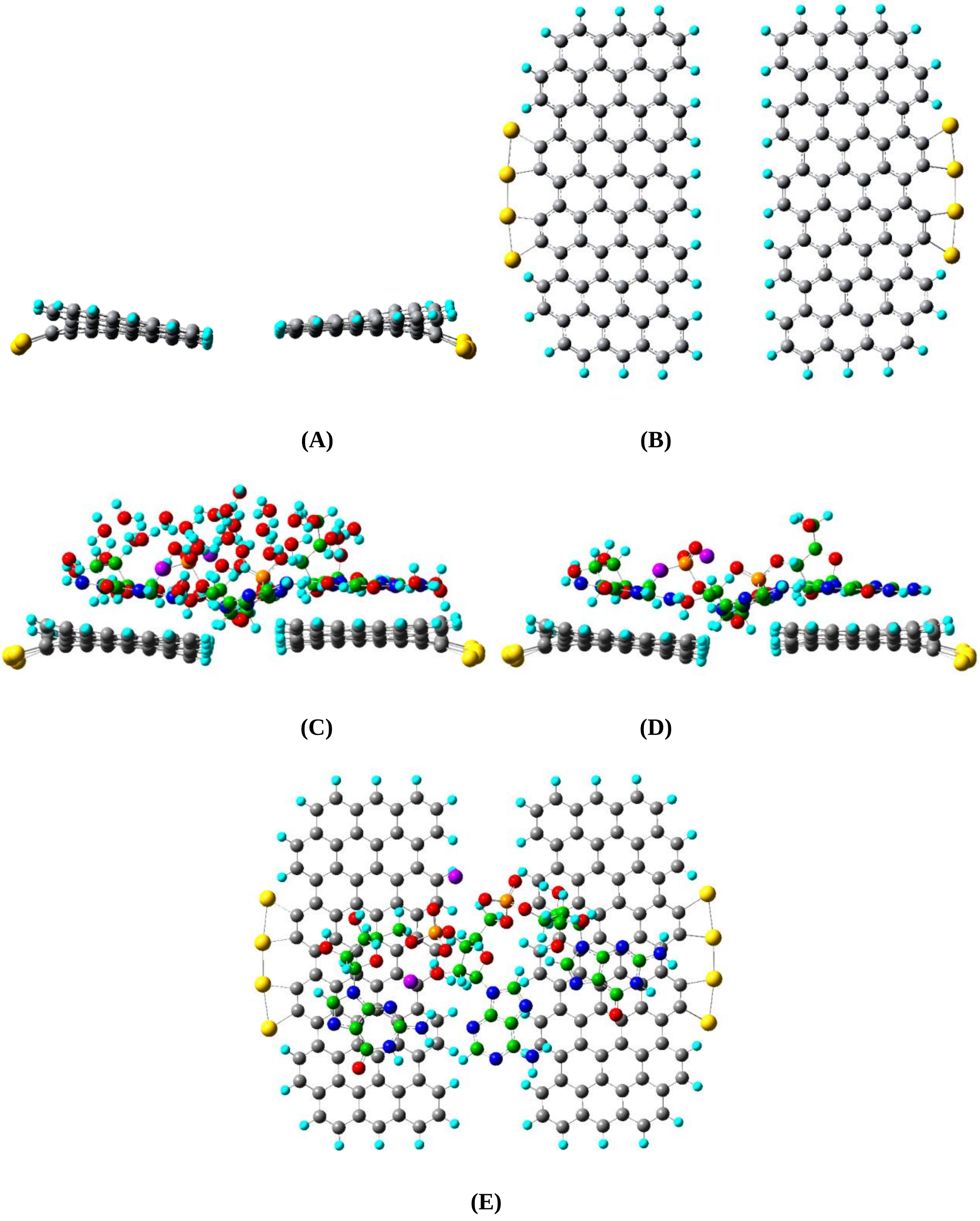

Figure 6.7. DFT optimized structure for gapped graphene and DNA junction. Initial structures are taken from MD simulations; gold and hydrogen atoms are added to the graphene initial structure. (A,B) views of the optimized geometry for gapped GNR. (C,D,E) views of the optimized geometry for the DNA junction; ssDNA sequence is GAG. (C,D) Side view and (E) top view of DNA junction. Gold (yellow), GNR carbon (gray), DNA carbon (green), nitrogen (blue), oxygen (red), sodium (purple) and hydrogen (cyan). In (D) and (E) water molecules are omitted for visualization purposes.

The energy levels that will enable an electrical current are those near to the equilibrium chemical potential and to the HOMO or LUMO orbitals; as a reference the work function for bulk gold is -5.3 eV.[261] In the DNA junction, we find molecular orbitals (MO) delocalized in graphene and guanine nucleobase (Table 6.1, Figure 6.8) in the left side (HOMO-4 and HOMO-6) as well as in the right side (HOMO-10). We observe molecular orbitals with similar energies (less than 0.1 eV difference) able to form energy bands in the molecular junction. Table 6.1 shows for the DNA junction: three energy bands below the HOMO orbital, a band from HOMO to HOMO-3 (associated to graphene and gold electrodes), a band from HOMO-4 to HOMO-6 (associated to graphene and DNA) and a band from HOMO-7 to HOMO-10 (associated to graphene, DNA and gold electrodes) as well as three energy bands above the LUMO. The formation of these energy bands implies delocalized MOs on the left and right side of the DNA junction; these MOs appear in the density of states (Figure 6.9) as three peaks below the HOMO and three peaks above the LUMO. Delocalized MOs are associated with conducting junctions, whereas localized MOs are indication of low conductivity [241, 262, 263]. When the ssDNA(GAG) fills the gap, the HOMO-4, -6, -9, and -10 are hybrid molecular orbitals of graphene, DNA and gold electrodes (Table 6.1, Figure 6.8g,i). DNA molecular orbitals appearing close to the HOMO are always hybridized with graphene nanoribbon orbitals.

Table 6.1. Molecular orbital (MO) energies for DFT optimized structure of gapped GNR and DNA junction. Molecular orbitals surface region is according to Figure 6.8. Only MOs close in energy to the HOMO and LUMO are reported.

Molecular Orbital	gapped GNR			DNA junction		
	Energy (eV)	Surface Region	Side	Energy (eV)	Surface Region	Side
LUMO+10	-1.79	GNR	Right	-1.91	GNR	Right
LUMO+9	-2.08	GNR-Au	Right	-2.14	GNR-Au	Left
LUMO+8	-2.09	GNR-Au	Left	-2.19	GNR-Au	Right
LUMO+7	-2.21	GNR	Left	-2.31	GNR	Left
LUMO+6	-2.21	GNR	Right	-2.33	GNR	Right
LUMO+5	-2.93	GNR-Au	Left	-2.98	GNR-Au	Left
LUMO+4	-2.94	GNR-Au	Right	-3.05	GNR-Au	Right
LUMO+3	-3.14	GNR	Left	-3.25	GNR	Left
LUMO+2	-3.15	GNR	Right	-3.27	GNR	Right
LUMO+1	-3.66	GNR-Au	Right	-3.71	GNR-Au	Left
LUMO	-3.66	GNR-Au	Left	-3.77	GNR-Au	Right
HOMO	-4.68	GNR-Au	Right	-4.74	GNR-Au	Left
HOMO-1	-4.69	GNR-Au	Left	-4.80	GNR-Au	Right
HOMO-2	-4.70	GNR	Left	-4.81	GNR	Left
HOMO-3	-4.70	GNR	Right	-4.82	GNR	Right
HOMO-4	-5.62	GNR	Left	-5.67	GNR-DNA	Left
HOMO-5	-5.62	GNR	Right	-5.72	GNR	Right
HOMO-6	-6.18	GNR	Left	-5.77	GNR-DNA	Left
HOMO-7	-6.18	GNR	Right	-6.27	GNR	Right
HOMO-8	-6.30	GNR	Right	-6.27	GNR	Left
HOMO-9	-6.30	GNR	Left	-6.35	GNR-Au	Left
HOMO-10	-6.44	GNR	Left	-6.39	GNR-DNA-Au	Right

HOMO-4 and HOMO-6 are associated to guanine nucleobase on the left side and HOMO-10 to guanine nucleobase on the right side. The central nucleobase adenine does not appear close to the HOMO and LUMO (Table 6.1). Therefore, the electrical current through the DNA junction is modulated mainly by guanine nucleobases.

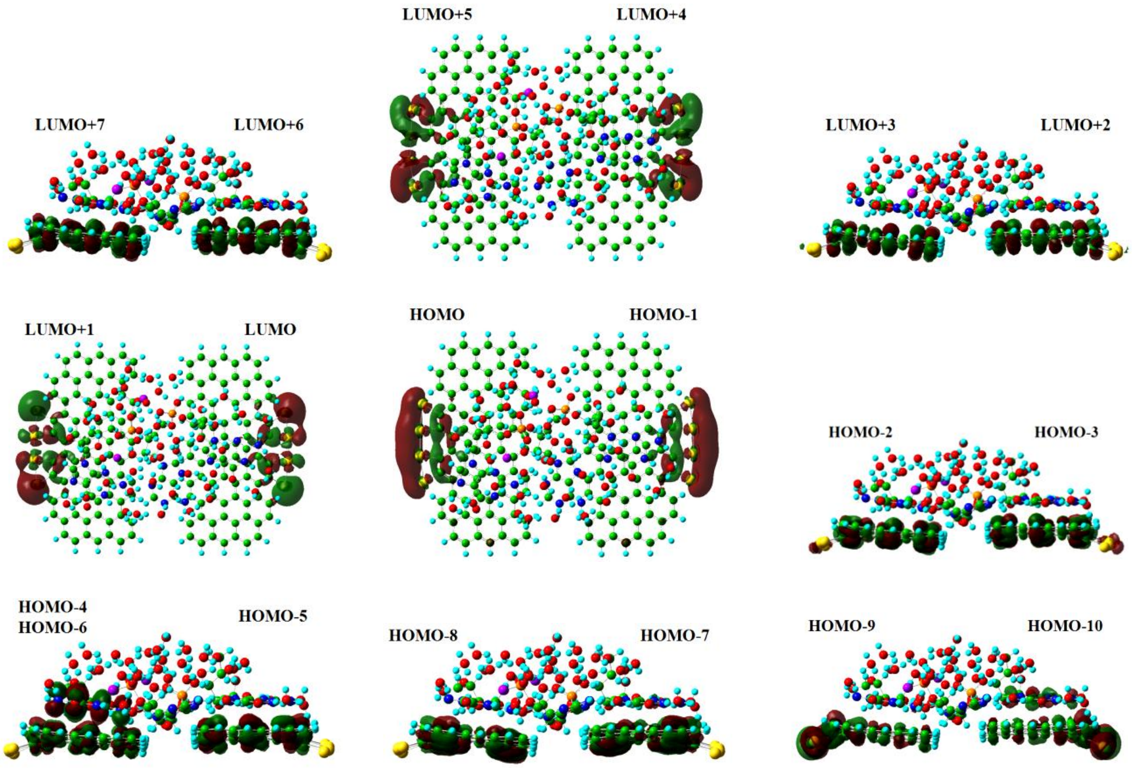

Figure 6.8. Molecular orbitals for the graphene-DNA junction at zero bias voltage. Molecular orbital energies are shown in Table 6.1.

The highest occupied molecular orbital (HOMO) and lowest unoccupied molecular orbital (LUMO) are localized at -4.74 eV and -3.77 eV respectively (Table 6.1); however, the density of states (arbitrary units) is small (less than 20) for energy levels close to the HOMO-LUMO (Figure 6.9a). When the DNA molecule is bridging the graphene gap and in the absence of a bias voltage, the DOS increases slightly around the HOMO-LUMO and the DOS peaks shift slightly towards lower energy levels (Figure 6.9a). This is accompanied by a significant increase in the electron transmission probability function (Figure 6.9b) of about three orders of magnitude around the TF peaks close to the HOMO-LUMO energy levels. The effect of the DNA molecule on the gapped graphene is therefore equivalent to a field-effect gating mechanism.

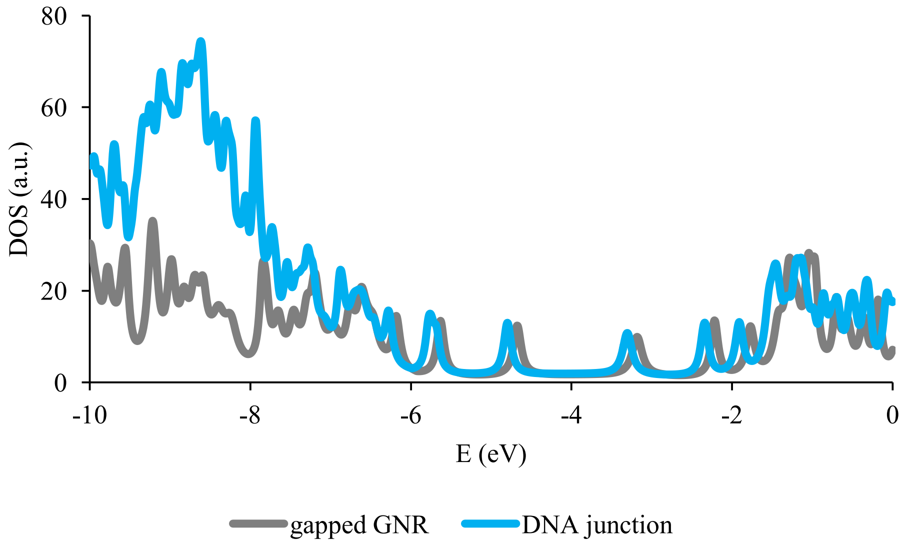

(A)

Figure 6.9. Effect of DNA molecule on DOS and TF of gapped graphene at zero bias voltage. (A) Density of states (DOS in arbitrary units, a.u.) and (B) electron transmission probability function (TF in arbitrary units, a.u.) for gapped GNR (gray colored) and GNR-DNA junction (cyan colored).

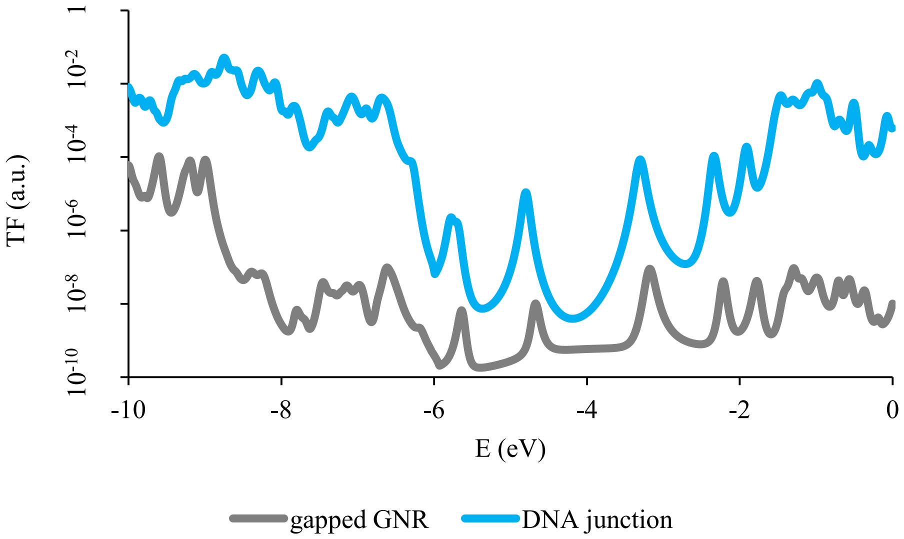

(B)

Figure 6.9. Continued.

6.3.3 Electron transport calculations

Single point energy calculations are performed on the previously DFT-optimized Au-GNR-DNA system following the same level of theory but under the application of an electric dipole field. The magnitudes of electrode dipole tested were 2, 4, 5, 6, 7, 8, 9, 10, 11, 12, 14, 16 au (1 au = 5.142206 x 10^{11} V-m^{-1}) and applied along the direction between gold electrodes (Figure 6.10).

Electron transport is mediated by molecular orbitals (MO) with probabilities of transfer (TF) depending on the barrier gap (Eg), the density of energy states (DOS), the relative location of molecular orbitals in energy with respect to the Fermi level (usually modulated by field effect gating) and their spatial localization/delocalization.

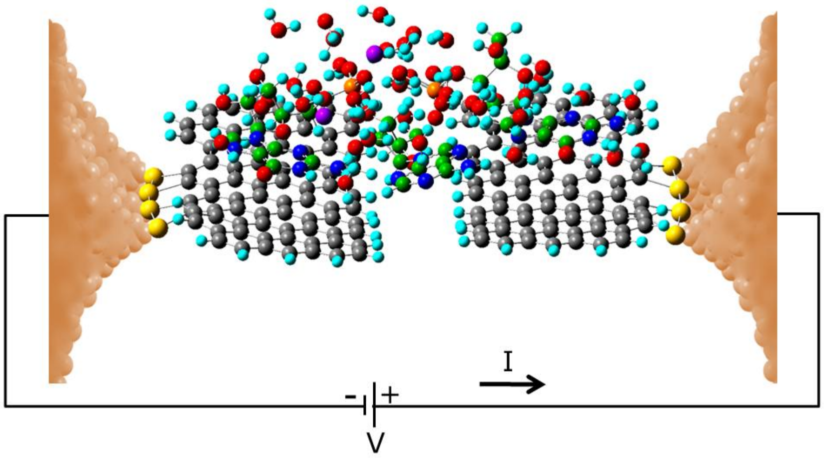

Figure 6.10. Graphene-DNA junction. Interfacial gold atoms (yellow), bulk electrodes (orange), graphene carbon atoms (grey), and DNA carbon atoms (green).

Upon application of a bias voltage, we observe in the DOS (Figure 6.11a,b) an splitting of the three peaks above the LUMO and the three peaks below the HOMO as we increase the bias voltage, with each 'red' peak at zero bias voltage splitting in two 'purple' peaks as bias voltage increases towards 2.2 V. This splitting of energy bands observed in the density of states (Figure 6.11a,b) is accompanied by a notorious increase of up to four orders of magnitude in the electron transmission probability function (TF) for energy levels close to the HOMO-LUMO (Figure 6.11c,d) and the appearance of new TF peaks around -5, -4.5, and -3 eV for the DNA junction at bias voltage higher than 1.4 V (Figure 6.11d). Furthermore, we observe the TF peaks around -4.8 eV of graphene-Au (HOMO to HOMO-3), around -5.8 eV of graphene-DNA (HOMO-4 to HOMO-6) and around -6.4 eV of graphene-DNA-Au (HOMO-7 to HOMO-10) hybridize at 1.4 V (Figure 6.11d), this suggests at this transition bias voltage the electronic energy levels associated to DNA begin to contribute to the electrical current.

In the DNA junction DOS (Figure 6.11b), the peak around the HOMO orbital (-4.8 eV) splits into two peaks and the lower peak is around -5 eV at which we observe the highest electron transmission probability (Figure 6.11d).

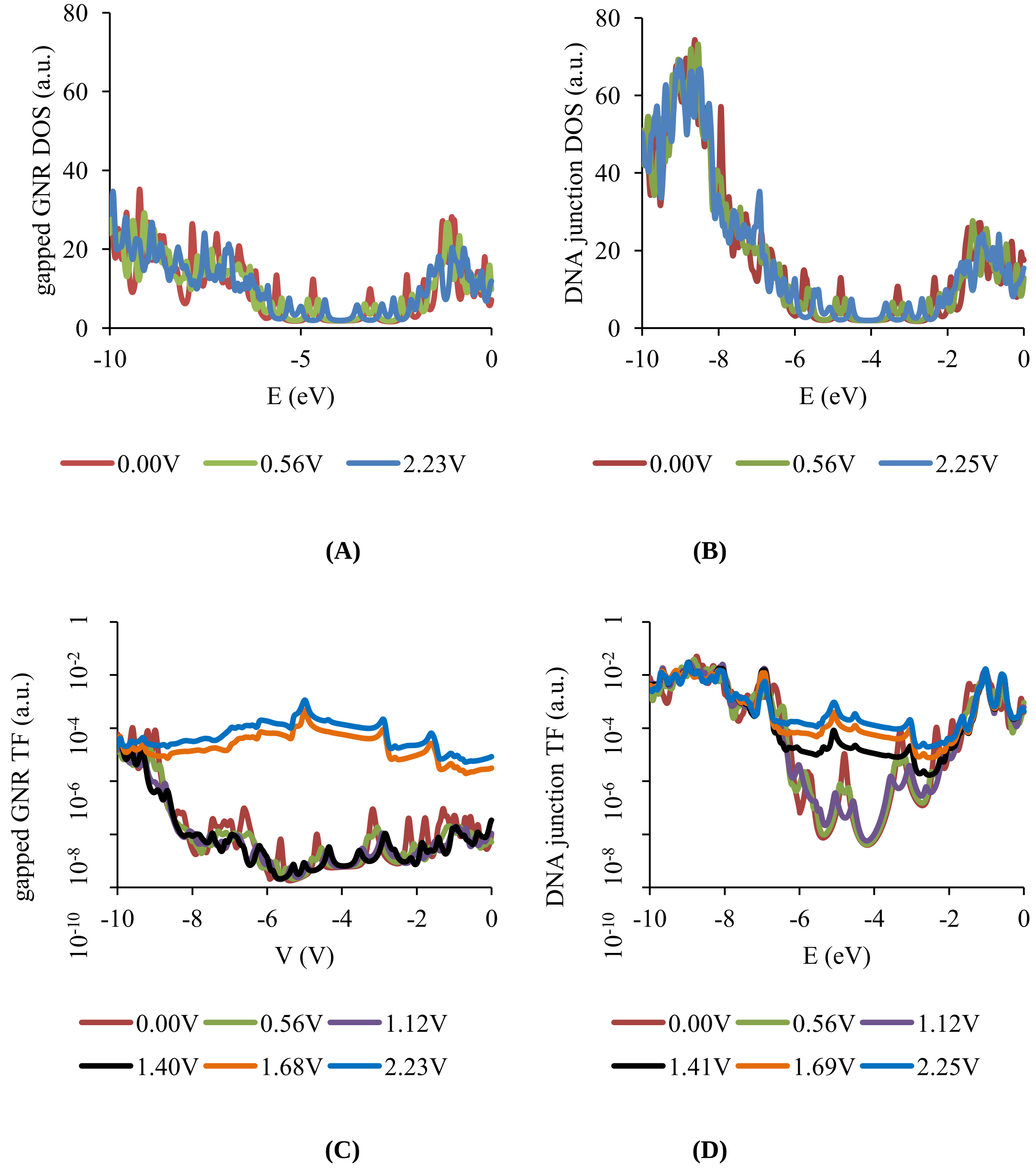

(A) **(B)**

(C) **(D)**

Figure 6.11. Density of states (DOS) for (a) gapped GNR, (b) DNA junction, (c) electron transmission function (TF) for gapped GNR, and (d) DNA junction.

The splitting of energy bands observed in the density of states produces a steady reduction of the HOMO-LUMO gap as we increase the bias voltage but reaching a constant value (0.15 eV) when the bias voltage magnitude is higher than 1.5 V (Figure 6.12).

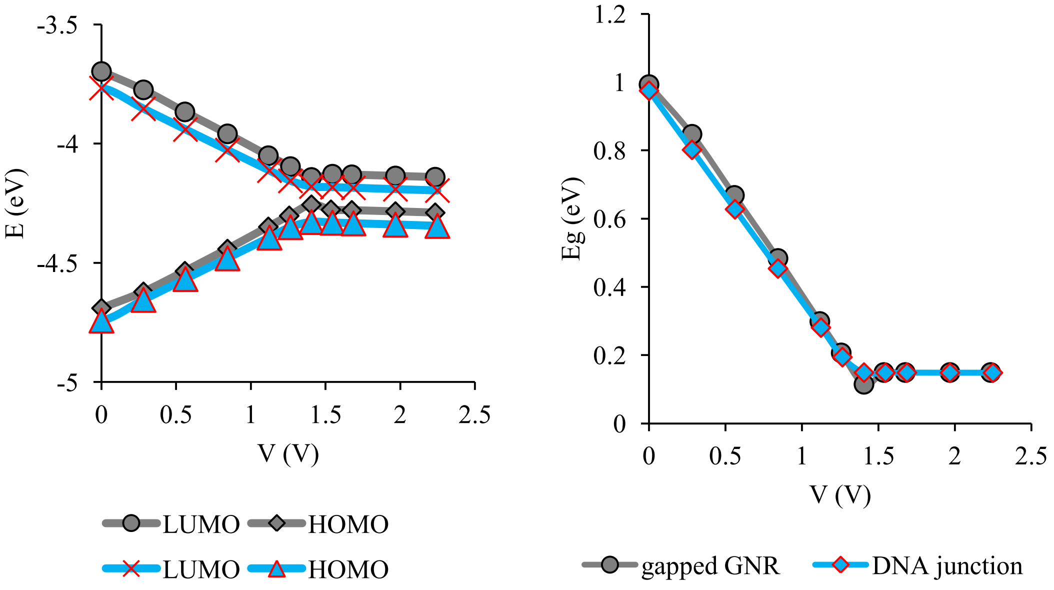

(A) **(B)**

Figure 6.12. Bias voltage dependence of (A) HOMO, LUMO and (B) HOMO-LUMO gap. Gapped GNR (gray), DNA junction (cyan).

We do expect a flat region at low bias voltage in the current-voltage characteristic due to the gap separation between graphene nanoribbons and the noncovalent nature of the DNA junction.

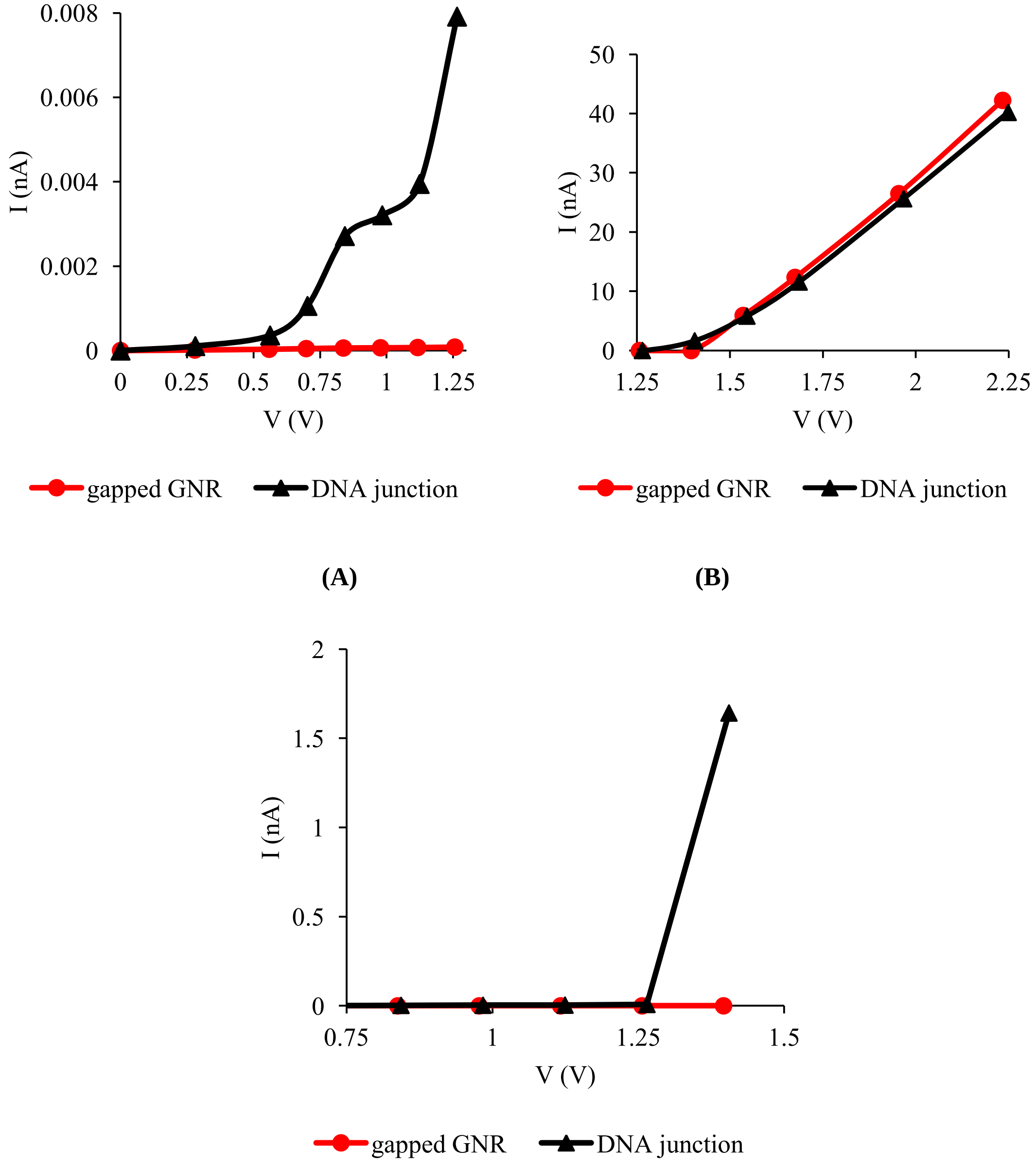

(A) **(B)**

(C)

Figure 6.13. Current-voltage characteristic at several bias voltage ranges for the GNR-DNA junction (black) and gapped GNR (red). (A) Low bias voltage range (0-1.25 V), (B) high bias voltage range (1.25-2.25 V), and (C) transition between electrically nonconductive (< 0.01 nA) to conductive state (>1 nA) for DNA junction.

For the DNA junction the current-voltage characteristic is nonlinear for bias voltage lower than 1.25 V (Figure 6.13a). In the DNA junction, we observe also a linear current-voltage characteristic and an electrical current magnitude higher than 1 nA for applied bias voltage higher than 1.25 V (Figure 6.13b). While for the gapped GNR the current is practically zero for bias voltage smaller than 1.5 V when compared to the DNA junction (Figure 6.13c), but higher than 1 nA for bias voltage higher than 1.5 V. The impedance in the linear regime (> 1.6 V) is ~20 MΩ for positive bias voltage for the gapped GNR and DNA junction.

The relative difference in current values (nA) for gapped GNR and DNA junction increases steadily with the highest difference appearing at 1.4 V and then abruptly drops to less than 0.1 for bias voltage higher than 1.5 V (Figure 6.14).

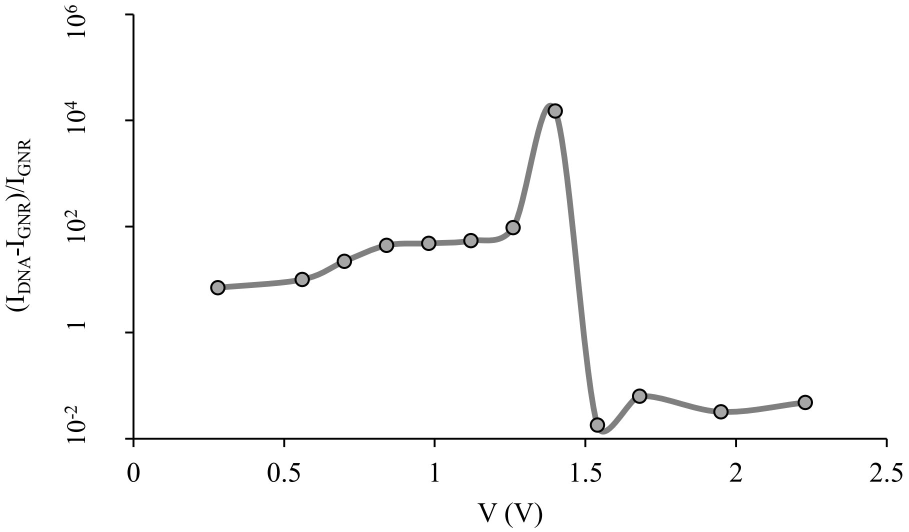

Figure 6.14. Relative difference of the currents for the gapped GNR (I_{GNR}) and DNA junction (I_{DNA}).

The biggest relative difference in current values for gapped GNR and DNA junction around 1.4 V (Table 6.1) would allow discriminating a DNA molecule filling the gapped GNR. The bias voltage range around 1.4 V corresponds to the transition between nonconductive to conductive state in the gapped GNR. Further experiments are needed to elucidate the dependence on type of DNA sequence of the current magnitude at the transition bias voltage.

Guo *et al*, [207] studied the electrical conductivity of a DNA molecule covalently bridging a gapped carbon nanotube, reporting the instability of a ssDNA junction associated with a decrease in the electrical current magnitude by about one order of magnitude after three cycles of current-voltage measurements. They suggest such instability results from voltage-induced oxidation of the exposed nucleobases. In the system we analyze, a non-covalent ssDNA junction, we expect a lower level of current compared to that of a covalent junction and therefore a lower probability for DNA oxidation. Furthermore ssDNA is more stable when physisorbed on graphene, and in a non-covalent junction ssDNA is partially absorbed on graphene.

For the particular case we analyze: a three-base ssDNA (GAG), a single nucleobase filling the gap and small width graphene electrodes; the energy corresponding to a conformational state when ssDNA bridges the gap is -80 kcal/mol while the energy when all nucleobases absorb to a graphene electrode is -90 kcal/mol (Figure 6.2d, Figure 6.6h). Therefore the relative difference of vdw energy is small. This small difference is due mainly to the small gap (0.6 nm) between graphene electrodes. For the same gap size and a longer ssDNA molecule, the relative difference will be even smaller. Small gaps (< 2 nm) have been reported by an electrical breakdown technique [112] in which the electrical characteristic is obtained of anthracene terminated curcuminoid wires, and the link of this molecule to graphene electrodes is non covalent, by pi-pi interactions.

6.4 Conclusions

The methodology presented enables an analysis of the electronic structure and electron transport property of a molecular junction closer to experimental conditions by taking into account the important effect of actual water molecules. Water molecules are essential in the present study; they provide structural stability to the DNA junction. In the standard methods for solving Kohn-Sham density functional theory, the computational cost increases as $\mathcal{O}(N^3)$ where N is an indicator of the size of the system such as number of electrons, atoms or basis functions. The final structure contains 424 atoms; with present technology, it is now suitable to perform the DFT-based quantum mechanical calculations in a reasonable time.

The gap between graphene nanoribbons (~ 0.6 nm) is small enough to accommodate a single nucleobase and the graphene nanoribbon-DNA noncovalent junction is stable in aqueous conditions at room temperature and at 330K. The ssDNA molecule bridging the nanogap causes a smooth transition between nonconductive (< 0.01 nA) and conductive (> 1 nA) states in the gapped graphene. We estimate a detectable electronic signal of ~2 nA around the transition bias voltage of 1.4 V. The ssDNA (GAG) modulation of electrical current at the transition bias voltage is not mainly due to the central nucleobase (adenine) but to the guanines on both sides of the central nucleobase absorbed on the graphene nanoribbons.

This short three-base ssDNA (GAG) binds to the graphene nanoribbons and an electric field of 0.8 V/nm is needed to aid on positioning the central nucleobase (A) in the gap between the graphene nanoribbbons within a short time span of 0.3 ns. For a higher number of bases in the DNA molecule we expect a stronger vdW attraction between DNA and graphene, therefore a higher electric field will be required to induce movement of a longer DNA along the graphene surface. For DNA sequencing applications, further studies are needed to analyze how fast a long ssDNA molecule will move along a gapped graphene upon application of a bias voltage. The degree of absorption of DNA on graphene will modulate this speed and this can be tuned by the graphene size due to the dependence of vdW forces on the number of graphene atoms and the corresponding interatomic distances between graphene and DNA. A width as small as~2 nm for the graphene nanoribbon will be required to avoid a strong absorption due to vdW forces and to ensure a DNA conformation close to linear. Sequence dependent sensitivity of DNA to different type of molecules can also be exploited; for chemical sensing applications; a rigid structure will be required and a large width (>100 nm) for graphene nanoribbon will ensure a strong absorption of DNA to graphene.

7. THE HYDRODYNAMIC VOLUME OF MAXIMUM PEGYLATED CARBON NANOTUBE[*]

Polyethylene glycol (PEG) functionalization of carbon nanotubes (CNTs) is widely used to render CNTs suitable as vectors for targeted drug delivery. One recently described PEGylated version uses an oxidized single-walled carbon nanotube called a hydrophilic carbon cluster (HCC). The resulting geometric dimension of the hybrid PEG-CNT or PEG-HCC is an important factor determining its ability to permeate the cellular membrane and to maintain its blood circulation. Molecular dynamics (MD) simulations were performed to estimate the maximum length and width dimensions for a PEGylated single-walled carbon nanotube in water solution as a model for the PEG-HCC. We ensured maximum PEGylation by functionalizing each carbon atom in a CNT ring with an elongated PEG molecule, avoiding overlapping between PEGs attached to different CNT rings.

7.1 Introduction

Carbon nanotubes constitute an emerging class of drug delivery platforms [264, 265]. The very small dimension of carbon nanotubes, especially in the radial direction, ensures efficient circulation through blood [266]. A very effective version of this consists of shortened (40-60 nm long) oxidized carbon nanotubes [267, 268] to which solubilizing addends, [269] namely 5000 molecular weight poly(ethylene glycol)

---

[*] Part of this chapter is reprinted with permission from A.D. Bobadilla, E.L.G. Samuel, J.M. Tour and J.M. Seminario, *J. Phys. Chem. B*, **2013**, *117* (1), pp 343–354. Copyright 2012 American Chemical Society.

moieties, have been attached [270]. The entire constructs are termed poly(ethylene glycol)-functionalized hydrophilic carbon clusters (PEG-HCCs) and these have recently been shown to have enormous efficacy and ultralow toxicity [271, 272]. These PEG-HCCs are very short compared to the CNTs used in earlier studies – they are short enough that they show efficient clearance via the kidneys and non-toxicity in mammals – and are proving to be exceedingly effective for *in vitro* and *in vivo* drug delivery [273-275].

A considerable number of drugs with high therapeutic efficacy are of hydrophobic nature [276, 277]. As carbon nanotubes themselves are inherently hydrophobic [278], we would expect some affinity of drugs to CNTs. In addition, in order to maintain the properties of these drugs, it is preferable that they be non-covalently loaded onto the CNT construct [270, 279]. Studies of hydrophobicity in toxicity prediction were performed by Cronin [280] and Moyano *et al*. [281]; however, further research is needed to explore biological responses to carbon nanomaterials. Fortunately, PEG has excellent solubility in water, and CNT functionalization with PEG imparts increased solubility in water solutions as well as reduced toxicity [282]. We therefore expect PEG-CNT constructs to have strategically localized hydrophobic and hydrophilic sites, making them excellent therapeutic carriers. HCCs do in fact have hydrophobic domains which ensure drug sequestration, but they also have oxidized sites for covalent PEG attachment. PEG-HCCs have demonstrated very high effectiveness for both untargeted and antibody-targeted delivery, but little is known regarding their actual hydrodynamic volume when water-association is manifested. This question is addressed here using a shortened single-walled carbon nanotube as the central core and PEG addends.

Molecular simulations provide complementary information to experimental techniques by enabling the analysis of the structure and fast dynamics with atomistic detail [39, 283, 284]. Classical molecular dynamics simulations are playing an increasingly important role in drug discovery [285, 286] to the point that they are becoming essential and not just complementary. Simulation techniques are used for example in the identification of binding sites, [287] prediction of ligand binding energies [288, 289] and to understand the atomistic energetics and mechanics of binding [290]. CHARMM is a widely used force field for molecular dynamics simulations and it has been parameterized for different types of biological molecules,[148, 291, 292] for ethers (CHARMM35),[293] for hybrid nanomaterials [294-296] and recently also for drug-like molecules [297]. A revised version CHARMM-35r for ethers reported by Lee *et al* [298], refitted the OCCO dihedral potential energy, yielding excellent agreement with experiment for persistence lengths and hydrodynamic radii at high and low molecular weights.

In the present work, we perform molecular dynamics calculations on a PEG 114-mer in water to obtain a PEG with globular shape. This 114-mer affords a 5,040 molecular weight chain, the typical chain length found in PEG-CNTs for biological applications [270, 279]. We then analyze the maximum number of PEG molecules that can possibly be covalently linked to a CNT sidewall. Finally, after equilibration at room temperature, we analyze the geometry of the PEG-CNT construct.

7.2 Methodology

So far to our knowledge, the precise structure of a HCC complex has not been reported yet and we consider a SWNT as the simplest structural model to represent a hydrophobic carbon nanostructure since HCC is derived from oxidation of SWCNT by a mixed acid [270].

We employ the CHARMM force field (Equations 7.1-7.3 and Tables 7.1-7.5) [148] as implemented in the LAMMPS software [146]. Covalent bonded interactions parameters and charges for PEG were taken from CHARMM35 version for ethers [293] and the Lennard-Jones parameters were taken from the work reported by Kenzabu Tasaki [299]. Bonds, angles and dihedrals were identified in a PEG molecule (Figure 7.1) to assign the corresponding force field parameters. The carbon nanotube was modeled with CHARMM parameters [300-302] for a benzene molecule, and the water solvent with the TIP3P model of Jorgensen [147].

$$V = \sum_b k_b (b - b_0)^2 + \sum_\theta k_\theta (\theta - \theta_0)^2 + \sum_{U-B} K_{UB} (r - r_{UB})^2 + \sum_\emptyset k_\emptyset [1 + \cos(n\emptyset - \delta)] + \sum_{nb} \epsilon_{ij} \left[\left(\frac{R_{0_{ij}}}{r_{ij}} \right)^{12} - \left(\frac{R_{0_{ij}}}{r_{ij}} \right)^{6} \right] + \frac{q_i q_j}{\varepsilon r_{ij}} \tag{7.1}$$

The first sum in Equation 7.1 corresponds to the harmonic stretching terms (Table 7.1), where k_b are the force constants and b_0 are the equilibrium bond lengths of all bonds, thus, this sum yields the total bond stretching energy, which depends directly on the instantaneous bond lengths, b, of all bonds. The second sum corresponds to bending terms (Table 7.2), where k_θ are the angle force constants, θ_0 are the equilibrium angles and θ are all the instantaneous angle values. The third sum, the Urey-Bradley component, accounts for angle bending due to 1,3 nonbonded interactions in the three-bonded atoms forming the angle, where k_{UB} is the respective force constant, r_{UB} are equilibrium distances between the 1,3 atoms and r the instantaneous distances between the 1,3 atoms. The fourth sum corresponds to torsion parameters (Table 7.3), where $k_\emptyset$ are the dihedral force constants, n are the multiplicities of the function, δ are the phase shifts and $\emptyset$ the instantaneous dihedral angles. The last sum corresponds to non-bonded parameters where ϵ_{ij} are the depth of the Lennard-Jones potential well, $R_{0_{ij}}$ are the distance at which the corresponding potential is zero (Table 7.4), ε is the effective dielectric constant, q_i, q_j are atomic charges and r_{ij} is the instantaneous distance between atoms i and j (Table 7.5).

Our intention is to gain a qualitative physical picture of the PEG-CNT construct in water without going through an extensive force field parameterization for the PEG-CNT link. Several of these geometries follow earlier ab initio [303-307] and MD [308-310] calculations. The C-O bond coefficients at the PEG-CNT link were considered to be an average value of C=C bond coefficients in the CNT and C-O bond coefficients in the PEG molecule. The dihedral energy coefficient C-O-C-C at the PEG-CNT link was considered to be 0.33 kcal/mol smaller than the one in a PEG molecule (0.43 kcal/mol) to speed up conformational changes and allow short time analysis of geometry.

Table 7.1. Stretching parameters for water [147], carbon nanotube (CNT) [148, 300] and polyethylene glycol (PEG) [293].

Molecule	Bond	k_b (kcal/mol/Å^2)	b_0 (Å^2)
water	OH	450	0.9572
	CC	222.5	1.53
PEG	CO	360	1.415
	CH	309	1.111
CNT	CC	600	1.335
CNT-PEG link	CO	480	1.375

Table 7.2. Bending parameters for water [147], CNT [148, 300] and PEG [293].

Molecule	Angle	k_θ (kcal/mol)	θ_0 (°)	K_{UB} (kcal/mol/Å^2)	r_{UB} (Å^2)
water	HOH	55	104.52	0	0
	OCC	45	111.5	0	0
	COC	95	109.7	0	0
PEG	HCH	35.5	109	5.4	1.802
	CCH	26.5	110.1	22.53	2.179
	OCH	60	109.5	0	0
CNT	CCC	40	120	35	2.4162
CNT-PEG link	CCO	45	104.5	0	0
	CCC	45	104.5	35	2.4162

Table 7.3. Torsion parameters for CNT [148, 300] and PEG [293].

Molecule	Dihedral	$k_\varnothing$ (kcal/mol)	n	δ (°)	Type of bonding[1]
PEG	OCCO	0.25	1	180	$O-C-C-O$
	OCCO	1.24	2	0	$O-C-C-O$
	COCC	0.43	3	0	$C-O-C-C$
	HCCO	0.19	3	0	$H-C-C-O$
	HCOC	0.284	3	0	$H-C-O-C$
	HCCH	0.19	3	0	$H-C-C-H$
CNT	CCCC	3.1	2	180	$C\simeq C\simeq C\simeq C$
CNT-PEG link	COCC	0.33	3	0	$C-O-C-C$

Simulations are performed with the original C35 model [293]; however, a revised version C35r has been reported by Lee *et al* [298]. After careful check of the revised parameters, we found that the only difference pertaining to our calculations is for the dihedral OCCO angles as shown in Table 7.4.

Table 7.4. Torsion parameters for the OCCO dihedral angles corresponding to the O_{CE}-C_{CT2}-C_{CT2}-O_{CE} (atom types) where C_{CT2} is the $C(sp^3)H_2$ carbon; O_{CE} is ether oxygen in linear ether(s); H_{CT2} is alkane H attached to $C(sp^3)H_2$.

n	δ (°)	$k_\varnothing$(kcal/mol) C35 [293]	$k_\varnothing$(kcal/mol) C35r [298]
1	180	0.25	0.59
2	0	1.24	1.16

---

[1] Bonding notation: $A-B$ is single covalent bond and $A\simeq B$ is resonant covalent bond.

The net effect of the correction is practically irrelevant to our calculations. The torsional barrier with the C35 version for this dihedral angle is 2.73 kcal/mol and the corrected value is 2.95 kcal/mol with maxima and minima laying exactly at the same points in both versions. Anyway, since one practical technique performing minimizations in MM is to reduce the value of the torsional barriers and then increase them to their correct values, we continue the simulations with the corrected values.

Table 7.5. Lennard-Jones parameters for water [147], PEG [299] and CNT [148, 300].

Molecule	Pair interaction	ε_{ij} (kcal/mol)	$R_{0_{ij}}$ (Å)
PEG	CC	0.095	3.44
	OO	0.199	2.85
	HH	0.098	3.0
	CO	0.138	3.15
	CH	0.031	3.23
	OH	0.044	2.93
water	O	0.1521	3.1507
	H	0.046	0.4
	OH	0.0836	1.7753
CNT	CC	0.11	3.563595

Table 7.6. Atomic charges defined as multiple of electron charge for water [147], PEG [299] and CNT [148, 300].

Molecule	Atom	q_i
PEG	C	-0.01
	O	-0.34
	H	0.09
water	O	-0.83
	H	0.415
CNT	C	0.0

The Lorentz-Berthelot mixing rule is applied to determine Lennard-Jones parameters for interactions between atoms of different type according to.

$$\varepsilon_{ij} = \sqrt{\varepsilon_i \times \varepsilon_j} \tag{7.2}$$

and

$$R_{0_{ij}} = \frac{R_{0_i} + R_{0_j}}{2} \tag{7.3}$$

Prior to every molecular dynamics simulation, an energy minimization is performed to ensure an initial structure close to a local minimum in the potential energy landscape. The minimization algorithm used is the Polak-Ribiere version of the conjugate gradient algorithm [311].

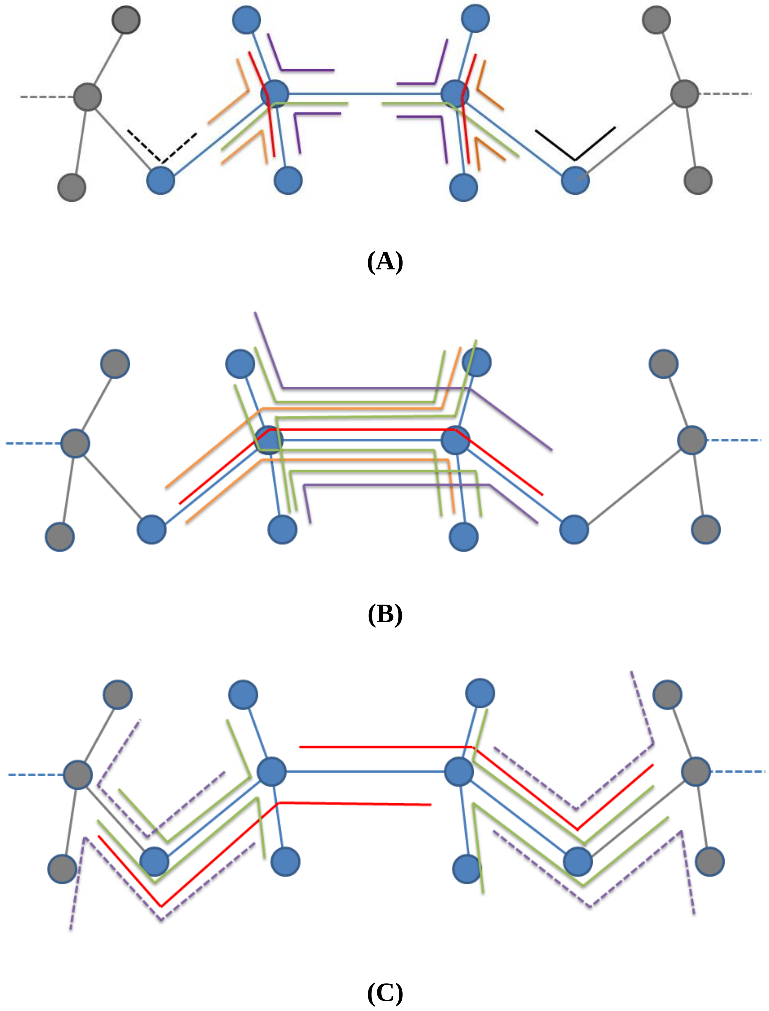

Figure 7.1. Angles and dihedrals identified in a repeat unit (mer) C_2H_4O of PEG molecule. (A) Angles are identified as OCC (green), COC (black), HCH (red), CCH (purple) and OCH (orange). (B) Dihedrals in every mer are identified as OCCO (red), OCCH (orange), HCCO (purple) and HCCH (green). (C) Dihedrals at the interface between mers are identified as CCOC (red) and HCOC (green).

A fluid can be subject to a constant pressure, constant temperature, or constant temperature and pressure [231]. An NPT ensemble is usually employed for MD simulations of polymer in water solvent. An isothermal–isobaric (NPT) ensemble corresponds most closely to laboratory conditions with a flask open to ambient temperature and pressure. We are actually mainly interested on PEG-HCC for drug delivery applications in which case the complex will penetrate the cell membrane, therefore a pressure control is not appropriate.

Therefore, all molecular dynamics simulations are performed under a canonical ensemble (NVT) with a 2 fs time step, temperature controlled by a Nose-Hoover thermostat [234, 235] with a 200 fs damping parameter, and 30 Å cutoff distance for non-bonded interactions. To compute long-range Coulombic interactions, a particle-particle particle-mesh solver (Hockney) [239] was employed with 10^{-4} accuracy on relative error in forces. The software PACKMOL [149] is used to construct the initial configuration of the system. Visualization of trajectories is performed using the Visual Molecular Dynamics (VMD) software [239].

Our PEG molecule was built with data from crystallographic studies by French *et al*. [312] (Figure 7.2) available at The Cambridge Crystallographic Data Centre web page. Three unit cells of the crystal structure CCDC 707050 were modified to obtain a PEG 114-mer length.

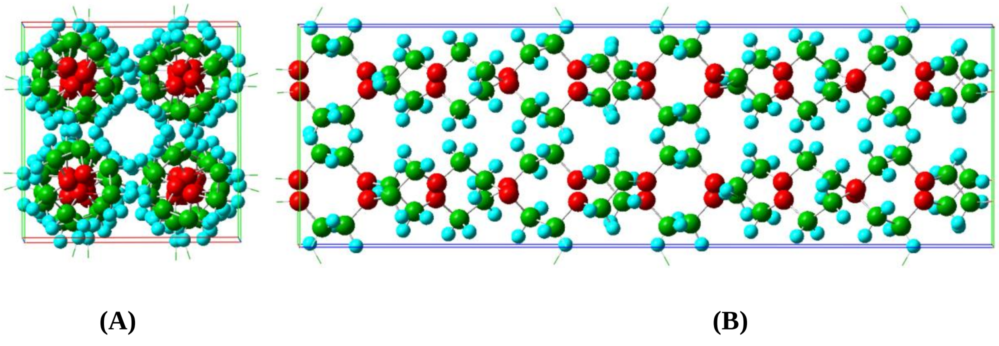

(A) **(B)**

Figure 7.2. (A) Cross sectional and (B) lateral view of a unit cell for PEG structure taken from The Cambridge Crystallographic Data Centre. Atoms are color coded: carbon (green), oxygen (red) and hydrogen (cyan).

7.3 Results and Discussion

A PEG 114-mer (Figure 7.3a) was placed at the center of a cubic box of edge length 80 Å with 16500 water molecules. The temperature was increased from 0.1 K to 300 K in a 50 ps linear ramp followed by an equilibration at 300 K for 1.05 ns until the root-mean-squared (RMS) end-to-end distance (h) of PEG was almost constant (Figure 7.3c). During this equilibration, the PEG molecule tends to adopt a globular shape (Figure 7.3b).

The initial PEG structure was not random but derived from X-ray crystal structure reported by French *et al*. [312] therefore we do expect a 1.5 ns MD run being enough time for equilibration. Furthermore, we do expect large fluctuations in the root mean squared end-to-end distance (h^{rms}); as a reference, a PEO 158-mer shows an oscillation of hrms from ~ 40 Å to ~75 Å [313] in a 800 ns MD run. In the present work the PEG molecule is shorter, 114-mer length, therefore we do expect the 35 Å value reached during the short equilibration being a good reference of the minimum value in the full oscillation range of h^{rms}. And we are interested in the minimum value for comparisons purposes with the h^{rms} value in the PEG-HCC model.

From single PEG equilibration in water solvent, the last structural configuration for PEG was taken as a reference to construct a PEGylated CNT. The PEG chain is terminated by oxygen atoms at both ends (Figure 7.3b).

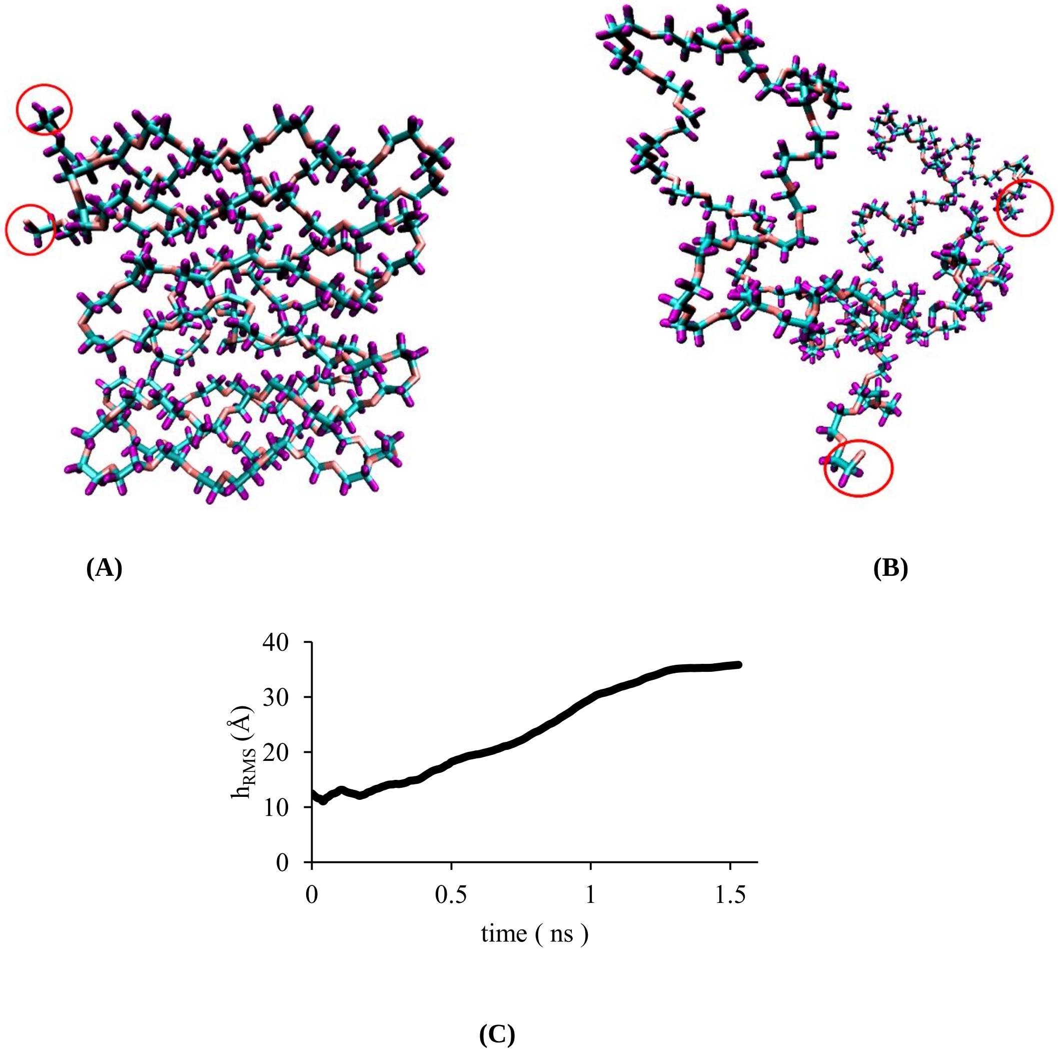

Figure 7.3. (A) PEG initial structure, before energy minimization and (B) PEG final structure at 300 K for MD simulation. Water molecules are omitted for visualization purposes. Atoms are color coded: oxygen (cyan), carbon (orange) and hydrogen (purple). Red circles highlight the PEG ends. (C) Time evolution of root-mean squared end-to-end distance for the PEG molecule.

In the first PEGylation test, four PEG molecules are covalently attached to the CNT sidewall (Figure 7.4a) every 34 Å. In total, 40 PEG molecules are attached to a 33.94 nm long single-walled (12,0) CNT (Figure 7.4b). Bond, angle and dihedral force field parameters for atoms at the PEG-CNT interface are considered the same as those for a PEG molecule. The construct is solvated with 146,997 water molecules in a

380×120×120 Å^3 simulation box. Molecular dynamics was performed, bringing the system to room temperature in 50 ps following a linear temperature ramp with time, at which point the system was equilibrated for 50 ps at room temperature. We observed a tendency for elongation in PEG molecules (Figure 7.4c). We took one of the PEG structures showing the largest elongation (Figure 7.4d) as a reference for a second test on a PEGylated CNT, aiming to achieve maximum PEGylation.

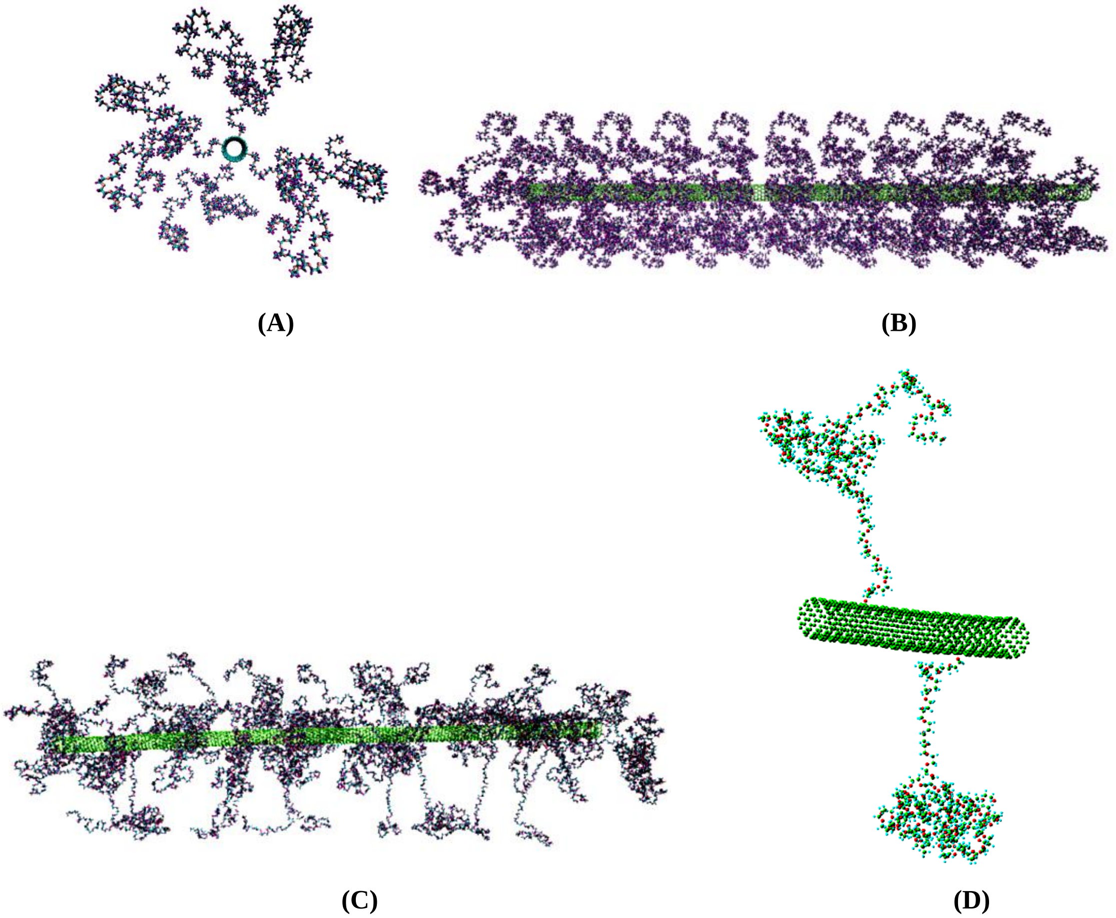

Figure 7.4. (A) Side view of initial structure. (B) PEG-CNT initial structure, including 40 PEG molecules, before energy minimization. (C) PEG-CNT final structure at 300 K for MD simulation. Water molecules are omitted for visualization purposes (D) PEG molecules attached to the CNT sidewall show globular and linear segments. Structure was extracted from PEG-CNT final conformation at 300 K.

To fully justify the results obtained from MD simulations of PEGylated CNT, we cite experimental results reported by Hong *et al*. [314] on atomic force microscopy (AFM) measurements of PEGylated single walled carbon nanotube in which SWCNT diameter was 1 nm and PEG molecular weight was 5 kDa. According to the AFM measurements, the average diameter for the PEG-CNT complex is 15 nm which corresponds to a radial thickness of 70 Å for the polymer wrapping CNT [314].

Our carbon nanotube (0.95 nm diameter) is functionalized with 40 PEG molecules, each PEG molecule with molecular weight 5.04 kDa. We denote by $rmax(t)$ the instantaneous value for maximum distance between a PEG atom and CNT sidewall (Figure 7.5a) and denote by $r(avg)$ the average over time of $rmax(t)$ value for every PEG molecule during a MD production run of 100 ps. The $rmax(t)$ value serves as a reference for the radial thickness of the polymer wrapping the carbon nanotube measured at every PEG molecule. We plot the $r(avg)$ distribution along CNT (Figure 7.4b) and we consider the AFM instrument will be able to see only those PEG molecules with $r(avg)$ higher than 60 Å. We therefore estimate the radial thickness (denoted as AFM) of the polymer wrapping CNT as the average of $r(avg)$ values above AVG (60 Å) obtaining a AFM value of 76.2 Å which is very close to the 70 Å value reported from AFM measurements [314]. When we estimate the AFM value from the instantaneous $rmax(t)$ values, we obtain the time evolution of AFM value and observe an oscillation between 74.3 Å (minimum) and 78.3 Å (maximum) (Figure 7.5c). The very small oscillations, only ~ 2Å deviation from average value for radial thickness of polymer wrapping CNT during the production run, justify the short time equilibration for the MD simulations.

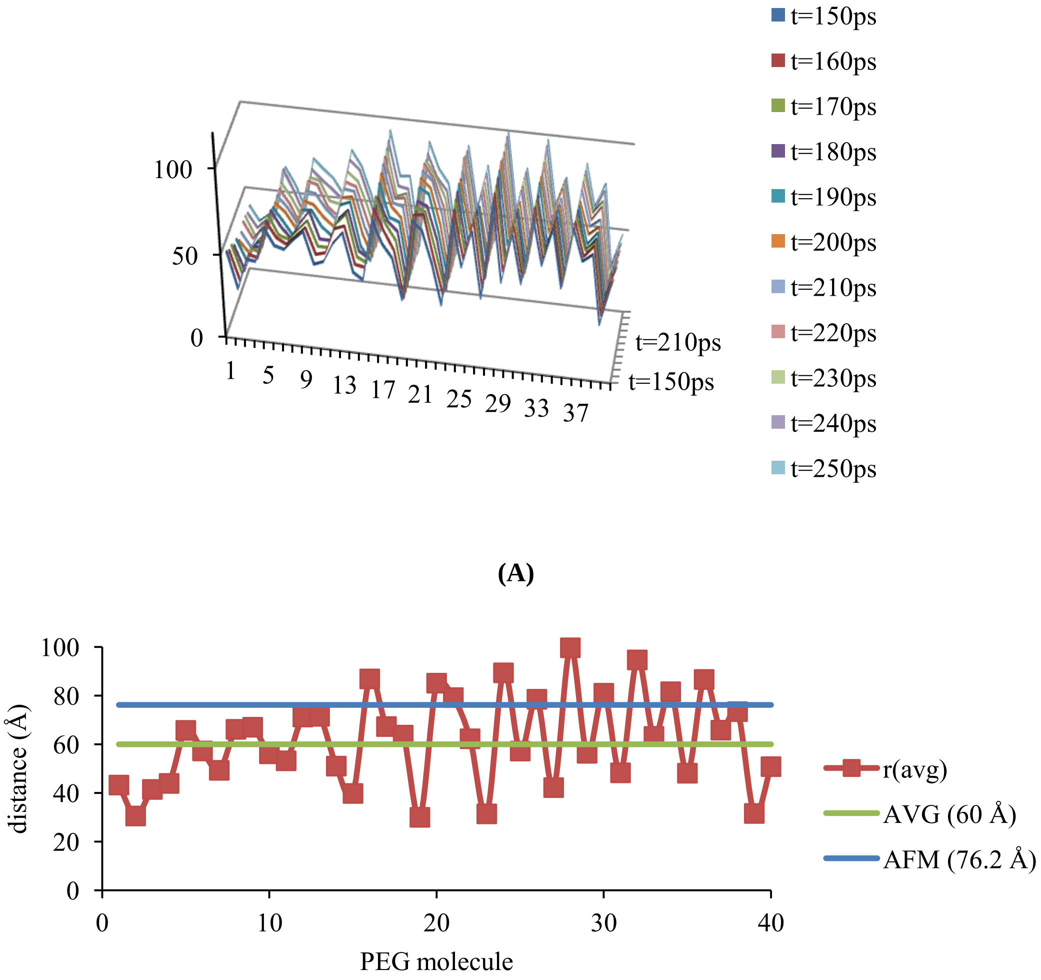

(A)

(B)

Figure 7.5. Estimation of polymer radial thicknes (AFM value) wrapping CNT. (A) Time evolution of $rmax(t)$, maximum distance between a PEG atom and CNT sidewall, for every PEG molecule. Vertical axis is in distance units (Å), horizontal axis is an identifier for PEG molecules with values 1, 2 .. 40, and curves are color coded for different time (picoseconds), (B) AFM value estimation from $r(avg)$ values. We calculate $r(avg)$ for every PEG molecule as the average over time of $rmax(t)$ value in a 100 ps MD run. AVG is the average value of $r(avg)$ and AFM is the average value of $r(avg)$ when $r(avg)$ is larger than AVG (60 Å), (C) AFM value estimation from instantaneous $rmax(t)$ values in a 100 ps MD run.

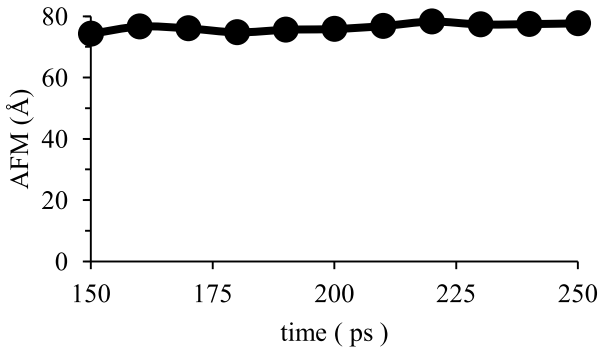

(C)

Figure 7.5. Continued.

The carbon nanotube of chirality (12,0) has a diameter ~1 nm which is the typical size reported on PEG-CNT complexes for drug delivery applications [270, 279, 314, 315]. We define a twelve-atom CNT ring (Figure 7.6a) to which PEG molecules will be attached. To avoid overlap between PEGs attached to the same CNT ring; the linear segment of each PEG was elongated as much as possible, increasing PEG length in the radial direction (Figure 7.6b). To accommodate the maximum number of PEG molecules in a CNT ring, the linear segment of each PEG molecule is covalently linked to a carbon atom in the CNT ring (Figure 7.6c). To ensure maximum PEGylation, PEGs attached to different CNT rings were positioned as close as possible without overlap between PEGs (Figure 7.6d). This resulted in twelve PEG molecules attached to a CNT ring every 21.3 Å along the CNT sidewall. In total, 204 PEG molecules were attached to a 36.5 nm long single-walled CNT.

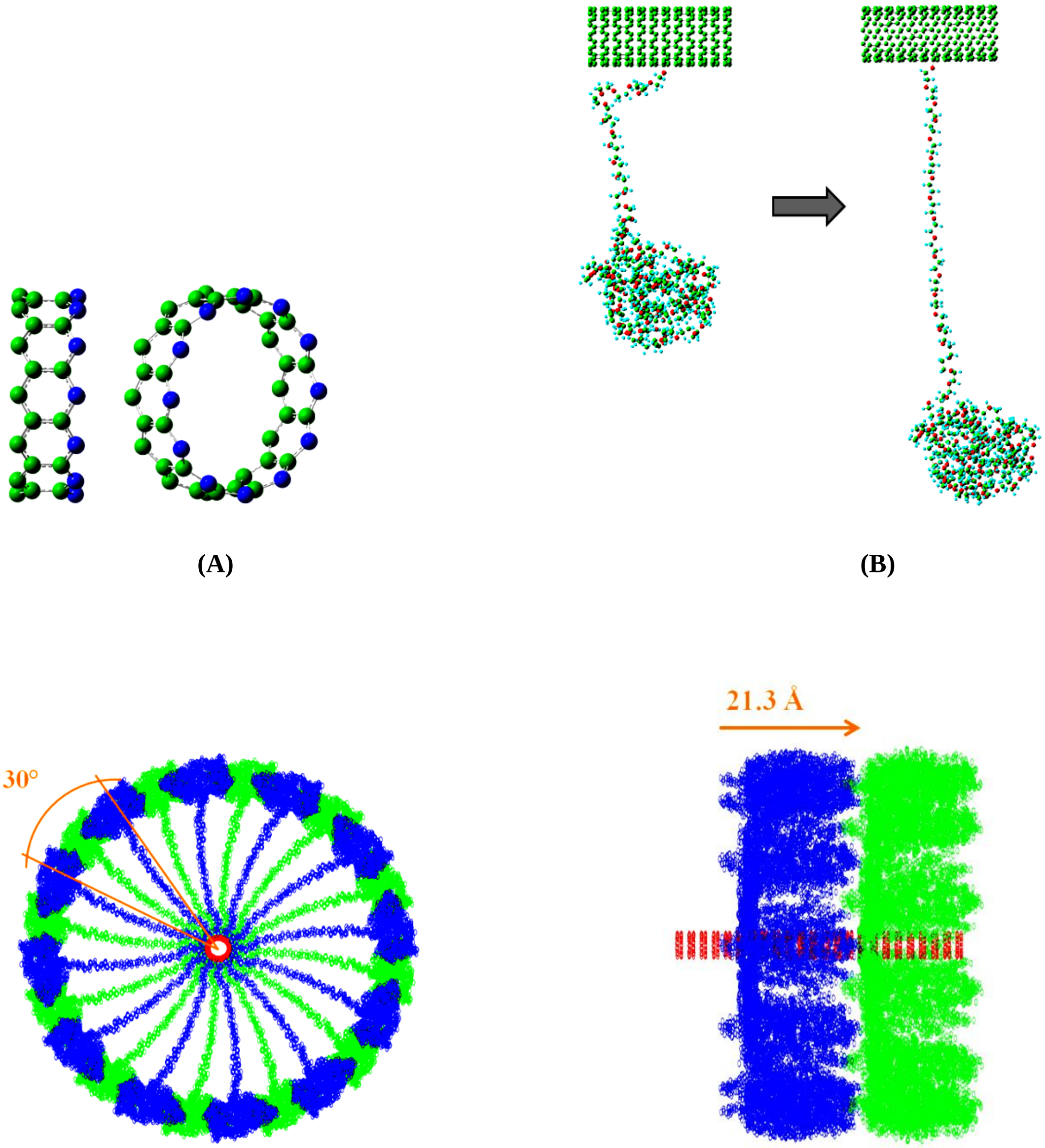

Figure 7.6. **(A) Side views of a twelve-atom carbon (blue) nanotube ring; there are four rings in this example (one blue and three greens). Some rings of the CNT will be chosen to be fully functionalized with PEG molecules. To achieve maximum PEGylation, (B) the linear segment of the PEG molecule is elongated, and (C,D) to avoid overlapping between PEG molecules attached to adjacent functionalized CNT rings, PEG molecules are shifted 15° between adjacent functionalized rings (green and blue). Twelve PEG molecules are attached to every CNT ring and the distance between functionalized CNT rings is 21.3 Å.**

Molecular dynamics simulations were performed for the PEGylated CNT in a 380×190×190 $Å^3$ simulation box, 152,430 water molecules were added to solvate the construct. The initial O-C_1-C_2 angle at the CNT-PEG link was considered almost orthogonal (95°) and the initial angles C_0-C_1-C_2 in carbon nanotube were 120°. After an energy equilibration at room temperature (Figure 7.7a,b), the O-C_1-C_2 angle as well as the angles C_0-C_1-C_2 in carbon nanotube were gradually changed every 2 ps towards 104.5° (tetrahedral configuration, Figure 7.7c) in a 16 ps run (Figure 7.7d).

The MD simulation considered PEG molecules attached to the CNT sidewall and oriented orthogonal to the CNT axis. The possibility of PEGs linked to the CNT ends is then considered by adding two PEG molecules at each CNT end to the final PEG-CNT structure at 300 K (Figure 7.7e); in the new construct these PEG molecules have their linear segment oriented parallel to the CNT axis (Figure 7.8). The new PEG-CNT construct is placed in a 480 × 180 × 180 $Å^3$ simulation box solvated with 171,309 water molecules.

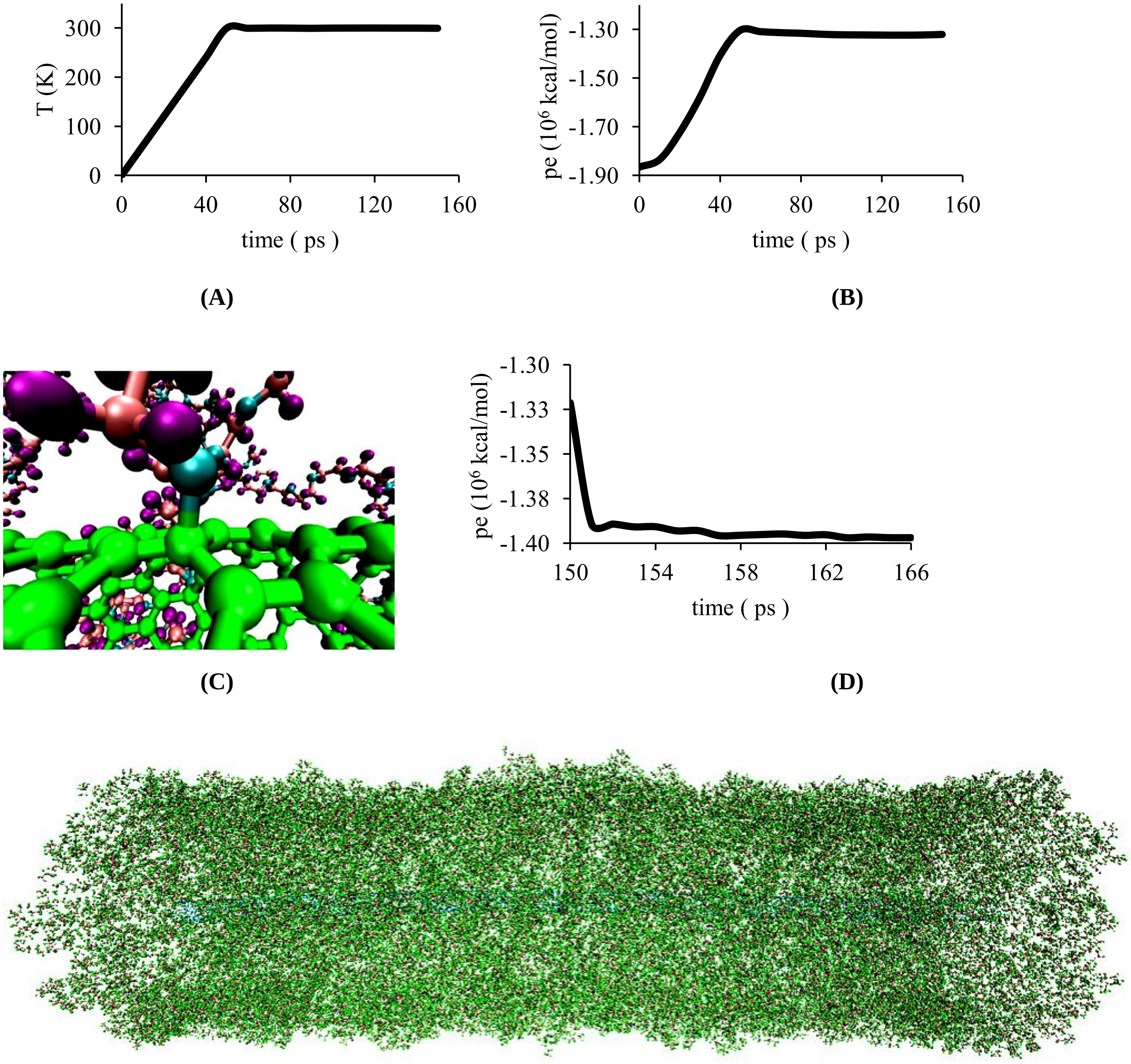

(A) **(B)**

(C) **(D)**

(E)

Figure 7.7. Time evolution of (A) temperature and (B) total potential energy for PEG-CNT construct with 204 PEG molecules. (C) Snapshot of final structure at 300K showing tetrahedral configuration at the PEG-CNT interface. Atoms are color coded: oxygen (cyan), carbon (orange), hydrogen (purple) and carbon nanotube (green). (D) Time evolution of total potential energy during gradual change of geometry at PEG-CNT interface from near orthogonal (OCC angle 95°) to tetrahedral (OCC angle 104.5°). (E) PEG-CNT at 300 K. Water molecules are omitted for visualization purposes.

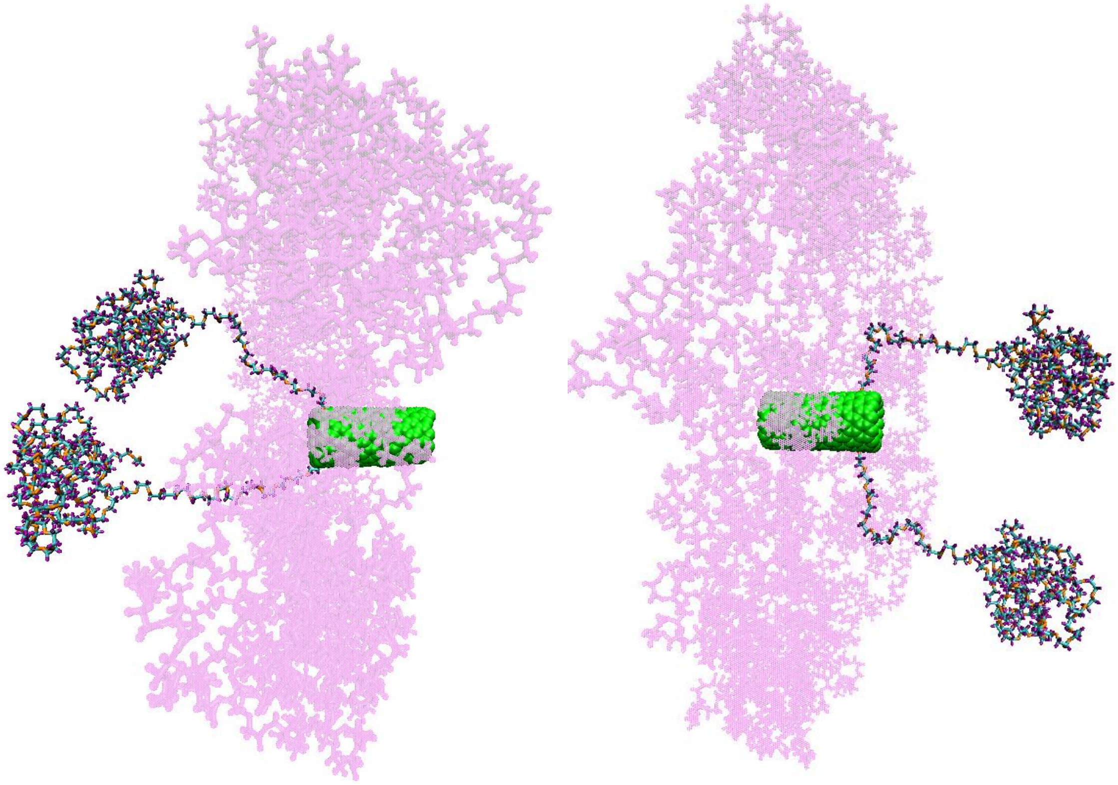

(A) (B)

Figure 7.8. Building of initial structure. Schematic of four PEG molecules added to CNT ends, (A) two on the left side and (B) two on the right side. For visualization purposes only a segment of CNT (green colored) is shown and other PEG molecules appear in purple color.

Room temperature was reached in a 50 ps linear ramp (Figure 7.9a), and 100 ps of energy equilibration at room temperature was required to observe a constant total potential energy (Figure 7.9b). The final structure for the equivalent model of a PEG-CNT is shown in Figure 7.9c.

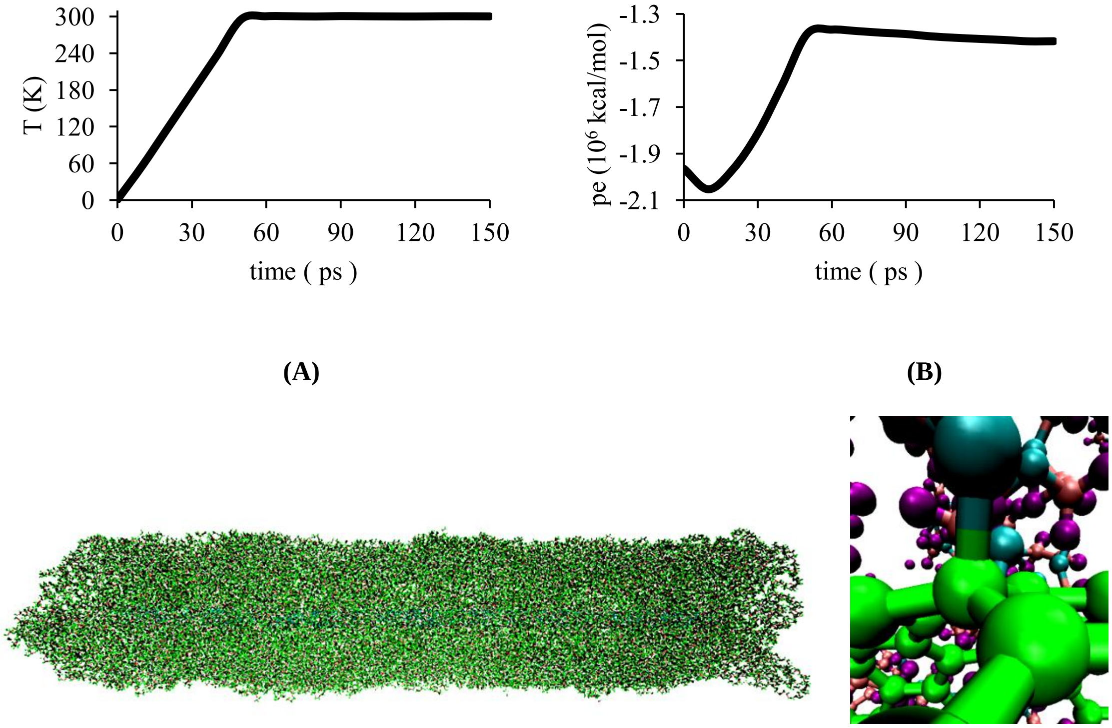

(A) **(B)**

(C) **(D)**

Figure 7.9. Time evolution of (A) temperature and (B) total potential energy for PEG-CNT construct with 208 PEG molecules. (C) PEG-CNT structure at t = 150 ps and room temperature, and (D) tetrahedral structure at a PEG-CNT link.

The final structure from MD simulations with a single PEG molecule (Figure 7.3) is used to derive the CNT functionalized with 40 PEG molecules, the final structure from MD simulations with 40 PEGs (Figure 7.4) is used to derive the initial structure of CNT functionalized with 204 PEG molecules, and the final structure from MD simulations with 204 PEGs (Figure 7.7) is used to derive the initial structure of CNT functionalized with 208 PEG molecules, which final version is used for analysis and to draw conclusions.

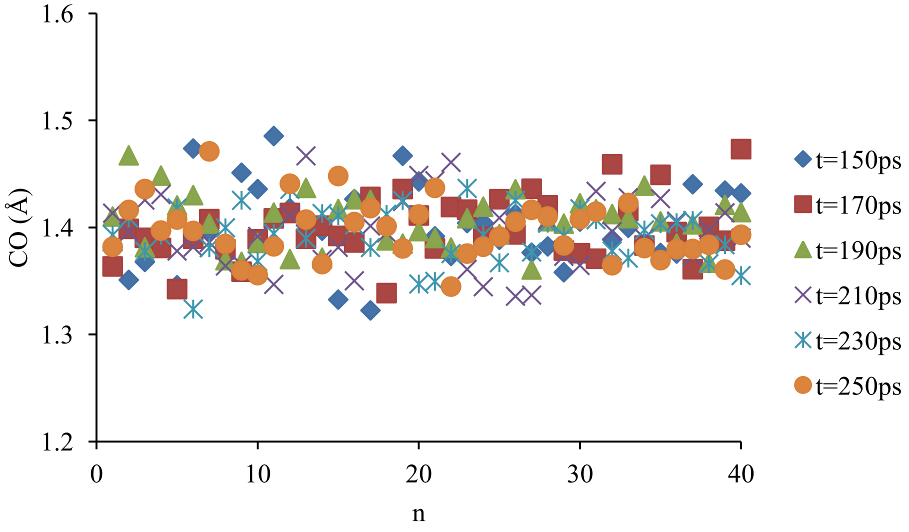

(A)

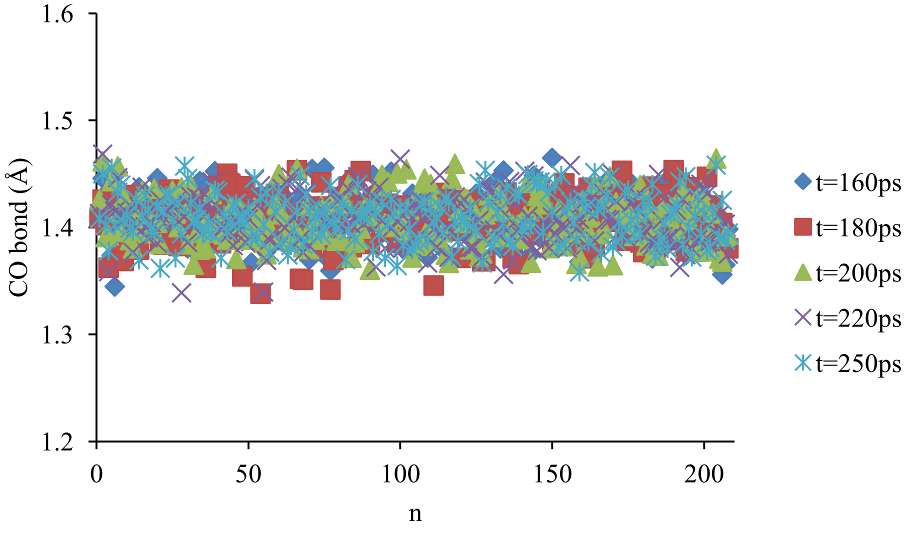

(B)

Figure 7.10. Carbon-oxygen bond distance at every PEG-CNT link for the CNT functionalized with (A) 40 PEG molecules and (B) 208 PEG molecules. *n* is the bookeeping index for the PEG-CNT links in the complex.

We check that all PEG molecules stay covalently attached to the CNT during the MD runs. Shown below is a plot of CO bond length (Å) at every PEG-CNT link (‘n’) from a MD run of 100 ps for the CNT functionalized with 40 (Figure 7.10a) and 208

PEG molecules (Figure 7.10b). Just by looking at the range of distances between a C from the CNT and the O from the PEG we can make sure that all PEGs are chemically bonded to the CNT

We calculate the interaction energies, including contributions from Coulombic and van der Waals forces as well as from bonded interactions. Bonded interactions include energy contributions coming from bonds, angles and dihedrals in which the carbon and oxygen atoms from the PEG and CNT are covalently bonded. The interaction energy per PEGmer is -9.2 and -10.3 kcal/mol for the PEG40-CNT and PEG208-CNT, respectively. These relatively close energy values (Table 7.7) provide evidence that full PEGylation is feasible in the CNT-PEG systems.

Table 7.7. Interaction energy of the PEG-CNT complex, averaged over the last 50 ps of the MD simulation. Each PEG molecule is a 114-mer. Interaction energy includes contributions from non-covalent interactions over the whole complex and contributions from bonded interactions at the PEG-CNT link.

Energy (kcal/mol)	PEG40-CNT	PEG208-CNT
Total	-4.176×10^4	-2.443×10^5
per PEG molecule	-1.044×10^3	$-1.175\text{E}\times10^3$
per PEGmer	-9.16	-10.30

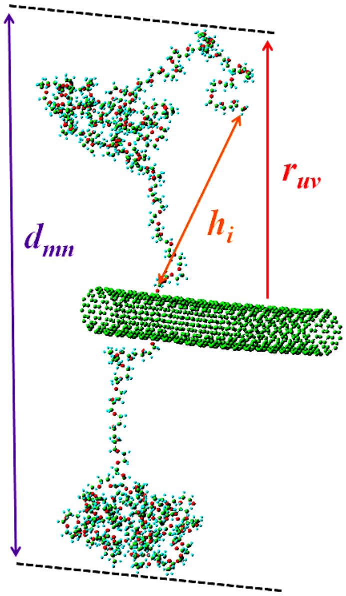

Figure 7.11. Distances calculated in the PEG-CNT complex. d_{mn} is the maximum distance between atoms of opposite PEG molecules attached to a same CNT ring and along a direction orthogonal to the CNT axis, *m* is an index for every CNT ring and *n* is an index for every pair of opposite PEG molecules attached to the ring. h_i is the end-to-end distance for every PEG molecule. r_{uv} is the maximum distance between a PEG atom and the CNT sidewall, *u* is an index for every CNT ring and *v* is an index for every PEG molecule attached to the ring.

If $\hat{k}$ is a unitary vector in the CNT axial direction and $\overline{w_p}$ the vector between a PEG atom and the CNT atom to which the PEG molecule is covalently linked, we can calculate r_{uvp}, the distance between a PEG atom and the CNT sidewall, as

$$r_{uvp} = norm(\overline{w_p} - (\overline{w_p}.\hat{k})\,\hat{k}) \tag{7.4}$$

Therefore the maximum distance between a PEG atom and CNT sidewall is defined as (Figure 7.11)

$$r_{uv} = max\,(|r_{uv(1)}|, \cdots, |r_{uv(799)}|) \tag{7.5}$$

Twelve PEG molecules are attached to every CNT ring (Figure 7.6c), therefore we define

$$r_u = \max\left(\left|r_{u(1)}\right|, \cdots, \left|r_{u(12)}\right|\right) \tag{7.6}$$

Calculus of d_{mn} is to estimate the width of our PEG-CNT construct at every section corresponding to a CNT ring, so based on the geometry of opposite PEG molecules n_1 and n_2 (Figure 7.11) we define

$$d_{mn} = r_{mn_1} + r_{mn_2} + CNT_{diameter} \tag{7.7}$$

and

$$d_m = max\left(\left|d_{m(1)}\right|, \cdots, \left|d_{m(6)}\right|\right) \tag{7.8}$$

The PEG-CNT construct has seventeen rings with attachment of twelve PEG molecules; r_u and d_m have different values at each of those CNT rings. If h_i is the end-to-end distance for every PEG molecule, we define h_i^{rms} as the corresponding root mean squared end-to-end distance. After the equilibration at 300 K, we estimate the minimum, average and maximum values for r_u and h_i^{rms} for the PEG-CNT complex with 40 PEGs (Figure 7.12), and we estimate the minimum, average, and maximum values for r_u, d_m and h_i^{rms} for the PEG-CNT complex with 208 PEGs (Figure 7.13). We calculate also the maximum length (L_{max}) of the PEG-CNT construct with 208 PEGs (Figure 7.9c) as the maximum distance between atoms of PEG molecules attached to CNT ends. Therefore, we are suing the final runs of the 40 and 208 PEG molecules (Figures 7.12, 7.13) to draw our conclusions. We observe small oscillations of only ~2 Å in the average values for the radial thickness of polymer wrapping CNT, thus, we consider we have enough statistics to draw conclusions.

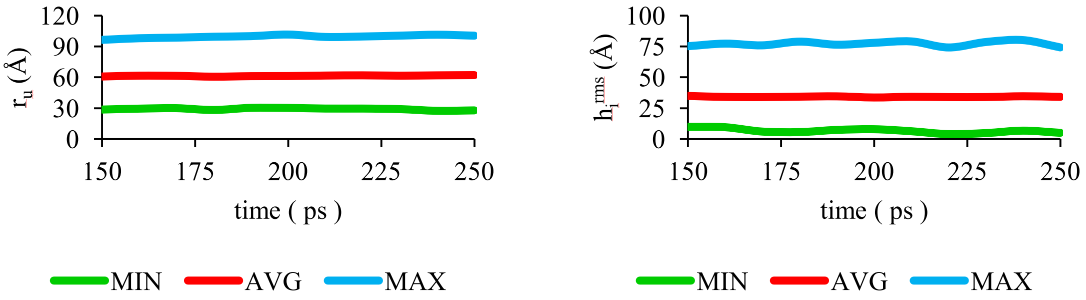

(A) **(B)**

Figure 7.12. Estimates for a PEG-CNT construct with 40 PEG molecules. (A) Maximum distance between a PEG atom and CNT sidewall, and (B) root mean squared end-to-end distance for a PEG molecule.

For a PEG-CNT complex with 40 PEG molecules, we observe for the maximum r_ua large value of 100.3 Å (Figure 7.12a) which indicates some PEG molecules elongates adopting a linear conformation and it would imply poor trapping of drug molecules. In our MD simulations of PEG-CNT in water solvent, one end of each PEG molecule is linked to the CNT sidewall. For the minimum h_i^{rms} we observe a small value of 5.3 Å (Figure 7.12b), this is due to some (hydrophilic) PEG molecules having enough freedom or space to wrap around the hydrophobic carbon nanotube and imply a not efficient covering of hydrophobic sites since we prefer the highest surface of hydrophobic carbon nanotube free of PEG wrapping to ensure sequestration of a hydrophobic drug. Furthermore, we observe a root mean squared end-to-end distance value of 34.2 Å (Figure 7.12b) for a PEG molecule linked to the CNT and this value is very close to the value of 35 Å (Figure 7.3c) observed for a single PEG molecule in water solvent.

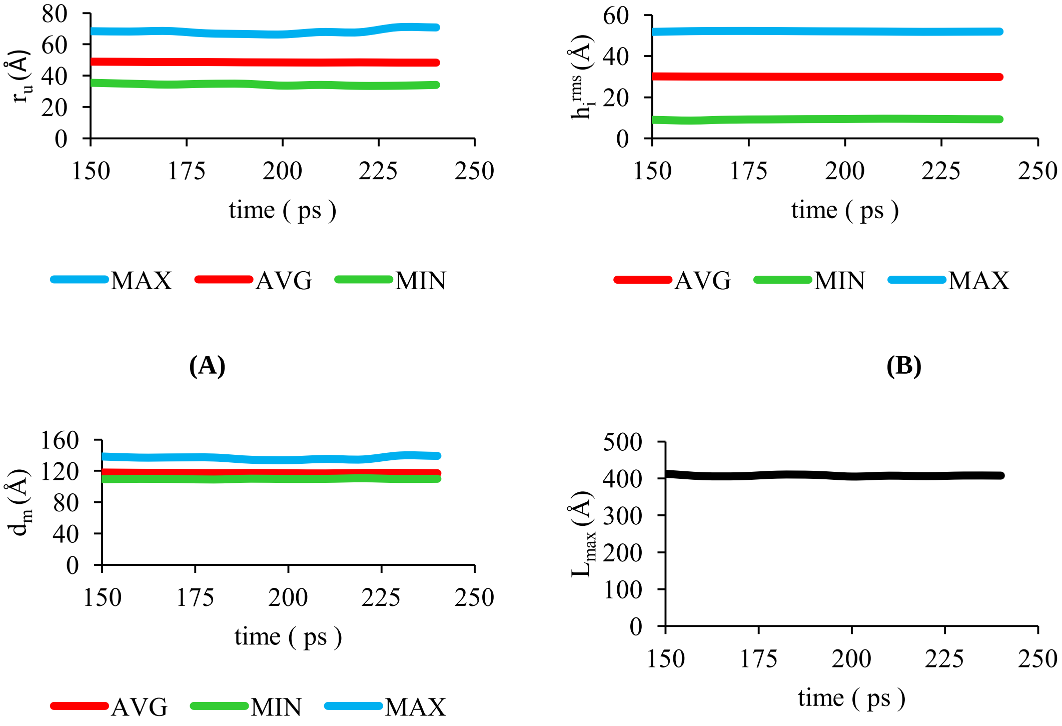

(A) **(B)**

(C) **(D)**

Figure 7.13. Estimates for a PEG-CNT complex including 208 PEG molecules. (A) Maximum distance between a PEG atom and CNT sidewall, (B) root mean squared end-to-end distance, (C) width of the PEG-CNT complex has a maximum value of 136.5 Å (averaged during the last 50 ps), and (D) the maximum length of the PEG-CNT complex is 407 Å (averaged during the last 50 ps).

The maximum and minimum values for r_u and h_i^{rms} are closer to the average value in the complex with 208 PEG molecules (Figure 7.13a,b) than in the complex with 40 PEGs (Figure 7.12a,b), meaning we have a more homogenous size distribution of PEG molecules, with no PEG molecule wrapping the carbon nanotube surface and no PEG molecule in linear (elongated) conformation. Furthermore, we noticed a root mean squared end-to-end distance value of 29.9 Å, averaged on 208 PEG molecules (AVG value in Figure 7.13b). This distance is smaller than the value of 35 Å (Figure 7.3c) observed for a single PEG molecule in water solvent and smaller than the value 34.2 Å observed in a complex with 40 PEGs (Figure 7.12b). It is noticeable this occurred when inducing maximum PEGylation by having only 21.3 Å spacing between PEG molecules along the CNT axis direction (Figure 7.6d). We attribute this to the induced maximum PEGylation and to a hydrophobic effect: the PEG molecules adopt a structural conformation which prevents water molecules from reaching the hydrophobic carbon nanotube sidewall; maximum PEGylation ensures an efficient protection of hydrophobic sites. In the case of HCCs, we suggest that this ensures better sequestration of drug molecules, since PEG molecules would allow hydrophobic drug molecules to reach a hydrophobic site in the HCC. We also suggest that drug liberation occurs mainly during PEG-HCC translocation through the cell membrane or inside the crowded cytoplasm; during these processes, stronger or more frequent interactions with biological molecules would affect or dominate PEG molecular conformation.

For the PEG-CNT construct with 208 PEG molecules, the resultant average values for r_u and d_m are 48.5 Å (Figure 7.13a) and 136.5 Å (Figure 7.13b), which are indicative of PEG size contribution to the PEG-HCC construct. We also noticed that the r_u maximum (68.7 Å) and r_u average (48.5 Å) are smaller than the values of 100.3 Å and 61.9 Å (Figures 12a, 13a) observed in a construct with only 40 PEGs. These suggest that a more homogenous and smaller size distribution for PEG molecules is attained when approaching maximum PEGylation. Thus a 114-mer PEG is short enough to obtain a width size within the nano regime, adequate for drug delivery platforms.

From our MD simulations at temperatures above 300K, we observe a tendency for PEG molecules to elongate towards linear conformations in which case it should be feasible attaching a higher number of PEG molecules to CNT sidewall. We suggest therefore performing PEGylation at high temperatures but further research is required to estimate the optimal temperature and conditions to achieve maximum PEGylation.

7.4 Summary and Conclusions

We performed molecular dynamics calculations on the real size of a PEG-CNT in a bath of water. The PEG was 114 units long and terminated with oxygen atoms at both ends. It was placed at the center of a cubic box 80 Å long with 16,500 water molecules, and the temperature was increased from 0.1 K to 300 K in a 50 ps linear ramp followed by equilibration at 300 K for 1.05 ns until the root-mean-squared end-to-end distance of the PEG was almost constant. During this equilibration, the PEG molecule adopted a globular shape. From this equilibration, the last structural configuration for PEG was taken as a reference and used to construct a PEGylated CNT. The MD simulation considered PEG molecules attached to the CNT sidewall and oriented orthogonal to the CNT axis. The possibility of PEGs linked to the CNT ends was considered by adding two PEG molecules at each end of the final PEG-CNT at 300 K; these four PEG molecules were oriented parallel to the CNT axis. The PEG-CNT was placed in a 480×180×180 Å^3 simulation box with 171,309 water molecules. After averaging for 50 ps of production runs, the width of the PEG-CNT complex reaches a maximum value of 136.5 Å and the maximum length of the full PEG-CNT complex is 407 Å.

Through this modeling of a shortened single walled carbon nanotube as the central core with 5040 molecular weight PEG addends, an approximation of the hydrodynamic volume of a PEG-CNT (and by extension, a PEG-HCC) is attained. Indeed, even in their hydrated form, as shown here, the PEG-CNT remains well within the nano-sized (40 nm) regime, providing a rational for their observed rapid clearance through the kidneys of mammals.[270] We elucidate the advantage of the hydrophilic character of PEG molecules and of maximum PEGylation, both favoring an optimal capture, protection and controlled release of drug molecules.

Approaching maximum PEGylation yields a decrease in radial thickness of polymer covering the CNT, a decrease in the probability for PEG wrapping of the CNT, and prevent water molecules from reaching the CNT. In the case of HCCs, maximum pegylation ensures better sequestration of drug molecules, since a decrease in the probability for PEG wrapping the CNT implies a higher surface area of hydrophobic sites available to capture drug molecules and a decrease in polymer radial thickness produces a denser polymer and therefore better protection of drug molecules from water.

Maximum PEGylation should be therefore considered an important design constraint to achieve an optimal drug delivery platform providing the ability of efficient release of drug molecules.

8. A GRAPHENE-BASED CHEMICAL SENSOR

We report the effect of a large bias gate voltage on the electrical conductivity of graphene ribbon devices when exposed to very low concentration of europium in an microfluidic device. We find a direct correlation between the level of concentration of europium ions in the solvent and the change in electrical conductivity of graphene, observing a change of up to three orders of magnitude at the lowest level of concentration tested (0.1 mM). Our results suggest that the microfluidic reservoir based graphene ribbon sensors is a promising procedure for detecting very low level of europium in liquid solutions.

8.1 Introduction

Identification of low concentrations of heavy metals belonging to the lanthanide and actinide series includes applications in environmental sampling [316, 317], water quality [318, 319], nuclear processing [320, 321], and nuclear forensics and safeguards [322-324]. Current techniques are complex and costly [19-21] and require special laboratory conditions [325, 326]. A key need is, therefore, a portable, low-cost device to detect trace heavy metals. In the present work, we analyze the electrochemical response of graphene to different concentrations of trivalent europium dissolved in water. Graphene has unique plasmonic characteristics that may permit ultrasensitive detection of sorbed species [84, 102, 143]. Indeed, ab initio molecular orbital calculations predict [107, 327] a strong, characteristic response of graphene nanoribbons to uranyl complexes sorbed to the surface. To improve surface complexation, research has focused on functionalized forms of graphene oxide employing hydroxyl, carboxyl, carbonyl, and epoxy moieties [23, 24, 328, 329] or more complex ligands and chelators [330-333]. As the speciation of lanthanide and actinide metals in solution is almost exclusively as cationic complexes in acidic waters [334], we tested a corollary method of inducing cationic sorption onto graphene by using electrical gate electrodes to induce a negative charge on the graphene [25, 26]. Therefore, we fabricate graphene electron devices whose response is modulated by an electrochemical mechanism, due to a negatively charged graphene and a layer of counter-ions at the graphene/water interface.

8.2 Methodology

A single layer graphene was grown by using thermal chemical vapor deposition (CVD) of methane gas on copper foil at 1000 °C, 50 sccm and 1 Torr. Before introducing methane gas, the copper foil (Alfa Aesar 0.025 mm thick, 99.8% metal basis, ~ 3.5 cm × 4 cm) was annealed in hydrogen gas at 800 °C for 30 minutes. Details about the graphene growth process can be found elsewhere [Gulotty *et al.* Carbon][335, 336]. Deionized (DI) water was from laboratory supply (16MΩ).

8.2.1 Graphene transfer process

Graphene was transferred from copper foil to a silicon dioxide coated Si wafer by a PMMA-assisted method. Briefly, during the CVD process graphene grows on both sides of the copper foil. After the CVD growth, one side of the graphene/copper foil is spin coated with a PMMA A8 e-beam resist at 3000 rpm for 60 seconds and air dried overnight (~ 12h) in a vented hood to obtain a uniform film. The unprotected side was etched in 1:10 mixture of nitric acid and distilled water (10 mL / 100 mL) for 10 minutes.

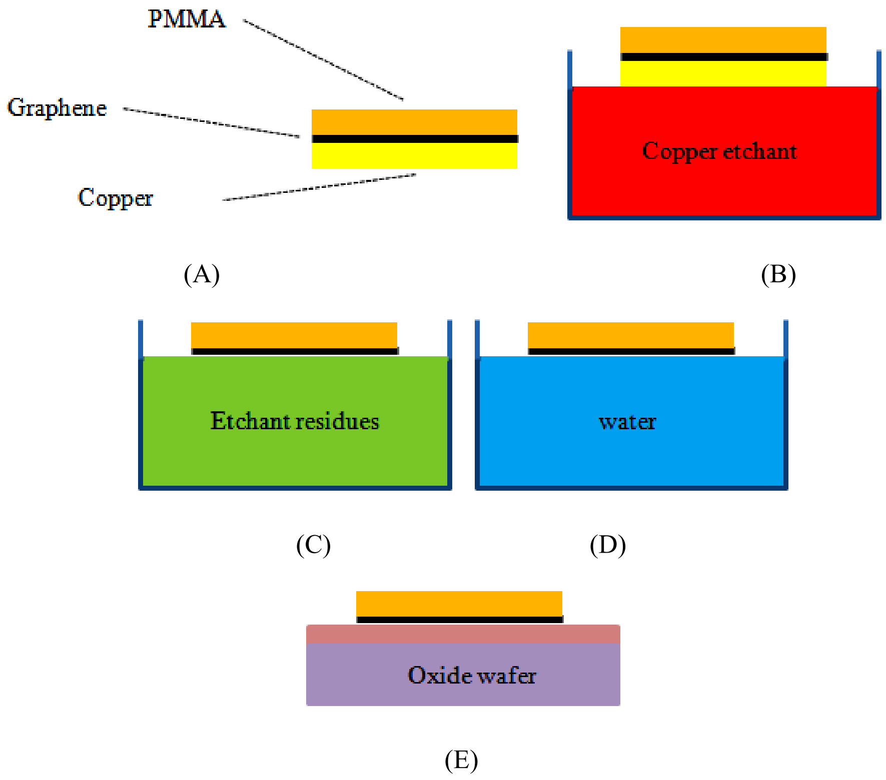

Figure 8.1. Depiction of the PMMA-assisted transfer process of CVD graphene. (A) CVD graphene is covering a copper foil, protected with a PMMA resist thin film and (B) placed into a copper etchant solution. (C) After copper etching, the PMMA/graphene membrane is nearly transparent and the solvent changes color. (D) Graphene is transferred to a beaker with distilled water to further dilute impurities from the etching process. (E) After rinse with water, the PMMA/graphene membrane is lifted from solution with an oxide wafer.

Then a 1 cm^2 sample of graphene/copper foil is immersed in the 1:5 copper etchant (iron chloride solution diluted in DI water) for 6 hours. After the copper completely dissolved in the etchant solution, the PMMA/graphene membrane is almost transparent. The PMMA/graphene membrane is then transferred to a beaker with DI water. Then, another four transfers to DI water are performed every three minutes to clean the PMMA/graphene membrane. Afterward, the PMMA/graphene membrane was lifted from solution with an oxide wafer. The SiO_2 thickness is 300 nm which ensure the best contrast to visualize graphene under the light microscope.

After transfer to the oxide wafer, a water layer is present between PMMA/graphene membrane and the oxide substrate. To effectively dry the membrane with minimum wrinkles, the sample was left overnight (~ 12 h) in a vented hood. Alternatively, baking at 37 °C for 2.5 hours works equally well. If the sample was not properly dried, the yield of graphene transfer was poor. After the sample fully dried, the PMMA resist covering graphene is removed in acetone for 3 hours, rinsed in isopropyl alcohol (IPA) for 10 minutes, and dried with a nitrogen gun. The sample was then baked on a hot plate at 150 °C for 15 minutes to ensure a strong adhesion of graphene to the oxide substrate and fewer defects (primarily in the form of holes on graphene). This baking process will also be critical to the integrity of interface electrodes during the liftoff process described next.

8.2.2 Graphene ribbon device fabrication

Metal electrodes (60 nm Au/ 2 nm Cr) were deposited on top of graphene by e-beam vapor deposition and patterned in a four-electrode configuration with two electrodes acting as interface to graphene and the other two electrodes for a gating mechanism. Patterning was performed by direct-write optical lithography using Shipley resist (S1805). The liftoff was performed by immersion in acetone at room temperature for 3 hours, rinsing by pipette with acetone for 2 minutes, and sonication in acetone for 5 seconds. Adhesion of interface electrodes and graphene to substrate is not very strong and sonication for one minute or longer can cause detachment.

To selectively pattern graphene ribbons, a resist mask is fabricated by direct-write optical lithography of Shipley resist (S1805). Under the light microscope, we could view the graphene and the electrodes through the transparent optical resist and position the ribbon mask pattern with respect to the metal electrodes. After the resist was developed, rinsed and dried, the sample was exposed to oxygen plasma (24 sccm, 160 mTorr, 20 W, 5 minutes) to etch the exposed zones of graphene. Once the etch process was completed the resist was removed using acetone for 3 hours at room temperature, rinsed in IPA for 10 minutes, and dried with a nitrogen gun. Acetone was an effective resist remover that did not damage the graphene layer, while a conventional resist remover (e.g., Shipley microposit remover 1165) will remove graphene.

8.2.3 Reservoir fabrication and sample preparation

To test of a liquid sample, a reservoir was made of optical resist by direct-write optical lithography. A thin resist was chosen (S1805, 0.5 μm thick) to minimize the amount of resist impurities after the development process. The reservoir size was about 4 mm × 4 mm and a resist coating for interface electrodes was also patterned to avoid interference from the electrical impedance of the liquid sample (Figure 8.2). Europium nitrate was prepared by dissolving 0.025 g of europium nitrate pentahydrate (99.9%

trace metals basis, from Sigma Aldrich) in 5 mL of DI water. Four different types of liquid samples were tested -- water and three solutions of different levels of concentration for europium nitrate (0.1 mM, 1 mM and 10 mM) made by serial dilution of the europium nitrate stock. To test the electrical response of graphene ribbons to europium nitrate solution a ~ 0.1 μL drop of the liquid sample was deposited into the fluidic reservoir with the aid of a micropipette. The drop typically covered a circular area of ~ 1 mm diameter (Figure 8.2b). The typical time for a sample drop to evaporate was about 2 minutes and the time to perform a current-voltage measurement was a few seconds.

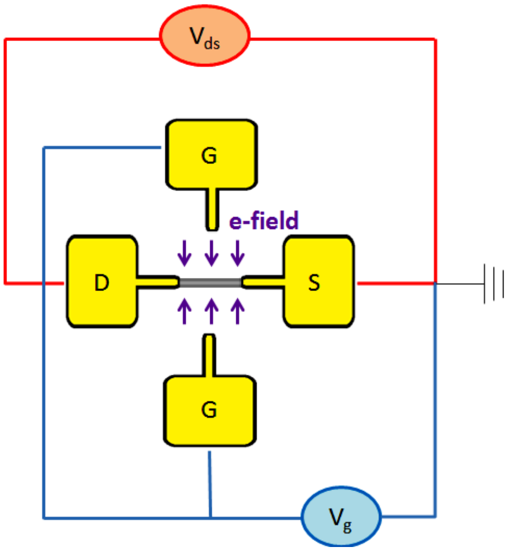

(A)

Figure 8.2. (A) Schematic representation of the four-electrode configuration for measurements of the electrical response of graphene ribbon. Two electrodes, Drain (D) and Source (S), act as interface to graphene while the other two electrodes (G) act as a gating mechanism by enabling an electric field that drives ions towards graphene ribbon. (B) Light microscope image of fluidic device showing five set of graphene ribbon devices. (C) Graphene ribbon in a four-electrode configuration. Interface electrodes (horizontal pair) are covered with resist. In a typical experiment, a small drop (~ 0.1 μL) is deposited on the fluidic reservoir. The diameter of the drop is 1-2 mm. Note the circular mark left on the fluidic reservoir after the drop dried.

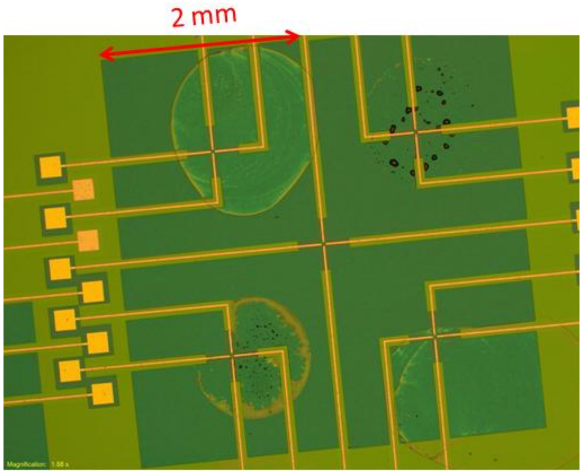

(B)

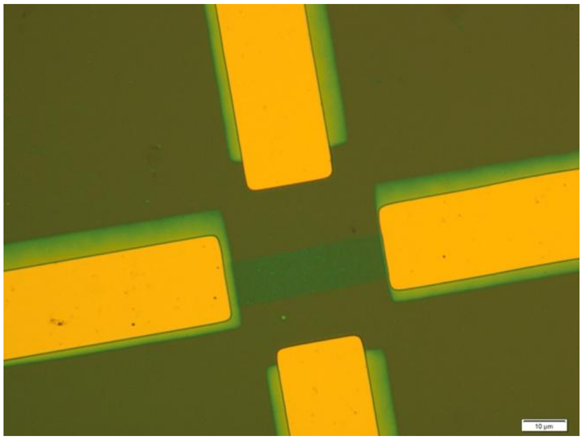

(C)

Figure 8.2. Continued.

8.2.4 Electrical measurements

The electrical measurements were performed in a four electrode configuration. Two gate electrodes (G) were used to drive europium ions towards the graphene ribbon and the other pair (D and S) to drive the ion-modulated electrical current through graphene (Figure 8.2b). We expect ions will modulate the drain-source (I) current. The drain-source bias voltage of graphene was V_{ds} ~10 mV (dc) and the gating voltage is V_g

~2-20V (dc), this implies graphene is close to zero volts with respect to gate electrodes ($V_{ds} << V_g$). The bias voltage between graphene and gate electrodes creates a negative charge on graphene that drives cations towards graphene and modulates its electrical conductivity. Furthermore a bias voltage larger than ~2 V induces water electrolysis [337-339], the splitting of water in hydrogen and hydroxyl ions.

8.2.5 Molecular simulations

Detection mechanism was studied with molecular dynamics simulations using the CHARMM force field [153] as implemented in the program LAMMPS [146]. These simulations allowed us to analyze the strength of non-bonded interactions between solution ions and graphene.

We consider a maximum negative charge of -0.2 (all charge units are in electrons in this work) per carbon atom in graphene [340]. Lennard-Jones parameters for europium (III) were taken from Veggel and Reinhoudt (1999) [341], while Lennard-Jones parameters for the hydrogen ion were taken from the TIP3P model for water [147]. Lennard-Jones parameters for interaction between water and graphene were taken from Zhang and Wang [342]. Molecular dynamics simulations were performed with non-periodic boundary conditions and with inner and outer cutoff distances of 20 Å and 22 Å for non-bonded interactions. A time step of 0.2 fs was used and the energy equilibration was performed at room temperature (300 K) in an NVT ensemble.

8.3 Results and discussion

8.3.1 Electrical measurements

We measure the I-V_{ds} and I-V_g response of graphene ribbon for each drop sample, I-V_{ds} is performed before and after sample deposition and always in dry conditions; while I-V_g is performed right after sample drop deposition, in wet conditions. Therefore I-V_{ds} provides the electrical conductivity of graphene in dry conditions and I-V_g the dynamics of ion-modulated graphene conductivity during wet conditions. I-V_g is always performed at constant V_{ds} of 10 mV.

We perform initial measurements at low (V_{gs}=0-2V) and high gate voltage (V_{gs}=0-10V), in both cases we observe a nonlinear characteristic in the I-Vg curve (Figure 8.3, 8.4). A high bias voltage was required for a change to occur in the electrical conductivity of graphene ribbon at dry conditions (Figure 8.4). The I-V_g nonlinear characteristic at low gate voltage (0-2V) was similar to that observed in graphene-based field-effect transistor (FET) devices (Figure 8.3).

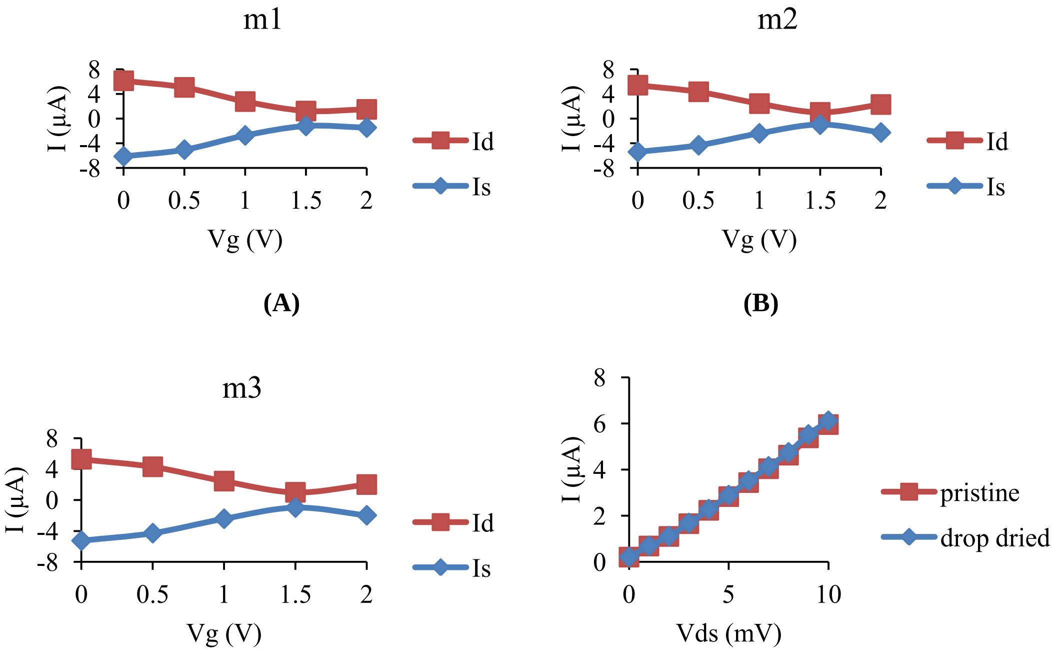

(A) (B)

(C) (D)

Figure 8.3. Electrical response of graphene ribbon device at low bias gate voltage, V_g=0-2V, to distilled water. 'm1' (A), 'm2' (B) and 'm3' (C) are three consecutive measurements performed for the same drop sample and ribbon device. In (D), 'pristine' corresponds to measurement before sample deposition, and 'drop dried' corresponds to measurement after sample drop dried.

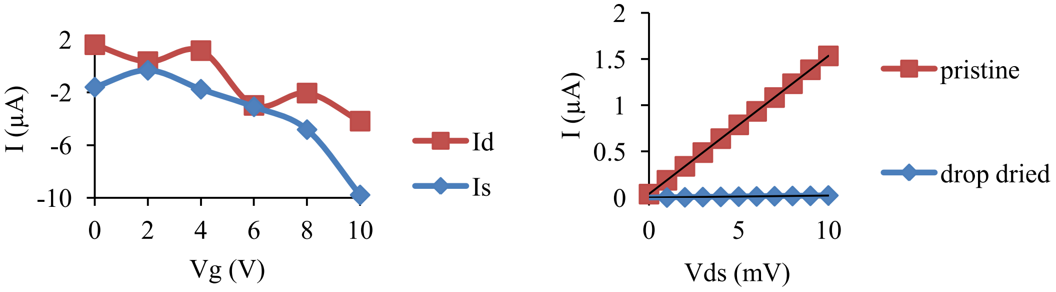

(A) (B)

Figure 8.4. Electrical response of graphene ribbon device at high bias voltage (V_g=0-10V) to DI water. I-V_g measurement (A) was performed in wet conditions, and I-V_{ds} (B) measurement was performed in dry conditions and with no gate voltage (V_g) applied; where 'pristine' corresponds to measurement before sample deposition, and 'drop dried' corresponds to measurement after sample drop has dried. In I-V_{ds} plot, a linear approximation 'a+bx' is shown, where 'a' corresponds to the graphene electrical conductivity in mSiemens units.

In the initial measurements at low gate voltage (Figure 8.3) we do not observe a correlation or difference in the electrical characteristic of graphene when interacting with distilled water or europium solution. However, at high gate voltage (Figure 8.4), we observed a clear change in the electrical conductivity of graphene. We, therefore, perform further measurements at high gate voltage (0-25 V) and looked fora correlation between the level of concentration of europium solution and a change in the electrical conductivity of graphene.

As the concentration of europium decreased, the electrical conductivity of graphene decreased, and the ratio g_1/g_2 increased (Fig. 8.5), where 'g_1' and 'g_2' represents the electrical conductivity of graphene before and after exposure to europium solution. After electrical measurements in DI water and after the sample drop dried, the current through graphene is zero during I-V_{ds} measurements and therefore the electrical conductivity of graphene is effectively zero; this $g_1/g_2=\infty$ event at 0.0 M (not shown in Fig. 8.5) occurred in three of four measurements with DI water.

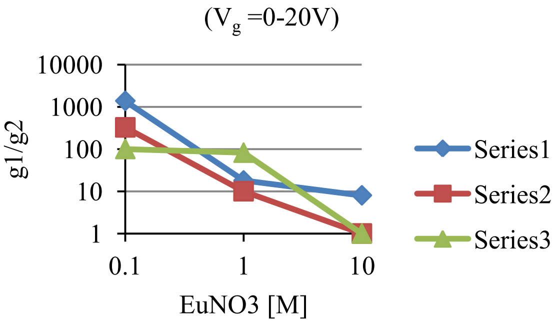

Figure 8.5. 'g_1' and 'g_2' represents the electrical conductivity of graphene before and after exposure to europium solution under a bias voltage. Four tests were performed with distilled water (not shown in the plot), of which three resulted in electrical breakdown ($g_1/g_2=\infty$) and one resulted in $g_1/g_2=1$.

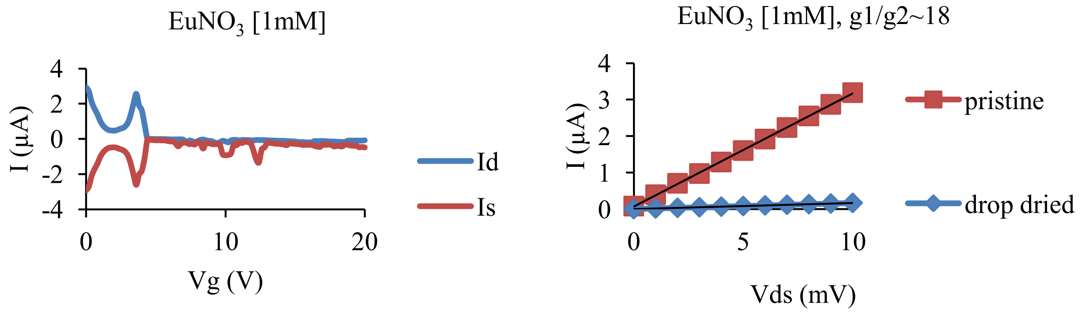

(A) (B)

Figure 8.6. Electrochemical response of graphene ribbon to europium solution. (a) The I-Vg curve performed at constant V_{ds} (10mV) allows monitoring the decrease in electrical conductivity (I/V_{ds}) of graphene. (b) The decrease in electrical conductivity of graphene is confirmed by measurement of the I-Vds curve after the sample drop dried.

We believe that at a positive bias gate voltage larger than 2V, hydrogen ions generated by electrolysis, given by

$$H_2O \rightarrow H^+ + OH^- , \tag{8.1}$$

are driven towards the negatively-charged graphene ribbon surface (Figure 8.7). Hydrogen ions are neutralized by graphene charges, recombining then to form hydrogen gas. We don't discard at the same time the event of hydrogen covalently binding to graphene. Hydrogen and hydroxyl ions are constantly being generated by electrolysis (Equation 8.1) while the amount of europium is fixed. Trivalent europium preferentially binds to graphene due to its higher charge density than hydrogen ions, partially blocking hydrogen interaction with graphene. We suggest the interaction of graphene with ions gives origin to a change in graphene ribbon structure or functionalization and the observed change in electrical conductivity of graphene. Further studies are needed to determine the change in graphene ribbon structure upon application of a high bias gate voltage in a microfluidic device.

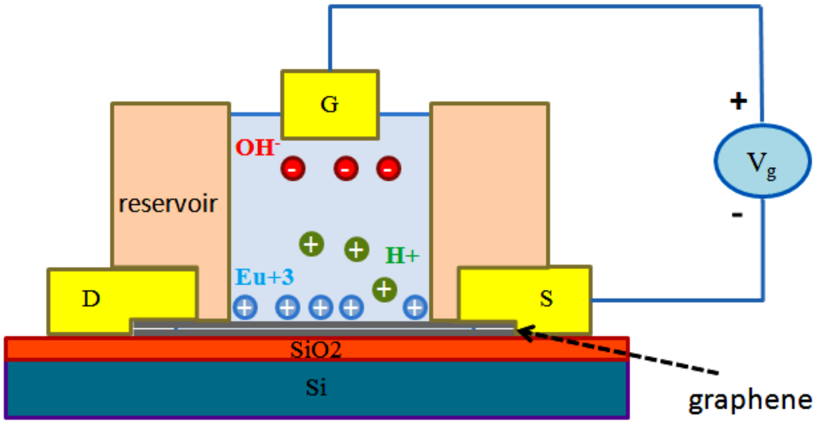

Figure 8.7. Suggested mechanism prevailing at V_g = 0-20 V. An electrical bilayer is formed by the negatively charged graphene and positive counterions. Europium ions compete with hydrogen ions for binding to graphene.

8.3.2 Molecular simulation results

At a small level of negative charge for graphene, -0.02 per carbon atom, the electrostatic attraction is not strong enough to induce binding of solution ions to graphene (Figure 8.8). We found that a relatively large concentration of ions (6 H^+ and 6 Eu^{+3} in a ~40 Å box) can induce freezing of water. We observed a low mobility of ions during equilibration at room temperature (300 K) and at 330 K. Electrofreezing of water due to a charged graphene has been reported by Zhu *et al*. [340]. We analyze then the same system under a maximum charge for graphene of -0.2 per carbon atom and find the electrostatic attraction between graphene and ions strong enough to overcome the water solvation layer normally surrounding ions in solution (Figure 8.8). We observe that the ion stabilizes around the center of a benzene ring on the graphene surface. For a maximum charge of -0.2 per carbon atom, the negative charge on the benzene ring totals -1.2 which effectively neutralizes a hydrogen ion (charged +1) and would not prevent other hydrogen ions from binding to graphene on adjacent sites. For a europium ion, even a maximum charge of -0.2 is not enough to neutralize the cation (+3) and the total charge of the ionic complex would continue being positive, preventing by electrostatic repulsion, the binding of other cations to graphene in adjacent atomic sites.

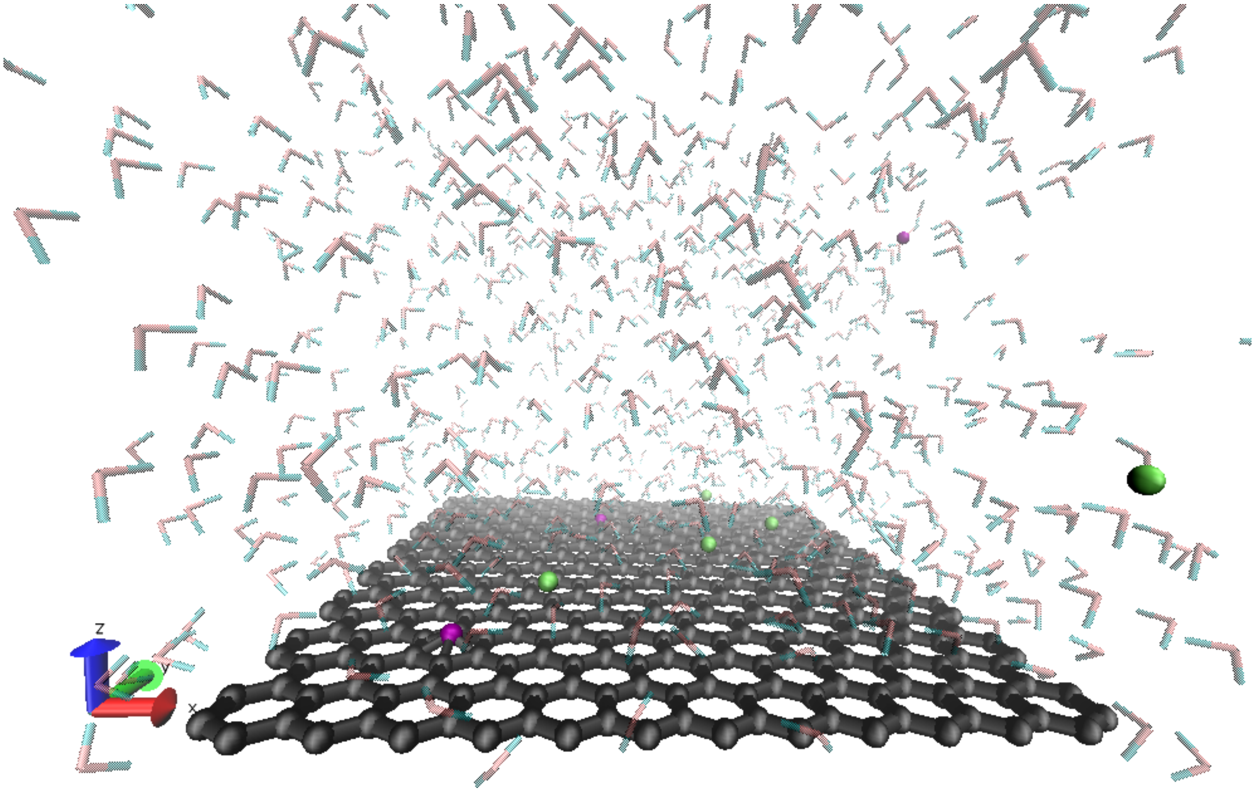

Figure 8.8. Binding of solution ions to negatively charged graphene (-0.2 per carbon atom) at room temperature. Atoms are color coded: europium ion (green), hydrogen ion (purple), graphene (gray), water (cyan and pink). Average bond distances are: Eu-C = 2.6 Å and H-C =1.6 Å.

To analyze the strength of ion binding to graphene we consider a hypothetical case of an ion positioned 3 Å above graphene as the initial structure (Figure 8.9) and analyze how the atomic charge of graphene affects the bond distance of ions to graphene. To predict the stable structure we perform an energy minimization and then an energy equilibration at 0.1 K under an NVT ensemble. This is followed by a calculation of the average bond distance between the ion and the six carbon atoms of the closest six-member ring from the graphene surface.

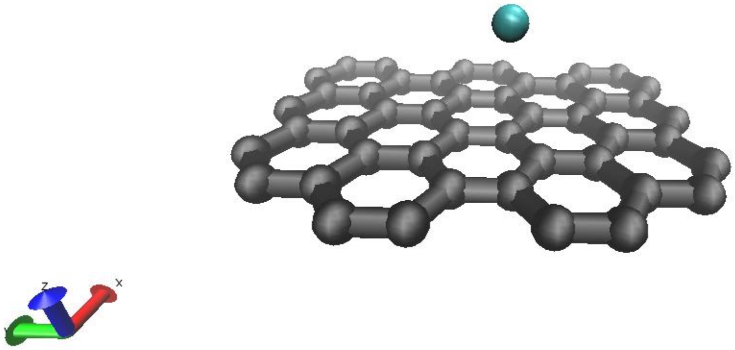

Figure 8.9. Structure for analyzing dependence of ion-graphene bond distance on graphene atomic charge.

We find a significant change in the ionic bond distance for the hydrogen ion (Table 8.1). When the atomic charge of graphene is -0.025, the bond distance decreases ~ 0.8 Å for europium and ~ 0.4 Å for hydrogen ion. When the atomic charge reaches a maximum value of -0.2, the bond distance decreases an additional 0.3 Å for both ions; however, the relative change is larger for the hydrogen ion since its bond distance to graphene is always smaller than that of europium. This would enhance the effect of the hydrogen ion on the electrical properties of graphene.

Table 8.1. Average ion-carbon bond distance after binding of ions to the negatively charged graphene.

q_C (e)	C-H^+ (Å)	C-Eu^{+3} (Å)
0	2.21	3.71
-0.025	1.81	2.92
-0.05	1.72	2.81
-0.1	1.63	2.73
-0.2	1.56	2.61

An ionic bond between two atoms contains partial covalent character, depending on the relative difference of their electronegativities. The smaller the difference the larger the covalent character of the ionic bond. Therefore, we consider that the ionic bonding of hydrogen to graphene has a strong covalent character while the binding of europium to graphene is close to purely ionic (Table 8.2). This implies that the ionic binding of hydrogen ion to graphene is capable of altering the electronic structure of graphene.

Table 8.2. Electronegativity of atoms participating in the ionic bonding.

atom type	electronegativity
Hydrogen	2.2
Europium	1.2
Carbon	2.55

8.4 Conclusions

A microfluidic device is suggested to test the electrochemical response of graphene. Under a four-electrode configuration, we find different behaviors at low (<2 V) and high (>2V) bias gate voltage. At low voltage, we find a FET-like electrical characteristic for graphene but europium ions have no effect on the FET characteristic. At high bias voltage, the change in electrical conductivity of graphene has an inverse relation with the level of concentration of europium ions.

We attribute the behavior at high voltage to water electrolysis, graphene interaction with hydrogen ions, and a passivation of this effect proportional to the level of concentration of europium ions. We suggest this passivation is due to the binding of europium ions to a negatively charged graphene, which partially prevents the hydrogen ions from binding to graphene.

Finally, graphene-ion interactions affect graphene ribbon structure and functionalization yielding changes in electrical conductivity of graphene. This effect has potential opportunity for the fabrication of nanosensors. Certainly, further studies are needed to determine the change in graphene ribbon structure upon application of a high bias gate voltage in a microfluidic device.

9. SUMMARY AND CONCLUSIONS

By using molecular dynamics, we are able to predict the structure of irradiated carbon nanotube, DNA-carbon hybrid nanostructures and PEGylated carbon nanotube. This allows a detailed analysis of the atomic structure, otherwise difficult and sometimes imposible to attain by coventional imaging tools. Furthermore, the structure found by molecular dynamics can serve as input for electronic structure calculations and we suggest the possibility of novel electron devices.

We have analyzed the effects of irradiation on carbon nanotube, we found a predominance of single vacancy defects upon exposure to very high energy argon ion and they constitute magnetic impurities; aided by oxygen plasma and an electrical breakdown technique we were able to induce an NDR behavior in suspended carbon nanotubes. We suggest defects on carbon nanotubes can be an important source of novel electronic properties.

By exploiting the strong van der Waals interaction in electron-rich pi systems, we suggest the assembly of novel nanostructures based on DNA and carbon nanostructures, we find DNA always induces a gating mechanism on the electronic structure of carbon, therefore the chemical sensitivity of DNA can be effectively coupled to the electrical property of the carbon nanodevice.

We were able to adapt conventional lithography techniques to the fabrication of graphene ribbon sensor devices for the detection of europium ions in liquid samples.

Our method allows a high yield of working devices which is necessary for an adequate testing of possible novel scenarios based on graphene electron devices.

REFERENCES

[1] A. V. Krasheninnikov and F. Banhart, "Engineering of nanostructured carbon materials with electron or ion beams," *Nat Mater,* 2007, 6, 723-733.

[2] J.-Y. Park, Y. Yaish, M. Brink, S. Rosenblatt, and P. L. McEuen, "Electrical cutting and nicking of carbon nanotubes using an atomic force microscope," *Appl Phys Lett,* 2002, 80, 4446-4448.

[3] L. Weng, L. Zhang, Y. P. Chen, and L. P. Rokhinson, "Atomic force microscope local oxidation nanolithography of graphene," *Appl Phys Lett,* 2008, 93, 093107.

[4] T. D. Yuzvinsky, W. Mickelson, S. Aloni, G. E. Begtrup, A. Kis*, et al.*, "Shrinking a carbon nanotube," *Nano Lett,* 2006, 6, 2718-2722.

[5] X. Guo, J. P. Small, J. E. Klare, Y. Wang, M. S. Purewal*, et al.*, "Covalently bridging gaps in single-walled carbon nanotubes with conducting molecules," *Science,* 2006, 311, 356-359.

[6] R. V. Seidel, A. P. Graham, B. Rajasekharan, E. Unger, M. Liebau*, et al.*, "Bias dependence and electrical breakdown of small diameter single-walled carbon nanotubes," *J Appl Phys,* 2004, 96, 6694-6699.

[7] P. G. Collins, M. Hersam, M. Arnold, R. Martel, and P. Avouris, "Current saturation and electrical breakdown in multiwalled carbon nanotubes," *Phys Rev Lett,* 2001, 86, 3128-3131.

[8] P. G. Collins, M. S. Arnold, and P. Avouris, "Engineering carbon nanotubes and nanotube circuits using electrical breakdown," *Science,* 2001, 292, 706-709.

[9] F. O. Hadeed and C. Durkan, "Controlled fabrication of 1–2 nm nanogaps by electromigration in gold and gold-palladium nanowires," *Appl Phys Lett,* 2007, 91, 123120.

[10] X. Guo, A. A. Gorodetsky, J. Hone, J. K. Barton, and C. Nuckolls, "Conductivity of a single DNA duplex bridging a carbon nanotube gap," *Nat Nano,* 2008, 3, 163-167.

[11] H. T. Maune, S.-p. Han, R. D. Barish, M. Bockrath, I. I. A. Goddard, *et al.*, "Self-assembly of carbon nanotubes into two-dimensional geometries using DNA origami templates," *Nat Nano,* 2010, 5, 61-66.

[12] M. Cha, S. Jung, M.-H. Cha, G. Kim, J. Ihm, *et al.*, "Reversible metal−semiconductor transition of ssDNA-decorated single-walled carbon nanotubes," *Nano Lett,* 2009, 9, 1345-1349.

[13] L. Ouellette, "Chemical and biological sensing with carbon nanotube in solution," PhD, Physics, Cornell University, Ithaca, New York, 2008.

[14] S. Gowtham, R. H. Scheicher, R. Pandey, S. P. Karna, and R. Ahuja, "First-principles study of physisorption of nucleic acid bases on small-diameter carbon nanotubes," *Nanotechnol,* 2008, 19, 125701.

[15] S. Gowtham, R. H. Scheicher, R. Ahuja, R. Pandey, and S. P. Karna, "Physisorption of nucleobases on graphene: density-functional calculations," *Phys Rev B,* 2007, 76, 033401.

[16] R. C. Ewing, W. J. Weber, and F. W. Clinard Jr, "Radiation effects in nuclear waste forms for high-level radioactive waste," *Prog Nucl Energ,* 1995, 29, 63-127.

[17] D. H. Day, A. E. Hughes, J. W. Leake, J. A. C. Marples, G. P. Marsh, *et al.*, "The management of radioactive wastes," *Rep Prog Phys,* 1985, 48, 101.

[18] R. C. Ewing, "Nuclear waste forms for actinides," *P Natl Acad Sci USA,* 1999, 96, 3432-3439.

[19] L. Zavodska, E. Kosorinova, L. Scerbakova, and J. Lesny, "Environmental chemistry of uranium," *Hung Electron J Sci,* 2008, Enviromental Engineering Section, ENV-081221-A.

[20] W. W. Meinke, "Trace-element sensitivity: comparison of activation analysis with other methods," *Science,* 1955, 121, 177-184.

[21] S. Wolf, "Trace analysis of actinides in geological, environmental, and biological matrices," in *The chemistry of the actinide and transactinide elements*, L. Morss, *et al.*, Eds., ed: Springer Netherlands, 2011, 3273-3338.

[22] H. M. H. Gad and N. S. Awwad, "Factors affecting on the sorption/desorption of Eu (III) using activated carbon," *Separ Sci Technol,* 2007, 42, 3657-3680.

[23] G. Zhao, J. Li, X. Ren, C. Chen, and X. Wang, "Few-layered graphene oxide nanosheets as superior sorbents for heavy metal ion pollution management," *Environ Sci Technol,* 2011, 45, 10454-10462.

[24] Y. Sun, Q. Wang, C. Chen, X. Tan, and X. Wang, "Interaction between Eu(III) and graphene oxide nanosheets investigated by batch and extended X-ray absorption fine structure spectroscopy and by modeling techniques," *Environ Sci Technol,* 2012, 46, 6020-6027.

[25] Z. M. Ao, W. T. Zheng, and Q. Jiang, "The effects of electronic field on the atomic structure of the graphene/α-SiO 2 interface," *Nanotechnol,* 2008, 19, 275710.

[26] J. Romaneh, A. J. Luis, L. Gabriel, T. Jifa, R. Caleb, *et al.*, "Scanning gate microscopy on graphene: charge inhomogeneity and extrinsic doping," *Nanotechnol,* 2011, 22, 295705.

[27] J. S. Bunch, A. M. van der Zande, S. S. Verbridge, I. W. Frank, D. M. Tanenbaum, *et al.*, "Electromechanical resonators from graphene sheets," *Science,* 2007, 315, 490-493.

[28] C. Li and T.-W. Chou, "Mass detection using carbon nanotube-based nanomechanical resonators," *Appl Phys Lett,* 2004, 84, 5246-5248.

[29] H. B. Peng, C. W. Chang, S. Aloni, T. D. Yuzvinsky, and A. Zettl, "Ultrahigh frequency nanotube resonators," *Phys Rev Lett,* 2006, 97, 087203.

[30] C. Xiangyu, D. Akinwande, L. Kyeong-Jae, G. F. Close, S. Yasuda, *et al.*, "Fully integrated graphene and carbon nanotube interconnects for gigahertz high-speed CMOS electronics," *IEEE T Electron Dev,* 2010, 57, 3137-3143.

[31] Y.-M. Lin, K. A. Jenkins, A. Valdes-Garcia, J. P. Small, D. B. Farmer, *et al.*, "Operation of graphene transistors at gigahertz frequencies," *Nano Lett,* 2008, 9, 422-426.

[32] P. Avouris, "Molecular electronics with carbon nanotubes," *Accounts Chem Res,* 2002, 35, 1026-1034.

[33] L. A. Agapito, E. J. Bautista, and J. M. Seminario, "Conductance model of gold-molecule-silicon and carbon nanotube-molecule-silicon junctions," *Phys Rev B,* 2007, 76, 115316.

[34] M. Bockrath, D. H. Cobden, J. Lu, A. G. Rinzler, R. E. Smalley, *et al.*, "Luttinger-liquid behaviour in carbon nanotubes," *Nature,* 1999, 397, 598-601.

[35] K. S. Novoselov, A. K. Geim, S. V. Morozov, D. Jiang, M. I. Katsnelson, *et al.*, "Two-dimensional gas of massless Dirac fermions in graphene," *Nature,* 2005, 438, 197-200.

[36] K. S. Novoselov, Z. Jiang, Y. Zhang, S. V. Morozov, H. L. Stormer, *et al.*, "Room-temperature quantum Hall effect in graphene," *Science,* 2007, 315, 1379.

[37] M. I. Katsnelson and K. S. Novoselov, "Graphene: new bridge between condensed matter physics and quantum electrodynamics," *Solid State Commun,* 2007, 143, 3-13.

[38] J. Nygard, D. H. Cobden, and P. E. Lindelof, "Kondo physics in carbon nanotubes," *Nature,* 2000, 408, 342-346.

[39] A. D. Bobadilla and J. M. Seminario, "DNA−CNT interactions and gating mechanism using MD and DFT," *J Phys Chem C,* 2011, 115, 3466-3474.

[40] J. Fujita, T. Takahashi, R. Ueki, T. Hikata, S. Okubo, *et al.*, "Enormous shrinkage of carbon nanotubes by supersonic stress and low-acceleration electron beam irradiation," *J Vac Sci & Technol B,* 2012, 30, 03D105.

[41] L. X. Li, J. B. Su, Y. Wu, X. F. Zhu, and Z. G. Wang, "New observations for electron beam-induced instability of single-wall carbon nanotube," *Acta Phys Sin,* 2012, 61, 036401.

[42] C. Thiele, M. Engel, F. Hennrich, M. M. Kappes, K.-P. Johnsen, *et al.*, "Controlled fabrication of single-walled carbon nanotube electrodes by electron-beam-induced oxidation," *Appl Phys Lett,* 2011, 99, 173105.

[43] J. L. Lu, G. L. Wang, F. Q. Gao, and P. Qiu, "Fabrication of coiled carbon nanotubes by chemical vapour deposition and focused ion beam," *Asian J Chem,* 2012, 24, 2695-2697.

[44] T. V. Panova and V. S. Kovivchak, "Formation of nanostructured carbon on steel targets irradiated by a high-power ion beam," *J Surf Investig-X-Ra,* 2012, 6, 241-243.

[45] R. Langegger, A. Lugstein, M. Glaser, E. Bertagnolli, and A. Steiger-Thirsfeld, "High temperature focused ion beam response of graphite resulting in spontaneous nanosheet formation," *J Vac Sci & Technol B,* 2011, 29, 061804.

[46] S. Akcoltekin, H. Bukowska, T. Peters, O. Osmani, I. Monnet, *et al.*, "Unzipping and folding of graphene by swift heavy ions," *Appl Phys Lett,* 2011, 98, 103103.

[47] L. Tapaszto, G. Dobrik, P. Lambin, and L. P. Biro, "Tailoring the atomic structure of graphene nanoribbons by scanning tunnelling microscope lithography," *Nat Nano,* 2008, 3, 397-401.

[48] M. C. Lemme, D. C. Bell, J. R. Williams, L. A. Stern, B. W. H. Baugher, *et al.*, "Etching of graphene devices with a helium ion beam," *ACS Nano,* 2009, 3, 2674-2676.

[49] D. C. Bell, M. C. Lemme, L. A. Stern, J. R. Williams, and C. M. Marcus, "Precision cutting and patterning of graphene with helium ions," *Nanotechnol,* 2009, 20, 455301.

[50] L. Xie, L. Jiao, and H. Dai, "Selective etching of graphene edges by hydrogen plasma," *J Am Chem Soc,* 2010, 132, 14751-14753.

[51] A. Hassanien and et al., "Selective etching of metallic single-wall carbon nanotubes with hydrogen plasma," *Nanotechnol,* 2005, 16, 278.

[52] J. A. Rodriguez-Manzo and F. Banhart, "Creation of individual vacancies in carbon nanotubes by using an electron beam of 1 Å diameter," *Nano Lett,* 2009, 9, 2285-2289.

[53] C. Andrey and et al., "From graphene constrictions to single carbon chains," *New J Phys,* 2009, 11, 083019.

[54] O. Lehtinen, T. Nikitin, A. V. Krasheninnikov, L. T. Sun, F. Banhart*, et al.*, "Characterization of ion-irradiation-induced defects in multi-walled carbon nanotubes," *New J Phys,* 2011, 13, 073004.

[55] Y. Beyer, R. Beanland, and P. A. Midgley, "Low voltage STEM imaging of multi-walled carbon nanotubes," *Micron,* 2012, 43, 428-434.

[56] J. C. Meyer, F. Eder, S. Kurasch, V. Skakalova, J. Kotakoski*, et al.*, "Accurate measurement of electron beam induced displacement cross sections for single-layer graphene," *Phys Rev Lett,* 2012, 108, 196102.

[57] A. V. Krasheninnikov, K. Nordlund, M. Sirviö, E. Salonen, and J. Keinonen, "Formation of ion-irradiation-induced atomic-scale defects on walls of carbon nanotubes," *Phys Rev B,* 2001, 63, 245405.

[58] Z. Osváth, G. Vértesy, L. Tapasztó, F. Wéber, Z. E. Horváth*, et al.*, "Atomically resolved STM images of carbon nanotube defects produced by irradiation," *Phys Rev B,* 2005, 72, 045429.

[59] Z. Osváth, L. Tapasztó, G. Vértesy, A. A. Koós, Z. E. Horváth, *et al.*, "STM imaging of carbon nanotube point defects," *Phys Status Solidi A,* 2007, 204, 1825-1829.

[60] A. Tolvanen, G. Buchs, P. Ruffieux, P. Gröning, O. Gröning, *et al.*, "Modifying the electronic structure of semiconducting single-walled carbon nanotubes by ion irradiation," *Phys Rev B,* 2009, 79, 125430.

[61] N. Inui, K. Mochiji, K. Moritani, and N. Nakashima, "Molecular dynamics simulations of nanopore processing in a graphene sheet by using gas cluster ion beam," *Appl Phys A-Mater,* 2010, 98, 787-794.

[62] J. A. V. Pomoell, A. V. Krasheninnikov, K. Nordlund, and J. Keinonen, "Ion ranges and irradiation-induced defects in multiwalled carbon nanotubes," *J Appl Phys,* 2004, 96, 2864-2871.

[63] I. Jang, S. B. Sinnott, D. Danailov, and P. Keblinski, "Molecular dynamics simulation study of carbon nanotube welding under electron beam irradiation," *Nano Lett,* 2003, 4, 109-114.

[64] S. K. Pregler and S. B. Sinnott, "Molecular dynamics simulations of electron and ion beam irradiation of multiwalled carbon nanotubes: The effects on failure by inner tube sliding," *Phys Rev B,* 2006, 73, 224106.

[65] E. P. Bellido and J. M. Seminario, "Molecular dynamics simulations of ion-bombarded graphene," *J Phys Chem C,* 2012, 116, 4044-4049.

[66] A. V. Krasheninnikov, K. Nordlund, and J. Keinonen, "Production of defects in supported carbon nanotubes under ion irradiation," *Phys Rev B,* 2002, 65, 165423.

[67] O. Lehtinen, J. Kotakoski, A. V. Krasheninnikov, A. Tolvanen, K. Nordlund, *et al.*, "Effects of ion bombardment on a two-dimensional target: Atomistic simulations of graphene irradiation," *Phys Rev B,* 2010, 81, 153401.

[68] O. Lehtinen, J. Kotakoski, A. V. Krasheninnikov, and J. Keinonen, "Cutting and controlled modification of graphene with ion beams," *Nanotechnol,* 2011, 22, 175306.

[69] S. Berber and A. Oshiyama, "Reconstruction of mono-vacancies in carbon nanotubes: Atomic relaxation vs. spin polarization," *Physica B,* 2006, 376–377, 272-275.

[70] W. Orellana and P. Fuentealba, "Structural, electronic and magnetic properties of vacancies in single-walled carbon nanotubes," *Surf Sci,* 2006, 600, 4305-4309.

[71] Z. Zanolli and J. C. Charlier, "Spin transport in carbon nanotubes with magnetic vacancy-defects," *Phys Rev B,* 2010, 81, 165406.

[72] R. Farghadan and A. Saffarzadeh, "The effect of vacancy-induced magnetism on electronic transport in armchair carbon nanotubes," *J Phys-Condens Matt,* 2010, 22, 255301.

[73] J. Tersoff, "New empirical approach for the structure and energy of covalent systems," *Phys Rev B,* 1988, 37, 6991.

[74] J. Tersoff, "Modeling solid-state chemistry: interatomic potentials for multicomponent systems," *Phys Rev B,* 1989, 39, 5566.

[75] J. F. Ziegler, J. P. Biersack, and U. Littmark, *The stopping and range of ions in matter*. New York: Pergamon, 1985.

[76] K. Nordlund, N. Runeberg, and D. Sundholm, "Repulsive interatomic potentials calculated using Hartree-Fock and density-functional theory methods," *Nucl Instrum Meth B,* 1997, 132, 45-54.

[77] A. Ruaudel-Teixier, M. Vandevyver, and A. Barraud, "Novel conducting Langmuir-Blodgett films," *Mol Cryst Liq Cryst,* 1985, 120, 319-322.

[78] A. K. Rappe, C. J. Casewit, K. S. Colwell, W. A. Goddard, and W. M. Skiff, "UFF, a full periodic table force field for molecular mechanics and molecular dynamics simulations," *J Am Chem Soc,* 1992, 114, 10024-10035.

[79] R. H. Baughman, A. A. Zakhidov, and W. A. de Heer, "Carbon nanotubes--the route toward applications," *Science,* 2002, 297, 787-792.

[80] A. Bianco, R. Sainz, S. Li, H. Dumortier, L. Lacerda, *et al.*, "Biomedical applications of functionalised carbon nanotubes," in *Medicinal chemistry and pharmacological potential of fullerenes and carbon nanotubes*, F. Cataldo and T. Da Ros, Eds., ed: Springer Netherlands, 2008, 23-50.

[81] P. Bondavalli, P. Legagneux, and D. Pribat, "Carbon nanotubes based transistors as gas sensors: State of the art and critical review," *Sensor Actuat B-Chem,* 2009, 140, 304-318.

[82] E. S. Snow, F. K. Perkins, E. J. Houser, S. C. Badescu, and T. L. Reinecke, "Chemical detection with a single-walled carbon nanotube capacitor," *Science,* 2005, 307, 1942-1945.

[83] N. L. Rangel, J. C. Sotelo, and J. M. Seminario, "Mechanism of carbon nanotubes unzipping into graphene ribbons," *J Chem Phys,* 2009, 131, 031105.

[84] N. L. Rangel and J. M. Seminario, "Vibronics and plasmonics based graphene sensors," *J Chem Phys,* 2010, 132, 125102.

[85] E. Katz and I. Willner, "Biomolecule-functionalized carbon nanotubes: applications in nanobioelectronics," *ChemPhysChem,* 2004, 5, 1084-1104.

[86] J. J. Davis, K. S. Coleman, B. R. Azamian, C. B. Bagshaw, and M. L. H. Green, "Chemical and biochemical sensing with modified single walled carbon nanotubes," *Chem Eur J,* 2003, 9, 3732-3739.

[87] K. Galatsis, K. L. Wang, M. Ozkan, C. S. Ozkan, Y. Huang, *et al.*, "Patterning and templating for nanoelectronics," *Adv Mater,* 2009, 22, 769-778.

[88] W. Lu and C. M. Lieber, "Nanoelectronics from the bottom up," *Nat Mater,* 2007, 6, 841-850.

[89] R. Martel, T. Schmidt, H. R. Shea, T. Hertel, and P. Avouris, "Single- and multi-wall carbon nanotube field-effect transistors," *Appl Phys Lett,* 1998, 73, 2447-2449.

[90] A. Bachtold, P. Hadley, T. Nakanishi, and C. Dekker, "Logic circuits with carbon nanotube transistors," *Science,* 2001, 294, 1317-1320.

[91] V. Sazonova, Y. Yaish, H. Ustunel, D. Roundy, T. A. Arias*, et al.*, "A tunable carbon nanotube electromechanical oscillator," *Nature,* 2004, 431, 284-287.

[92] P. Poncharal, Z. L. Wang, D. Ugarte, and W. A. de Heer, "Electrostatic deflections and electromechanical resonances of carbon nanotubes," *Science,* 1999, 283, 1513-1516.

[93] J. Chung, K.-H. Lee, J. Lee, and R. S. Ruoff, "Toward large-scale integration of carbon nanotubes," *Langmuir,* 2004, 20, 3011-3017.

[94] S. G. Rao, L. Huang, W. Setyawan, and S. Hong, "Nanotube electronics: large-scale assembly of carbon nanotubes," *Nature,* 2003, 425, 36-37.

[95] M. S. Strano, C. A. Dyke, M. L. Usrey, P. W. Barone, M. J. Allen*, et al.*, "Electronic structure control of single-walled carbon nanotube functionalization," *Science,* 2003, 301, 1519-1522.

[96] M. Burghard, "Electronic and vibrational properties of chemically modified single-wall carbon nanotubes," *Surf Sci Rep,* 2005, 58, 1-109.

[97] C. A. Dyke and J. M. Tour, "Covalent functionalization of single-walled carbon nanotubes for materials applications," *J Phys Chem A,* 2004, 108, 11151-11159.

[98] S. Banerjee, T. Hemraj-Benny, and S. S. Wong, "Covalent surface chemistry of single-walled carbon nanotubes," *Adv Mater,* 2005, 17, 17-29.

[99] J. M. Seminario, Y. Ma, and V. Tarigopula, "The nanocell: a chemically assembled molecular electronic circuit," *IEEE Sens,* 2006, 6, 1614-1626.

[100] A. J. Gimenez, G. Luna-Barcenas, and J. M. Seminario, "Analysis of nano and molecular arrays of negative differential resistance devices for sensing and electronics," *IEEE Sens,* 2009, 9, 1136-1141.

[101] D. Cristancho, L. Benitez, and J. Seminario, "Coupling of mechanical and electronic properties of carbon nanotubes," *J Mol Model,* 2013, 19, 5237-5244.

[102] N. L. Rangel and J. M. Seminario, "Single molecule detection using graphene molecules," *J Phys B,* 2010, 43, 155101.

[103] S. Meka and J. M. Seminario, "Single-electron transistor-tunable tunnel barrier based non-volatile memory," in *8th IEEE conference on nanotechnology*, Arlington, TX, 2008, 711-714.

[104] R. M. Tovar, K. P. Johnson, K. Ashline, and J. M. Seminario, "Effects of substituents on molecular devices," *Int J Quantum Chem,* 2008, 108, 1546-1554.

[105] Y. Liuming, J. B. Eddy, and M. S. Jorge, "Ab initio analysis of electron currents through benzene, naphthalene, and anthracene nanojunctions," *Nanotechnol,* 2007, 18, 485701.

[106] G. I. Cárdenas-Jirón, P. León-Plata, D. Cortes-Arriagada, and J. M. Seminario, "Electron transport properties through graphene oxide–cobalt phthalocyanine complexes," *J Phys Chem C,* 2013, 117, 23664-23675.

[107] N. Kumar and J. M. Seminario, "Design of nanosensors for fissile materials in nuclear waste water," *J Phys Chem C,* 2013, 117, 24033-24041.

[108] A. D. Bobadilla and J. M. Seminario, "Assembly of a noncovalent DNA junction on graphene sheets and electron transport characteristics," *J Phys Chem C,* 2013, 117, 26441-26453.

[109] R. H. Mathews, J. P. Sage, T. C. L. G. Sollner, S. D. Calawa, C. Chang-Lee*, et al.*, "A new RTD-FET logic family," *Proc IEEE,* 1999, 87, 596-605.

[110] E. Pop, D. Mann, J. Cao, Q. Wang, K. Goodson*, et al.*, "Negative differential conductance and hot phonons in suspended nanotube molecular wires," *Phys Rev Lett,* 2005, 95, 155505.

[111] M. inki , A. Johansson, V. otim ki, and P. i. T r m , "Negative differential resistance in carbon nanotube field-effect transistors with patterned gate oxide," *ACS Nano,* 2010, 4 (6), 3356–3362.

[112] F. Prins, A. Barreiro, J. W. Ruitenberg, J. S. Seldenthuis, N. Aliaga-Alcalde*, et al.*, "Room-temperature gating of molecular junctions using few-layer graphene nanogap electrodes," *Nano Lett,* 2011, 11, 4607-4611.

[113] M. J. Frisch, G. W. Trucks, H. B. Schlegel, G. E. Scuseria, M. A. Robb*, et al.*, "Gaussian 09, Revision B.01," ed. Wallingford CT, 2009.

[114] A. D. Becke, "Density-functional thermochemistry. III. The role of exact exchange," *J Chem Phys,* 1993, 98, 5648-5652.

[115] J. P. Perdew, J. A. Chevary, S. H. Vosko, K. A. Jackson, M. R. Pederson*, et al.*, "Atoms, molecules, solids, and surfaces: applications of the generalized gradient approximation for exchange and correlation," *Phys Rev B,* 1992, 46, 6671-6687.

[116] P. A. Derosa and J. M. Seminario, "Electron transport through single molecules: scattering treatment using density functional and green function theories," *J Phys Chem B,* 2000, 105, 471-481.

[117] L. A. Agapito, E. J. Bautista, and J. M. Seminario, "Conductance model of gold-molecule-silicon and carbon nanotube-molecule-silicon junctions," *Physical Review B,* 2007, 76, 115316.

[118] L. A. Jauregui, K. Salazar-Salinas, and J. M. Seminario, "Transverse electronic transport in double-stranded DNA nucleotides," *J Phys Chem B,* 2009, 113, 6230-6239.

[119] X. Tang, S. Bansaruntip, N. Nakayama, E. Yenilmez, Y.-l. Chang, *et al.*, "Carbon nanotube DNA sensor and sensing mechanism," *Nano Lett,* 2006, 6, 1632-1636.

[120] E. Pop, D. A. Mann, K. E. Goodson, and H. Dai, "Electrical and thermal transport in metallic single-wall carbon nanotubes on insulating substrates," *J Appl Phys,* 2007, 101, 093710.

[121] R. J. Chen, H. C. Choi, S. Bangsaruntip, E. Yenilmez, X. Tang, *et al.*, "An investigation of the mechanisms of electronic sensing of protein adsorption on carbon nanotube devices," *J Am Chem Soc,* 2004, 126, 1563-1568.

[122] V. Derycke, R. Martel, J. Appenzeller, and P. Avouris, "Controlling doping and carrier injection in carbon nanotube transistors," *Appl Phys Lett,* 2002, 80, 2773-2775.

[123] E. P. Bellido, A. D. Bobadilla, N. L. Rangel, H. Zhong, M. Norton, *et al.*, "Current-voltage-temperature characteristics of DNA origami," *Nanotechnol,* 2009, 20, 175102.

[124] J. A. Lin, D. Teweldebrhan, K. Ashraf, G. X. Liu, X. Y. Jing, *et al.*, "Gating of single-layer graphene with single-stranded deoxyribonucleic acids," *Small,* 2010, 6, 1150-1155.

[125] S. Hong, L. A. Jauregui, N. L. Rangel, H. Cao, S. Day, *et al.*, "Impedance measurements on a DNA junction," *J Chem Phys,* 2008, 128, 201103.

[126] A. D. Bobadilla, E. P. Bellido, N. L. Rangel, H. Zhong, M. Norton, *et al.*, "DNA origami impedance measurement at room temperature," *J Chem Phys,* 2009, 130, 171101.

[127] N. L. Rangel and J. M. Seminario, "Vibronics and Plasmonics Based Graphene Sensors," *J. Chem. Phys.,* 2010, 132, 125102.

[128] D. Christancho and J. M. Seminario, "Polypeptides in alpha-helix conformation perform as diodes," *J Chem Phys,* 2010, 132, 065102.

[129] N. L. Rangel, J. C. Sotelo, and J. M. Seminario, "Mechanism of carbon-nanotubes unzipping into graphene ribbons," *J Chem Phys,* 2009, 131, 031105.

[130] N. L. Rangel and J. M. Seminario, "Nano-micro interface to read molecular potentials into current-voltage based electronics," *J Chem Phys,* 2008, 128, 114711

[131] J. M. Seminario, R. A. Araujo, and L. Yan, "Negative differential resistance in metallic and semiconducting clusters," *J Phys Chem B,* 2004, 108, 6915-6918.

[132] P. A. Derosa, S. Guda, and J. M. Seminario, "A programmable molecular diode driven by charge-induced conformational changes," *J Am Chem Soc,* 2003, 125, 14240-14241.

[133] J. M. Seminario, C. De La Cruz, P. A. Derosa, and L. Yan, "Nanometer-size conducting and insulating molecular devices," *J Phys Chem B,* 2004, 108, 17879-17885.

[134] C. Staii, A. T. Johnson, M. Chen, and A. Gelperin, "DNA-decorated carbon nanotubes for chemical sensing," *Nano Lett,* 2005, 5, 1774-1778.

[135] C. L. Chen, C. F. Yang, V. Agarwal, T. Kim, S. Sonkusale*, et al.*, "DNA-decorated carbon-nanotube-based chemical sensors on complementary metal oxide semiconductor circuitry," *Nanotechnol,* 2010, 21, 095504.

[136] G. Lu, P. Maragakis, and E. Kaxiras, "Carbon nanotube interaction with DNA," *Nano Letters,* 2005, 5, 897-900.

[137] S. Meng and E. Kaxiras, "Interaction of DNA with CNTs: properties and prospects for electronic sequencing," in *Biosensing using nanomaterials*, A. Merkoci, Ed., 1st ed: Wiley-Interscience, 2009, 67-96.

[138] K. Wang, N. L. Rangel, S. Kundu, J. C. Sotelo, R. M. Tovar*, et al.*, "Switchable molecular conductivity," *J Am Chem Soc,* 2009, 131, 10447-10451.

[139] N. L. Rangel, K. S. Williams, and J. M. Seminario, "Light-activated molecular conductivity in the photoreactions of vitamin D_3," *J Phys Chem A,* 2009, 113, 6740-6744.

[140] L. A. Jauregui, K. Salazar-Salinas, and J. M. Seminario, "Transverse Electronic Transport in Double-Stranded DNA Nucleotides," *J. Phys. Chem. B,* 2009, 113, 6230-6239.

[141] A. J. Gimenez, G. Luna-Bárcenas, and J. M. Seminario, "Emulation of molecular programmability using microelectronic programmable devices," *J Phys Chem C,* 2009, 36, 16254 - 16258.

[142] A. J. Gimenez, G. Luna-Barcenas, and J. M. Seminario, "Analysis of Nano and Molecular Arrays of Negative Differential Resistance Devices for Sensing and Electronics," *IEEE Sensors,* 2009, 9, No 9.

[143] N. L. Rangel and J. M. Seminario, "Graphene terahertz generators for molecular circuits and sensors," *J Phys Chem A,* 2008, 112, 13699-13705.

[144] L. A. Juarregui and J. M. Seminario, "A DNA sensor for sequencing and mismatches based on electron transport through Watson-Crick and non-Watson-Crick base pairs," *IEEE Sens J,* 2008, 8, 803-814.

[145] R. R. Johnson, A. T. C. Johnson, and M. L. Klein, "Probing the structure of DNA−carbon nanotube hybrids with molecular dynamics," *Nano Lett,* 2008, 8, 69-75.

[146] S. Plimpton, "Fast parallel algorithms for short-range molecular dynamics," *J Comput Phys,* 1995, 117, 1-19.

[147] W. L. Jorgensen, J. Chandrasekhar, J. D. Madura, R. W. Impey, and M. L. Klein, "Comparison of simple potential functions for simulating liquid water," *J Chem Phys,* 1983, 79, 926-935.

[148] A. D. MacKerell, D. Bashford, Bellott, R. L. Dunbrack, J. D. Evanseck*, et al.*, "All-atom empirical potential for molecular modeling and dynamics studies of proteins," *J Phys Chem B,* 1998, 102, 3586-3616.

[149] L. Martínez, R. Andrade, E. G. Birgin, and J. M. Martínez, "PACKMOL: a package for building initial configurations for molecular dynamics simulations," *J Comput Chem,* 2009, 30, 2157-2164.

[150] R. W. Hockney and J. W. Eastwood, *Computer simulation using particles*. New York: Taylor & Francis, Inc., 1988.

[151] H. J. C. Berendsen, J. P. M. Postma, W. F. Vangunsteren, A. Dinola, and J. R. Haak, "Molecular dynamics with coupling to an external bath," *J Chem Phys,* 1984, 81, 3684-3690.

[152] W. Humphrey, A. Dalke, and K. Schulten, "VMD: visual molecular dynamics," *J Mol Graphics,* 1996, 14, 33-38.

[153] B. R. Brooks, R. E. Bruccoleri, B. D. Olafson, D. J. States, S. Swaminathan*, et al.*, "CHARMM: A program for macromolecular energy, minimization, and dynamics calculations," *J Comput Chem,* 1983, 4, 187-217.

[154] S. Miertus, E. Scrocco, and J. Tomasi, "Electrostatic interaction of a solute with a continuum. A direct utilizaion of AB initio molecular potentials for the prevision of solvent effects," *Chem Phys,* 1981, 55, 117-129.

[155] S. V. Rotkin, "Electronic properties of nonideal nanotube materials: helical symmetry breaking in DNA hybrids," in *Annual review of physical chemistry, vol 61*, ed Palo Alto: Annual Reviews, 2010, 61, 241-261.

[156] E. Katz and I. Willner, "Biomolecule-Functionalized Carbon Nanotubes: Applications in Nanobioelectronics," *Chem. Phys. Chem.,* 2004, 5, 1084-1104.

[157] F. Bergeron, D. Houde, D. J. Hunting, and J. R. Wagner, "Electron transfer in DNA duplexes containing 2-methyl-1,4-naphthoquinone," *Nucl Acids Res,* 2004, 32, 6154-6163.

[158] D. L. Woolard, T. R. Globus, B. L. Gelmont, M. Bykhovskaia, A. C. Samuels*, et al.*, "Submilimeter-wave phonon modes in DNA macromolecules," *Phys Rev E,* 2002, 65, 051903.

[159] B. M. Fischer, M. Walther, and P. U. Jepsen, "Far-infrared vibrational modes of DNA components studied by terahertz time-domain spectroscopy," *Phys Med Biol,* 2002, 47, 3807-3814.

[160] M. Bixon and J. Jortner, "Charge transport in DNA via thermally induced hopping," *J Am Chem Soc,* 2001, 123, 12556-12567.

[161] B. Szafran, J. Adamowski, and S. Bednarek, "Single-electron charging of self assembled quantum dots," *Thin Solid Films,* 2000, 367, 93-96.

[162] D. Porath, A. Bezryadin, S. d. Vries, and C. Dekker, "Direct measurement of electrical transport through DNA molecules,," *Nature,* 2000, 403, 635-638.

[163] D. Porath, A. Bezryadin, S. de Vries, and C. Dekker, "Direct measurement of electrical transport through DNA molecules," *Nature,* 2000, 403, 635-638.

[164] J. J. Storhoff and C. A. Mirkin, "Programmed materials synthesis with DNA," *Chem Rev,* 1999, 99, 1849-1862.

[165] S. W. Davies, M. Eizenman, and S. Pasupathy, "Optimal structure for automatic processing of DNA sequences," *IEEE T Bio-Med Eng,* 1999, 46, 1044-56.

[166] K. Fukui and K. Tanaka, "Distance dependence of photoinduced electron transfer in DNA," *Angew Chem Int Edit,* 1998, 37, 158-161.

[167] D. A. Smith, C. W. Ulmer II, and M. J. Gilbert, "Structural studies of aromatic amines and the DNA intercalating compounds m-amsa and o-amsa: comparison of MNDO, AM1, and PM3 to experimental and ab initio results," *J Comput Chem,* 1992, 13, 640-650.

[168] T. Takada, K. Kawai, M. Fujitsuka, and T. Majima, "Direct observation of hole transfer through double-helical DNA over 100 Å," *P Natl Acad Sci USA,* 2004, 101, 14002-14006.

[169] A. D. Bobadilla, E. P. Bellido, and J. M. Seminario, "Transmission of vibrational signals through a CNT-DNA interface," in *Nanoelectronic devices for defense and security*, Bahia Mar Beach Resort, Fort Lauderdale, Florida, 2009,

[170] L. A. Jauregui and S. J. M., "Transversal characteristics of DNA devices," presented at the 8th IEEE conference on nanotechnology, Arlington, TX, 2008, 725-728.

[171] H. v. Zalinge, D. J. Schiffrin, A. D. Bates, E. B. Starikov, W. Wenzel, *et al.*, "Variable-temperature measurements of the single-molecule conductance of double-stranded DNA," *Angew Chem Int Edit,* 2006, 45, 5499-5502.

[172] R. Marches, P. Chakravarty, I. H. Musselman, P. Bajaj, R. N. Azad, *et al.*, "Specific thermal ablation of tumor cells using single-walled carbon nanotubes targeted by covalently-coupled monoclonal antibodies," *Int J Cancer,* 2009, 125, 2970-2977.

[173] L. A. Agapito, E. J. Bautista, and J. M. Seminario, "Conductance model of gold-molecule-silicon and carbon nanotube-molecule-silicon junctions," *Phys. Rev. B,* 2007, 76, 115316 1-12.

[174] J. M. Tour, "Functionalization of carbon nanotubes," *Abstr Pap Am Chem S,* 2004, 227, U265.

[175] G. C. Liang, A. W. Ghosh, M. Paulsson, and S. Datta, "Electrostatic potential profiles of molecular conductors," *Phys Rev B,* 2004, 69, 115302.

[176] P. G. Collins and P. Avouris, "Nanotubes for electronics," *Sci Am,* 2000, 283, 62-69.

[177] T. W. Odom, J.-L. Huang, P. Kim, and C. M. Lieber, "Atomic structure and electronic properties of single-walled carbon nanotubes," *Science,* 1998, 391, 62.

[178] S. J. Tans, M. H. Devoret, H. Dai, A. Thess, S. Richard E, *et al.*, "Individual single-wall carbon nanotubes," *Nature,* 1997, 386, 474-477.

[179] M. Bockrath, D. H. Cobden, P. L. McEuen, N. G. Chopra, A. Zettl, *et al.*, "Single-electron transport in ropes of carbon nanotubes," *Science,* 1977, 275, 1922-1925.

[180] B. F. Pan, D. X. Cui, P. Xu, H. Chen, F. T. Liu, *et al.*, "Design of dendrimer modified carbon nanotubes for gene delivery," *Chin J Cancer Res,* 2007, 19, 1-6.

[181] P. W. K. Rothemund, "Folding DNA to create nanoscale shapes and patterns," *Nature,* 2006, 440, 297-302.

[182] I. Otero-Navas and J. M. Seminario, "Molecular electrostatic potentials of DNA base-base pairing and mispairing," *J Mol Modeling,* 2012, 18, 91-101.

[183] A. Kuzyk, B. Yurke, J. J. Toppari, V. Linko, and P. Törmä, "Dielectrophoretic trapping of DNA origami," *Small,* 2008, 4, 447-450.

[184] V. Linko, S.-T. Paasonen, A. Kuzyk, P. Törmä, and J. J. Toppari, "Characterization of the conductance mechanisms of DNA origami by AC impedance spectroscopy," *Small,* 2009, 5, 2382-2386.

[185] X. Tu, S. Manohar, A. Jagota, and M. Zheng, "DNA sequence motifs for structure-specific recognition and separation of carbon nanotubes," *Nature,* 2009, 460, 250-253.

[186] S.-P. Germarie and et al., "DNA-mediated self-assembly of carbon nanotubes on gold," *J Phys Conf Ser,* 2007, 61, 1017.

[187] S. Li, P. He, J. Dong, Z. Guo, and L. Dai, "DNA-directed self-assembling of carbon nanotubes," *J Am Chem Soc,* 2004, 127, 14-15.

[188] Y. Li, X. Han, and Z. Deng, "Grafting single-walled carbon nanotubes with highly hybridizable DNA sequences: potential building blocks for DNA-programmed material assembly," *Angew Chem Int Edit,* 2007, 46, 7481-7484.

[189] J. M. Seminario and L. Yan, "Ab initio analysis of electron currents in thioalkanes," *Int J Quantum Chem,* 2005, 102, 711-723.

[190] J. M. Seminario, P. A. Derosa, L. E. Cordova, and B. H. Bozard, "A molecular device operating at terahertz frequencies," *IEEE Trans Nanotech,* 2004, 3, 215-218.

[191] J. M. Seminario, L. Yan, and Y. Ma, "Scenarios for molecular-level signal processing," *Proc IEEE,* 2005, 93, 1753-1764.

[192] R. R. Johnson, A. Kohlmeyer, A. T. C. Johnson, and M. L. Klein, "Free energy landscape of a DNA−carbon nanotube hybrid using replica exchange molecular dynamics," *Nano Lett,* 2009, 9, 537-541.

[193] M. Zheng, A. Jagota, M. S. Strano, A. P. Santos, P. Barone*, et al.*, "Structure-based carbon nanotube sorting by sequence-dependent DNA assembly," *Science,* 2003, 302, 1545-1548.

[194] S. K. Min, W. Y. Kim, Y. Cho, and K. S. Kim, "Fast DNA sequencing with a graphene-based nanochannel device," *Nat Nanotechnol,* 2011, 6, 162-165.

[195] C. A. Merchant, K. Healy, M. Wanunu, V. Ray, N. Peterman*, et al.*, "DNA translocation through graphene nanopores," *Nano Lett,* 2010, 10, 2915-2921.

[196] Y. Lin, S. Taylor, H. P. Li, K. A. S. Fernando, L. W. Qu*, et al.*, "Advances toward bioapplications of carbon nanotubes," *J Mater Chem,* 2004, 14, 527-541.

[197] C. H. Lu, H. H. Yang, C. L. Zhu, X. Chen, and G. N. Chen, "A graphene platform for sensing biomolecules," *Angew Chem Int Edit,* 2009, 48, 4785-4787.

[198] C. T. Lin, P. T. K. Loan, T. Y. Chen, K. K. Liu, C. H. Chen*, et al.*, "Label-free electrical detection of DNA hybridization on graphene using hall effect measurements: revisiting the sensing mechanism," *Adv Funct Mater,* 2013, 23, 2301-2307.

[199] J. Chen, Y. Huang, M. Shi, S. L. Zhao, and Y. C. Zhao, "Highly sensitive multiplexed DNA detection using multi-walled carbon nanotube-based multicolor nanobeacon," *Talanta,* 2013, 109, 160-166.

[200] W. Wei, D. M. Zhang, L. H. Yin, Y. P. Pu, and S. Q. Liu, "Colorimetric detection of DNA damage by using hemin-graphene nanocomposites," *Spectrochim Acta A,* 2013, 106, 163-169.

[201] B. R. Novak, D. Moldovan, D. E. Nikitopoulos, and S. A. Soper, "Distinguishing single DNA nucleotides based on their times of flight through nanoslits: a molecular dynamics simulation study," *J Phys Chem B,* 2013, 117, 3271-3279.

[202] H. W. C. Postma, "Rapid sequencing of individual DNA molecules in graphene nanogaps," *Nano Lett,* 2010, 10, 420-425.

[203] X. C. Dong, Y. M. Shi, W. Huang, P. Chen, and L. J. Li, "Electrical detection of DNA hybridization with single-base specificity using transistors based on CVD-grown graphene sheets," *Adv Mater,* 2010, 22, 1649-1653.

[204] G. F. Schneider, S. W. Kowalczyk, V. E. Calado, G. Pandraud, H. W. Zandbergen, *et al.*, "DNA translocation through graphene nanopores," *Nano Lett,* 2010, 10, 3163-3167.

[205] S. J. He, B. Song, D. Li, C. F. Zhu, W. P. Qi, *et al.*, "A graphene nanoprobe for rapid, sensitive, and multicolor fluorescent DNA analysis," *Adv Funct Mater,* 2010, 20, 453-459.

[206] T. Y. Chen, T. K. L. Phan, C. L. Hsu, Y. H. Lee, J. T. W. Wang, *et al.*, "Label-free detection of DNA hybridization using transistors based on CVD grown graphene," *Biosens Bioelectron,* 2013, 41, 103-109.

[207] X. Guo, A. A. Gorodetsky, J. Hone, J. K. Barton, and C. Nuckolls, "Conductivity of a single DNA duplex bridging a carbon nanotube gap," *Nat. Nano,* 2008, 3, 163-167.

[208] J. D. Slinker, N. B. Muren, S. E. Renfrew, and J. K. Barton, "DNA charge transport over 34 nm," *Nat Chem,* 2011, 3, 228-233.

[209] A. A. Gorodetsky, M. C. Buzzeo, and J. K. Barton, "DNA-mediated electrochemistry," *Bioconjugate Chem,* 2008, 19, 2285-2296.

[210] D. Branton, D. W. Deamer, A. Marziali, H. Bayley, S. A. Benner, *et al.*, "The potential and challenges of nanopore sequencing," *Nat Biotech,* 2008, 26, 1146-1153.

[211] S. W. Kowalczyk, M. W. Tuijtel, S. P. Donkers, and C. Dekker, "Unraveling single-stranded DNA in a solid-state nanopore," *Nano Lett,* 2010, 10, 1414-1420.

[212] D. Fologea, M. Gershow, B. Ledden, D. S. McNabb, J. A. Golovchenko, *et al.*, "Detecting single stranded DNA with a solid state nanopore," *Nano Lett,* 2005, 5, 1905-1909.

[213] D. C. Bell, M. C. Lemme, L. A. Stern, J. R. Williams, and C. M. Marcus, "Precision cutting and patterning of graphene with helium ions," *Nanotechnol.,* 2009, 20, 455301.

[214] X. Wang and H. Dai, "Etching and narrowing of graphene from the edges," *Nat Chem,* 2010, 2, 661-665.

[215] D. V. Kosynkin, A. L. Higginbotham, A. Sinitskii, J. R. Lomeda, A. Dimiev, *et al.*, "Longitudinal unzipping of carbon nanotubes to form graphene nanoribbons," *Nature,* 2009, 458, 872-876.

[216] L. Jiao, X. Wang, G. Diankov, H. Wang, and H. Dai, "Facile synthesis of high-quality graphene nanoribbons," *Nat Nano,* 2010, 5, 321-325.

[217] L. Jiao, L. Zhang, X. Wang, G. Diankov, and H. Dai, "Narrow graphene nanoribbons from carbon nanotubes," *Nature,* 2009, 458, 877-880.

[218] M. Y. Han, B. Özyilmaz, Y. Zhang, and P. Kim, "Energy band-gap engineering of graphene nanoribbons," *Phys Rev Lett,* 2007, 98, 206805.

[219] D. Wei, Y. Liu, L. Cao, Y. Wang, H. Zhang, *et al.*, "Real time and in situ control of the gap size of nanoelectrodes for molecular devices," *Nano Lett,* 2008, 8, 1625-1630.

[220] J. Lin, D. Teweldebrhan, K. Ashraf, G. Liu, X. Jing, *et al.*, "Gating of single-layer graphene with single-stranded deoxyribonucleic acids," *Small,* 2010, 6, 1150-1155.

[221] X. Dong, Y. Shi, W. Huang, P. Chen, and L.-J. Li, "Electrical detection of DNA hybridization with single-base specificity using transistors based on CVD-grown graphene sheets," *Adv Mater,* 2010, 22, 1649-1653.

[222] C.-T. Lin, P. T. K. Loan, T.-Y. Chen, K.-K. Liu, C.-H. Chen, *et al.*, "Label-free electrical detection of DNA hybridization on graphene using hall effect measurements: revisiting the sensing mechanism," *Adv Funct Mater,* 2013, 23, 2301-2307.

[223] F. Yavari, C. Kritzinger, C. Gaire, L. Song, H. Gulapalli, *et al.*, "Tunable bandgap in graphene by the controlled adsorption of water molecules," *Small,* 2010, 6, 2535-2538.

[224] A. D. Bobadilla and J. M. Seminario, "DNA−CNT Interactions and Gating Mechanism Using MD and DFT," *J. Phys. Chem. C,* 2011, 115, 3466-3474.

[225] V. I. Puller and S. V. Rotkin, "Helicity and broken symmetry of DNA-nanotube hybrids," *Europhys Lett,* 2007, 77, 27006.

[226] Y. Wang, "Theoretical evidence for the stronger ability of thymine to disperse SWCNT than cytosine and adenine: self-stacking of DNA bases vs their cross-stacking with SWCNT," *J Phys Chem C,* 2008, 112, 14297-14305.

[227] J.-H. Lee, Y.-K. Choi, H.-J. Kim, R. H. Scheicher, and J.-H. Cho, "Physisorption of DNA nucleobases on h-BN and graphene: vdW-corrected DFT calculations," *J Phys Chem C,* 2013, 117, 13435-13441.

[228] L. Martínez, R. Andrade, E. G. Birgin, and J. M. Martínez, "PACKMOL: A package for building initial configurations for molecular dynamics simulations," *J. Comput. Chem.,* 2009, 30, 2157-2164.

[229] E. Polak and G. Ribiere, "Note sur la convergence de méthodes de directions conjuguées," *Rev Fr Inform Rech Ope,* 1969, 3, 35-43.

[230] B. R. Brooks, R. E. Bruccoleri, B. D. Olafson, D. J. States, S. Swaminathan, *et al.*, "CHARMM: A program for macromolecular energy, minimization, and dynamics calculations," *J. Comput. Chem.,* 1983, 4, 187-217.

[231] H. C. Andersen, "Molecular dynamics simulations at constant pressure and/or temperature," *J Chem Phys,* 1980, 72, 2384-2393.

[232] S. Nosé, "A molecular dynamics method for simulations in the canonical ensemble," *Mol Phys,* 1984, 52, 255-268.

[233] S. Nose, "A unified formulation of the constant temperature molecular dynamics methods," *J Chem Phys,* 1984, 81, 511-519.

[234] W. G. Hoover, "Canonical dynamics: equilibrium phase-space distributions," *Phys Rev A,* 1985, 31, 1695-1697.

[235] W. Shinoda, M. Shiga, and M. Mikami, "Rapid estimation of elastic constants by molecular dynamics simulation under constant stress," *Phys Rev B,* 2004, 69, 134103.

[236] E. T. Mark, A. José, L.-R. Roberto, L. J. Andrea, and J. M. Glenn, "A Liouville-operator derived measure-preserving integrator for molecular dynamics simulations in the isothermal–isobaric ensemble," *J Phys A-Math Gen,* 2006, 39, 5629.

[237] J. W. Eastwood, R. W. Hockney, and D. N. Lawrence, "P3M3DP-the three-dimensional periodic particle-particle/particle-mesh program," *Comput Phys Commun,* 1980, 19, 215-261.

[238] R. W. Hockney, S. P. Goel, and J. W. Eastwood, "A 10000 particle molecular dynamics model with long range forces," *Chem Phys Lett,* 1973, 21, 589-591.

[239] W. Humphrey, "VMD: visual molecular dynamics," *J Mol Graphics,* 1996, 14, 33-38.

[240] W. Kohn and L. J. Sham, "Self-consistent equations including exchange and correlation effects," *Phys Rev,* 1965, 140, A1133.

[241] P. A. Derosa and J. M. Seminario, "Electron Transport through Single Molecules: Scattering Treatment Using Density Functional and Green Function Theories," *J. Phys. Chem. B,* 2000, 105, 471-481.

[242] L. A. Agapito, E. J. Bautista, and J. M. Seminario, "Conductance model of gold-molecule-silicon and carbon nanotube-molecule-silicon junctions," *Phys. Rev. B,* 2007, 76, 115316.

[243] C. Roetti, "The CRYSTAL code," in *Quantum-mechanical ab-initio calculation of the properties of crystalline materials*, C. Pisani, Ed., ed Berlin: Springer-Verlag, 1996.

[244] A. D. Becke, "Density-functional thermochemistry. III. The role of exact exchange," *J. Chem. Phys.,* 1993, 98, 5648-5652.

[245] J. P. Perdew, J. A. Chevary, S. H. Vosko, K. A. Jackson, M. R. Pederson*, et al.*, "Atoms, molecules, solids, and surfaces: Applications of the generalized gradient approximation for exchange and correlation," *Phys. Rev. B,* 1992, 46, 6671-6687.

[246] Y. Zhao and D. Truhlar, "The M06 suite of density functionals for main group thermochemistry, thermochemical kinetics, noncovalent interactions, excited states, and transition elements: two new functionals and systematic testing of four M06-class functionals and 12 other functionals," *Theor Chem Acc,* 2008, 120, 215-241.

[247] D. Umadevi and G. N. Sastry, "Quantum mechanical study of physisorption of nucleobases on carbon materials: graphene versus carbon nanotubes," *J Phys Chem Lett,* 2011, 2, 1572-1576.

[248] H. Xiao, J. Tahir-Kheli, and W. A. Goddard, "Accurate band gaps for semiconductors from density functional theory," *J Phys Chem Lett,* 2011, 2, 212-217.

[249] G. I. Csonka, A. D. French, G. P. Johnson, and C. A. Stortz, "Evaluation of density functionals and basis sets for carbohydrates," *J Chem Theory Comput,* 2009, 5, 679-692.

[250] J. M. Seminario, C. E. De La Cruz, and P. A. Derosa, "A theoretical analysis of metal-molecule contacts," *J Am Chem Soc,* 2001, 123, 5616-5617.

[251] J. Seminario and J. Tour, "Density functional theory for the study of single-molecule electronic systems," in *Electron correlations and materials properties*, A. Gonis*, et al.*, Eds., ed: Springer US, 1999, 439-450.

[252] P. J. Hay and W. R. Wadt, "Ab initio effective core potentials for molecular calculations. Potentials for K to Au including the outermost core orbitals," *J Chem Phys,* 1985, 82, 299-310.

[253] G. A. Petersson, A. Bennett, T. G. Tensfeldt, M. A. Al-Laham, W. A. Shirley, *et al.*, "A complete basis set model chemistry. I. The total energies of closed-shell atoms and hydrides of the first-row elements," *J Chem Phys,* 1988, 89, 2193-2218.

[254] G. A. Petersson and M. A. Al-Laham, "A complete basis set model chemistry. II. open-shell systems and the total energies of the first-row atoms," *J Chem Phys,* 1991, 94, 6081-6090.

[255] W. R. Wadt and P. J. Hay, "Ab initio effective core potentials for molecular calculations. Potentials for main group elements Na to Bi," *J Chem Phys,* 1985, 82, 284-298.

[256] P. J. Hay and W. R. Wadt, "Ab initio effective core potentials for molecular calculations. Potentials for the transition metal atoms Sc to Hg," *J Chem Phys,* 1985, 82, 270-283.

[257] E. G. Hohenstein, S. T. Chill, and C. D. Sherrill, "Assessment of the performance of the M05−2X and M06−2X exchange-correlation functionals for noncovalent interactions in biomolecules," *J Chem Theory Comput,* 2008, 4, 1996-2000.

[258] J. M. Seminario, L. A. Agapito, L. Yan, and P. B. Balbuena, "Density functional theory study of adsorption of OOH on Pt-based bimetallic clusters alloyed with Cr, Co, and Ni," *Chem Phys Lett,* 2005, 410, 275-281.

[259] J. M. Seminario and J. M. Tour, "Systematic study of the lowest energy states of Au_n (n=1-4) using DFT," *Int J Quantum Chem,* 1997, 65, 749-758.

[260] J. M. Seminario, A. G. Zacarias, and M. Castro, "Systematic study of the lowest energy states of Pd, Pd_2, and Pd_3," *Int J Quantum Chem,* 1997, 61, 515-523.

[261] W. M. H. Sachtler, G. J. H. Dorgelo, and A. A. Holscher, "The work function of gold," *Surf Sci,* 1966, 5, 221-229.

[262] J. M. Seminario, A. G. Zacarias, and P. A. Derosa, "Theoretical analysis of complementary molecular memory devices," *J Phys Chem A,* 2000, 105, 791-795.

[263] J. M. Seminario and L. Yan, "Ab initio analysis of electron currents in thioalkanes," *Int. J. Quantum Chem.,* 2005, 102, 711-723.

[264] M. Bottini, N. Rosato, and N. Bottini, "PEG-modified carbon nanotubes in biomedicine: current status and challenges ahead," *Biomacromolecules,* 2011, 12, 3381-3393.

[265] E. Heister, V. Neves, C. Lamprecht, S. R. P. Silva, H. M. Coley*, et al.*, "Drug loading, dispersion stability, and therapeutic efficacy in targeted drug delivery with carbon nanotubes," *Carbon,* 2012, 50, 622-632.

[266] H. Jin, D. A. Heller, R. Sharma, and M. S. Strano, "Size-dependent cellular uptake and expulsion of single-walled carbon nanotubes: single particle tracking and a generic uptake model for nanoparticles," *ACS Nano,* 2009, 3, 149-158.

[267] Z. Chen, K. Kobashi, U. Rauwald, R. Booker, H. Fan*, et al.*, "Soluble ultra-short single-walled carbon nanotubes," *J Am Chem Soc,* 2006, 128, 10568-10571.

[268] B. K. Price, J. R. Lomeda, and J. M. Tour, "Aggressively oxidized ultra-short single-walled carbon nanotubes having oxidized sidewalls," *Chem Mater,* 2009, 21, 3917-3923.

[269] J. J. Stephenson, J. L. Hudson, A. D. Leonard, B. K. Price, and J. M. Tour, "Repetitive functionalization of water-soluble single-walled carbon nanotubes. Addition of acid-sensitive addends," *Chem Mater,* 2007, 19, 3491-3498.

[270] J. M. Berlin, A. D. Leonard, T. T. Pham, D. Sano, D. C. Marcano, *et al.*, "Effective drug delivery, in vitro and in vivo, by carbon-based nanovectors noncovalently loaded with unmodified paclitaxel," *ACS Nano,* 2010, 4, 4621-4636.

[271] D. Sano, J. M. Berlin, T. T. Pham, D. C. Marcano, D. R. Valdecanas, *et al.*, "Noncovalent assembly of targeted carbon nanovectors enables synergistic drug and radiation cancer therapy in vivo," *ACS Nano,* 2012, 6, 2497-2505.

[272] M. A. Sharpe, D. C. Marcano, J. M. Berlin, M. A. Widmayer, D. S. Baskin, *et al.*, "Antibody-targeted nanovectors for the treatment of brain cancers," *ACS Nano,* 2012, 6, 3114-3120.

[273] J. Cheng, K. A. S. Fernando, L. M. Veca, Y.-P. Sun, A. I. Lamond, *et al.*, "Reversible accumulation of PEGylated single-walled carbon nanotubes in the mammalian nucleus," *ACS Nano,* 2008, 2, 2085-2094.

[274] P. Zhang and D. B. Henthorn, "Synthesis of PEGylated single wall carbon nanotubes by a photoinitiated graft from polymerization," *AIChE J,* 2010, 56, 1610-1615.

[275] H. Nie, W. Guo, Y. Yuan, Z. Dou, Z. Shi, *et al.*, "PEGylation of double-walled carbon nanotubes for increasing their solubility in water," *Nano Res,* 2010, 3, 103-109.

[276] L. Di, E. H. Kerns, S. Q. Li, and S. L. Petusky, "High throughput microsomal stability assay for insoluble compounds," *Int J Pharm,* 2006, 317, 54-60.

[277] C. A. Lipinski, "Drug-like properties and the causes of poor solubility and poor permeability," *J Pharmacol Toxicol,* 2000, 44, 235-249.

[278] G. Hummer, J. C. Rasaiah, and J. P. Noworyta, "Water conduction through the hydrophobic channel of a carbon nanotube," *Nature,* 2001, 414, 188-190.

[279] L. Chee Leng, L. Hui Qi, T. Hui Ru, and L. Ye, "Delivery of paclitaxel by physically loading onto poly(ethylene glycol) (PEG)-graftcarbon nanotubes for potent cancer therapeutics," *Nanotechnol,* 2010, 21, 065101.

[280] M. T. D. Cronin, "The role of hydrophobicity in toxicity prediction," *Curr Comput-Aid Drug,* 2006, 2, 405-413.

[281] D. F. Moyano, M. Goldsmith, D. J. Solfiell, D. Landesman-Milo, O. R. Miranda, *et al.*, "Nanoparticle hydrophobicity dictates immune response," *J Am Chem Soc,* 2012, 134, 3965-3967.

[282] F. M. Veronese and G. Pasut, "PEGylation, successful approach to drug delivery," *Drug Discov Today,* 2005, 10, 1451-1458.

[283] E. P. Bellido and J. M. Seminario, "Molecular dynamics simulations of folding of supported graphene," *J Phys Chem C,* 2010, 114, 22472-22477.

[284] N. L. Rangel, J. C. Sotelo, and J. M. Seminario, "Mechanism of carbon nanotubes unzipping into graphene ribbons," *J Chem Phys,* 2009, 131, 031105-4.

[285] D. Borhani and D. Shaw, "The future of molecular dynamics simulations in drug discovery," *J Comput-Aided Mol Des,* 2012, 26, 15-26.

[286] Y. Li and T. Hou, "Computational simulation of drug delivery at molecular level," *Curr Med Chem,* 2010, 17, 4482-4491.

[287] P. F. Salazar and J. M. Seminario, "Identifying receptor−ligand interactions through an ab initio approach," *J Phys Chem B,* 2008, 112, 1290-1292.

[288] B. C. Johnson, M. Metifiot, Y. Pommier, and S. H. Hughes, "Molecular dynamics approaches estimate the binding energy of HIV-1 integrase inhibitors and correlate with in vitro activity," *Antimicrob Agents Ch,* 2012, 56, 411-419.

[289] J. Åqvist, V. B. Luzhkov, and B. O. Brandsdal, "Ligand binding affinities from MD simulations," *Accounts Chem Res,* 2002, 35, 358-365.

[290] J. D. Durrant and J. A. McCammon, "Molecular dynamics simulations and drug discovery," *BMC Biol,* 2011, 9, 71.

[291] N. Foloppe and J. A. D. MacKerell, "All-atom empirical force field for nucleic acids: I. Parameter optimization based on small molecule and condensed phase macromolecular target data," *J Comput Chem,* 2000, 21, 86-104.

[292] S. E. Feller and A. D. MacKerell, "An improved empirical potential energy function for molecular simulations of phospholipids," *J Phys Chem B,* 2000, 104, 7510-7515.

[293] I. Vorobyov, V. M. Anisimov, S. Greene, R. M. Venable, A. Moser, *et al.*, "Additive and classical drude polarizable force fields for linear and cyclic ethers," *J Chem Theory Comput,* 2007, 3, 1120-1133.

[294] M. L. Mayo, Z. Q. Chen, and S. V. Kilina, "Computational studies of nucleotide selectivity in DNA–carbon nanotube hybrids," *J Phys Chem Lett,* 2012, 3, 2790-2797.

[295] A. o. Furmanchuk, J. Leszczynski, S. Tretiak, and S. V. Kilina, "Morphology and optical response of carbon nanotubes functionalized by conjugated polymers," *J Phys Chem C,* 2012, 116, 6831-6840.

[296] D. A. Yarotski, S. V. Kilina, A. A. Talin, S. Tretiak, O. V. Prezhdo, *et al.*, "Scanning tunneling microscopy of DNA-wrapped carbon nanotubes," *Nano Lett,* 2008, 9, 12-17.

[297] K. Vanommeslaeghe, E. Hatcher, C. Acharya, S. Kundu, S. Zhong, *et al.*, "CHARMM general force field: a force field for drug-like molecules compatible

with the CHARMM all-atom additive biological force fields," *J Comput Chem,* 2010, 31, 671-690.

[298] H. Lee, R. M. Venable, A. D. MacKerell, and R. W. Pastor, "Molecular dynamics studies of polyethylene oxide and polyethylene glycol: hydrodynamic radius and shape anisotropy," *Biophys J,* 2008, 95, 1590-1599.

[299] K. Tasaki, "Poly(oxyethylene)–cation interactions in aqueous solution: a molecular dynamics study," *Comput Theor Polym S,* 1999, 9, 271-284.

[300] B.-D. Huang, Y.-Y. Xia, M.-W. Zhao, F. Li, X.-D. Liu, *et al.*, "Single-walled carbon nanotubes acting as controllable transport channels," *Chinese Phys Lett,* 2004, 21, 2388.

[301] W. H. Noon, K. D. Ausman, R. E. Smalley, and J. Ma, "Helical ice-sheets inside carbon nanotubes in the physiological condition," *Chem Phys Lett,* 2002, 355, 445-448.

[302] C. Y. Guo, B. Montgomery Pettitt, and L. T. Wheeler, "Force field comparisons of the heat capacity of carbon nanotubes," *Mol Simulat,* 2006, 32, 839-848.

[303] P. Politzer, J. Seminario, and P. Bolduc, "A proposed interpretation of the destabilizing effect of hydroxyl-groups on nitroaromatic molecules," *Chem Phys Lett,* 1989, 158, 463-469.

[304] J. Murray, P. Redfern, J. Seminario, and P. Politzer, "Anomalous energy effects in some aliphatic and alicyclic aza systems and their nitro-derivatives," *J Phys Chem,* 1990, 94, 2320-2323

[305] J. S. Murray, J. M. Seminario, and P. Politzer, "Does antiaromaticity imply net destabilization," *Int J Quantum Chem,* 1994, 49, 575-579.

[306] J. M. Seminario, M. C. Concha, and P. Politzer, "Calculated structures and relative stabilities of furoxan, some 1,2-dinitrosoethylenes and other isomers," *J Comput Chem,* 1992, 13, 177-182.

[307] D.-S. Choi, S. Huang, M. Huang, T. S. Barnard, R. D. Adams, *et al.*, "Revised structures of N-substituted dibrominated pyrrole derivatives and their polymeric products. Termaleimide models with low optical band gaps," *J Org Chem,* 1998, 63, 2646-2655.

[308] J. M. Seminario, M. C. Concha, and P. Politzer, "A density functional/molecular dynamics of the structure of liquid nitromethane," *J Chem Phys,* 1995, 102, 8281-8282.

[309] J. M. Seminario, M. C. Concha, J. S. Murray, and P. Politzer, "Theoretical analyses of O_2/H_2O systems under normal and supercritical conditions," *Chem Phys Lett,* 1994, 222, 25-32.

[310] J. M. Seminario, P. A. Derosa, L. E. Cordova, and B. H. Bozard, "A molecular device operating at terahertz frequencies: theoretical simulations," *IEEE Trans Nanotech,* 2004, 3, 215-218.

[311] E. Polak and G. Ribiere, "Note sur la convergence de méthodes de directions conjuguées," *Rev Fr Inform Rech Ope,* 1969, 3, 35-43.

[312] A. C. French, A. L. Thompson, and B. G. Davis, "High-purity discrete PEG-oligomer crystals allow structural insight," *Angew Chem Int Edit,* 2009, 48, 1248-1252.

[313] H. Lee, A. H. de Vries, S.-J. Marrink, and R. W. Pastor, "A coarse-grained model for polyethylene oxide and polyethylene glycol: conformation and hydrodynamics," *J Phys Chem B,* 2009, 113, 13186-13194.

[314] G. Hong, J. Z. Wu, J. T. Robinson, H. Wang, B. Zhang, *et al.*, "Three-dimensional imaging of single nanotube molecule endocytosis on plasmonic substrates," *Nat Commun,* 2012, 3, 700.

[315] A. A. Bhirde, S. Patel, A. A. Sousa, V. Patel, A. A. Molinolo, *et al.*, "Distribution and clearance of PEG-single-walled carbon nanotube cancer drug delivery vehicles in mice," *Nanomedicine-UK,* 2010, 5, 1535-1546.

[316] A. V. Filgueiras, I. Lavilla, and C. Bendicho, "Chemical sequential extraction for metal partitioning in environmental solid samples," *J Environ Monitor,* 2002, 4, 823-857.

[317] C. R. M. Rao, A. Sahuquillo, and J. F. Lopez Sanchez, "A review of the different methods applied in environmental geochemistry for single and sequential extraction of trace elements in soils and related materials," *Water Air Soil Pollut,* 2008, 189, 291-333.

[318] G. Characklis and M. Wiesner, "Particles, metals, and water quality in runoff from large urban watershed," *J Environ Eng,* 1997, 123, 753-759.

[319] D. Lenat and J. K. Crawford, "Effects of land use on water quality and aquatic biota of three north carolina piedmont streams," *Hydrobiologia,* 1994, 294, 185-199.

[320] S. A. Ansari, P. Pathak, P. K. Mohapatra, and V. K. Manchanda, "Aqueous partitioning of minor actinides by different processes," *Sep Purif Rev,* 2011, 40, 43-76.

[321] D. D. Sood and S. K. Patil, "Chemistry of nuclear fuel reprocessing: current status," *J Radioanal Nucl Chem,* 1996, 203, 547-573.

[322] K. Mayer, M. Wallenius, and I. Ray, "Nuclear forensics-a methodology providing clues on the origin of illicitly trafficked nuclear materials," *Analyst,* 2005, 130, 433-441.

[323] K. Mayer, M. Wallenius, and T. Fanghänel, "Nuclear forensic science—from cradle to maturity," *J Alloy Compd,* 2007, 444–445, 50-56.

[324] J. H. Buchmann, J. E. S. Sarkis, M. H. Kakazu, and C. Rodrigues, "Environmental monitoring as an important tool for safeguards of nuclear material and nuclear forensics," *J Radioanal Nucl Ch,* 2006, 270, 291-298.

[325] Y. Hanzawa, M. Magara, F. Esaka, K. Watanabe, S. Usuda, *et al.*, "Program to develop analytical techniques for ultra trace amounts of nuclear materials in

environmental samples," in *INMM 40th annual meeting*, Phoenix, Arizona, 1999, 40, 280136.

[326] H. J. Ache, "Analytical chemistry in nuclear technology," *Fresen J Anal Chem,* 1992, 343, 852-862.

[327] N. Kumar and J. M. Seminario, "A quantum chemistry approach for the design and analysis of nanosensors for fissile materials," in *Design and applications of nanomaterials for sensors*, J. M. Seminario, Ed., ed: Springer Netherlands, 2014, 16, 1-29.

[328] A. Y. Romanchuk, A. S. Slesarev, S. N. Kalmykov, D. V. Kosynkin, and J. M. Tour, "Graphene oxide for effective radionuclide removal," *Phys Chem Chem Phys,* 2013, 15, 2321-2327.

[329] N. Pan, D. Guan, T. He, R. Wang, I. Wyman*, et al.*, "Removal of Th4+ ions from aqueous solutions by graphene oxide," *J Radioanal Nucl Ch,* 2013, 298, 1999-2008.

[330] M. R. Ganjali, N. Davarkhah, H. Ganjali, B. Larijani, P. Norouzi*, et al.*, "A novel europium (III) sensor based on 4E-4-(2-phenylviazenyl)-2-((E)-(2-aminoethylimino) methyl) phenol," *Int J Electrochem Sci,* 2009, 4, 762-771.

[331] J. Liu, A. K. Brown, X. Meng, D. M. Cropek, J. D. Istok*, et al.*, "A catalytic beacon sensor for uranium with parts-per-trillion sensitivity and millionfold selectivity," *P Natl Acad Sci USA,* 2007, 104, 2056-2061.

[332] H. Boukhalfa, S. D. Reilly, W. H. Smith, and M. P. Neu, "EDTA and mixed-ligand complexes of tetravalent and trivalent plutonium," *Inorg Chem,* 2004, 43, 5816-5823.

[333] M. R. Ganjali, S. O. Ranaei-Siadat, H. Rashedi, M. Rezapour, and P. Norouzi, "Thulium selective sensor based on nanographene/RTIL/ionophore/graphite," *Int J Electrochem Sci,* 2011, 6, 3684-3693.

[334] G. Choppin and M. Jensen, "Actinides in solution: complexation and kinetics," in *The chemistry of the actinide and transactinide elements*, L. Morss, *et al.*, Eds., ed: Springer Netherlands, 2006, 2524-2621.

[335] R. Gulotty, S. Das, Y. Liu, and A. V. Sumant, "Effect of hydrogen flow during cooling phase to achieve uniform and repeatable growth of bilayer graphene on copper foils over large area," *Carbon,* 2014, 77, 341-350.

[336] S. Das, R. Gulotty, A. V. Sumant, and A. Roelofs, "All two-dimensional, flexible, transparent, and thinnest thin film transistor," *Nano Lett,* 2014, 14, 2861-2866.

[337] R. de Levie, "The electrolysis of water," *J Electroanal Chem,* 1999, 476, 92-93.

[338] O. Diaz-Morales, F. Calle-Vallejo, C. de Munck, and M. T. M. Koper, "Electrochemical water splitting by gold: evidence for an oxide decomposition mechanism," *Chem Sci,* 2013, 4, 2334-2343.

[339] J. Rossmeisl, A. Logadottir, and J. K. Norskov, "Electrolysis of water on (oxidized) metal surfaces," *Chem Phys,* 2005, 319, 178-184.

[340] X. Zhu, Q. Yuan, and Y.-P. Zhao, "Phase transitions of a water overlayer on charged graphene: from electromelting to electrofreezing," *Nanosc,* 2014, 6, 5432-5437.

[341] F. C. J. M. van Veggel and D. N. Reinhoudt, "New, accurate Lennard-Jones parameters for trivalent lanthanide ions, tested on [18]crown–6," *Chem–Eur J,* 1999, 5, 90-95.

[342] L. Zhang and X. Wang, "Computational insights of water droplet transport on graphene sheet with chemical density," *J Appl Phys,* 2014, 115, 194306.